

Investigation of Direct Injection Fuel Sprays in High Velocity Air Flows

by

Aaron Pereira

A thesis
presented to the University of Waterloo
in fulfilment of the
thesis requirement for the degree of
Master of Applied Science
in
Mechanical Engineering

Waterloo, Ontario, Canada, 2013

©Aaron Pereira 2013

I hereby declare that I am the sole author of this thesis. This is a true copy of the thesis including any required final revisions, as accepted by my examiners.

I understand that my thesis may be made electronically available to the public.

Abstract

The study of single-plume sprays into cross-flowing air is found extensively in literature, however, with the continued development of the Spark Ignition Direct Injection (SIDI) engine, the behaviour of multi-plume sprays in cross-flowing conditions is of interest.

In the present work, the injection of a multi-plume spray into a high-velocity cross-flow is investigated; an experimental apparatus capable of providing a cross-flow with core velocities higher than 200 m/s is developed; analysis techniques are developed to characterize the cross-flow and multi-plume spray independently; the multi-plume spray is characterized as it issues into the cross-flowing air.

The round air jet used for the cross-flow was designed using the concepts put forth for the design of wind tunnel contractions. The axial and radial velocities were measured using a Particle Image Velocimetry system from LaVision Inc. and the potential core length determined for the core velocities corresponding to Mach numbers of 0.35 and 0.58. It was determined that the potential core length increases with increasing Mach number and that increased compressibility, leads to reduced mixing within the core. Furthermore, velocity profiles of the air jet show that self-similarity is preserved within the shear layer of the initial region.

The multi-plume spray was also characterized in quiescent conditions for 10 and 15 MPa injection pressures. It was found that the penetration depth and spray width increased with increasing injection pressure, but that the spray angle decreased with increasing pressure. The increase in penetration depth is consistent with the findings presented in literature, while the decrease in spray angle with increasing pressure is contrary to literature.

Next, the multi-plume spray, injected at 10 and 15 MPa, is characterized as it issues into the cross-flowing air stream at Mach numbers equal to 0.35 and 0.58. The tail length and penetration are measured and it is found that for the first, the cross-flow velocity is the primary factor with higher cross-flow velocity resulting in a longer tail length, while for the latter, the injection pressure is the major factor, with higher injection pressures resulting in higher penetrations. That being said, the injection pressure does play a small role in the tail length, with the 15 MPa injection having a slightly longer tail length than the 10 MPa injection in the Mach number 0.58 cross-flow. This is attributed to the finer atomization, which is expected from the 15 MPa injection which leads to quicker entrainment of fuel droplets into the cross-flow.

The spray axis was predicted for each set of conditions from 0.1 ms to 1.0 ms after Start of Fuel (SOF). It was found that before 0.3 ms, the spray retains its multi-plume nature, while after 0.3 ms it behaves like a single-plume spray. Once the spray has crossed this transition point, the spray axis is temporally independent and can be predicted by the logarithmic models, similar to those used for single-plume sprays in cross-flow. The accuracy of this fit is improved upon, with the presentation of a modified correlation, which includes the momentum flux ratio inside of the logarithmic term.

Finally, the multi-plume spray issuing into the cross-flow is characterized using PIV to measure droplet velocities. It is observed that the cross-flow momentum is imparted to the smaller droplets within the 15 MPa spray more easily than to those of the 10 MPa injection, but that the 15 MPa sprays also retain their momentum in the radial direction longer than the 10 MPa sprays. As such, the 10 MPa sprays align with the cross-flow axis faster.

Acknowledgements

I would like to thank the Green Auto Power Train Project funded by the Ontario Research Fund and General Motors USA for supporting this research initiative and would especially like to thank Dr. Xianguo Li, for his guidance throughout my Master's program and for the numerous opportunities he has presented me with.

A special thanks to the staff from the Engineering Machine Shop and the MME support staff who were instrumental in helping us meet all our deadlines for this project.

Furthermore, my progress in this research would not have been possible without the extensive support and assistance of Queenie So who spent countless hours assisting with the design, construction, and operation of the experimental equipment; Dr. Doug Neal and the team at LaVision, who helped me manoeuvre my way through the PIV equipment; Dr. Sean Peterson for his insight into PIV techniques, and the world of experimentation. Also, thank you to Kaushik Saha, Dr. Ehab Abu-Ramadan, and Dr. Yi Ren for offering their expertise at every stage of this project.

Thank you to my wife Jasmine, and all of my family, who continued to support me through this process and have spent the last 5 years trying to understand my thesis topic. To my baby girl, Josephine, thank you for motivating me to finish my Master's so that I can now focus on getting to know you.

Contents

List of Tables	x
List of Figures	xiv
Nomenclature	xv
1 Introduction	1
1.1 Background	1
1.1.1 Operating Principles	1
1.2 Objectives	4
1.3 Organization	4
2 Review of Literature	5
2.1 Liquid Jets	5
2.2 Single-Plume jets in Cross-flows	8
2.3 Multi-Plume jets in Cross-Flows	20
2.4 Summary of Literature	20
3 Experimental Apparatus	22
3.1 Fuel Delivery System	22
3.2 Air Delivery System	25

3.2.1	Air Nozzle Design	25
3.2.2	Enclosure Configuration	27
3.3	Measurement System	29
3.3.1	Air Pressure and Temperature Measurements	29
3.3.2	Velocity and Planar Measurements	31
3.3.3	PIV Seeding	32
4	Experimental Procedure and Conditions	38
4.1	Calibration	38
4.2	Data Acquisition	41
4.2.1	Particle Imaging Velocimetry	41
4.2.2	Spray Imaging	45
4.3	Data Processing	46
4.3.1	Particle Imaging Velocimetry	47
4.3.2	Spray Imaging	51
5	Experimental Error	60
5.1	Calibration Error	60
5.2	Imaging Uncertainty	61
5.2.1	Imaging Averaging Error	61
5.2.2	Thresholding Error	64
5.3	PIV Uncertainty	66
5.3.1	Peak Locking	66
5.3.2	Perspective Error	68
5.3.3	PIV Averaging Error	71
5.3.4	Discussion of Errors from Literature	73
5.3.5	Summary of Overall Error	73

6	Results and Discussion	77
6.1	Air Flow Characterization	77
6.1.1	Jet Characteristics	78
6.2	Sprays in Quiescent Ambient Air	93
6.2.1	Spray Penetration	99
6.2.2	Spray Angle	100
6.2.3	Spray Width	102
6.3	Sprays in Cross-Flow Conditions	104
6.3.1	Planar Images	105
6.3.2	Spray PIV	127
7	Conclusions and Recommendations	135
7.1	Conclusions	136
7.2	Recommendations	138
	References	139
	APPENDICES	147
	Appendix A Axial and Radial Velocity, and TKE Plots for Air Jet	148
	Appendix B Images of Temporal Evolution of Quiescent Sprays	155
	Appendix C Images of Spray Axis and Raw Data for Sprays into Cross-flows	164
	Appendix D Curve Fit Parameters for Spray Axis and Correlation Values	184

List of Tables

2.1	Power-law Axis Deflection Correlations	16
2.2	Logarithmic Axis Deflection Correlations	17
3.1	Fuel Rail Pressure Transducer Parameters	23
3.2	Converging Section Design Parameters	27
3.3	Air Pressure Measurement Hardware	29
3.4	Pressure Transducers Specifications	30
3.5	Temperature measurement hardware	31
3.6	Camera Specifications	33
3.7	Local Stokes Number	36
5.1	Averaging Uncertainty on Spray Characteristics in Quiescent Conditions .	63
5.2	Averaging Uncertainty on Spray Characteristics in Cross-flow Conditions .	64
5.3	Spray Characteristic Uncertainty from Threshold in Quiescent Conditions .	65
5.4	Spray Characteristic Uncertainty from Threshold in Cross-flow Conditions	65
5.5	Peak Locking	67
5.6	Total measurement uncertainty for quiescent spray parameters	74
5.7	Total measurement uncertainty for cross-flow spray parameters	74
5.8	Total measurement uncertainty for PIV of cross-flow potential core	75
5.9	Total measurement uncertainty for PIV measurement of cross-flow shear layer	75

5.10	Total measurement uncertainty for PIV measurement of sprays	76
6.1	Air Flow Characteristics	78
6.2	Non-dimensional parameters for sprays in cross-flows	105
6.3	Legend for Spray Axis Graphs	120
6.4	Correlation curve fit parameters	125
6.5	Conditions for the new multi-plume spray axis correlation(Eq. 6.8 and the existing spray axis correlation(Eq. 2.23)	126
D.1	Definition for spray axis predictions	185

List of Figures

1.1	Methods of guiding fuel spray in partial load operation [4]	3
2.1	Spray Regimes [6]	6
2.2	Atomization Regime [7]	7
2.3	Secondary Breakup Regimes [1]	7
2.4	Deformation of Liquid Columns in Cross-flows	9
2.5	Illustration of Angled Spray	19
3.1	Fuel Injection System Schematic	23
3.2	Injector Hole Layout	24
3.3	Fuel Injector Current Profile Parameters	24
3.4	Cross-Sectional View of Air Nozzle	25
3.5	Air Nozzle Settling Region Component Dimensions	26
3.6	Experimental Setup	28
3.7	Traversing System	28
3.8	Pressure probes and thermocouple locations	31
3.9	Sheet Forming Optics	32
3.10	Laskin Nozzle Aerosol Generator	34
3.11	Vortex Formation	35
4.1	Scaled Calibration Board	39

4.2	Dot Matrix Calibration Board	40
4.3	PIV Timing Graph	42
4.4	Spray Geometry Timing Chart	47
4.5	Image processing of volumetric images	54
4.6	Definition of Spray Angle as Recommended by SAE J2715 [45]	55
4.7	Planar Illumination Light Intensity Variation Across Spray	58
4.8	Spray Tail Length Definition	59
5.1	Convergence of Parameters with Increasing Number of Images	62
5.2	Peak Locking Effect	67
5.3	Perspective Error Diagram	69
5.4	Perspective Error for Cross-flow Air Jet	70
5.5	Convergence of Mean Velocity with Increasing Number of Images	72
6.1	Illustration of a time-averaged air jet adapted from [61]	79
6.2	Cross-flow Velocity Contour Plots	80
6.3	Definition of Potential Core	81
6.4	$Ma_g=0.35$ and $Ma_g=0.58$ Mean Velocity Distribution	83
6.5	Cross-flow TKE Contour Plot	84
6.6	$Ma_g=0.35$ Instantaneous Velocity Vector Plots	85
6.7	$Ma_g=0.58$ Instantaneous Velocity Vector Plots	86
6.8	$Ma_g=0.35$ RMS Velocity Vector Plots	87
6.9	$Ma_g=0.58$ RMS Velocity Vector Plots	88
6.10	Cross-flow Measurement Locations	88
6.11	Cross-flow Velocity Profile Axis Definitions	89
6.12	Cross-flow Velocity Self-Similarity	90
6.13	Cross-flow Mean Velocity Profiles	91

6.14	Cross-flow Axial Mean Velocity Profiles	92
6.15	Cross-flow Radial Mean Velocity Profiles	94
6.16	Cross-flow TKE Profiles	95
6.17	10 MPa Quiescent Spray Development	97
6.18	15 MPa Quiescent Spray Development	98
6.19	Quiescent Spray Temporal Evolution of Penetration Depth	99
6.20	Quiescent Spray Temporal Evolution of Spray Angle	101
6.21	Quiescent Spray Temporal Evolution of Spray Width	103
6.22	Definition of Spray Width	104
6.23	Temporal Evolution of 15 MPa injection into $Ma_g = 0.35$ Cross-flow	106
6.24	Temporal Evolution of 10 MPa injection into $Ma_g = 0.35$ Cross-flow	107
6.25	Temporal Evolution of 15 MPa injection into $Ma_g = 0.58$ Cross-flow	108
6.26	Temporal Evolution of 10 MPa injection into $Ma_g = 0.58$ Cross-flow	109
6.27	Temporal Evolution of Spray Penetration in Cross-flow	111
6.28	Temporal Evolution of Spray Total Tail Length in Cross-flow	113
6.29	Droplet Size Distribution in Quiescent and Cross-flow Conditions	114
6.30	Droplet Size Distribution in Cross-flow Conditions	115
6.31	Temporal Evolution of Spray Downwind Tail Length in Cross-flow	116
6.32	Temporal Evolution of Spray Upwind Tail Length in Cross-flow	117
6.33	Schematic of Ellipse Defining Equivalent Diameter	119
6.34	Spray Axis for 15 MPa Injection into $Ma_g=0.35$ Cross-flow	121
6.35	Spray Axis for 10 MPa Injection into $Ma_g=0.35$ Cross-flow	122
6.36	Spray Axis for 15 MPa Injection into $Ma_g=0.58$ Cross-flow	123
6.37	Spray Axis for 10 MPa Injection into $Ma_g=0.58$ Cross-flow	124
6.38	Spray Axis Correlation Comparison	126

6.39 Velocity Vector Map for Sprays 1 ms After SOF	128
6.39 Velocity Vector Map for Sprays 1 ms After SOF	129
6.40 Velocity Variability Map for Sprays 1 ms After SOF	131
6.40 Velocity Variability Map for Sprays 1 ms After SOF	132
6.41 Number of Vectors Map for Sprays 1 ms After SOF	133
6.41 Number of Vectors Map for Sprays 1 ms After SOF	134

Nomenclature

Roman Symbols

A_C	Cross-sectional Area
A_F	Frontal Area
a	Speed of Sound
c_p	Specific heat capacity at constant pressure
d	Injector Diameter
d_P	Droplet Diameter
D	Air Nozzle Outlet Diameter
$D(x)$	Converging Section Diameter as a Function of X
D_1	Converging Section Inlet Diameter
D_2	Converging Section Outlet Diameter
g	Gravitational Acceleration
h	Height of Fluid Element
J	Mechanical Heat Equivalent
L	Injector Hole Length
L_o	Potential Core Length
m	Mass
P	Pressure
P_1	Air Nozzle Inlet Pressure
P_2	Air Nozzle Outlet Pressure
R_*	Gas Constant for Air
t	time
T	Temperature
T_1	Air Nozzle Inlet Temperature

T_2	Air Nozzle Outlet Temperature
T_o	Reference Temperature
T_{stag}	Stagnation Temperature
T_{static}	Static Temperature
u	Velocity
U_o	Cross-flow Velocity at Air Nozzle Outlet
x	Axial Coordinate
y_m	Maximum Penetration

Greek Symbols

α	Angle Between Spray and Cross-flow
ϵ	Percentage Error
γ	Specific Heat Ratio
μ	Dynamic viscosity
ν	Kinematic viscosity
ρ	Density
ρ_f	Non-cavitating Fluid Density
θ_{CA}	Cone Angle
θ_B	Bend Angle
θ_L	Left Half of Spray Angle
θ_R	Right Half of Spray Angle
θ_S	Spray Angle
σ	Surface Tension
τ_A	Particle Response Time
τ_F	Characteristic Time of Large Scale Structures

Non-dimensional Numbers

Cd	Drag Coefficient
C_V	Discharge Coefficient
Ma	Mach Number

Oh	Ohnsorge Number
q	Momentum Flux Ratio
Re	Reynolds Number
St	Stokes Number
We	Weber Number

Subscripts and Superscripts

<i>eq</i>	Ignition value
<i>g</i>	Gas/Air Phase
<i>H₂O</i>	Liquid Water
<i>i</i>	Inlet
<i>l</i>	Liquid/Fuel Phase
<i>inj</i>	Ignition value
<i>o</i>	Outlet
<i>P</i>	Droplet
<i>r</i>	Cross-flow Radial Direction
<i>rms</i>	root mean squared
<i>x</i>	Cross-flow Axial Direction
<i>y</i>	Injector Axial Direction
<i>z</i>	Out-of-plane Direction

Other Notation

Δt	Light Source Pulse Width
<i>dt</i>	Interframe time

Acronyms

EGR	Exhaust Gas Recirculation
-----	---------------------------

ECU	Engine Control Unit
FEV	Fully Electric Vehicle
GDI	Gasoline Direct Injection
HCCI	Homogeneous Charge Compression Ignition
HEV	Hybrid Electric Vehicle
MPI	Multi-port Injection
NO_x	Nitrous Oxide
PDF	Probability Density Function
PIV	Particle Image Velocimetry
RMS	Root Mean Square
RMSE	Root Mean Square of Error
SADI	Stand Alone Direct Injection
SIDI	Spark Ignition Direct Injection
SMD	Sauter Mean Diameter
SOF	Start of Fuel
SOI	Start of Injection
SSE	Squared Sum of Error
TKE	Turbulent Kinetic Energy
UHC	Unburned Hydro-carbons
VFD	Variable Frequency Drive

Chapter 1

Introduction

With increasing pressure from regulatory bodies to reduce emissions, auto makers have begun introducing low emission vehicles into their fleet to increase their average fuel economy and reduce the production of carbon dioxide. While the production of hybrid electric vehicles (HEV) and full electric vehicles (FEV) represents a major step towards these goals, issues with affordability and performance prevent widespread adoption. As a result, regular petroleum fuelled internal combustion power trains are still used in the vast majority of passenger vehicles, with HEV and FEV automobiles considered as longer term solutions. In the near term, the implementation of direct injection technologies in gasoline engines resulting in the spark ignition direct injection (SIDI) engine, also commonly referred to as the gasoline direct injection (GDI) engine, is becoming popular. The SIDI engine represents an advancement in gasoline engine technology, which directly reduces the emissions and improves fuel economy over the traditional multi-point injection (MPI) strategy which is commonly used. The benefits of the SIDI engine are especially prevalent in its cold start performance and its partial load operation [1].

1.1 Background

1.1.1 Operating Principles

The operating principles of the SIDI allow for fuel to be injected directly into the cylinder instead of into the intake manifold as is common with MPI. While MPI allows for the use of

lower fuel pressures and less atomization in the resultant spray, vaporization is dependant on fuel droplet impingement on the hot rear face of the closed intake valve and the wall of the cylinder head. During cold start applications, over spraying to achieve the required air fuel vapour mixture can produce liquid films and increase the emissions of unburned hydro carbons (UHC) [2]. It also means induction of fuel and air into the cylinder occur simultaneously during the intake stroke of the engine cycle. This provides a well-mixed (stoichiometric) or homogeneous charge to the engine, with the air-fuel ratio maintained at 14.7:1, regardless of the load or power output of the engine. Control of the engine output power is achieved through the use of a throttle, which controls the mass flow into the cylinder but, as a result, increases pumping losses under part loads when the throttle is not fully open [1, 2].

During cold start, the SIDI engine is able to inject fuel directly into the cylinder, unlike the MPI engine. The higher injection pressures necessary for direct injection, combined with the injector design, allows for substantially improved fuel atomization, with 87% smaller droplet Sauter Mean Diameters (SMD), which leads to improved fuel vaporization [2]. Furthermore, the SIDI engine can control engine power through the quantity of injected fuel mass, rather than air flow throttling, reducing the associated pumping losses. During partial load operation, the reduction in the required fuel mass allows for the engine to operate ultra lean, with the air fuel mixtures approaching 65:1[3]. In order to achieve ignition under ultra lean conditions, fuel is injected late during the compression stroke just before ignition. This allows the fuel mass to remain in an ignitable fuel rich cloud near the spark plug. As such a stratified charge is formed where the fuel rich zone is surrounded by a region of pure air or exhaust gas at the periphery of the cylinder. The stratified charge presents the added benefits of reducing thermal losses from the combusted material to the cylinder walls and the reduction of NO_x through exhaust gas recirculation (EGR).

In order to achieve the stratified charge used under partial loads, three different combinations of injector design and positioning, and piston head design are used to ensure that the fuel cloud remains ignitable and near the spark plug. The wall guided, air guided and spray guided techniques combine the design and positioning of the injector, and the design of the piston head to control the fuel mixture location as illustrated in Figure 1.1. The wall guided technique relies on the shape of the piston head to direct the impinging spray towards the spark plug, while the air guided technique uses the piston head shape and upward momentum to produce air currents which push the fuel towards the spark plug.

Finally, the spray guided technique relies on the position and design of the injector to spray directly near the spark plug. The design scenarios presented in Figure 1.1 also impact the

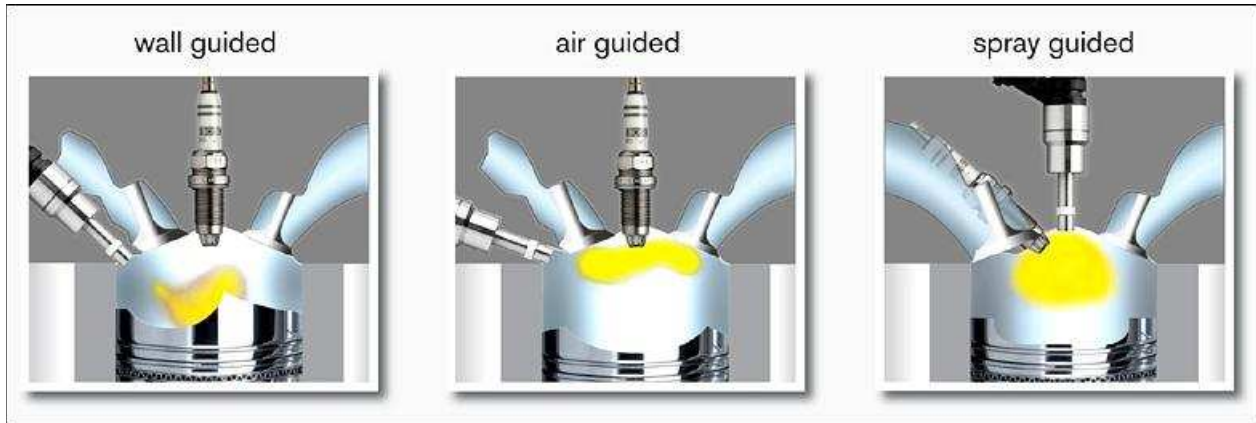


Figure 1.1: Methods of guiding fuel spray in partial load operation [4]

full load operation of the engine which relies on a homogeneous charge with an air fuel ratio reaching the stoichiometric 14.7:1. This is similar to an MPI strategy where the throttle is fully open without any restriction of flow. In the case of the SIDI engine, the fuel is injected into the cylinder during the intake stroke where the cylinder motion produces a lower pressure and draws air past the intake valves. This produces high instantaneous velocities near the intake valve which are dependent on the crank angle of the engine and the valve lift. Instantaneous air velocities around the valve can reach as high as 200m/s as noted by Ren et al.[5] who numerically investigated the effects of turbo-charging on the flow field near the intake port. The result is a strong cross-flow effect on the injected fuel mass combined with significant swirling and tumbling motion. Mixing is achieved through the interaction of the fuel and the incoming air.

The ability to predict the level of atomization, mixing and vaporization using numerical models is increasingly important as changes to injection and control strategies continue to evolve, in order to assist with design and improvements of the technology. This requires validation of each component of the numerical tools against experimental data including the ability of the intake air to interact with the injected fuel mass under homogeneous charge operation.

1.2 Objectives

The objective of this work is to study a multi-plume spray injected into high velocity cross-flow in conditions which emulate those experienced within an SIDI engine. To achieve this objective, an apparatus is designed and manufactured which is capable of producing air flows with velocities greater than 200 m/s to reflect the instantaneous velocities in a SIDI engine. A fuel injection system which uses a commercial multi-hole fuel injector, from General Motors, is used to inject fuels at pressures up to 15 MPa which is in the range of injection pressures for gasoline direct injection engines.

Characterization of the cross air flows is performed by Particle Image Velocimetry (PIV) using a system from LaVision Inc. Shadowgraphy techniques and PIV are also employed in analysing the spray behaviour as it interacts with the air cross-flow.

The results presented will be used as benchmark data for the purpose of spray model validation when modelling SIDI engines.

1.3 Organization

Chapter 2 reviews existing literature and the progress made in the area of sprays issuing into cross-flows. Chapter 3 describes the design of the experimental apparatus which will be used in the present work. Chapter 4 highlights the various measurement techniques applied and the associated uncertainty accompanying the measurement results. Characterization of the high speed cross-flow, spray patterns and the fuel air interactions are provided along with a discussion of the results in Chapter 6. A summary of the findings and recommendations for work are presented in Chapter 7.

Chapter 2

Review of Literature

2.1 Liquid Jets

In looking at the impact of air flows on liquid jets it is important to first consider the atomization process typical of injected fuels. In quiescent gases the breakup regimes used to describe the breakup of liquid columns into droplets are: drip, stable liquid jet, Rayleigh breakup, first and second wind-induced breakup and atomization breakup [1, 6]. Of these regimes, the formation of dense sprays is best described by the Rayleigh, first and second wind-induced and atomization regimes transitioning with increasing flow as illustrated in Fig. 2.1. The Rayleigh breakup regime involves the interactions between the liquid inertia and the surface tension while the remaining regimes involve aerodynamic forces. Atomization breakup generates droplet sizes which are smaller than the injector diameter and occurs when breakup occurs at the injector exit [6]. The atomization regime of a pressure atomized spray is popular amongst combustion cycles as it can provide rapid liquid/gas phase mixing to support the process [7]. As such, it will be the only breakup regime considered moving forward.

The images of the atomization breakup regime in Figs. 2.1 and 2.2 show that the dense spray contains both a liquid core region which is similar, although typically longer in lengths to the potential core in a single phase jet, and a dispersed flow region which surrounds the liquid core and is composed of droplets and ligaments. In the instance of fuel injection pertaining to automotive applications, injections which are in the atomization

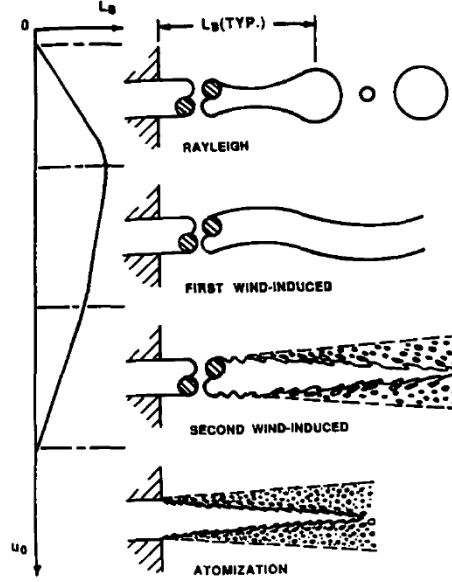


Figure 2.1: Spray Regimes [6]

regime are considered to have a negligible liquid core length and breakup occurs at the injector outlet. The droplets which form from these injections have diameters less than that of the injector diameter.

Droplets are produced via two mechanisms. Primary Breakup and Secondary Breakup. Primary breakup occurs due to aerodynamic forces which cause instabilities to form on the surface of the liquid core. These surface waves develop and are eventually stripped from the surface into droplets. Turbulence breakup is also a form of primary breakup, in which turbulent disturbances overcome the surface tension to form droplets, although, for automotive fuel injectors breakup due to aerodynamic forces is more prevalent [6].

Secondary breakup is responsible for the further breakup of droplets and ligaments into smaller droplets. As illustrated in Figure 2.3 secondary breakup begins with the deformation of the droplets and the liquid Weber number We_l and the Ohnesorge number Oh defined below Eqns. 2.1 and 2.2 dictating which form of deformation and breakup occurs [8].

$$We_l = \frac{\rho_l u_p^2 d_p}{\sigma} \quad (2.1)$$

$$Oh = \frac{\mu_l}{\sqrt{\sigma \rho_l d_p}} \quad (2.2)$$

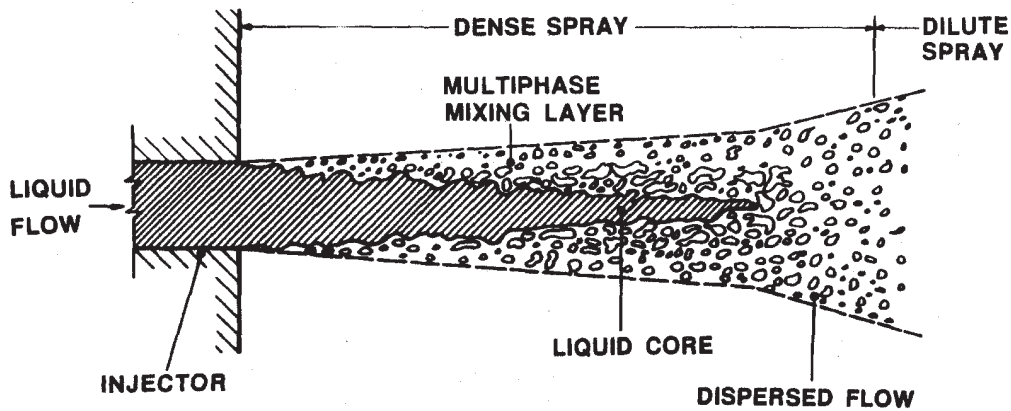


Figure 2.2: Atomization Regime [7]

Here, We_1 describes the ratio between drag and surface tension forces and is calculated using the relative velocity between the liquid droplet and the gas phase, and the initial droplet diameter. When considering sprays in quiescent air, liquid velocity u_l to be representative of the relative velocity u_p as the air velocity is negligible, and the injector diameter (d) can be used in place of the initial droplet diameter d_p . Oh represents the ratio between the liquid viscous forces and the surface tension forces and is based on the liquid properties. It is shown that with increasing Oh number the breakup time increases as the increased liquid viscosity resists deformation and thus the breakup in any of the three regimes.

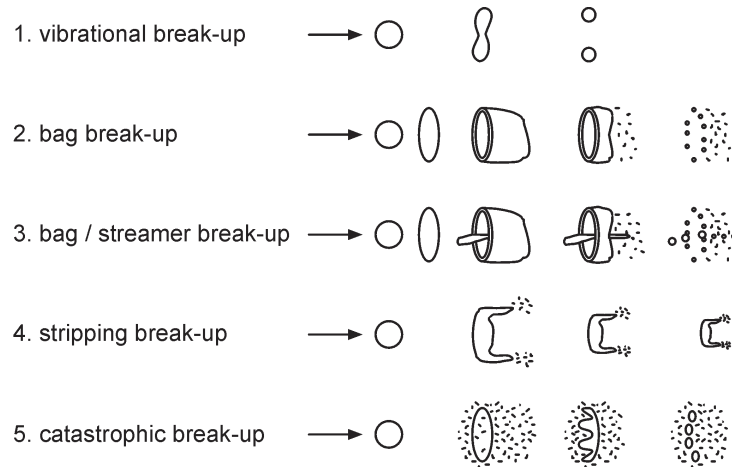


Figure 2.3: Secondary Breakup Regimes [1]

Bag breakup involves the deformed droplet forming a dome shape where the stagnation point on the droplet surface is at the center and involves both drag and surface tension interactions in the breakup [9].

Shear breakup, or stripping breakup as it is termed in Fig. 2.3 is almost opposite of the bag breakup where the stagnation points form on the outer edge of the deformed droplet and involves the drag and viscous forces and is observed at higher relative velocities.

The common theme amongst the breakup regimes and breakup modes is the existence of instabilities due to an increase in aerodynamic, viscous or turbulent forces that are able to overcome the surface tension forces which hold the liquid droplets together. With the introduction of the air cross-flow the discussion of breakup holds intact although the added momentum of the air flow and the implied relative velocity leads to increased instabilities and thus breakup.

2.2 Single-Plume jets in Cross-flows

As discussed in the previous sections, the atomization of fuel sprays is used to produce droplets with high surface area to volume ratios to promote rapid vaporization. The ability of a fuel nozzle to promote atomization in stagnant air is dependent mostly on the fuel properties and the injection itself, with the disintegration of the liquid column and larger droplets being attributed to instabilities in the fluid. Leong [10] noted that the injection of fuel transversely into a gaseous cross-flow with strong enough momentum is one method of inducing additional instability to promote atomization. Mashayek et al.[11] further explains that the penetration of the liquid jet into the cross-flow allows for an increased exposure of the jet to the air flow and as a result is one of the main characteristics of a liquid column in a cross-flow.

In considering the penetration of the liquid jets into the cross-flow, the relative strength of the gas phase relative to the liquid phase as expressed by the momentum ratio q , defined by Eq. 2.3, becomes a useful non-dimensional parameter.

$$q = \frac{\rho_l u_l^2}{\rho_g u_g^2} \quad (2.3)$$

This ratio is typically used to describe the ability of the cross-flow to deflect or change the spray trajectory [11]. Increasing q means higher fuel spray momentum which leads to a greater penetration into the the air flow and less deflection, while the opposite holds true for lower values of q .

The aerodynamic forces, which impact the liquid jet as it penetrates the cross-flow, also serve to change the cross-sectional shape of the liquid jet. A jet, with an initially circular cross-section, will begin to flatten and turn elliptical, as seen in Fig. 2.4. Eventually, as it continues to flatten and the aerodynamic forces continue to act upon it, the cross-section will resembling a fish-head structure, as noted by Mashayek et al.[11]. This phenomenon increases both with decreasing q , increased momentum of the cross-flow, and increasing distance from the jet outlet.

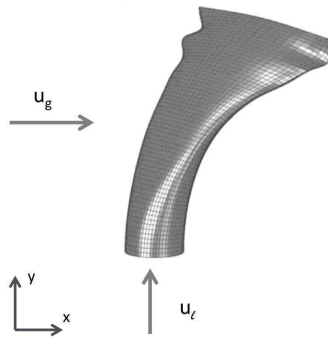


Figure 2.4: Deformation of liquid column in cross-flows adapted from [12]

During the deformation of the liquid column, surface waves and internal waves lead the column to breakup into ligaments and large droplets. The point at which the tip of the liquid column begins shedding ligaments and droplets is referred to as the column breakup point [11].

In describing the penetration of the liquid jet it is important to note that the terminology of the spray penetration, which refers to the upper boundary or windward boundary of the spray, and the spray trajectory, which refers to the axis of the spray, begin to have the same meaning as the jet begins to flatten [11, 13]. The leeward side or lower boundary is not similar to the jet trajectory as it is defined by the droplets and ligaments which are stripped from the surface of the jet, and are no longer connected to the liquid column.

Predicting the trajectory of the spray in the presence of a cross-flow can be performed

using two methodologies as illustrated by Mashayek et al.[11]. For the first method, it is assumed that:

Method I:

- Liquid momentum is initially only in the transverse direction and gas momentum is initially only in the axial direction
- The cross-sectional area, shape and mass of the spray remains constant along the length of the jet
- Gas velocity acts uniformly on the jet

These assumptions allow for the drag force to be the only force acting on the liquid column, and lead to the assumption that the drag coefficient (C_d) remains constant. This drag force is responsible for the axial displacement of the fluid element while the initial liquid momentum is responsible for the transverse displacement of the fluid element. A force balance expressing the acceleration of the element in the axial direction in terms of the drag force, can be written as:

$$\frac{1}{2}\rho_g u_g^2 A_F C_d = \rho_l A_C h \frac{d^2 x}{dt^2} \quad (2.4)$$

where A_F represents the frontal area of the fluid disc with diameter d and thickness h , A_C is the cross sectional area of the disc.

Integrating twice and recognizing that the location of this disc in transverse y direction is governed by $y = u_j t$ results in an equation of the form

$$\frac{y}{d} = Aq^m \left(\frac{x}{d}\right)^s \quad (2.5)$$

where q is the momentum ratio and A , m and s are constants. From the force balance m and s are found to be equal to 1/2, and A incorporates C_d . From Eqn. (2.5) the momentum ratio is proven to be an influential parameter on the jet deflection.

Method II: The second methodology predicts the trajectory by considering the motion of the droplets formed at the point of column breakup. Acknowledging that the trajectory and the upper boundary of the deflected spray (seen on the windward side of the spray) typically follow the same relationship and are in close proximity for the range of typical

momentum ratios it is convenient to consider them as redundant terms. With this similarity, the larger droplets which tend to carry the majority of the fluid momentum will define the upper boundary of the spray with their ability to penetrate further. Applying a similar force balance on an individual droplet for the axial and transverse direction independently, and further assuming that the droplets do not evaporate or interact, yields

$$\frac{1}{2}A_F\rho_g\left(u_g - \frac{dx}{dt}\right)^2C_{dx} = m\frac{d^2x}{dt^2} \quad (2.6)$$

$$-\frac{1}{2}A_F\rho_g\left(\frac{dy}{dt}\right)^2C_{dy} = m\frac{d^2y}{dt^2} \quad (2.7)$$

Here m represents the droplet mass, A_F represents the frontal area of the droplet and C_{dx} and C_{dy} are the drag coefficients acting in each direction. Integrating these expressions and applying the boundary conditions of $x = 0$ and $dx/dt = 0$ at $t = 0$ and $y = 0$ and $dy/dt = u_l$ at $t = 0$ gives

$$x = u_g t - \frac{2m}{A_F\rho_g C_{dx}} \ln\left(1 + u_g \frac{A_F\rho_g C_{dx}}{2m} t\right) \quad (2.8)$$

$$y = \frac{2m}{A_F\rho_g C_{dy}} \ln\left(1 + \frac{A_F\rho_g C_{dy}}{m} u_l t\right) \quad (2.9)$$

Mashayek et al.[11] note that sub-millimetre droplet diameters, and the ability of the droplets to reach their settling velocity in under a second allow the natural logarithm in Eq. (2.8) to become 0, giving $x = u_l t$, which can be substituted into Eq. (2.9). Furthermore, Mashayek et al.[11] acknowledge that C_{dy} is dependent on both u_g and u_l , and conclude that a dependence on momentum ratio exists where C_{dy} is found. These assumptions give

$$\frac{y}{d} = A \ln\left(1 + C \left(\frac{u_l}{u_g}\right) \left(\frac{x}{d}\right)\right) \quad (2.10)$$

where A and C incorporate the drag coefficients, liquid and gas densities, and geometric parameters.

Both solutions for the trajectory have been applied experimentally with researchers modifying the exponents and the coefficients to improve the accuracy of the fit. Wu et al.[14] evaluated the near field spray trajectory of a single liquid column up until the

location of breakup using the power law formulation in Eq. (2.5). The study examined momentum ratios between 3.38-185 noting that the breakup regimes experienced by a liquid column are similar in nature to the secondary aerodynamic breakup modes with deformation of the column initiating breakup. Furthermore, it was observed, that the gas phase Weber number We_g defined below was an indicator for the type of breakup, from bag-breakup occurring at low values to a shearing process at larger values similar to that experienced by droplets.

$$We_g = \frac{u_g^2 d \rho_g}{\sigma} \quad (2.11)$$

Larger values of q led to the stripping of droplets from the surface of the deformed edges and then to waves. The prominence of the waves was also impacted by the viscosity of the injected liquid with higher viscosity leading to larger and more distinct waves. The point of fracture was found to occur at a constant distance of 8 injector diameters (d) downstream of the injector for varying values of d and injection conditions.

We_g , is similar to We_l when it is calculated for the liquid column, but uses the air velocity of the free stream u_g rather than the liquid velocity u_l . Since the liquid injection occurs normal to the cross-flow, u_g is considered to be the relative velocity in the cross-flow direction. Wu et al.[14] finally presented the correlation for the spray trajectory as follows

$$\frac{y}{d} = 1.37q^{0.5} \left(\frac{x}{d}\right)^{0.5} \quad (2.12)$$

Mashayek et al.[15] compared a number of correlations for the spray axis at a momentum ratio of 15 and for $0 \leq \frac{x}{d} \leq 10$, illustrating that discrepancies exist between the predicted axes. These discrepancies were attributed to experimental errors and the difficulties associated with defining the spray boundaries, as well as the fact that each correlation caters to the prescribed range of experimental conditions for which it was developed. Thus, they asserted that parameters other than the momentum ratio play an important role in the prediction of the spray axis as well.

Desantes et al.[13] performed a numerical and experimental study on turbulent gas jets and diesel sprays in cross-flows with the intention of finding the normalized coordinates to assist in understanding the deflection phenomenon and the relationship between the parameters. Varying the injection pressures from 30 to 100 MPa, the cross-flow density from 10 to 30 kg/m^3 and velocity from 1 to 8.4 m/s , Desantes et al.[13] analyzed a matrix

of scenarios. While not explicitly listing the momentum ratios studied it can be estimated that with the high injection pressures, the liquid velocity would be as high as 390 m/s given the relationship for velocity used by Desantes et al.[13] as

$$u_l = C_V \sqrt{2P_{inj}/(C_\rho \rho_f)} \quad (2.13)$$

where C_V accounts for losses in the nozzle (equal to 0.8) [13], C_ρ the effect of cavitation on the density (assumed equal to 1), ρ_f is the non-cavitating liquid density, and P_{inj} is the injection pressure.

This estimate would result in the momentum ratios in the order of 10^3 for the extremely low cross-flow velocities. Their expression for the jet trajectory is

$$\frac{y}{d} = 0.582q^{0.302} \left(\frac{x}{d}\right)^{0.36} \left[\tan\left(\frac{\theta_{CA}}{2}\right)\right]^{-0.64} \quad (2.14)$$

Eq. 2.14 has been non-dimensionalized in order to allow for a direct comparison with the form presented by Wu et al.[14]. Through the normalization process, Desantes et al.[13] introduced the term $\tan(\frac{\theta_{CA}}{2})$ which is the half cone angle of the spray plume under quiescent conditions.

As shown by Varde [16] the spray cone angle for a non-evaporating atomized spray is proportional to the density ratio, the liquid Reynold number and the liquid Weber number as given below

$$\tan \theta_{CA} = A_1 \left(\frac{\rho_g}{\rho_l}\right)^{1/3} (\text{Re}_l)^{1/3} (\text{We}_l)^{A_2} \quad (2.15)$$

where $A_2 = d/L - 1/3$ and A_1 is an empirical constant. In the power law form the density ratio is considered in the momentum ratio and hence, the addition of $\tan(\frac{\theta_{CA}}{2})$ results in an addition of the liquid Reynold and Weber numbers into the power law.

The effect of the Reynolds number on the spray axis is also considered in the work of Amighi et al.[17] who considered the effects of elevated pressures and temperatures of the cross-flow on the centerline trajectory and the windward boundary trajectory. The correlations presented by Amighi et al.[17] are developed for $10 \leq q \leq 80$, $298K \leq T \leq 573K$, $207kPa \leq P \leq 517kPa$, and given below

$$\frac{y}{d} = 0.91q^{0.30} \left(\frac{x}{d}\right)^{0.43} Re_g^{0.12} Re_1^{0.14} \quad (2.16)$$

$$\frac{y}{d} = 0.167q^{0.31} \left(\frac{x}{d}\right)^{0.37} Re_g^{0.11} Re_1^{0.15} \quad (2.17)$$

where Eq. (2.16) is for the spray axis while Eq. (2.17) is for the windward edge. Amighi et al.[17] considered both the gas phase and liquid phase Reynolds number in the correlation attesting that consideration of the liquid atomization and droplet distribution is also important. Introduction of the gas phase Reynolds number accounts for the ability of the cross-flow to enhance the atomization and breakup of the liquid column. The effect of the gas phase on atomization was recognized by Ingebo[18] when he proposed spray trajectory should be dependent on the maximum droplet size as the larger droplets would penetrate further into the cross-flow. Experimentally Ingebo[18] found that the maximum droplet diameter was proportional to $We_g^{-0.7}$ where We_g is known as the gas phase Weber number, a ratio between the momentum of the gas phase and the surface tension force of the liquid. This term, as defined in Eq. (2.11), characterizes the ability of the aerodynamic forces present in the cross-flow to break up the liquid jet and form droplets, ligaments and smaller droplets.

Ingebo[18] used the relationship between the droplet size and We_g in his correlation for the maximum penetration given below

$$\frac{y_m}{d} = 1.8 \left(\frac{Re_1}{We_g}\right)^{0.7} \quad (2.18)$$

where y_m is the maximum penetration at a prescribed distance downstream of the injector. The gas phase Weber number has since been used in the prediction of the spray axis [19, 20]. Stenzler et al.[19] developed a correlation for both heated and unheated cross-flow air conditions which would account for the effect that the liquid viscosity has on the windward trajectory. The conditions studied were $9 \leq q \leq 18$, $0.9 \leq We_g \leq 164.3$, and $291K \leq T \leq 573K$. The resulting correlations for the heated and unheated air flows, respectively are given below

$$\frac{y}{d} = 2.63q^{0.442} We_g^{-0.088} \left(\frac{x}{d}\right)^{0.391} \left(\frac{\mu_1}{\mu_{H_2O}}\right)^{-0.027} \quad (2.19)$$

$$\frac{y}{d} = 2.898q^{0.43}We_g^{-0.11} \left(\frac{x}{d}\right)^{0.384} \left(\frac{\mu_1}{\mu_{H_2O}}\right)^{-1.08} \quad (2.20)$$

Here μ_1 represents the liquid viscosity and μ_{H_2O} the viscosity of liquid water. Both values are taken at 293 K which is the temperature of the injected liquid.

Ragucci et al.[20] used a similar correlation in the study of the spray axis at an elevated cross-flow temperature of 600K. The study considered $5 \leq q \leq 280$ and $7 \leq We_g \leq 340$, leading to the correlation

$$\frac{y}{d} = 2.28q^{0.422}We_g^{-0.015} \left(\frac{x}{d}\right)^{0.367} \left(\frac{\mu_g}{\mu_{g,300K}}\right)^{0.186} \quad (2.21)$$

Unlike Stenzler et al.[19], Ragucci et al.[20] considered the variation of air viscosity, μ_g , with temperature, hypothesizing that higher air viscosities would lead to increased deflection of the liquid jet.

Mashayek et al.[15] identified 2 major parameters which affect the jet penetration and trajectory prediction. Their model uses We_g as calculated by Eq. (2.11), and the drag coefficient.

The ability of We_g to detect the amount of breakup from the liquid column, directly impacts the trajectory of the main column. As droplets are stripped away, or the column deforms the mass and diameter will change as will the cross sectional shape. These changes impact the frontal area and mass, upon which the air stream is acting, affecting the drag and deflection.

As such, the prediction of the drag coefficient which is typically considered as a constant value such as that for a cylinder or ellipse [15, 21] or an empirical constant [14, 22] should be ideally considered as an adaptive value which is dependent on the local conditions of the jet at every distance from the injector outlet [15]. Similarly, the We_g should be considered locally to account for the local conditions, and the probability of droplet formation at that specific location.

From the preceding review of literature, a general form of the power law spray correlation may be presented as follows:

$$\frac{y}{d} = Aq^m We_g^n \left(\frac{x}{d}\right)^s (Z)^t \quad (2.22)$$

it includes the impacts of the q , We_g and the varying constant Z which can represent a number of other parameters as previously discussed. Table 2.1 gives the constants and exponent values used in the previously discussed studies as well as the main conditions for which they are valid.

	A	m	n	s	Z	t	q	We_g	Ma_g (Vel m/s)	T K (P kPa)
Wu et al.[14]	1.37	0.5	0	0.5	0	0	4-185	57-1179	0.2-0.4 (68-141)	30 (140)
Desantes[13]	0.582	0.302	0	0.360	$\tan(\frac{\theta_{CA}}{2})$	-0.64	0	0	(1-8.4)	NA
Amighi a)[17]	0.191	0.30	0	0.43	$Re_g^{0.12}Re_l^{0.14}$	1	10-80	20-487	(22-156)	298-573 (206-517)abs
Amighi b)[17]	0.167	0.31	0	0.43	$Re_g^{0.11}Re_l^{0.15}$	1	10-80	20-487	(22-156)	298-573 (206-517)abs
Ragucci b)[20]	2.28	0.442	-0.015	0.367	$\frac{\mu_g}{\mu_{g,300K}}$	0.367	5-280	7-340	(20-55)	300-600 (2000)
Stenzler a)[19]	2.63	0.442	-0.088	0.391	$\frac{\mu_l}{\mu_{H_2O}}$	-.027	9-18	1-164	(10-119)	291-673
Stenzler b)[19]	2.898	0.43	-0.11	0.384	$\frac{\mu_l}{\mu_{H_2O}}$	-.108	9-18	1-164	(10-119)	291

Table 2.1: Power-law Axis Deflection Correlations

The logarithmic spray axis correlation which is the other major form used to predict the spray axis in literature can be represented by the following form:

$$\frac{y}{d} = Aq^m \ln[B + C \left(\frac{x}{d}\right)]Z^t \quad (2.23)$$

where A, m, B, C, Z, t are constants which are manipulated by researchers based on the conditions of their individual studies. The conditions and values for the constants have been summarized in Table 2.2.

	A	m	B	C	Z	t	q	We_g	Ma_g (Vel m/s)	T K (P kPa)
Inamura et al.[23]	1.18 + 0.24d	0.36	1	1.56 + 0.48d	0	0	3- 12	NA	(55-140)	NA
Becker et al.[24]	1.48	0.42	1	3.56	0	0	1- 40	90- 2120	(50-100)	290 (150-1500)
Lakhamraju a)[25]	2.004	0.438	1	1.267	$\frac{T_{stag}}{T_o}$	-0.251	1.1- 49.7	48.6- 968.4	0.21-0.68 (85.8- 285.5)	294.3-499.8
Lakhamraju b)[25]	1.971	0.438	1	1.279	$\frac{T_{static}}{T_o}$	-0.236	1.1- 49.7	48.6- 968.4	0.21-0.68 (85.8- 285.5)	294.3-499.8
Lakhamraju c)[25]	1.792	0.477	1	1.338	$\frac{T_l}{T_o}$	-0.422	1- 50.5	48.6- 968.4	0.21-0.68 (85.8- 285.5)	294.3-501.4

Table 2.2: Logarithmic Axis Deflection Correlations

Inamura et al. [23] compared slurry jets and liquid jets under momentum ratios between 3 to 12 with air velocities in the range of 55 to 140 m/s . From Table 2.2 it is evident that the spray axis is impacted only by the momentum ratio. This is consistent through the works of Becker et al.[24], Tambe [26] and Lakhamraju [25].

Becker et al.[24] extended the momentum range from 1 to 40 with We_g varying between 90 and 2120 with the chamber pressure varying between 150 to 1500 kPa at a constant temperature. Becker et al.[24] noted that at higher We_g numbers surface breakup was dominant due to the ability of the cross-flow to overcome the surface tension of the liquid column. Alternatively, if the kinetic energy of the cross-flow is not high enough then breakup is dependent on the ability of the cross-flow to amplify instabilities that already exist in the liquid column after it is deflected in the axial direction. Mazallon et al.[27] found that for values of q greater than 100 the breakup is dependent on We_g in the case of non turbulent liquid jets.

Lakhamraju [25] investigated the effects that temperature increases in the cross-flow and liquid column would have on the spray trajectory and the breakup, specifically noting that increases in the liquid temperature resulted in a decrease in liquid penetration. The correlations a) and b) found in Table 2.2 are for the cases with a heated cross-flow and

include a modifier based on the air temperature. Here T_o in Z shown in Table 2.2 is the reference temperature taken to be 294 K, T_{stag} is the stagnation temperature due to the orientation of the thermocouple in the airflow, and T_{static} is the static temperature which is calculated from the measured parameters. The cross-flow static temperature ranged from 294.3 K to 501.4 K.

For the Lakhamraju c) correlation, shown in Table 2.2, T_l is the liquid temperature for the cases where the liquid jet was heated. Here the liquid is heated from 294.3 K to 338.7 K. For all three correlations, the momentum ratio is varied between 1.1 and 50.5 while the We_g is varied between 48.6 and 968.4. As illustrated, Lakhamraju [25] used normalized temperatures of the liquid column and the air column to account for the changes in the spray trajectory.

Angled Sprays in Cross-Flow

The previous section considered the scenarios where the spray issued into the cross-flow transversely to the cross-flow axis. However, the effect of injection angle on the breakup and spray trajectory when injecting into cross-flows is important in the application of direct injection engines. The use of multi-plume injectors leads to oblique injections into the cross-flow. As a result, the impact of the injection angle on the breakup and spray trajectory is important when analyzing the overall mixing and atomization. Available literature considering this impact of the injection angle is limited. The injection angle is represented by α in Fig. 2.5. Acute angles align the spray with the cross-flow while obtuse angles create a counter flowing scenario.

Kim et al.[28] varied α from 30° to 150° to asses the impacts of injection angle on the spray for a range of injection pressures corresponding to momentum ratios between 21 and 105. The coordinates of the breakup point of the liquid column was used to illustrate the impact of injection angle. Their study presented correlations which account α when predicting the breakup point. Kim et al.[28] found that for $60^\circ \leq \alpha \leq 120^\circ$, axial penetration remained similar to that of injections issuing normal to the cross-flow. For $\alpha = 30^\circ$ and $\alpha = 150^\circ$ the axial break up locations were the same in magnitude although occurred in opposite directions, and were larger than break up locations of smaller angles. In these instances it was found that the orientation of the injector led to breakup due to the liquid velocity rather than the aerodynamic forces of the cross-flow since the injector

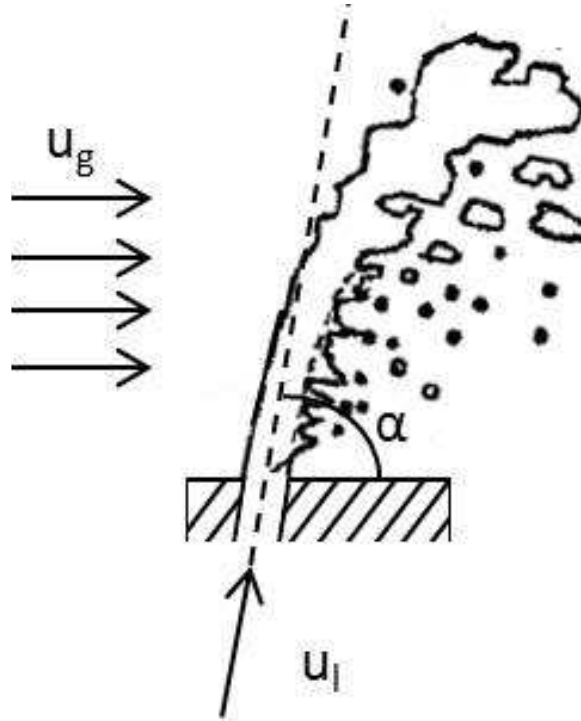


Figure 2.5: Illustration of Angled Spray adapted from [14]

approached a co-flow arrangement.

For the transverse penetration Kim et al.[28] found that the maximum occurred with the injection occurring normal to the cross-flow, decaying as the injector became more parallel.

Costa et al.[29] considered injection angles between 15° and 45° for momentum ratios between 25.7 and 637.4 with We_g ranging from 1.32 to 3.42. Their study investigated at the droplet size and droplet velocities and the impact that the injection angles had on these parameters. They noted that mean droplet diameters decreased as the injection angle increased due to the increase in aerodynamic forces from the cross-flow. Furthermore, their study found for the specified conditions that the injection angle played a larger role in controlling the penetration and atomization quality of the injector than the momentum ratio.

2.3 Multi-Plume jets in Cross-Flows

The study of multiple or interacting jets is another aspect of the multi-plume injection for SIDI which is found in literature. Due to the shaping of the injector multi-plume SIDI sprays experience interaction between jets under ambient conditions as noted by Abraham et al.[30]. Abraham noted that there exists an optimum angle between adjacent jets, and decreasing this angle resulted in increased jet to jet interaction with decreased mixing. Furthermore, Yu et al.[31] studied the behaviour of multiple jets aligned in tandem when exposed to a cross-flow. In this study the initial cross-flow velocity varied from 0.04 to 0.28 m/s with the jet velocity ranging between 59.8 to 89 m/s . The results suggest that the leading jet has a sheltering effect on the downstream jets and that there exists a reduced effective cross-flow velocity which acts on the subsequent downstream jets. This velocity was found to depend on the velocity ratio between the cross-flow and the jet as well as the spacing between jets. Jet trajectories were predicted until the point where the multiple jets merge.

2.4 Summary of Literature

As illustrated through a search of literature, it is apparent that the research focus is mainly on single liquid columns injected transversely into cross-flows with substantial background on the breakup of liquid columns in quiescent environments. Parallels have been drawn between the secondary breakup regimes and the breakup experienced by a liquid column, noting that deformation of the liquid remains an initial condition in the breakup process. Researchers have used various techniques to identify the level of mixing and have noted that the spray trajectory and penetration are related to the level of mixing that occurs in a transverse injection into a cross-flow. In quantifying the spray trajectory, literature reports that either the center axis of the spray or the windward edge are commonly used with both approaching one another as the spray is deflected and the column is deformed. Two main models are used in when considering the spray trajectory of a single liquid column, the first being a force balance between the drag forces on a cylinder and the liquid acceleration. The second considers the same balance using the geometry of a droplet. Regardless, correlations agree that for all flow conditions the momentum ratio has a significant impact on the deflection experienced by the spray. Other secondary parameters which have been used

include the gas phase Weber number, or the Reynolds numbers of the gas and or liquid phases. The purpose of these secondary parameters is to capture the effects of the loss of mass through surface stripping and breakup of the liquid column as well as the varied drag force which accounts for the changing cross sectional area. Numerical work has pointed out that increased predictive capabilities are attained through a local consideration of these secondary parameters.

Furthermore researchers have investigated the effects of elevated temperatures in both the gas phase and liquid phases and the effects of elevated temperatures in the injected liquid.

While the subject of single injections in cross-flows seems relatively well researched, there is little study for the impacts of changing injection angles or the case of multiple plumes injected into cross-flows. In comparing with the conditions in SIDI engines, it appears that few studies have considered the conditions of low momentum flux ratio (relatively high cross-flow momentum) and high gas phase Weber number (indicative of high pressure sprays) simultaneously. Moreover, experimental investigations of angled and multi-plume sprays are currently performed for limited cases approaching low liquid momentum flow rates which are not applicable to SIDI technology.

As such it appears that an investigation into multi-plume injections into high velocity cross-flows in the order of 200 m/s and injection pressures in the range of practical operating conditions of SIDI engines is necessary, and it is the subject and focus of the present study.

Chapter 3

Experimental Apparatus

The experimental apparatus consists of two essential components: the fuel delivery system and the air delivery system. A measurement system is used for the characterization of the resulting sprays. The components of these systems and their set-up will be described in this chapter.

3.1 Fuel Delivery System

The fuel delivery system highlighted by the red border in Fig. 3.1 is designed to deliver pressurized fuel sprays between 0 and 15 MPa. The system supplies compressed Nitrogen gas at the desired fuel pressure to a constant pressure cylinder or accumulator provided by Welker. This cylinder contains a floating piston which allows for the pressurized fuel and nitrogen to remain isolated from one another. This cylinder can hold pressurized fuel up to 24 MPa. The accumulator, which acts as a storage container, delivers the pressurized fuel to a common rail. The common rail acts as a manifold delivering fuel to each of the injectors. For the present study, the unused injector ports remain plugged.

The common rail monitors pressure using a built in transducer, which measures pressures from 0 to 20 MPa. The measured pressure scales linearly with the voltage of the transducer which ranges from 0.5 to 4.5 VDC as listed in Table 3.1.

The injector is a solenoid injector which hosts 6 holes from which fuel is injected. The holes are arranged in an elliptical pattern and are symmetric about the major and minor

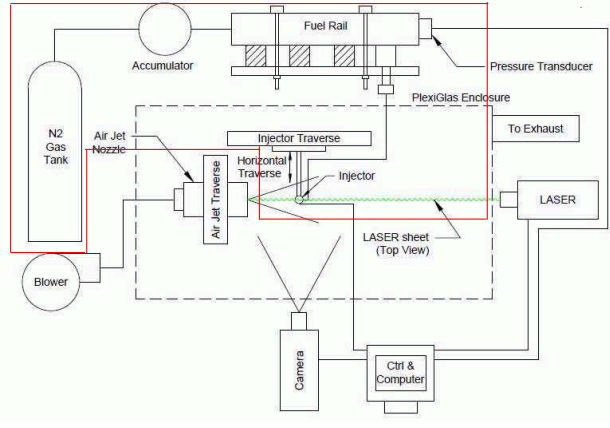


Figure 3.1: Schematic of the fuel injection system used in the present study (components inside the red border)

Parameter	Value
Measured Pressure Range	0-20 MPa
Equivalent Voltage Readout	0.5-4.5 V

Table 3.1: Voltage and pressure range for fuel rail pressure transducer

axis as illustrated by Fig. 3.2. The center of this elliptical arrangement does not correspond to the injector axis which results in a canted spray geometry when viewing in the minor axis plane. The injector orientation for the purpose of this study is referred to as the 3 plume orientation in which plumes 1, 2, 3 or 4, 5, 6 are visible by the observer or the 4 plume orientation in which plumes 2, 3, 4, 5 or 2, 1, 6, 5 remain visible to the observer.

The fuel injector is controlled using the Stand-Alone Direct Injection (SADI) Driver System controller supplied by Drivven Inc. This system which is designed to operate DI injectors monitors the fuel rail pressure and controls the injector current profile and injection triggering. The parameters, illustrated in Fig. 3.3, are selected to define the current profile based on the manufacturer specifications, and control the spray behaviour.

The values used for the 10 MPa and 15 MPa sprays differ slightly due to premature needle closing under the latter injection pressure. The High Voltage Peak Time controls the time duration during which the initial peak current is applied to open the solenoid valve. As such it is important to realize that a delay exists between when the solenoid begins to

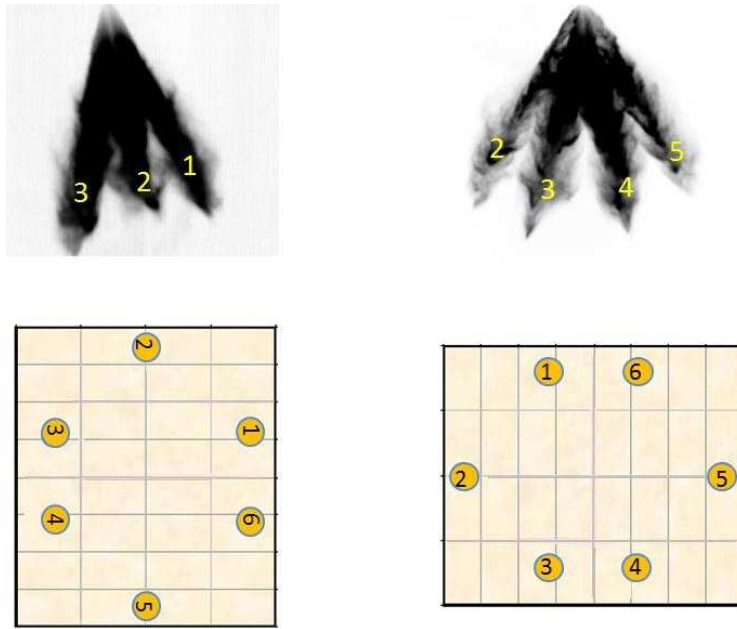


Figure 3.2: Injector hole location and the resulting sprays viewed from the 3- and 4-plume orientation.

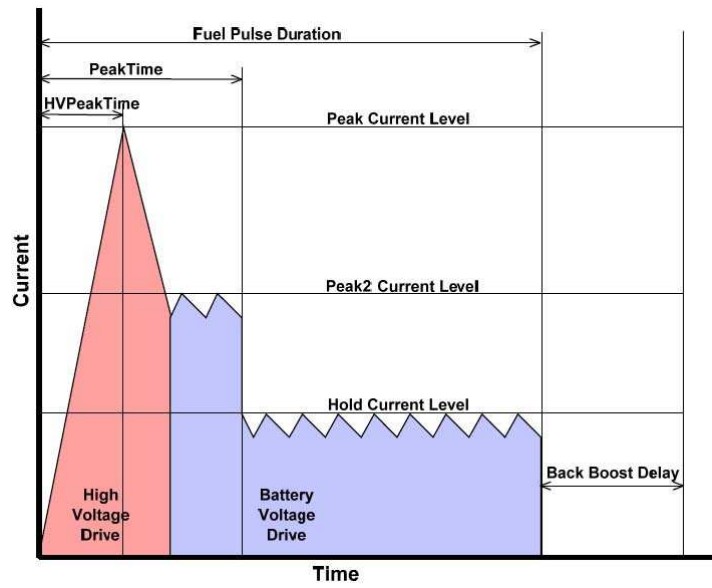


Figure 3.3: Fuel injector current profile parameters

open and when the fuel first exists in the injector. Also, the Hold Time is primarily used to control the duration during which the solenoid remains open.

The fuel used throughout this study was 2,2,4 Trimethylpentane which is also called iso-octane and is representative of gasoline fuel.

3.2 Air Delivery System

The delivery of air is governed by a ring compressor coupled with a variable frequency drive (VFD) supplied by Air Power Products Limited. The system is able to provide air flow rates between 0 and 85L/s.

3.2.1 Air Nozzle Design

A specially designed air nozzle is used to provide a high velocity air jet. The design of the air nozzle considered the principles of wind tunnel test section design to provide a uniform and low turbulence jet. The air nozzle consists of three sections as is illustrated in Fig. 3.4.

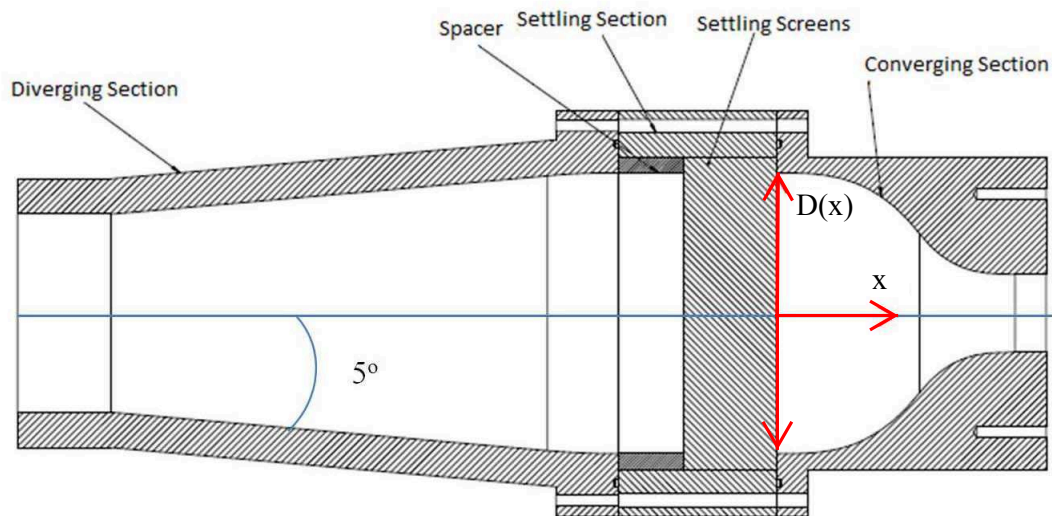


Figure 3.4: Cross-sectional view of air nozzle

The first section is the diverging section which diverges at an angle of 5° from the axis. This 5° angle is selected to reduce the probability of separation as recommended by Tavoularis [32]. Once the flow has undergone a gradual expansion it is passed through a settling region designed to reduce the size of turbulence structures and straighten the flow before it is compressed and accelerated in the converging section. The honeycomb and the mesh which make up the settling region of the air nozzle are selected by the guidelines presented by Idelchik [33]. The percentage of open space (porosity) was maintained above 62% or higher, with the honeycomb section having a thickness of 5.08 cm and dimensions as listed in Fig. 3.5.

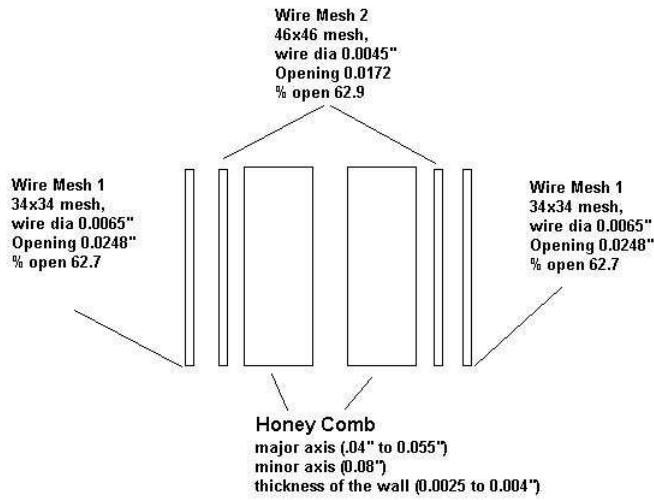


Figure 3.5: Schematic of the air nozzle settling region and its components used in the present study.

The mesh screens were arranged on either side of the honeycomb structure with the smaller pore sizes adjacent to the honeycomb and the larger pore sizes on the outside of this sandwich.

The profile of the converging section was designed according to the methodology presented by Morel [34] which was validated experimentally by Tulapurkara et al.[35]. From Bradshaw and Pankhurst [36], a contraction ratio of 13 was selected with a nozzle outlet diameter of 25 mm [36]. The final profile of the converging section can be expressed as

follows:

$$\frac{(D(x) - D_2)}{(D_1 - D_2)} = \begin{cases} 1 - (\frac{1}{X})^2(\frac{x}{L})^3 & \text{if } \frac{x}{L} \leq X \\ (\frac{1}{1-x})^2(1 - \frac{x}{L})^3 & \text{if } \frac{x}{L} > X \end{cases} \quad (3.1)$$

The values for the parameters in Eq. 3.1 are given in Table 3.2.

Parameter	Value	
D_1	9 cm	\emptyset at x=0
D_2	2.5 cm	\emptyset at x=7.65 cm
X	0.6	Location where curves meet
x	0 - 7.65 cm	Distance from entrance of converging section
L	7.65 cm	Total length of converging section

Table 3.2: Design parameters for the converging section of the air nozzle used in the present study.

The combination of the ring compressor and air nozzle allowed the air jet to reach velocities of up to 230 m/s at an operating temperature of 82 ° C at the nozzle exit.

3.2.2 Enclosure Configuration

The experiments performed in this study were enclosed in a wind tunnel, with a rectangular cross-section. The tunnel was manufactured from PMMA in order to maintain optical access from all angles. The tunnel, which measures 7 ft long by 3 ft high and 2 ft wide, was designed to be large enough so that the cross-flow was not influenced by wall effects and recirculation zones which could impact the air jet.

The air nozzle and injector were placed inside the tunnel, with the front end remaining open to the ambient. The downstream end contained an exhausting section angled at 45° upwards and then an angled face at the bottom end with a vertical portion in the middle. The vertical portion is in place so that either the laser or camera can be positioned with a clear unobstructed view of the spray. The necessity for this optical access led to the unique design of the upper and lower exhaust regions. Initial designs which only had the upper exhaust led to significant recirculation within the chamber. Subsequent designs aimed to reduce these effects although due to the high velocities, recirculation still occurred within

the enclosure. Since the recirculating velocities compared with those in the fuel spray and the air jet were negligible, and were deemed to not affect the jet core where the fuel was being injected. Figure 3.6 shows the enclosure.

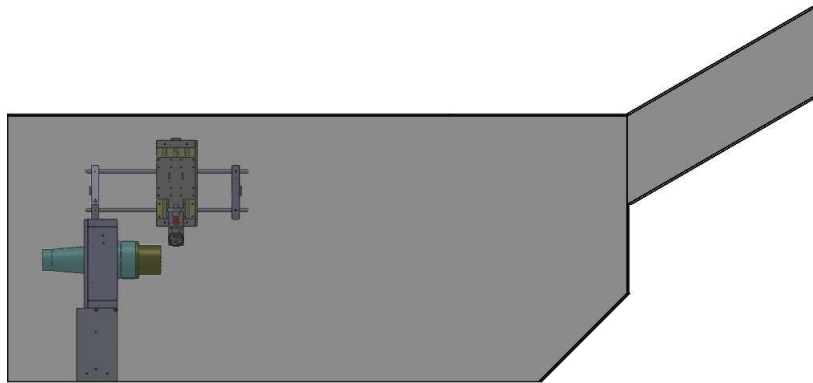


Figure 3.6: Experimental set-up

The air nozzle and fuel injector were mounted onto separate traversing systems as shown in Fig. 3.7. This system allows for independent control of the location between the two components. Furthermore, the injector mount allows for rotation of the injector to change the angle of injection into the cross-flow. The location of the air nozzle with respect to the enclosure surroundings can be seen in Appendix C.

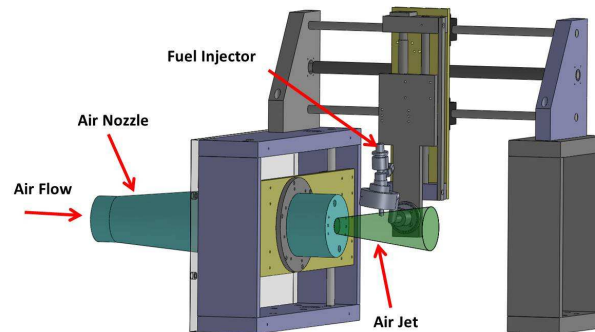


Figure 3.7: Traversing system

In the present work, two main set-ups were used. The first was for the purpose of planar techniques which include PIV and regular Mie scattered images. The second is for volumetric imaging.

The set-up used for the planar techniques orients the camera orthogonal to the axis of the cross-flow, such that it can capture the vertical plane. The laser sheet which defines the plane of interest and is used to focus the camera, illuminates the vertical plane along the jet axis, and the spray axis. Furthermore, the orientation of the injector is in the 4 plume configuration with plumes 2 to 5 from Fig. 3.2. This means that the major axis of the spray is aligned with the laser sheet and the jet axis.

For the second technique of volumetric imaging, the camera remained in the same location, however, two stroboscopic lights (Strobotac 1531) each with a pulse width of 0.5-3 s were used to illuminate the spray from underneath. The use of two light sources was found to provide the highest quality images where the clouds of finely atomized particles surrounding the spray plumes are visible.

3.3 Measurement System

3.3.1 Air Pressure and Temperature Measurements

Pressure and temperature measurements are used within this study to characterize the air and fuel flow and indicate that test conditions are constant from one test to the next. The total gage pressure was measured across the air nozzle, with sensors positioned according to Fig. 3.8. Sensors located at the outlet of the air nozzle are removed when measurements of air velocity, or spray interaction are captured. Some notable specifications for the Kiel probes from United Sensor Corporation are listed in Table 3.3.

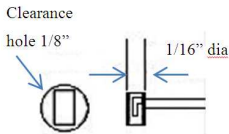
Probe	Sensor	Probe Diameter	Yaw Range	Pitch Range	Time Constant
Kiel Probe (KAC-12)		$\frac{1}{8}$ "	$\pm 52^\circ$	$+ 47^\circ - 40^\circ$	36 s

Table 3.3: Specifications for the air pressure measurement hardware

One source of error for the pressure measurement using probes is the misalignment of

the probe head to the fluid flow. The allowable yaw and pitch angles of the Kiel probe head are used to limit and control these errors. Due to their low sensitivity to yaw angle variation and isotropic turbulence, and their overall good performance in turbulent environments, Kiel probes were selected over Pitot tubes. The yaw and pitch range for the Kiel probe is defined based on Mach numbers of 0.25 and can reduce when the Mach number increases or when turbulence is extremely high. The error associated with this range is 1% of the pressure reading, and consideration is observed when aligning the probes with the air flow to maintain $\pm 10^\circ$. The Kiel probes were measured using Omega's PX40-15G5 pressure transducer. The specifications can be found in Table 3.4. The transducer readings were recorded using NI PCI-6221 card which is capable of sampling at a rate of 250 kHz.

	Transducer	Range	Voltage Range	Accuracy	Repeatability	Temp Range
Air:	PX40-15G5	0 to 103.42 kPa	0.5 to 4.5 Vdc	± 0.11 Vdc $\pm 1.2\%$ FS	$\pm 0.15\%$ FS	-45 to 125°C
Fuel:	NA	0 to 20 MPa	0.5 to 4.5 Vdc	@0MPa to $\pm 2.0\%$ FS @20MPa	NA	NA

Table 3.4: Specifications for the pressure transducers

The pressure transducer installed on the common rail assembly operates between 0 to 20 MPa, as previously mentioned, with accuracies listed in Table 3.4. The accuracy of the common rail pressure transducer translates to ± 0.336 MPa at a reading of 0 MPa increasing linearly to ± 0.56 MPa at a reading of 20 MPa.

The thermocouples from Omega were T-type, ungrounded, sheathed thermocouples with a 1.57 mm sheath diameter. They were used for measuring the temperatures of the air flow, the fuel in the rail, and the wind tunnel environment. Due to the high velocities, the sheathed model was selected to prevent damage to the thermocouples throughout the test. The thermocouples were wired into a high accuracy data logger, which monitored the temperatures of the air and fuel. Table 3.5 summarizes the temperature measurement hardware.

The locations of the Kiel probes and the thermocouples are indicated in Fig. 3.8. For

Hardware	Supplier/Part Number	Accuracy
Thermocouple	Omega/TMQSS-062U-	1.0°C or 0.75%
High Accuracy Data Logger	Omega/HH506A	$\pm (0.05\% \text{ rdg} + 0.3^\circ\text{C})$

Table 3.5: Temperature measurement hardware

the cross-flow, pressure and temperature are measured upstream of the jet and at the outlet of the jet. The measurement locations are indicated by the \otimes symbol. Probes are inserted perpendicular to each other with the Kiel probe centred along the axis of the jet and the thermocouple slightly offset to avoid interference between the two measurements.

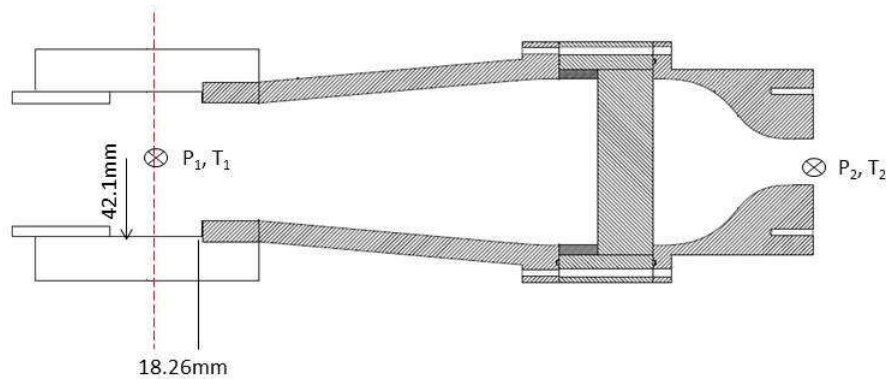


Figure 3.8: Pressure probes and thermocouple locations

3.3.2 Velocity and Planar Measurements

The measurement system provided by LaVision Inc. is a high resolution Particle Imaging Velocimetry (PIV) unit. The system uses Quantel's Evergreen 70 Nd:YAG dual cavity pulsed laser to produce beams at a wavelength of 532 nm with a pulse energy of 70 mJ. This class IV laser has the ability to fire pulses simultaneously with a 0.5 ns separation. Adjustable optics provided by LaVision Inc. are used to create a thin light sheet which is required for capturing the fluid motion in the test section. The adjustable sheet forming optics are illustrated in Fig. 3.9. A combination of spherical lenses with adjustable spacing change the beam waist of the laser from 300 to 2000 mm. A cylindrical lens with a diverging

angle of 10° is used to form the beam into a sheet. The beam waist has a thickness of 1 to 2 mm, which is positioned in the measurement field of view.

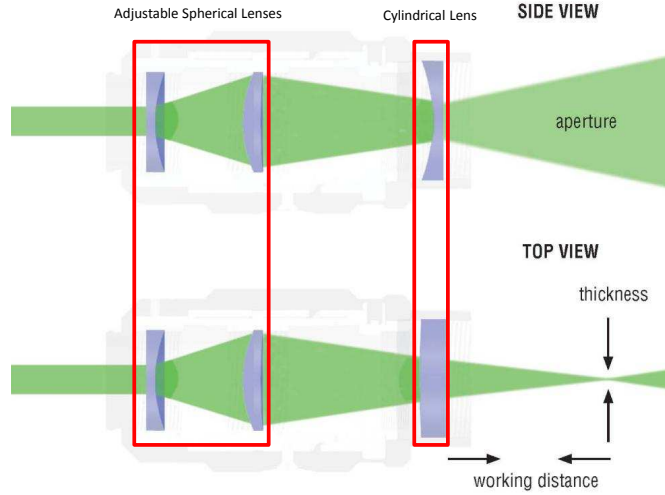


Figure 3.9: Sheet forming optics provided by LaVision Inc. [37]

LaVisions Imager Pro X 2M and Imager Intense CCD cameras listed in Table 3.6 were used in this study. The camera was mounted orthogonal to the laser sheet during planar imaging configurations. A Nikon lens (60 mm F2.8 or 50 mm F1.8) is used to allow for imaging of the field of view, and a 532 nm bandpass interference filter is mounted on the lens to mitigate noise from the ambient light sources. The band pass filter preferentially allows 532nm wavelength light to pass to the CCD camera, which allows for higher quality imaging without the necessity of operating without ambient lighting. Triggering of the camera, laser, and fuel injector was achieved using a programmable timing unit (PTU) which syncs with LaVisions Davis 8 software. This software package is capable of both capturing images and processing the images.

3.3.3 PIV Seeding

An important consideration in successfully performing PIV is the selection of the seeding material. To accurately measure the velocity of the fluid, the tracer particles must be able to properly follow the structures present in the flow.

Camera	Resolution	Interframing Time (ns)	Bits	Exposure Time (ns)	Frame Rate (Hz)	Pixel Size (μs)
Imager Intense	1376x1040	500	12	500	10	6.45
Imager Pro X 2M	1648x1214	110	14	500	30	7.4

Table 3.6: Camera specifications

Adrian et al. [38] suggested He filled soap bubbles, polystyrene spheres, Expancel and liquid droplets as possible seeding materials for gas flows. Of these options, liquid droplets were selected as the primary option for seeding the air flow. Solid particles such as the polystyrene or Expancel were rejected due to the fact that the wind tunnel used for this study is an open loop tunnel which exhausts to the ambient. This would mean the collection and filtering of solid particles would be more difficult and complicated, and particles would collect in the wind tunnel. While Helium soap filled bubbles would allow for continuous generation of bubbles, the minimum spatial resolution of systems capable of producing high quantities of bubbles is in the order of 0.6 mm with bubbles on the order of 1.27 mm diameter.

The most promising option of seeding the air jet proved to be the use of liquid droplets with diameters in the order of 1 to 2 μm . The combination of DEHS (Di-2-Ethylhexyl Sebacate) oil and LaVision’s Laskin Nozzle Aerosol generator seen in Fig. 3.10 delivers particles at a rate of 1.4×10^8 to 20×10^8 particles/sec.

Seeding Particle Suitability

An important consideration in assessing the suitability of the seeding particles is their ability to follow the structure of the air flows. Crowe et al. [39] looked at the ability of particles to adhere to large scale structures in non-isotropic flows using a ratio between the response time of the particle τ_A and the characteristic time of the large scale structures τ_F defined respectively as



Figure 3.10: Laskin Nozzle Aerosol Generator

$$\tau_A = \rho_P \frac{(d_P)^2}{18\mu} \quad (3.2)$$

$$\tau_F = \frac{\delta_v}{\Delta U_v} \quad (3.3)$$

where ρ_P is the particle density, d_P is the particle diameter, μ is the fluid viscosity, δ_v is the mixing layer width or the width of the large scale structure, and ΔU_v is the velocity difference between the layers. For scenarios where the ratio of $\frac{\tau_A}{\tau_F}$, known as the Stokes number, is between 0.01 and 0.1 the particle mixing rate is higher than that of the jet and particles tend to centrifuge out of the center of vortex structures. For Stokes number near unity, the particles do not mix as quickly and are unable to adequately represent the flow. Thus for values below 0.01, the particles are able to follow the large scale structures and represent the flow.

The numerical work of Luo et al. [40], who based the characteristic length scale on the jet inlet, agrees with Crowe et al.[41] for stokes number 0.01 to 0.1. Furthermore both authors suggest that particles preferentially map to the low-vorticity and high strain regions of the flow field, but because the characteristic length scale of the turbulent structure is significantly smaller the local stokes number changes and the particles appear evenly distributed.

In assessing the suitability of the particles for the present study, the Stokes number is calculated based on the parameters of the air. The Reynolds number (Re_g) at the outlet of the air nozzle, ranges from 1.9×10^5 to 2.7×10^5 , well above 3000, which indicates fully turbulent flow.

In calculating the Stokes number Crowe et al. [39, 41] used the jet diameter and the jet velocity. Longmire et al. [42], who studied the effect that particles have on the airflow of the round jet, found that the characteristic time scale τ_F should be based on the properties of the vortex rings that formed $\frac{x}{D} = 0.8$ from the jet outlet. Instead of using the diameter of the vortex rings and the propagation velocity of these structures, as they travel in the shear layer of the jet, the core to core distance of adjacent rings and the mean velocity between the jet potential core and the ambient was used. Figure 3.11 illustrates the adjacent vortex rings. It can be seen that in the present diagram which is for an average jet velocity of 50 m/s the jet appears to have a fish bone structure. This is typical of jets and is indicative of the particles centrifuging to the outward boundaries of the vortex.

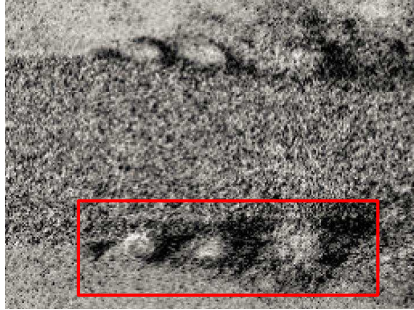


Figure 3.11: Vortex formation for 50m/s flows

Using the approach of Longmire et al. [42] the Stokes number for the air jet was evaluated on a variety of conditions. Table 3.7 gives a measure of the Stokes number calculated for the jet outlet. The procedure considered 3 to 4 vortex structures on either side of the jet between x/D of 0.5 and 1. The distance between adjacent vortex structures was estimated by the distance between the leading edge of adjacent vortices. Furthermore, the Stokes number was calculated for particles with 1 to 2 μm diameters which is the range of particles produced by the Laskin atomizer. Considering the smallest and largest distances and the largest and smallest particle diameters, a range of Stokes numbers were calculated.

U ($\frac{m}{s}$)	T_2 ($^{\circ}C$)	ρ_p ($\frac{kg}{m^3}$)	μ ($\frac{kg}{ms}$)	δ_v (mm)	Re	d_P (μm)	τ_A (s)	τ_F (s)	St
129.22	37.6	891.5	1.90E-5	5.79	1.93E+5	1.00	2.64E-6	2.49E-5	0.106
						2.00	1.06E-5		0.424
129.22	37.6	891.5	1.90E-5	1.61	1.93E+5	1.00	2.64E-6	8.96E-5	0.030
						2.00	1.06E-5		0.118
220.20	67.7	879.20	2.05E-5	1.60	2.80E+5	1.00	2.39E-6	1.45E-5	0.164
						2.00	9.55E-6		0.657
220.20	67.7	879.20	2.05E-5	4.84	2.80E+5	1.00	2.39E-6	4.40E-4	0.054
						2.00	9.55E-6		0.217

Table 3.7: Local Stokes Number

It can be observed that the stokes number varies from 0.03 to 0.66. While the values of 0.03 and 0.054 reside in the range specified by Crowe et al. [39] for sufficient tracking, the values of 0.66 appear to be very close to the threshold of unity suggesting that these particles might not track the flow adequately considering that Chung et al. [43] found particle dispersion was greater than fluid dispersion for Stokes numbers between 0.5 and 5.

In discussing the particles, the method of seeding the airflow become important. The Laskin Atomizer was situated upstream of the ring compressor and so particles were drawn through an air filter, accelerated in a rotary vane blower and then passed through the air nozzle settling region before exiting the air nozzle. As such, it is expected that since the larger particles do not track well with rapid acceleration (Stokes number 0.424 and 0.657 for the 129 and 220 m/s flows respectively) and that the ring compressor and filter would remove these larger particles, only allowing those with satisfactory responsiveness into the wind tunnel. Also, in predicting an adequate Stokes number, it can be seen that the size of the vortex increased with increasing distance from the outlet. This indicates that particles are better able to trace the shear layer as it increases in size.

Finally, in the potential core region of the jet, the acceleration is more gradual than in the shear layer and the particles are considered to be able to better trace the potential core even if they do slightly over predict the shear region.

Seeding Particle Slip Velocity

The slip velocity of a particle is another consideration when thinking of a particle's ability to accurately predict velocity. When considering particle dynamics, a particle which is being accelerated by an air flow tends to move at a velocity which is slightly different than the air flow even under steady conditions. This relative velocity is considered as the slip velocity and in an instance where there is no changes in the flow, is the maximum velocity that the particle can obtain.

Adrian et al. provides an iterative solution for the slip velocity based on the following equations:

$$Re_P = \frac{|u_g - u_P|d_P}{\nu_f} \quad (3.4)$$

$$u_P - u_g = \frac{\bar{\rho} - 1}{\bar{\rho}} \frac{g\tau_0}{\phi} \quad (3.5)$$

$$\tau_0 = \frac{\rho_P d_P^2}{18\nu_f \rho_f} \quad (3.6)$$

$$\phi = \frac{2}{3} + \left[\frac{12}{Re_P} + 0.75 \left(1 + \frac{3.315}{Re_P^{1/2}} \right) \right]^{-1} \quad (3.7)$$

$$\bar{\rho} = \frac{\rho_P}{\rho_f} \quad (3.8)$$

Here u_g represents the air velocity, u_P represents the particle velocity, d_P is the droplet diameter, ν_f is the is kinematic viscosity of the air stream, ρ_f is the density of the air stream, ρ_P is the density of the particle, and ϕ represents an empirical formulation for the drag modifier for a droplet.

The iterative approach begins with an assumption that $\phi=1$. This allows for a first guess calculation of $|v_P - u|$ which can in turn be used to find a value for Re_P leading to a new value of ϕ .

Using this method, the slip velocity of the particles is determined to be on the order of $150 \mu m/s$. When compared with average core velocities, this becomes a negligible value.

Chapter 4

Experimental Procedure and Conditions

4.1 Calibration

In order to provide quantitative analysis of images including prediction of the velocity and details of the geometric characteristics of the sprays in the cross-flow. A proper calibration must be in place to map image space to the physical space. This process of calibration not only assigns physical sizes to the pixels of the image but also assists in locating the experimental components like the air nozzle outlet and the injector tip with respect to each other.

Two methods of calibration were used during this study. The first method, a manual scaling technique, was employed for that majority of the results, and was substituted only for the 15 MPa sprays into cross-flowing conditions due to the availability of an improved and more automated method. The manual scaling technique involved the manufacture of a calibration board with a linear scale engraved on its surface. The board with known dimensions and location was designed so that the linear scale would allow for the image to be properly mapped, and the front face of the air nozzle to be known. Figure 4.1 shows a picture taken during the manual scaling process.

The calibration board was manufactured so that the air nozzle axis is co-planar with the front face, and so that the ruled markings correspond to distances from the front face

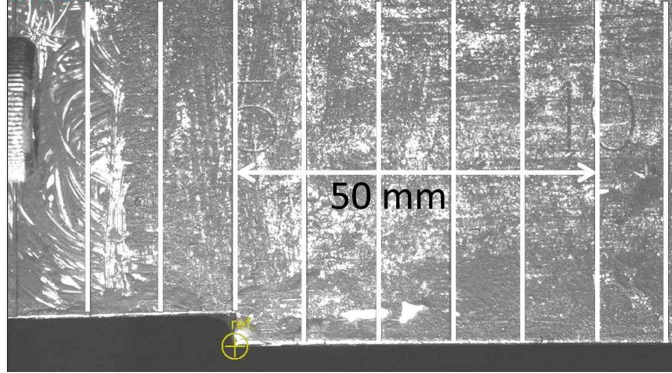


Figure 4.1: Scaled Calibration Board

of the air nozzle. In this manner, the center point of the air nozzle outlet can always be taken as the (0,0) reference point. For this calibration board, the spacing of the ruled markings was 1 cm with the ruled marking having a width of 0.6 mm.

The scaling procedure involved taking an image of the board, with high exposure and only ambient lighting, and then selecting two reference points along the bottom edge of the board. The distance between these reference points, and their location from the (0,0) location would be well defined and allow for the image to be calibrated.

To achieve an adequate scaling, attention was paid to position the reference points as far apart as possible. This would minimize the influence of minor discrepancies in the selection of the reference points, the impacts of which will be discussed in section 5.1. Furthermore, this method allows for the correction of minor rotations around the Z axis (out of plane) but still assumes that the camera sensor is 100% parallel to the field of view.

The second calibration method known as the Camera Pinhole method was an automated process incorporated into the imaging software which mitigates error of manual reference point selection from the process. Instead of a ruled scale, the method detects a matrix of evenly spaced, and equal sized dots. Although a grid of crosses could be used, implementation of the algorithm is easier with circular dots. [44] In this instance a similar calibration board was manufactured with the front face corresponding to the vertical bisecting plane of the air jet, with markings of known dimensions all in reference to the (0,0) location of the air nozzle. The matrix of dots is illustrated in Fig. 4.2. This style of calibration board while it still requires an image to be taken of the board allows for a more seamless scaling of the image and can correct misalignments about any of the 3 axes.

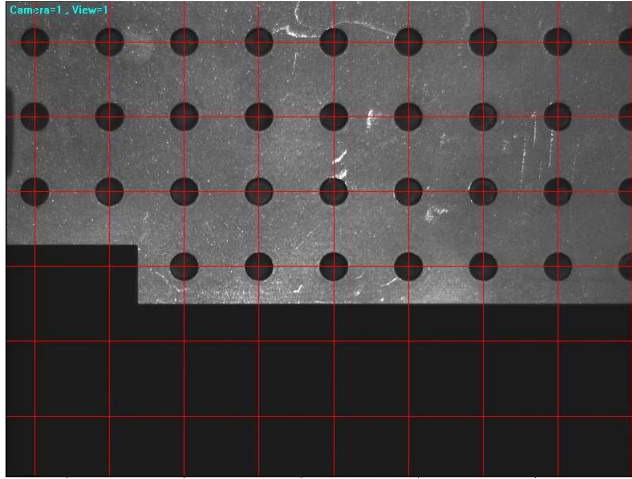


Figure 4.2: Dot Matrix Calibration Board

In the design of this board, the diameter of the dots was selected as 6mm with the dots center to center spacing of 16mm resulting in a spacing to diameter ratio of $2\frac{2}{3}$. Important considerations in the design of the plate include ensuring that a high contrast exists between the dots and the plate material and that the dots are perfectly circular. The high contrast allows for an accurate detection of the edge of the dot allowing for accurate detection misalignment which would result in the circles appearing elliptical. Moreover, the dot diameter, in this case selected as 16mm, is sized so that there exists a large number of pixels across its diameter. The error associated with ± 1 pixel when detecting the center of each dot decreases as the diameter of the dot increases. This effect is balanced with the desire to include as many dots as possible within the field of view, while allowing enough distance between adjacent dots. In this case, the the board was designed to have more than 24 dots visible in the field of view.

Once the image was calibrated, the laser sheet could be properly aligned. This procedure involved orienting the laser sheet so that the center of the sheet was aligned with the front face of the board, and the board remained evenly illuminated. To achieve this, markers were placed on the downstream edge and the upstream edge of the calibration board to illustrate where the center of the board was with respect to the center of the laser sheet.

4.2 Data Acquisition

4.2.1 Particle Imaging Velocimetry

Particle Imaging Velocimetry is a spatial and time average imaging technique which allows for the determination of velocity in a flow field. This technique can be used to determine 3 components of velocity (Stereo or Tomographic PIV), and in its simplest form 2 components of velocity in a plane (Planar PIV). The present study is concerned with the later and so the following discussion will focus on the planar technique, referred to as PIV from here on.

Fundamentals

PIV is an imaging technique which measures the velocity field of a flow through the detection of particles as they move within a flow. As mentioned in Section 3.3.3 the flow is seeded with some sort of tracer which is able to accurately track the flow structures. As the particles move, a camera images the flow field of interest either through double exposure in which the initial particle location and displaced location appear on the same frame, or through two successive images in which case frame 1 corresponds to the initial location, and frame 2 corresponds to the displaced location. For the present study the double frame technique is employed. In either case the time lapse between the exposures or frames is precisely controlled and measured. Processing techniques allow for the precise detection of particle locations for the initial condition and the displaced condition and then the velocity is calculated for that particle. Typically the time lapse between the frames is so short that the displacement is considered at the velocity at a point in time. The technique involving only one single particle refers to a technique known as Particle Tracking Velocimetry. The more common approach, PIV, considers a larger amount of particles present within the frame, allowing for multiple velocity vectors to be resolved. This higher particle density requires more complex algorithms to detect particle motion, a process which is referred to as cross-correlation. Moreover, to provide a spatial resolution, frame 1 and frame 2 are subdivided into interrogation regions. Each region on frame 1 has a corresponding region on frame 2 which represents the same physical space. Each interrogation region contains multiple particles and so the cross-correlation algorithm compares the particles from frame 1 with the particles from frame 2 to detect the most probable displacement.

The size of the interrogation region is selected so that all the particles generally have the same bulk motion, so the cross-correlation technique checks the possible displacements of all the particles and selects the one with the highest frequency of occurrence. As a result, the calculated velocity is representative of the interrogation region which explains how this technique is a spatial average [38].

Triggering

PIV requires careful coordination of all the components. LaVision's PIV system uses a Programmable Timing Unit which is controlled by their DaVis software. This unit is responsible for the synchronization of the laser, the camera and the injector. An example timing diagram is seen in Fig. 4.3

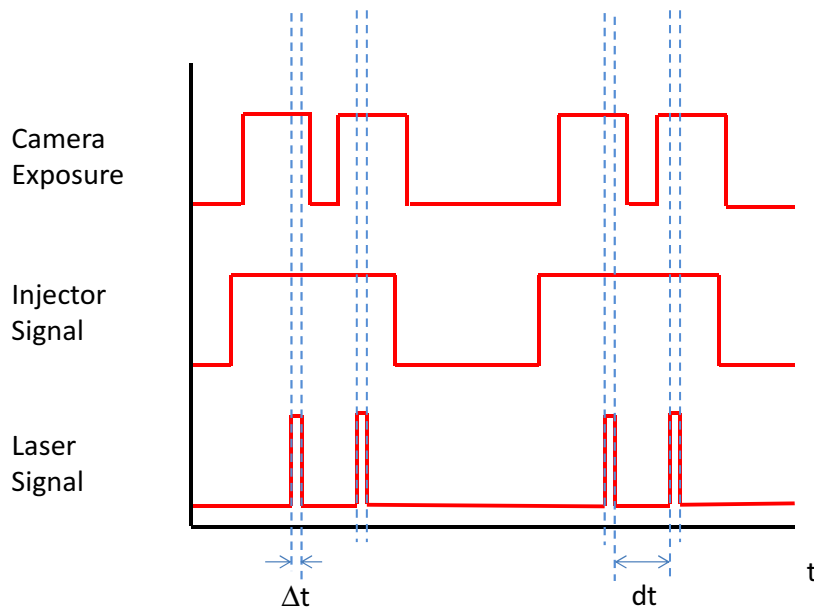


Figure 4.3: PIV Timing Graph

In PIV techniques there are two methods of controlling the exposure time of the image. To clarify, the exposure time of the camera refers to the amount of time that the shutter remains open, while the exposure time of the image refers to the amount of time that the image is exposed to light. The reason for making this distinction relates to the two

methods of controlling the image exposure time and are dependent on the conditions of the flow and the hardware involved. The control of the exposure time is primarily important in ensuring that particles are "frozen" in the image. This means that particle travel during the image exposure is minute to avoid streaking or blurring. As such, the timing of the image exposure must be tailored to the flow conditions.

The two methods of controlling this image exposure time are: to allow the camera exposure time act as the image exposure time or to allow the light source Δt limit the duration that the light source is active. In the case of the latter method which is employed in the present study, the laser pulses for a very short duration during which the camera sensor is exposed. After this pulse, the sensor is exposed to minimal light although the shutter may remain open after the laser pulse has ended.

Since the velocities of interest are particularly high in this study, the method of using the laser pulse duration to control the image exposure allows for exposure times in the order of 10 ns for the present laser. This control strategy is depicted in Fig. 4.3 where the laser pulse, Δt , is of a shorter duration than the camera exposure. The inter frame time denoted by dt is controlled by the pulse separation and is controlled to allow enough pixel displacement between images. Selection of dt is another important parameter. Since the PIV technique relies on particles being within the same interrogation window during image 1 and image 2, it is crucial to limit the amount of particle which will cross into another interrogation region between frames. In this case these particles would not be properly considered in the cross-correlation. A general rule which is applied when performing PIV is to select your dt to allow for particles to travel 1/4 of the interrogation window size. As such dt is application specific and depends not only on the flow conditions but also on the field of view.

When performing PIV on the fuel spray, the injector trigger is also controlled by DaVis. In this instance the trigger is used to initiate the current profile set in the Drivven software as discussed in section 3.1. The present study is concerned with characterizing the fuel spray and since this is a transient process, images are taken at different times during the injection. The reference time for the injector is the Start of Fuel (SOF). As mentioned earlier, the time at which the injector begins to receive current, known as the Start of Injection (SOI), does not correspond to time at which the fuel leaves the holes of the injector. There is a delay time present during which the solenoid opens and the fuel is able to flow through the injector internals. This delay time is somewhat related to the injector

current profile that is supplied.

The SOF for the present injector and current profile combination occurred 0.385 ms after SOI. This was determined by moving SOI earlier than the camera and laser triggers. This procedure allows for the SOF to be accurate to within $\pm 5\mu\text{s}$.

Image Quality

Control of the image quality is important in attaining quality PIV images. While modern post-processing techniques can assist in improving the quality of poor images, the biggest improvement can be made through preparation during the data acquisition stage. The first element to consider is the elimination of background noise. Sources of noise which can reduce image quality are out of plane particles, reflections from laser sheet, and ambient lighting.

In order to eliminate the impact of ambient lighting a 532 nm bandpass filter was used as mentioned in Section 3.3.2. This filter only allows light with the same wavelength of the laser to transmit through the camera sensor. This cuts out ambient light of all other wavelengths. Since ambient light still contains 532 nm wavelengths, there will still be some noise, but it will be substantially reduced.

Another common issue is reflections from the apparatus. As the laser sheet enters the domain it contacts different surfaces such as the air nozzle, the injector tip or the mounting table. All of these metallic components result in reflections which can impact the image quality and potentially damage the image sensor. To protect the image sensor and reduce these reflections, a formulation of Rhodamine and black paint were used to coat all potential reflecting surfaces. This paint, which performs better than anodizing, absorbs the incident laser light and shifts the wavelength of the emitted reflections to 566 nm. The narrow bandpass filter then blocks these reflections from reaching the image sensor.

Out of plane particles present another source of poor image quality. Typically the depth of field of the PIV experiment is governed by the laser sheet thickness. The high intensity of the laser sheet allows it to define a plane and to only illuminate articles within that plane. In the ideal case these particles are the sole objects detected by the image sensor. However, articles outside of the plane can still receive enough illumination from scattered light which is emitted by droplets within the laser sheet. The amount of scattered light

increases with increasing droplet concentration, and so for high density sprays similar to the injected fuel spray, scattered light can illuminate out of plane droplets. These droplets if outside of the field of view can lead to image blurring and noise, making it harder to detect individual droplet motion.

4.2.2 Spray Imaging

Spray Imaging Considerations

Measurement of the spray geometry characteristics has been completed using two methods. The first is using 2-D planar imaging, which allows for the spray to be captured at the same plane as the PIV analysis. The second is a volumetric illumination approach which uses triggered-stroboscopic lighting to illuminate the entire viewable spray surface. Planar imaging is employed for the spray interacting with the cross-flow while volumetric imaging is employed for sprays in quiescent conditions.

For the planar imaging technique, the data acquisition follows the same procedure as for the PIV. As such this section will focus on the acquisition of volumetric images and the quiescent spray conditions, primarily the aspects that differ from the above acquisition considerations.

The spray imaging employed in this study allows for visualization of the spray as it interacts with the cross-flow. From these images, observations about the spray's characteristics can be derived although this is mostly done using post processing tools.

Capturing the volumetric images is quite similar to the process of capturing PIV images except that illumination is achieved by a pair of strobe lights rather than a laser sheet. Although many researchers use shadowgraphy techniques [45] such as back light imaging to capture volumetric images, this study used Mie scattering techniques where the scattered light from the strobe images was detected in the image. The back lighting system which was first used in this experiment was not large enough to provide uniform illumination of the entire spray domain. Furthermore, it was found that scattered light from smaller particles near the tips of each spray plume was not detected leading to a reduced penetration and spray width. As such, the under lighting approach was employed.

For the acquisition of spray images in quiescent conditions, the procedure was fashioned after that put forth in the SAE international in document J2715 [45] and then further elab-

orated on by Hung et al. [46] in their recommended practices for fuel spray measurement and characterization in gasoline sprays based on the SAE J2715 document.

Triggering

For all the volumetric images, the injector, light source and camera are triggered using the DaVis 8 software with the camera exposure time set to $1 \mu s$ with the strobe light on high intensity ($3 \mu s$ flash). SAE J2715 [45] recommends a total of 5 images should be captured in order to provide sufficient numbers for averaging while Mitroglou [47] considers averaging as many as 20 images. For the present study 15 images were captured with this number shown to be sufficient in Section 5.2.1. SAE J2715 [45] also, only considers characterizing the spray at 1.5 ms SOI, however, in the present study the temporal characteristics are of interest and so images are recorded every 0.1 ms from SOF. Finally, one of the main considerations which is of importance is the frequency of imaging. In SAE J2715 [45], it is acknowledged that a minimal amount of ventilation is required to purge the environment from fuel vapours which could effect the spray and atomization. The recommendation is to supply an airflow of 1 m/s through the enclosure and to image at 1 hz allowing vapours to be moved 1 m away. In the present study, a controlled source of ventilation was not used but an imaging frequency of 1 hz was used. The wind tunnel which did have a minimal draft from the exhaust system was kept on to assist in purging the area, but this flow was not characterized. Figure 4.4 illustrates the trigger signals used to capture volumetric and planar spray images, where the strobe signal represents a single pulse either from the laser or the strobes.

4.3 Data Processing

The processing of the data for each of set of measurements depends on the measurement technique involved. As such, the following section will discuss the methods employed in processing the PIV images as well as the spray geometry images.

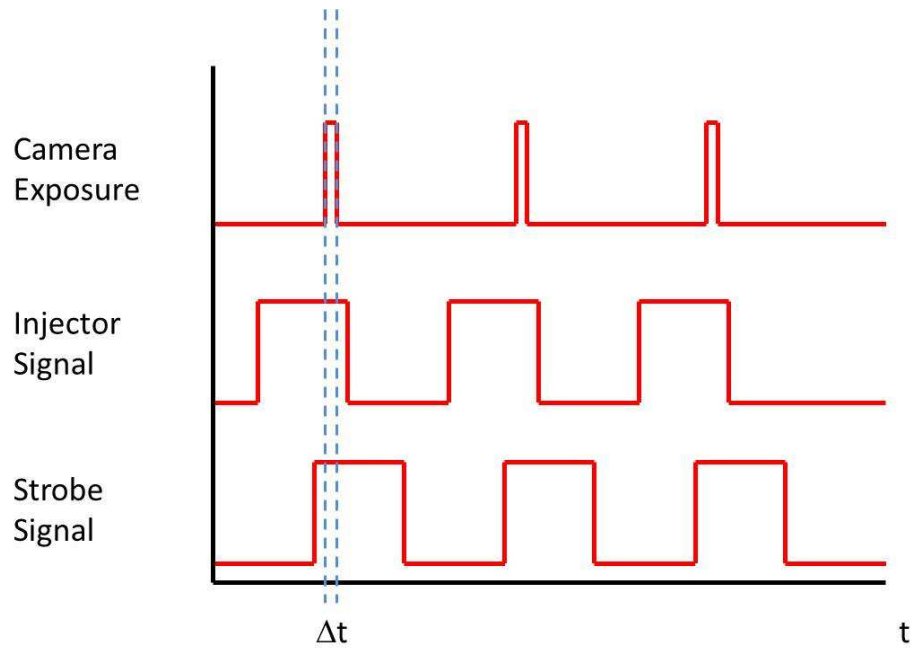


Figure 4.4: Schematic of timings for spray imaging during the experiment

4.3.1 Particle Imaging Velocimetry

The cross-correlation technique discussed in section 4.2.1 is the primary technique used to extract velocity measurements from the PIV images. To produce reliable measurements a series of processing techniques are employed to ensure the accuracy of the correlation. These techniques will be discussed below.

Image Preprocessing

Section 4.2.2 discussed methods of improving image quality through careful control of the experimental conditions, however in some instances background reflections, experimental hardware, or image noise cannot be removed through the control of experimental conditions. As such, the following image processing techniques are employed to further improve image quality and improve the performance and accuracy of the cross-correlation technique.

- Subtract sliding average, minimum or maximum

- Subtract absolute average, minimum, or maximum over time
- Min/max intensity normalization

Subtraction of the sliding average, minimum or maximum are techniques which determine the average, minimum or maximum intensity for groups of pixels, where the group size is user-defined, and then subtract the computed values from every pixel within that group. Thus the removing local reflections or glare which are restricted to isolated images.

The subtraction of an absolute average, minimum or maximum over time, is a technique which can be used to remove background intensities which appear through an entire time series. This filter scans through the entire set of images and produces a background image based on the average, minimum or maximum pixel intensity for each pixel location. Eq. (4.1) illustrates the equational form for the absolute minimum of the time series [48]:

$$\text{new count}(x, y) = \text{count}(x, y) - \text{minimum count}(x, y) \text{ of time series} \quad (4.1)$$

Finally, the min/max intensity normalization allows for the correction of minor intensity gradients within an image. Again the user defines a length scale which corresponds to the size of the region surrounding each pixel which is considered in the filter. This filter normalizes all the pixel intensity values within the region by the min and max values in the region.

Mask Definitions

Masks used within the DaVis software allow for the removal or masking of areas which provide no useful information to the calculation of velocity. These areas can include strong reflections, blurred spots, or equipment in the imaging plane. If these regions are included in the cross-correlation they can actually lead to errors in the calculation as the correlation will try and detect pixel shift from frame 1 to frame 2. Two types of masks are used in the present study. The geometric mask and the algorithmic mask.

The geometric mask is used to prevent the cross-correlation technique from analysing the regions where the fuel injector appeared in the image. To apply this mask, the user manually selects the boundary of the fuel injector in a reference image and then applies the mask so that these pixels are ignored during the calculations.

The algorithmic mask on the other hand is useful in identifying pixels with useless information which may vary from frame to frame. For example. This mask can be used to remove background noise or sharp reflections by detecting all pixel intensities less than or greater than a certain threshold and setting the intensity equal to 0. The selection of the appropriate thresholds is based on a preliminary examination of the data set and varies for each experimental condition.

Vector Calculation

When performing the cross-correlation technique, it is customary to overlap interrogation windows. This overlap not only allows for an increased spatial resolution but also allows for data at the edges of the interrogation windows to be considered in the overlapping correlation [49]. The present study uses an overlap of 50% for all cases.

The option for multiple passes allows for two improvement options. The first is the ability to reduce the interrogation window with subsequent passes. The second is to offset and deform the interrogation window based on preliminary displacement estimates.

The present study performed a total of 3 passes with the larger interrogation size and then continued with 2 passes using the refined grid size. 64 x 64 and 32 x 32 were the grid sizes used when performing PIV on the air jet while 48 x 48 and 32 x 32 were the grid sizes used for PIV of the fuel spray. The first pass size was chosen for each scenario based on the maximum particle displacement within the image.

The combination of the multiple passes with decreasing window size provides two benefits. The first is provided by the multiple pass option. When multi-pass is selected, the first pass is used to generate a relative velocity field for the image. The next pass uses this velocity field to shift the interrogation windows in the second frame by average pixel displacement determined in the first pass. This shift allows for improving the probability that the correct pixels are correlated and increases the signal to noise ratio. Moreover, combining the multi-pass approach with a reduction in grid size allows for further improvements to the resolution and the accuracy. The cross-correlation applied to the smaller window size has a higher accuracy since the adaptive window shift ensures that the particles contained within the second frame are properly correlated [48].

This adaptive window shift also enables the detection of larger particle displacements as the window shift is locally matched to the mean displacement.

Vector Post Processing

Further reductions in noise and validation of the vector field are achieved through several operations within the DaVis software package.

The first step is the evaluation of the peak ratio. Through the cross-correlation technique a correlation map is produced. The correlation map displays the peaks which correspond with the possible average displacements for the particles within the interrogation region. The largest peak is selected to be the representative displacement. To assess the validity of this selection, the ratio of the height of the correlation peak to the height of surrounding peaks can be considered. To avoid selection of erroneous vectors, a threshold can be applied to disregard instances where this ratio is low and little distinction is made between background noise and the selected peak [48].

The application of a median filter is another tool for the removal of erroneous vectors. This operation calculates a median vector from the neighbouring vectors and then rejects the selected vector if it is outside the range of the median \pm rms. This filter has the ability to reject single spurious vectors, but cannot detect groups of spurious vectors. The filter *strongly remove and iteratively replace* is set to reject vectors whose difference to the median is larger than 1.5 times the rms to the neighbours and re-insert them if this difference is less than 2.5 times the rms to the neighbours. This filter is ideal for removing the majority of false vectors and is ideally suited for large data sets where interest lies in the averages or standard deviations [48].

The final filter which is used to ensure that spurious vectors are eliminated is the filter for removing groups which contain less than a selected amount of vectors. This allows for isolated small groups which may pass through the previous filters to be removed.

Average Velocity

The average velocity flow field is a standard calculation which involves the averaging of the velocity vector at each location in the field of view over the entire time series. During this calculation, further filters can be applied to ensure that only true vectors are considered. To ensure that the average is accurate, strong rejection filters are selected. This often results in the dismissal of good vectors along with the spurious vectors, however a large enough sample size leads to accurate averaging.

Turbulent Kinetic Energy

Calculation of the turbulent kinetic energy (TKE) of the flow field is performed using the velocity vectors present in the 2 dimensional flow field. Although turbulence is 3-dimensional the DaVis software makes the assumption that the magnitude of the turbulence in the out of plane direction is the same as the magnitude of the in-plane turbulence components. This leads to the calculation as given below [50]:

$$TKE = \frac{3}{4}(u_{rms}^2 + v_{rms}^2) \quad (4.2)$$

Here u_{rms} and v_{rms} represent the root mean square for the x and y velocity components, respectively. Since the third (out of plane) component of velocity is not measured in the present experiments, it is assumed that the root mean square of the third component of velocity is equal to the mean of the x and y rms components. This leads to the coefficient of 3/4 which includes the effects of the unmeasured component of velocity.

The TKE can be used to indicate the magnitude of the fluctuating velocity components within the flow field. It is expected however that for the cross-flow, this level of turbulence will be slightly damped due to the presence of particles in the flow. While these particles may be able to adhere to general flow structures, it is expected that their mass and response time would lead to the damping of smaller scale turbulent structures.

4.3.2 Spray Imaging

The spray imaging technique focuses on the acquisition of images in order to evaluate the geometric features of the spray. The characteristics of importance vary depending on the conditions being considered. For the volumetric images of the spray in quiescent conditions, the main characteristics are the spray angle, the spray penetration, and the spray width. For the interacting spray and cross-flow conditions, the spray penetration and the spray tail lengths are considered but attention is mostly on the spray axis or trajectory.

The following section will cover the processing methods applied to the images in order to capture and quantify these aspects.

Volumetric Image Processing

In order to evaluate the spray characteristics of the volumetric images, image processing techniques need to first be applied. This process which is depicted in Fig. 4.5 begins with the averaging of the 15 images which were collected. The averaging technique used in DaVis adds the pixel intensities in each pixel location then divides by the number of images. This allows for the main spray features to be enhanced, and reduces the background noise. The averaging of the images has a smoothing effect on the spray shape due to the averaging of surface waves and droplet clouds near the edges of the spray. This effect is clearly seen in Figs. 4.5(a) and 4.5(b). A background subtraction, depicted in Fig. 4.5(c), is then applied to subtract the background image from the averaged image to remove the injector, reflections and noise which may interfere with feature detection of the spray. The background subtraction also serves to further eliminate noise and sharpen the contrast between the background and the spray. The next step is the binarization process which removes any intensity gradients which may be present due to variations in fuel concentration or light intensity variation. It converts the image into a black and white binary representation of the spray where 1 represents the spray and 0 represents the background. The binarization process is performed by selecting a threshold intensity value and then converting everything above this value to 1 and everything below this value to 0. Since the scattered light varies with the fuel concentration, the intensity range also varies for each time step. As a result, the threshold value used in the binarization process was selected manually for each time step so as to ensure that the spray was properly depicted. An example of a binarized image is seen in Fig. 4.5(d).

Selection of the threshold value is a delicate process that can heavily impact the accuracy of the results. Many statistical schemes exist to allow for automation of this process but these schemes have varying levels of accuracy [51]. Macian et al. [52] compared popular algorithms used for threshold selection, assessing their performance over multiple images taken in a variety of conditions. Their findings showed that errors as high as 24.4 % could exist between the results of the two methods.

The threshold value used in the present study was evaluated for each image individually. Due to the reduction in noise after the background subtraction, it was found that the ideal threshold was the same for each set of images. As such, a threshold of 25 % was applied to the entire set of 10 MPa quiescent spray images. For the 15 MPa quiescent spray images, a

threshold of 25 % was used for images taken 0.1 to 1.2 ms after SOF, while 30 % was used for 1.3 to 1.5 ms SOF due to a change in camera position to increase the field of view for the larger sprays. The calculation of error associated with this technique is discussed further in section 5.2.2. In order to account for the bias of under predicting spray angles due to errors stemming from manual threshold selection, values ± 10 % of the ideal threshold value were also considered to quantify the deviation that ensued in the spray angle measurement.

The last step in preparing the image for analysis is the application of an in-house segmentation algorithm. This algorithm detects edges on the binarized and outlines the spray boundary. It then identifies the main body of the spray and removes small droplet clusters which are not attached to the main spray region as depicted by Fig. 4.5(e).

Spray Penetration Length

The spray penetration length at a specified time is defined as the distance along the injector axis from the injector tip to the furthest existence of spray droplets along the vertical axis at that time step. Using the segmented image this value can be obtained by detecting the last white pixel of the image. SAE J2715 [45] noted that penetration curves could be obtained by finding the penetration at 0.5ms, 1.0ms, 1.5ms, 2.0ms and 2.5ms after SOI, however the current study instead defines this curve from 0 ms SOF until 1.5 ms SOF based on 0.1ms intervals. In this manner a clear trend is depicted. This parameter is also measured on sprays interacting with the cross-flow as it is a preliminary measure of the ability of the cross-flow to completely redirect the spray.

Spray Angle

The spray angle measures the angular spread of the fuel spray from the injector tip, and is often used as a method of characterizing the injector. In the methodology provided by SAE J2715 [45] this angle is calculated using a trapezoidal approach, illustrated in Fig. 4.6 [45], where θ_L is the left side spray angle and θ_R is the right side spray angle, which sum to give the total spray angle, θ_S . Also, θ_B , the bend angle, which represents the angle between the spray axis and the injector axis, can be calculated. In this approach points on the each edge of the spray are selected at heights of 5mm and 15mm from the injector tip.

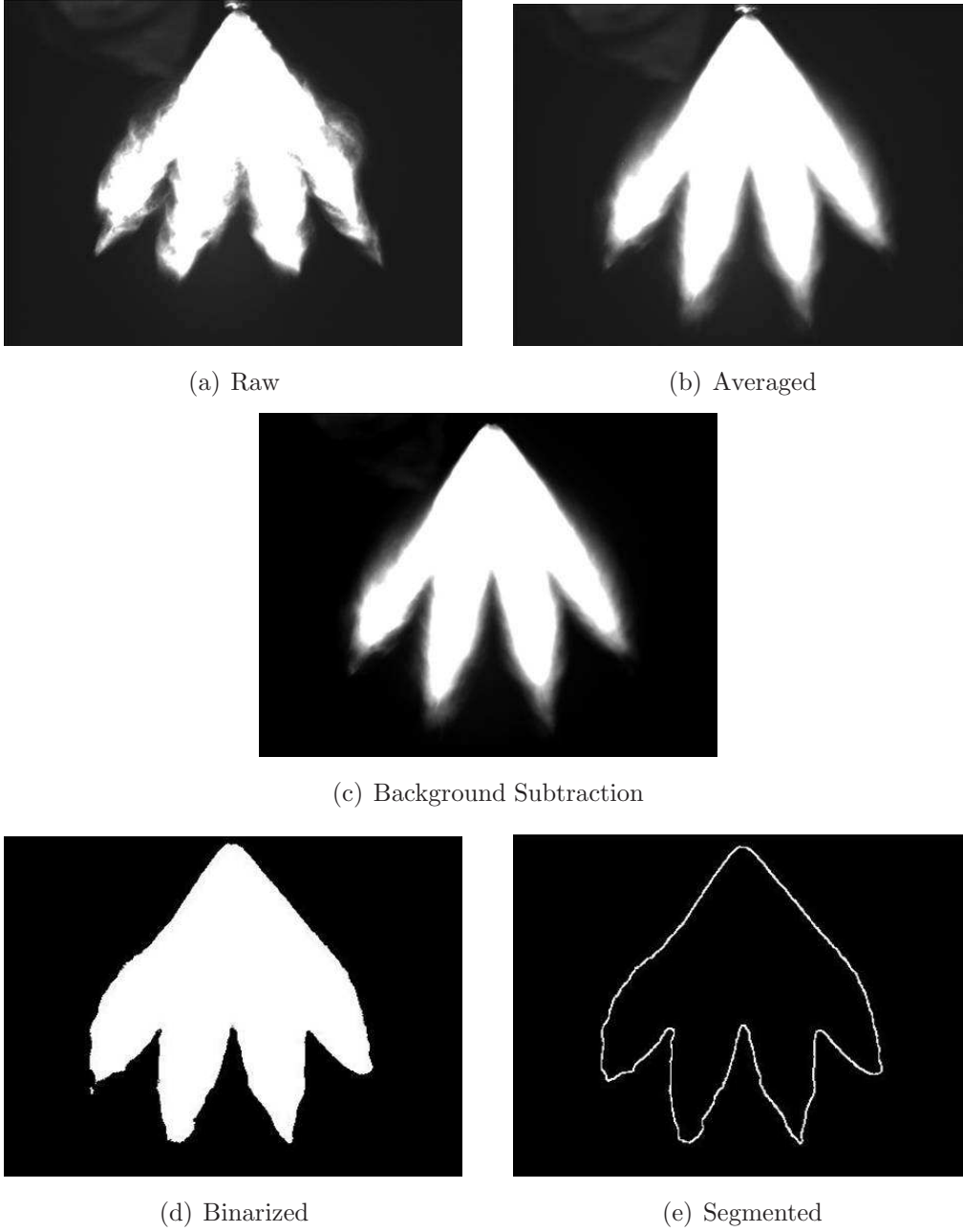


Figure 4.5: Image processing of volumetric images

The points form two lines on each edge which are then used to calculate the angle with the vertical to produce the left and right spray angle.

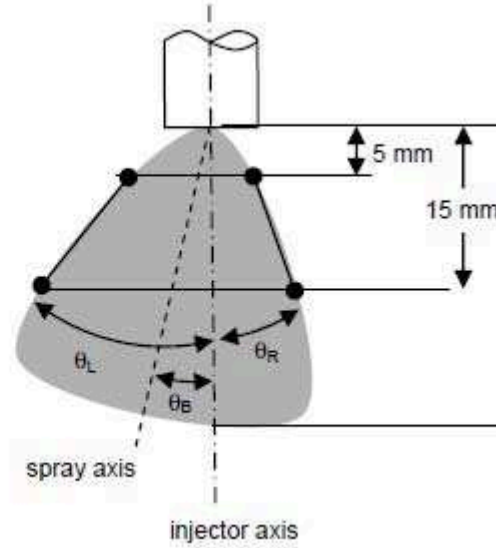


Figure 4.6: Definition of spray angle as recommended by SAE J2715 [45]

Summing these values leads to the spray angle. The bend angle is also depicted in this diagram and is used to describe the angular difference between the axis of the spray plume and the axis of the injector. The application of the spray angle measurement in SAE J2715 [45] is reserved for sprays at 1.5 ms after SOI, but can be used for higher values.

Initial attempts at implementing this definition led to high amounts of variability in the spray angle, the generation of spray edges using fixed distances from the injector tip inhibits the calculation of spray angle for early injection times. The method was therefore modified to apply the trapezoidal approach to locations corresponding to 5% and 25% of the penetration length for the given time step. The use of 5% and 25% was modified from the 5 mm and 15 mm approach at 1.5 ms which for the 10 MPa spray studied would correspond to 7% and 22%. Moreover, rather than use two points to generate the line used for the angle calculation, 5 points were generated on each edge and linear fits were applied to each edge. This further reduced variability by minimizing the impact of surface phenomena which may have passed through the averaging process.

Spray Axis

When evaluating sprays in cross-flows, researchers consider the windward edge or the central axis when analysing the trajectory as illustrated in Section 2.2. The present study focuses on the spray axis for the purpose when discussing trajectory, with the following section identifying the method for defining this axis. The spray axis was selected as the pertinent parameter to evaluate the spray trajectory for a multi-plume spray, because the windward and leeward edges are heavily impacted by the design of the injector. As illustrated in Section 3.1 the sprays evaluated in this study act as canted plumes and so the windward and leeward edges follow this trend.

The spray axis remains a parameter that is relatively difficult to define. Desantes et al. [53] outline a method of analysing Mie-scattered images in order to reduce inherent errors that can develop within imaging techniques. Through the use of the Likelihood Ratio Test (LRT) and a segmentation procedure, background noise is removed and the spray boundaries are identified. Desantes et al. [53] noted 3 methods which can be used for defining the spray axis which are:

- Location of the maximum velocity within the spray plume
- Location of the maximum concentration within the spray plume
- Midpoints between the upper and lower boundaries of the spray plume

With the assumption that regions with high droplet concentration scatter more light, it can be justified that the region of maximum concentration also correlates to the maximum light intensity within the image. From this assumption, Desantes et al. [53], applied a local threshold to the gray scale image. This local threshold scanned each row of the image and set pixels with intensities less than 50% of the row maximum to 0. Then a curve fit was applied to the range of intensities between the newly defined boundaries. The peak of this curve fit was selected as the spray axis. This procedure was continued for each row.

This procedure was amended in the present study to account for variations in the experimental set-up. Since the laser sheet was consistently positioned downwind of the injector, a bias was noticed where the intensity on the leeward edge of the spray was higher than the windward edge as illustrated by Fig. 4.7. This effect was assumed to be a

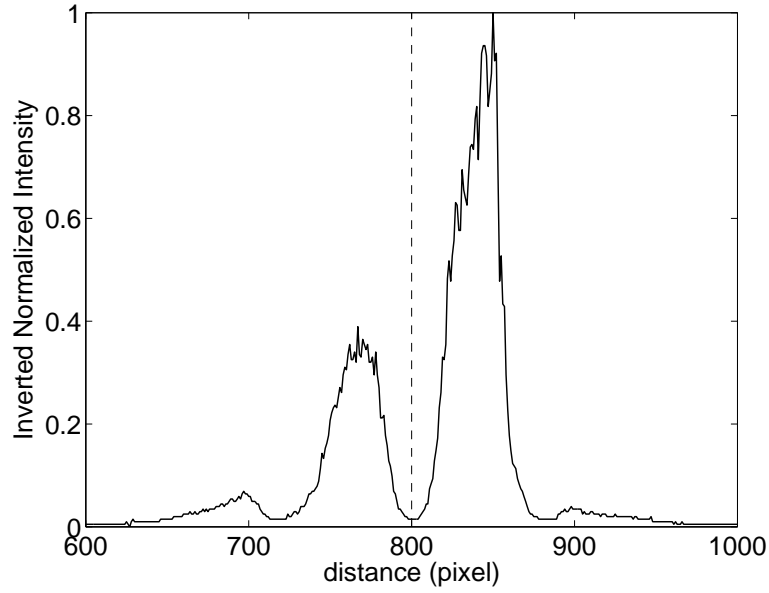
result of the high particle density within the spray plumes which would dissipate the light intensity and reduce the amount of light incident on the windward spray plume.

As such, rather than applying a curve fit between edges defined by the 50% threshold as per Desantes et al. [53], the center location between these boundaries was selected. To reduce the bias further, the local threshold used on the windward edge was selected as 11.85 % for injections occurring between 0.1 and 0.3 ms after SOF, and 22.55% for injections occurring between 0.4 and 1.5 ms after SOF. These values were calculated based on planar images of the 10 MPa injection in ambient conditions and reflects the increased intensity at the leading edge of the spray which is illuminated by the laser light initially. The assumption here is that the spray is symmetric about the planar projection of the spray axis, and hence the maximum intensity should be reflected about the spray axis. This would shift the axis towards the windward edge.

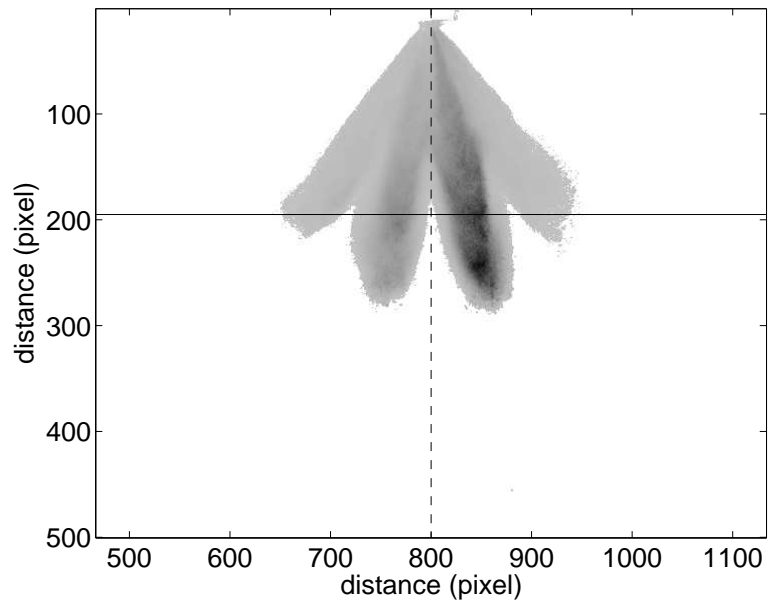
Spray Tail Length

The downstream spray tail length applies to the spray images under cross-flow conditions, and is used to evaluate the ability of the cross-flow to strip and carry droplets from the main spray plumes. It is defined as the distance between the injector axis and the edge of the spray downstream of the air cross-flow, as illustrated in Fig. 4.8. This value can be calculated by applying a binarization scheme similar to that used for the volumetric images to the planar images of sprays in cross-flow.

Another measure known as the upwind spray tail length measures the penetration of the spray upstream of the nozzle. As the injector orientation leaves one of the plumes angled upstream, this parameter measures the ability of this single plume to penetrate into the cross-flow before it experiences breakup. The addition of the upwind and downwind tail length gives the total tail length which expresses the separation between the most upstream spray and the furthest downstream spray.



(a)



(b)

Figure 4.7: Example of intensity variation across fuel spray due to laser illumination in ambient conditions: a) intensity taken at 60% of spray length; b) Image showing 10 MPa spray 0.3 ms after SOF, where the solid horizontal line illustrates the location of the intensity plot shown in a) and the dashed vertical line illustrates the spray axis on both figures.

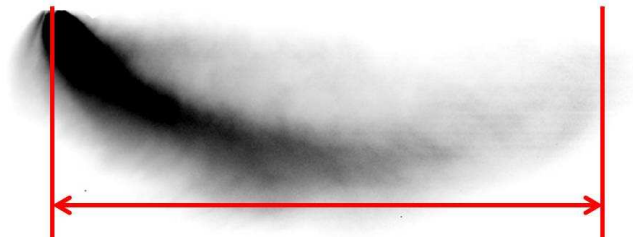


Figure 4.8: Definition for the spray tail length.

Chapter 5

Experimental Error

The following section discusses the uncertainty which is present within the measured data contained in this study. The discussion of uncertainty begins with errors that are introduced through the calibration techniques used for all measurements, and then continues by looking at errors that are specific to the planar and volumetric imaging techniques in Section 5.2 and the PIV technique in Section 5.3.

5.1 Calibration Error

Calibration error is a systematic error that will depend on the accuracy of the calibration method. In the present study two different calibration methods were used each with its own sources of error.

The scaling method discussed in Section 4.1 relies on the user input to select the appropriate scale. With the calibration board used in this study, accuracy is determined by the ability of the user to select the reference points. Increasing the separation between the reference points decreases the resulting error. The width of the lines used to indicate the scale are 0.6mm. Typically either the leading or trailing edge was used to define the reference point, with the selection accuracy being within ± 2 pixels or ± 0.15 mm depending on the scaling applied. Assuming that both reference points have the same level of error, then the maximum error could be as high as ± 0.3 mm. Since reference points were selected with a minimum distance of 40 mm, the resultant scaling error would be

$\pm 0.75\%$. Increasing the separation of the reference points to 60 mm reduces this error to $\pm 0.5\%$. This error would apply to both the lengths measured for spray geometry as well as the velocities calculated in the PIV measurements.

The pin-hole camera calibration method allows for further reduction in error. Here, the error depends on the accuracy with which the software can detect and locate the centres of each dot and the edges. The software is typically able to locate the dot centres to within ± 1 pixel. The RMS of fit calculated for the calibrations was as high as 0.26415 pixels, which when combined with the scale of 9.48757 pixels/mm and the reference point separation of 101.6mm would give an error of 0.027%. For air flow velocities, this is only 0.06m/s for the 220 m/s, and hence can be considered negligible.

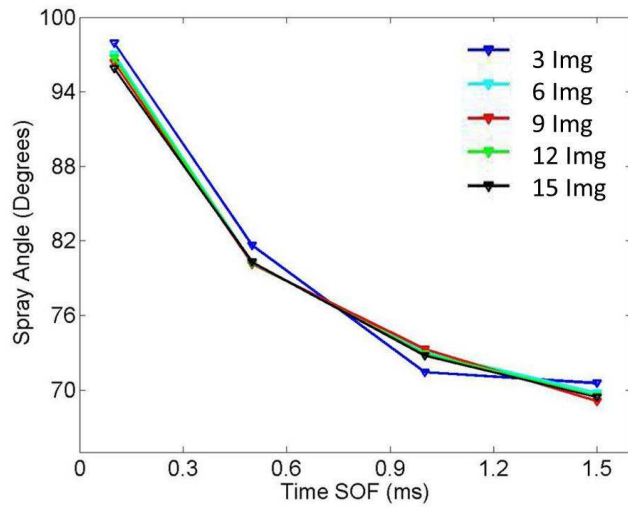
Finally, for the spray angle which is calculated for the non-interacting fuel sprays, the calibration error does not impact the measurement. This is because the angle is independent of the scaling applied to the image.

5.2 Imaging Uncertainty

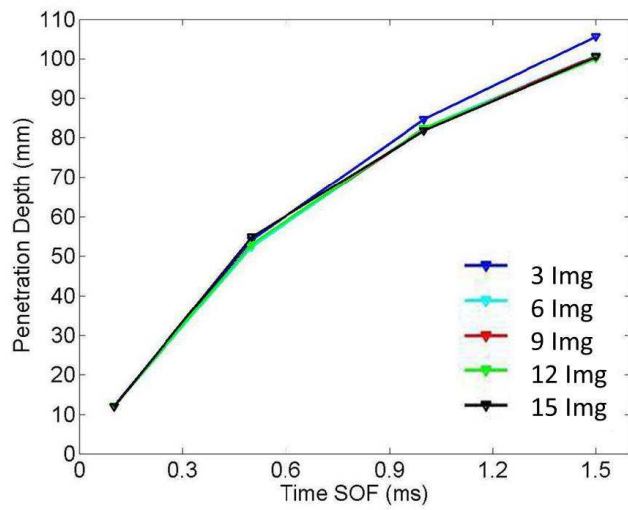
Aside from the errors introduced from the calibration methods, there are two sources of error which impact the measurements taken from the volumetric and planar images. They are the averaging of the instantaneous images, and the selection of the threshold value which differentiates between the background noise and the spray field. The following subsections look at how these sources of uncertainty are considered within the present study.

5.2.1 Imaging Averaging Error

Averaging of instantaneous images is a technique which allows for the reduction in variability of measured parameters through the smoothing of image boundaries. In the present study, geometric characteristics are measured from the ensemble average of 15 instantaneous images taken at specific time intervals after SOF. Figure 5.1 illustrates the impact of increasing the number of images averaged on the the spray angle and penetration depth at four different times. It is immediately obvious that more than 3 images provides a satisfactory result for both the spray angle and the penetration depth for the spray occurring in ambient conditions. However, it is important to realize that each parameter experiences



(a) Spray Angle



(b) Penetration Depth

Figure 5.1: Convergence of average spray angle and penetration depth with increasing number of averaged images for 15 MPa injection.

a natural fluctuation from spray to spray which is attributed to pressure fluctuations in the fuel rail. As a result, increasing the number of averaged images will not capture these fluctuations and hence instead they are considered in the uncertainty values found in Table 5.1. The uncertainty in this table is calculated following Eqs:

$$\overline{P}_i = \frac{\sum_{j=0}^n P_{ij}}{n} \quad (5.1)$$

$$E_{ij} = \frac{P_{ij}}{\overline{P}_i} \quad (5.2)$$

$$\overline{E} = \frac{\sum_{j=0}^n \sum_{i=0}^m E_{ij}}{n} \quad (5.3)$$

$$\sigma = \sqrt{\frac{1}{m \times n - 1} \sum_{j=0}^n \sum_{i=0}^m (E_{ij} - \overline{E})^2} \quad (5.4)$$

$$\epsilon = 1.96 \times \sigma \times 100 \quad (5.5)$$

Here P_{ij} represents the value of the parameter measured off of the ensemble average.

	10 MPa Injection	15 MPa Injection
Spray Angle	±1.4%	±2.1%
Penetration Depth	±1.7%	±2.8%
Spray Width	±2.0%	±1.0%

Table 5.1: Uncertainty from averaging on spray angle, penetration depth, and spray width

Subscript i indexes the time step after SOF at which the parameter is measured and can have values of 0.1, 0.5, 1.0, 1.5 ms after SOF. Index j indicates the number of images which are used to calculate the ensemble average at each time step and changes from 3, 5, 6, 9, 10, 12, 15. \overline{P}_i , found in Eq. 5.1, is the average of the parameter calculated for each ensemble average at the specified time step i. Furthermore, E_{ij} normalizes the parameter using the average for the given time step \overline{P}_i . Next \overline{E} , expressed by Eq. (5.3), is calculated, which gives the overall average of the normalized values. This allows the

standard deviation (σ), seen in Eq. (5.4), to be calculated for a given parameter for the entire range of time steps considered, and for the entire range of ensemble averages considered. Finally, the percentage uncertainty of the measured parameter is quantified in terms of the 95% confidence interval and is expressed as ϵ . The same set of equations was used to account for the uncertainty in the average for the planar images capturing the spray interacting with the cross-flow. It can be noticed from Table 5.2 that the resultant uncertainty for the planar image parameters is significantly higher than for the ambient images. This is indicative of the variability from image to image of the spray structure resulting from the fuel air interaction. Looking at the parameters that were measured, it is

Mach #	Injection		Upwind tail length	Downwind tail length	Total tail length
	Pressure (MPa)	Penetration			
0.35	10	$\pm 3.9\%$	$\pm 5.1\%$	$\pm 1.5\%$	$\pm 1.6\%$
0.35	15	$\pm 2.7\%$	$\pm 6.4\%$	$\pm 5.8\%$	$\pm 5.7\%$
0.58	10	$\pm 2.1\%$	$\pm 4.7\%$	$\pm 0.7\%$	$\pm 1.0\%$
0.58	15	$\pm 3.6\%$	$\pm 3.9\%$	$\pm 1.4\%$	$\pm 1.2\%$

Table 5.2: Uncertainty from averaging on penetration, downwind tail length, upwind tail length and total tail length

also noticeable that the upwind tail length consistently has the highest level of variability. This is attributed to the smaller magnitude of the upwind tail length, which increases the significance of any small changes.

5.2.2 Thresholding Error

For the measurement of spray characteristics one of the most influential parameters is the threshold value which is used to differentiate between the spray and the background. As mentioned in Section 4.3.2, measures to improve the selection of this parameter can be employed although variability still exists.

In the present study, the threshold value is selected for the specific application, with different values being used for the 10 and 15 MPa injections in quiescent conditions and

then substantially different values being used for the planar imaging of the sprays in the cross-flow.

For the quiescent sprays, the effect of a $\pm 10\%$ variance in the threshold value was studied and the effect quantified for the spray angles, penetration depth and the spray width. The error associated with the 95% confidence interval for each parameter is characterized in Table 5.3. The selection of the threshold is also a critical consideration in the evaluation

	10 MPa Injection	15 MPa Injection
Spray Angle	$\pm 3.2\%$	$\pm 4.7\%$
Penetration Depth	$\pm 2.5\%$	$\pm 4.5\%$
Spray Width	$\pm 6.3\%$	$\pm 4.4\%$

Table 5.3: Uncertainty from threshold selection on spray angle, penetration depth, and spray width

of the planar images of sprays in cross-flow. Similar to the ambient sprays, a $\pm 10\%$ variation in threshold was studied for each parameter. The resulting uncertainty is reflected in Table 5.4. These calculations were computed using Eqns. 5.1-5.5, except here j indexes the threshold value applied to the image and is assigned values of 90%, 100% and 110% of the nominal value. This method assumes that a $\pm 10\%$ variation in threshold will still produce a valid result, and so quantifies the uncertainty associated with this range.

Mach #	Injection		Downwind tail length	Upwind tail length	Total tail length
	Pressure (MPa)	Penetration			
0.35	10	$\pm 9.2\%$	$\pm 16.7\%$	$\pm 11.0\%$	$\pm 11.8\%$
0.35	15	$\pm 5.4\%$	$\pm 17.5\%$	$\pm 4.3\%$	$\pm 5.7\%$
0.58	10	$\pm 14.3\%$	$\pm 14.3\%$	$\pm 1.8\%$	$\pm 2.1\%$
0.58	15	$\pm 5.2\%$	$\pm 10.8\%$	$\pm 1.6\%$	$\pm 1.8\%$

Table 5.4: Uncertainty from Thresholding on penetration length as well as downwind, upwind and total tail length

5.3 PIV Uncertainty

The measurement of error associated with PIV measurements is a complex process. Since the measurement technique is able to capture an entire flow field simultaneously, the error is typically different depending on the location within the flow field. Factors which impact the accuracy of PIV include, but are not limited to peak lock, perspective errors, particle slip, particle selection, cross-correlation algorithms which detect and quantify particle motion, pre-processing tools, the selection of interrogation window size, and the auto displacement/deformation techniques.

The following section will consider the impacts of the first 4 sources of error as they pertain to the measured results. Since the estimation of error can be quite involved, the present work will look into studies in literature which quantify and discuss the accuracy of the latter 4 sources of error under similar experimental conditions.

5.3.1 Peak Locking

Locating particles and calculating the displacement of a particle is heavily dependent on the number of pixels which make up the particle in the image. If the particle image diameter is too small, less than 1.5 pixels, the displacement becomes biased towards integer values [54]. Adrian et al. [38] note that the ideal particle image diameter is around 2 pixels, with values between 1 and 2 resulting in pixel biasing effects of an acceptable range. When values fall increasingly below 1, then the effect on the correlation peak is strong. The peak estimation algorithms attempt to locate displacement peaks with sub-pixel accuracy by applying curve fits to the pixels corresponding to the particles [38]. The result of peak locking is most noticeable when viewing the probability density function (PDF) of the measured particle displacements within the field of view. Figure 5.2 shows an example of a PDF plot where peak locking is prominent. The strong peaks clearly illustrate the tendency for pixel displacements to congregate near integer values when peak locking is present.

DaVis also calculates a peak lock parameter which measures the level of peak locking. when this parameter is equal to 0 there is no peak locking while a value of 1 indicates strong peak locking. In practical applications values less than 0.1 indicate that the level of peak locking is considered to be minimal and therefore acceptable.

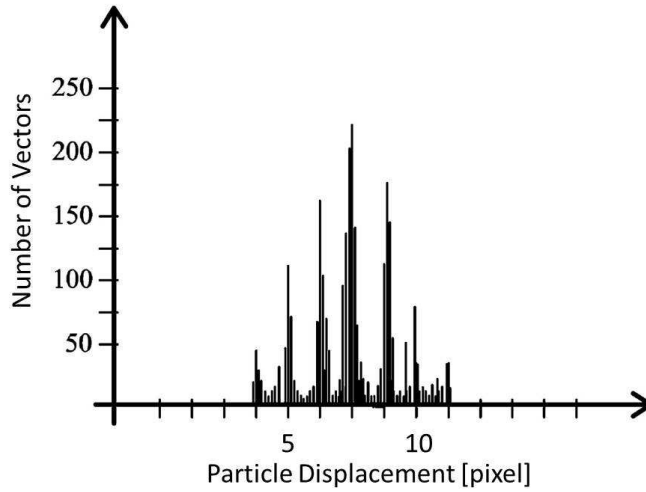


Figure 5.2: Probability Density Function illustrating the effects of peak locking [55]

Table 5.5 gives the values for the peak locking parameter for each experimental conditions studied. It is seen that for the airflow measurements (where the injection pressure is 0) the peak locking coefficient is as high as 0.36 signifying that peak locking is an issue. Alternatively, for the measurements of the fuel spray interacting with the air flow, the peak locking parameter is well below 0.1 showing that peak locking is not significant. The only exception is the scenario with an air velocity of 129 m/s and the injection pressure of 15 MPa, which has a value of 0.13 which is considered to signify mild peak locking effects.

Air Velocity (m/s)	Mach #	Injection Pressure (MPa)	Peak Lock
125	0.35	0	0.32
125	0.35	10	0.00
125	0.35	15	0.13
215	0.58	0	0.36
215	0.58	10	0.02
215	0.58	15	0.01

Table 5.5: Peak Locking

The impact of peak locking effect on the air jet measurements can be considered at

most to be 0.5 pixels which for the 129 m/s air flow corresponds to $\pm 4.5 m/s$ or 3.5% of the core velocity and for the 220 m/s air flow corresponds to $\pm 6.4 m/s$ or 2.9% of the core velocity. This error has the largest impact in the shear layer of the flow, where the radial velocity magnitude is two orders of magnitude smaller than the core velocity. However, since the core region is of principle interest in this study, this impact on the shear layer is not considered further.

5.3.2 Perspective Error

Perspective error, is the error which occurs from capturing three-dimensional motion in a two-dimensional image. Theoretically, PIV, would use a sufficiently thin laser sheet such that, out-of-plane motion within the laser sheet is negligible. Furthermore, the laser sheet is typically oriented such that the major components of velocity are captured. However, in practice, the laser sheet still has a thickness and so represents a volume. Thus, perspective error occurs when particles within the illumination volume of the light sheet have an out-of-plane velocity component. As the image sensor can only record two-dimensional motion, this out of plane component is translated into in-plane motion and leads to a variance between the actual particle displacement and the recorded particle displacement. Figure 5.3 illustrates this effect.

Here the particle which travels out of plane, is perceived to have a displacement of $\Delta x'$ rather than Δx which is the physical displacement in the plane of interest. The error between these two values is expressed by Prasad [56] as

$$(\epsilon_x, \epsilon_y) = \left(\frac{\Delta z}{\Delta x} \tan \theta_x, \frac{\Delta z}{\Delta y} \tan \theta_y \right) \quad (5.6)$$

As is illustrated, the components of the perspective error are heavily influenced by the magnitude of the displacement in the out of plane direction as well as the viewing angle formed between the lens, the optical center of the image, and the particle in question. As such, particles that have out of plane components but are imaged at the optical center of the sensor have a low perspective error, because the viewing angle is zero, while particles which are at the edges of the image sensor and have larger out of plane components have a larger error.

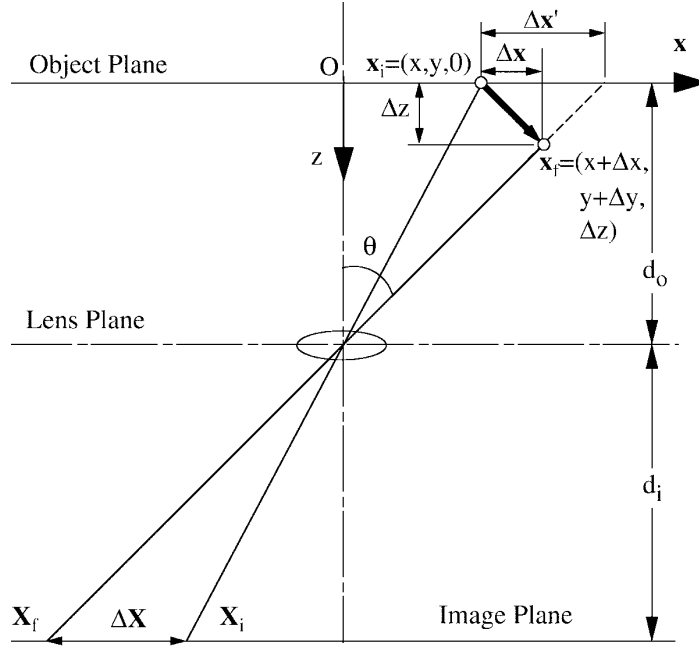


Figure 5.3: Diagram illustrating the development of perspective error when trying to capture 3-dimensional motion with a single camera [56]

Reduction of perspective error is highly important, as it can result in 10% error for instances where the out-of-plane component and in-plane component have equal magnitudes and the angle to the viewing angle on the order of 5° [56]. The two simplest methods for reducing this error are: reducing the thickness of the planar light sheet and increase the distance between the lens and the field of view.

For the present conditions, two instances of perspective error are considered. The first is the perspective error for the air jet velocity calculations and the second is the perspective error for the fuel spray velocity calculations. For both instances the distance between the lens and the field of view was held constant at 0.5 m.

The calculation of error for the air jet velocities considers the impact that the 4mm laser sheet thickness had on the results. The out of plane component of velocity is calculated by finding the z-component of radial velocities which are not aligned with the vertical V_y component, as illustrated by Fig. 5.4. Here it is assumed that these particles initiate at the center of the laser sheet travelling towards the edge. Furthermore, this error is calculated for velocities occurring in the shear layer (where the radial component of velocity

is maximized) and at the edge of the viewing plane (where the distance from the optical center is maximized). As such, these particles are offset from the optical center in the x and y directions and so impact both the measured V_x and V_y velocities. To properly account for the thickness of the shear layer, points were selected near boundary of the potential core and the shear layer, and at the boundary of the shear layer and ambient air. The errors were calculated using Eq. (5.6) with the error in the V_x component of velocity, ϵ_x , remaining below 0.2% and the error in V_y, ϵ_y , remaining below 1%.

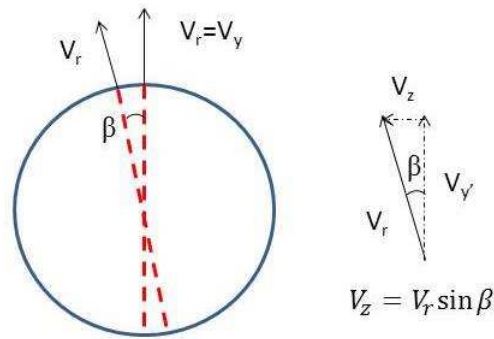


Figure 5.4: Diagram illustrating perspective error due to out-of-plane radial velocity component for cross-flowing air jet

The second instance, where perspective error is considered, is PIV of the fuel spray droplets. In this case, the error is considered at 2 different locations and calculated using Eqn. (5.6). The first is in the shear layer at the edge of the image (similar locations as measured for the air jet), where droplets have mixed with the air flow. The results show that ϵ_x remains below 0.3% with a value of 2.53% appearing for the 15 MPa spray issuing into the 215 m/s cross-flow, and ϵ_y remains below 1%.

The second location where the perspective error is considered is close to the injector tip. Here the fuel spray is known to have a significant out-of-plane component due to the injector design. Even in the cross-flow conditions, the fuel spray retains its shape near the injector tip, until the airflow can sufficiently atomize the spray plumes and carry the droplets downstream. These out of plane plumes, numbered 3 and 4 in Fig. 3.2, have penetration velocities of 80 m/s for the 10 MPa injections and 110 m/s for the 15 MPa injections and are penetrating out-of-plane at angles of 22.7° and 23°. This potentially leads to an out of plane velocity magnitude greater than the in-plane velocity component

which significantly increases error in this region. Furthermore, although the thickness of the laser sheet is 2-4 mm, it is not considered as a limiting factor when assessing whether the particles or spray plumes will be resolved in the image. This is because in the near region of the injector tip, significant amounts of scattered light are absorbed by the dense plumes allowing them to remain visible even as they proceed outside of the illumination volume. As such, the errors (ϵ_x, ϵ_y) in this region appear to be as high as 42 % which leads to the assumption that the PIV accuracy in this location is inadequate to resolve the velocity field.

5.3.3 PIV Averaging Error

Consideration of the averaging error for the PIV analysis is performed in a similar fashion to that for the spray geometry images. In this case, the axial or x-component of velocity, the radial or y-component of velocity and the turbulent kinetic energy are calculated based on sets of 500, 1000, 1500, 1800, 1900, and 2000 images. The profiles are considered at locations of x/d of 1 and 4 for each parameter. Figures 5.5(a)-(f) illustrate the convergence of the average values towards the average of 2000 images, which is taken as the true value for the purpose of this study. As a result of this convergence, conclusions about the error associated with the sample size can be made.

Figure 5.5 illustrates the convergence of the mean values for the axial and radial velocities, and the TKE values for the 215 m/s cross-flow velocity. It is evident that the mean axial velocity values converge quickly, with even 500 images being enough to achieve sufficient accuracy. While the same can be said for the mean radial velocity at a distance of $x/D = 1$, it is noticed that 1000 images are required to accurately calculate the average value within the shear layer, which is found at ± 12 mm in the radial direction, at $x/D = 4$. Even after averaging 2000 images, an error of 6.7% still exists for the mean radial velocity within this shear region. Finally, looking at the TKE, it is evident that within the shear layer, arriving at a suitable value requires upwards of 2000 images. It is also noted that increasing the number of images within the sample results in diminishing returns, with the improvements in averaged TKE values becoming smaller. As such, a data set of 2000 images is taken to be sufficient, acknowledging that an error of 3.5% can exist for the TKE within the shear layer.

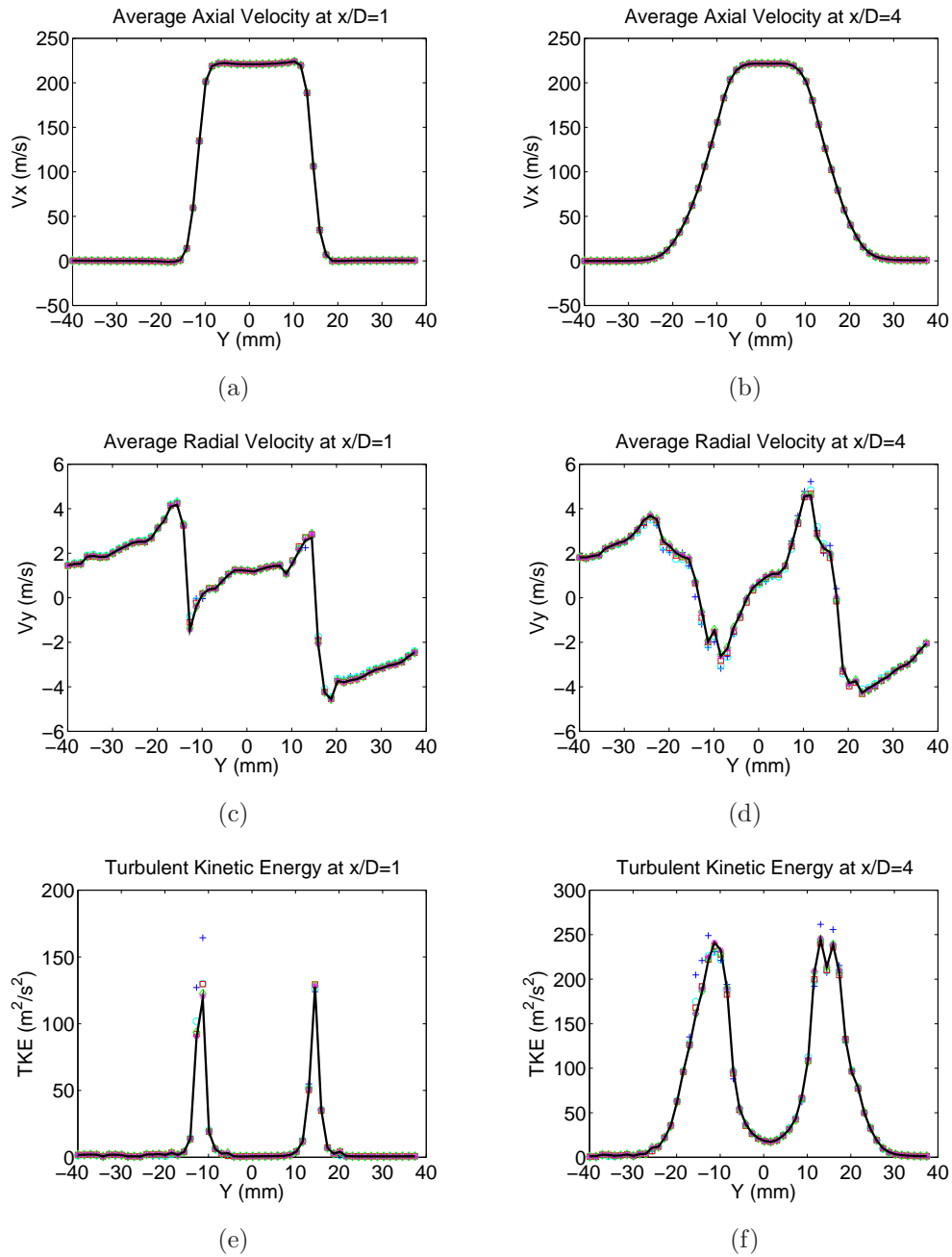


Figure 5.5: Convergence of velocity and TKE for 125 m/s cross-flow inlet velocity (blue cross=500 images averaged, cyan circle=1000 images averaged, red square=1500 images averaged, green diamond=1800 images averaged, pink asterisk=1900 images averaged, black line=2000 images averaged).

5.3.4 Discussion of Errors from Literature

The calculation of uncertainty within PIV is an extensive process which involves the consideration of many sources of error aside from peak locking, perspective error, particle size, and particle tracking. Some other possible sources of uncertainty, which are not directly addressed in the present study include, the numerous pre-processing tools which are used to improve image quality, the ability of the cross-correlation algorithms to accurately detect particle motion, the selection of interrogation window size and auto displacement/deformation techniques. As such, the uncertainty associated with the PIV is assigned based on techniques used to improve the PIV process, and how these improvements have impacted known studies within literature. Wilson et al. [57], measured the uncertainty on the mean and fluctuating components using DaVis 7.2. The study looks at an air jet with Reynolds numbers of 2.57×10^4 and 8.94×10^4 , with oil droplet seeding introduced upstream of the blower, in a similar fashion to the present study. Droplet diameters were assumed to be in the order of $1 \mu\text{m}$ and data sets of 1000 images were recorded at 3 Hz to ensure convergence. As such, the experimental conditions of the work of Wilson et al. [57] are considered to be sufficiently similar to the present study. The algorithm employed in this study, is the standard cross-correlation algorithm. Three passes were used when processing images each with a 50 % overlap of the interrogation region, which was 32×32 for the first pass and then 16×16 for the final two passes. The uncertainty present in the algorithm is evaluated based on 4 parameters, particle image size, particle seeding density, shear rate and displacement which are investigated by Timmins et al. [58]. The findings show that the main contributors to uncertainty are sub-pixel displacement which typically occurs within the shear region of the air jet or the periphery of the spray, and shear rate which again is found at the edge of the air jet. Comparing with LaVision's performance in the second international PIV challenge, which are documented by Stanislas et al. [59], it can be estimated that within the core region of the jet, the accuracy of the PIV algorithm in calculating the mean parameters is on the order of 1.7 %.

5.3.5 Summary of Overall Error

To combine the individual errors into a single representative value, the overall error for either the planar and volumetric imaging measurements or the PIV measurements is cal-

culated by using the root sum squared method defined as

$$\epsilon_{tot} = \sqrt{\sum_{i=0}^n \epsilon_i^2} \quad (5.7)$$

Here ϵ_i represents the individual source of error, and n is determined by the number of sources of error which are included in the total. For the spray imaging technique the effects of calibration (ϵ_{cal}), averaging (ϵ_{avg}), and threshold selection (ϵ_{thresh}) are considered as the main sources of error as discussed previously. The overall uncertainties associated with the measured data for sprays in quiescent conditions are listed in Table 5.6, and are given for each parameter measured and the corresponding injection pressure. Similarly, the overall uncertainties for the measured parameters associated with the planar images of sprays issuing into cross-flows are listed in Table 5.7 for each set of conditions.

ϵ_{tot}		
	10 MPa Injection	15 MPa Injection
Spray Angle	$\pm 3.5\%$	$\pm 5.1\%$
Penetration Depth	$\pm 3.0\%$	$\pm 5.3\%$
Spray Width	$\pm 6.6\%$	$\pm 4.6\%$

Table 5.6: Total measurement uncertainty for quiescent spray parameters

Mach #	Injection Pressure (MPa)	Penetration	Upwind tail length	Downwind tail length	Total tail length
0.35	10	$\pm 9.2\%$	$\pm 16.7\%$	$\pm 11.0\%$	$\pm 11.8\%$
0.35	15	$\pm 5.4\%$	$\pm 17.5\%$	$\pm 4.3\%$	$\pm 5.7\%$
0.58	10	$\pm 14.4\%$	$\pm 15.1\%$	$\pm 2.1\%$	$\pm 2.4\%$
0.58	15	$\pm 6.3\%$	$\pm 11.5\%$	$\pm 2.1\%$	$\pm 2.2\%$

Table 5.7: Total measurement uncertainty for cross-flow spray parameters

The overall uncertainty associated with PIV measurements is also calculated using Eqn. 5.7, however, as mentioned previously, the accuracy needs to be considered for different

regions within the flow. As such, the overall uncertainty is quantified for the cross-flow mean velocity within the potential core, shear layer and finally the main body of the spray plume within the cross-flow, and are presented in Tables 5.8-5.10.

Mach #	Velocity Component	Perspective	Calibration	Peak Lock	Algorithm	Total
0.35	V_x	$\pm 0.2\%$	$\pm 0.5\%$	$\pm 3.5\%$	$\pm 1.7\%$	$\pm 3.9\%$
0.35	V_y	$\pm 1.0\%$	$\pm 0.5\%$	$\pm 3.5\%$	$\pm 1.7\%$	$\pm 4.0\%$
0.58	V_x	$\pm 0.2\%$	$\pm 0.5\%$	$\pm 2.9\%$	$\pm 1.7\%$	$\pm 3.4\%$
0.58	V_y	$\pm 1.0\%$	$\pm 0.5\%$	$\pm 2.9\%$	$\pm 1.7\%$	$\pm 3.5\%$

Table 5.8: Total measurement uncertainty for PIV of cross-flow potential core

It is evident that mean velocity within the potential core of the cross-flow is accurate up to $\pm 4.0\%$ while for the shear region the mean velocity components have an uncertainty less than $\pm 7.6\%$. It should also be pointed out that the uncertainty of mean velocity within the shear layer considers the impacts of the number of images included in the ensemble average; a value which is considered negligible within the potential core.

Mach #	Velocity Component	Total from Core	Averaging	Total
0.35	V_x	$\pm 3.9\%$	$\pm 6.5\%$	$\pm 7.6\%$
0.35	V_y	$\pm 4.0\%$	$\pm 6.5\%$	$\pm 7.2\%$
0.58	V_x	$\pm 3.4\%$	$\pm 6.5\%$	$\pm 7.3\%$
0.58	V_y	$\pm 3.5\%$	$\pm 6.5\%$	$\pm 7.4\%$

Table 5.9: Total measurement uncertainty for PIV measurement of cross-flow shear layer

Finally, the uncertainty of the mean velocity within the spray, with the exception of the area near the injector tip, is less than $\pm 8.0\%$. In this region, the uncertainty within the shear layer is used as sharp velocity gradients are expected throughout the spray volume.

Mach #	Velocity Component	Shear Total		
		Less Perspective	Perspective	Total
0.35	V_x	$\pm 7.6\%$	$\pm 2.5\%$	$\pm 8.0\%$
0.35	V_y	$\pm 7.6\%$	$\pm 1.0\%$	$\pm 7.7\%$
0.58	V_x	$\pm 7.3\%$	$\pm 2.5\%$	$\pm 7.6\%$
0.58	V_y	$\pm 7.3\%$	$\pm 1\%$	$\pm 7.4\%$

Table 5.10: Total measurement uncertainty for PIV measurement of sprays

Furthermore, the perspective error is increased from that used for the cross-flow due to the strong out-of-plane component of velocity present in the fuel spray.

While the uncertainty for the mean velocities is characterized, the values for the fluctuating components which would impact TKE, or near the injector tip are not calculated as the algorithms used for PIV are generally more sensitive to uncertainty in these values.

In summary, the overall uncertainty has been quantified for measurements taken from planar and volumetric spray images and for mean velocities quantified using PIV techniques. The overall uncertainties calculated are used within the analysis and discussion of the measurement results presented in the next chapter.

Chapter 6

Results and Discussion

The experimental measurements taken in this study can be assessed in three parts. The measurement and characterization of the air jet which is used to produce the cross-flow conditions, the fuel spray characterization in ambient conditions, and the fuel spray injected into the air cross-flow.

6.1 Air Flow Characterization

The present section covers the characterization of the air jet independent of the fuel spray. Two non-dimensional parameters at the air nozzle exit are used in this study to characterize the air jet. They are the Mach number (Ma_g) and the Reynolds number (Re_g) of the air stream. The Ma_g , given below

$$Ma_g = \frac{U_o}{a} \quad (6.1)$$

gives the ratio between the average core velocity of the air jet U_o and the speed of sound a in air at the same conditions. a is calculated from the properties of the air and is given as $a = \sqrt{\gamma R_* T_{static}}$, where $\gamma = 1.4$ and $R_* = 287 \frac{J}{Kg \times K}$. Re_g represents the ratio of the fluid momentum to the viscous forces as defined by

$$Re_g = \frac{\rho_g U_o D}{\mu_g} \quad (6.2)$$

and is commonly used to verify that the flow is turbulent. Here the density (ρ_g) and the dynamic viscosity (μ_g) are the air properties at the given temperature, while D represents

the outlet diameter of the air nozzle. The critical Reynolds number, for a round jet, is 1500 and indicates the transition of the flow from laminar to turbulent, with the flow becoming fully turbulent above $Re_g = 3000$ [60].

Table 6.1, gives the Ma_g and the Re_g numbers which are calculated for the given air jet mean velocity values and the associated measured static temperature (T_{static}) at the outlet of the air nozzle. In comparing the Ma_g numbers for the air flows with the critical Ma_g

U_o ($\frac{m}{s}$)	T_s ($^{\circ}C$)	a ($\frac{m}{s}$)	Ma_g	Re_g
125	37.6	353.35	0.35	1.9×10^5
215	67.7	370.07	0.58	2.7×10^5

Table 6.1: Air Flow Characteristics

number of 0.3, which is typically taken as the upper limit when assuming compressibility is negligible, it is evident that the air flows are compressible although only slightly in the case of $Ma_g = 0.35$. The Re_g numbers of the flows are an order of magnitude greater than the critical value indicating that the flow is fully turbulent.

6.1.1 Jet Characteristics

The jet discussed in this study is a submerged jet, which issues into a medium which is initially at rest. It is common to classify the jet using 3 regions as illustrated in Fig. 6.1. These three regions are known as the initial or flow development region, the transitional region and the far or fully developed region. The initial region of the jet is characterized by the existence of a potential core region. This core region which extends from the jet outlet contains fluid which retains the inlet velocity of the jet, and gradually decays as the jet spreads and ambient air is entrained and mixed with the jet. The boundaries of the core region marks the inner boundary of the jet shear layer. In this region where the viscous forces are more important, energy is transferred from the jet to the surrounding medium. As a result the shear layer contains a mixture of fluid from the jet and from the surrounding medium and the resulting velocity profile decays from the core velocity to the surrounding medium velocity. The initial region ends once the potential core disappears and is marked by the merging of the inner boundaries of the shear layer as indicated in

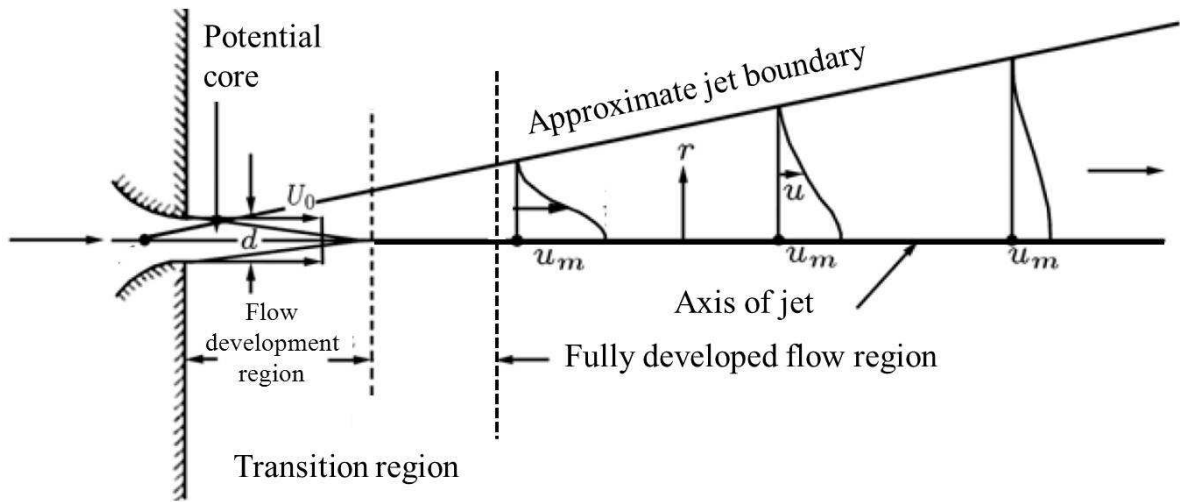


Figure 6.1: Illustration of a time-averaged air jet adapted from [61]

Fig. 6.1. The next region which is the transition from the initial to the fully developed region, is often considered to be negligible for most applications. The fully developed region, is commonly referred to as the mixing region with the flow field resembling that from a point source [62]. The fully developed region is also known as the self-similar region where non-dimensionalization of the velocity profiles allows them to collapse onto the same curve. Figure 6.2 shows the contours of the $Ma_g=0.35$ (top) and $Ma_g=0.58$ (bottom) air jets. Here the initial region and the fully developed region are clearly visible, with the development of the shear layer clearly visible. As is evident, the potential core is the only region which contains a relatively uniform average air flow, and hence this region is ideally suited for sprays in the cross-flow since the cross-flow velocity is well defined.

Potential Core

The primary focus of this study is the injection of the fuel spray into a high velocity cross-flow. As such, the initial region of the air jet and more specifically the potential core remains the focus when characterizing velocity of the air jet. The potential core length, L_o , which defines the distance from the jet outlet at which the potential core disappears is reported in literature to be independent of the exit velocity and fluid properties for an incompressible turbulent round jet, but is instead directly proportional to the outlet

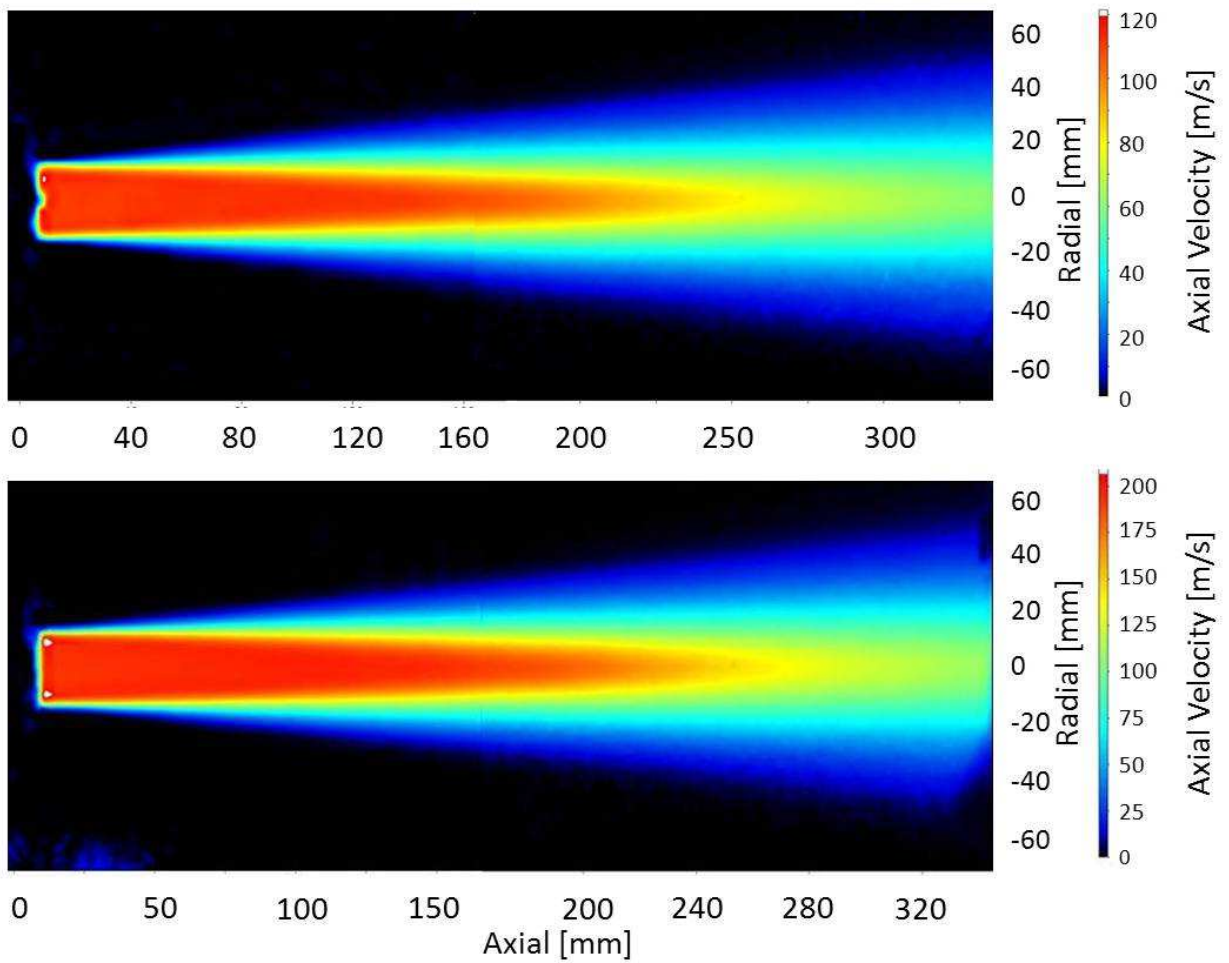


Figure 6.2: Contour plots for the $Ma_g=0.35$ (top) and $Ma_g=0.58$ (bottom) air flows, illustrating the potential core and shear layers.

diameter, D , as noted by Lee et al.[63]:

$$L_o = KD \tag{6.3}$$

Where K is the proportionality constant. For Lee et al. this constant was found to be 6.2, while, Abramovich [62] uses a coefficient of 4 for an isothermal jet. Antoine et al.[64] noted that this length could be between 5-10 for $1.0 \times 10^4 < Re_g < 9.5 \times 10^4$. Discrepancies in the value of K have a number of explanations such as the tendency to neglect the transitional region making the main and initial regions of the jet adjacent as applied by Zaman et al. [65]. Another source of variability arrives from the calculation of this potential core boundary. Abramovich [62] and Milanovic et al. [66] defined the boundary of the potential core and the shear layer as the point at which the velocity reaches 90%, with the outer edge of the shear layer defined as 10% of the core velocity. The dependence of the potential core

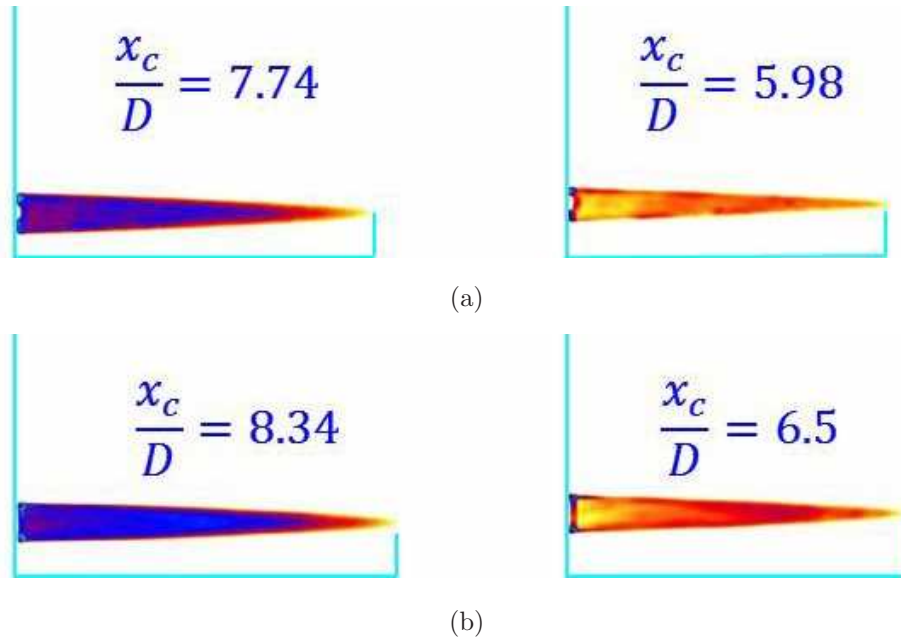


Figure 6.3: Length of the potential core defined by using 90% of U_o (left image) and 99% of U_o (Right image) boundaries for a) $Ma_g=0.35$ and b) $Ma_g=0.58$

length on the selection criteria is obvious from Fig. 6.3 which uses $0.90 U_o$ as the criterion for the left hand column of images, and $0.99 U_o$ criterion for the right hand column. It is also apparent that with either criterion, the potential core measurements are within

the range noted by Antoine et al.[64]. Although not displayed, the potential core was also measured for $Ma_g=0.14$. With an outlet temperature of 24.5°C this air jet is incompressible and non-isothermal, the potential core length for this flow was 6.70, with $0.90 U_o$ as the boundary criterion and 4.77, with $0.99 U_o$ as the boundary criterion. These values are close to the constants used by Lee et al.[63] and Abramovich [62] for the incompressible and isothermal flows. A noted characteristic of compressible flows is that with increasing Ma_g the core length also increases. This effect, which is evident in the results, is brought about by a reduction in the level of mixing, as well as changes at the nozzle exit in static pressure and density [65, 67, 68].

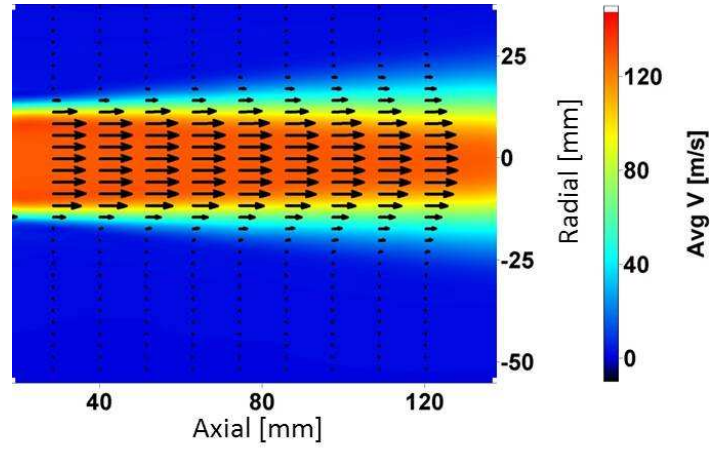
Another aspect of the present flows is the non-isothermal conditions that exist. The ring compressor used to achieve the required air velocities, introduces a significant amount of heat into the system which leads to the increased temperature of the air jet. Abramovich [62] notes that the effect on the boundary layer velocity profile, and thus the outer boundary layer location, by thermal variation between the jet and the ambient can be considered negligible when the following criterion is satisfied:

$$U_o^2 \ll JgC_pT_s \quad (6.4)$$

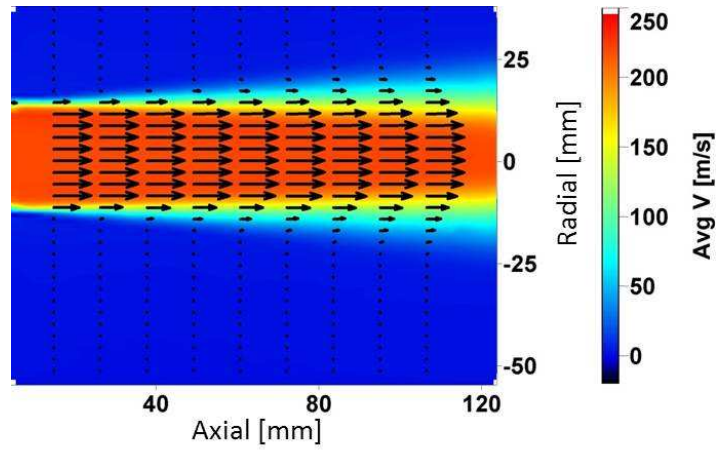
Where J represents the mechanical heat equivalent which is $427 \frac{kg \cdot m}{cal}$, g is gravitational acceleration, C_p is the specific heat capacity and T_s is the static temperature. For the present study, U_o^2 is less than 0.02 % for both Ma_g which is sufficient to conclude that the thermal effects on the potential core are negligible.

Velocity Distribution

The potential core region of the air jet contains a uniform velocity profile which allows it to be treated as a uniform cross-flow. The region of interest is between 20 to 140 mm from the jet outlet or x/D values of 0.8 to 5.6. The average velocity field in the region of interest are depicted in Figs. 6.6 and 6.7 which correspond to the $Ma_g = 0.35$ and $Ma_g = 0.58$ air flows respectively. A total of 2000 images were taken for each air flow. In comparing the initial regions, the velocity appears to be uniform within the core region with the shear layer gradually developing along the periphery. As is expected from the measurement of the potential core, the $Ma_g = 0.35$ air flow experiences a higher level of entrainment which is reflected through the more prominent shear layer and the increased parabolic nature of the velocity profile which develops at an axial distance of 100 mm.



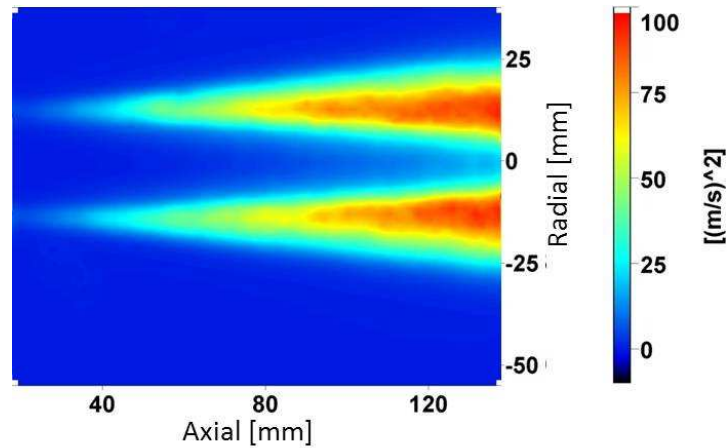
(a)



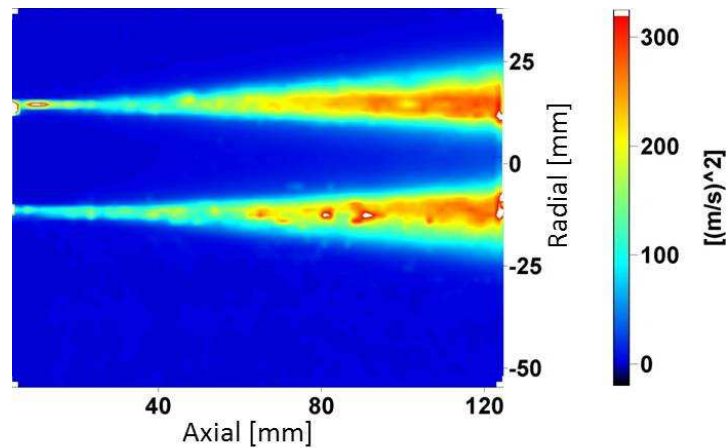
(b)

Figure 6.4: The velocity distribution in the air jet for a) $Ma_g=0.35$ and b) $Ma_g=0.58$.

For the average turbulent kinetic energy (TKE) for both the $Ma_g = 0.35$ and $Ma_g = 0.58$ air flows, it is evident that the core of the jet has a relatively low TKE value with the majority of the TKE residing in the shear layer. It is evident that the TKE increases with increasing Ma_g . Furthermore, it is evident that both airflows appear quite symmetric about the center axis.



(a)



(b)

Figure 6.5: The turbulent kinetic energy distribution for a) $Ma_g=0.35$ and b) $Ma_g=0.58$

Figures 6.6 and 6.7 shows a sample of 6 instantaneous images taken at a frequency of $4.973Hz$.

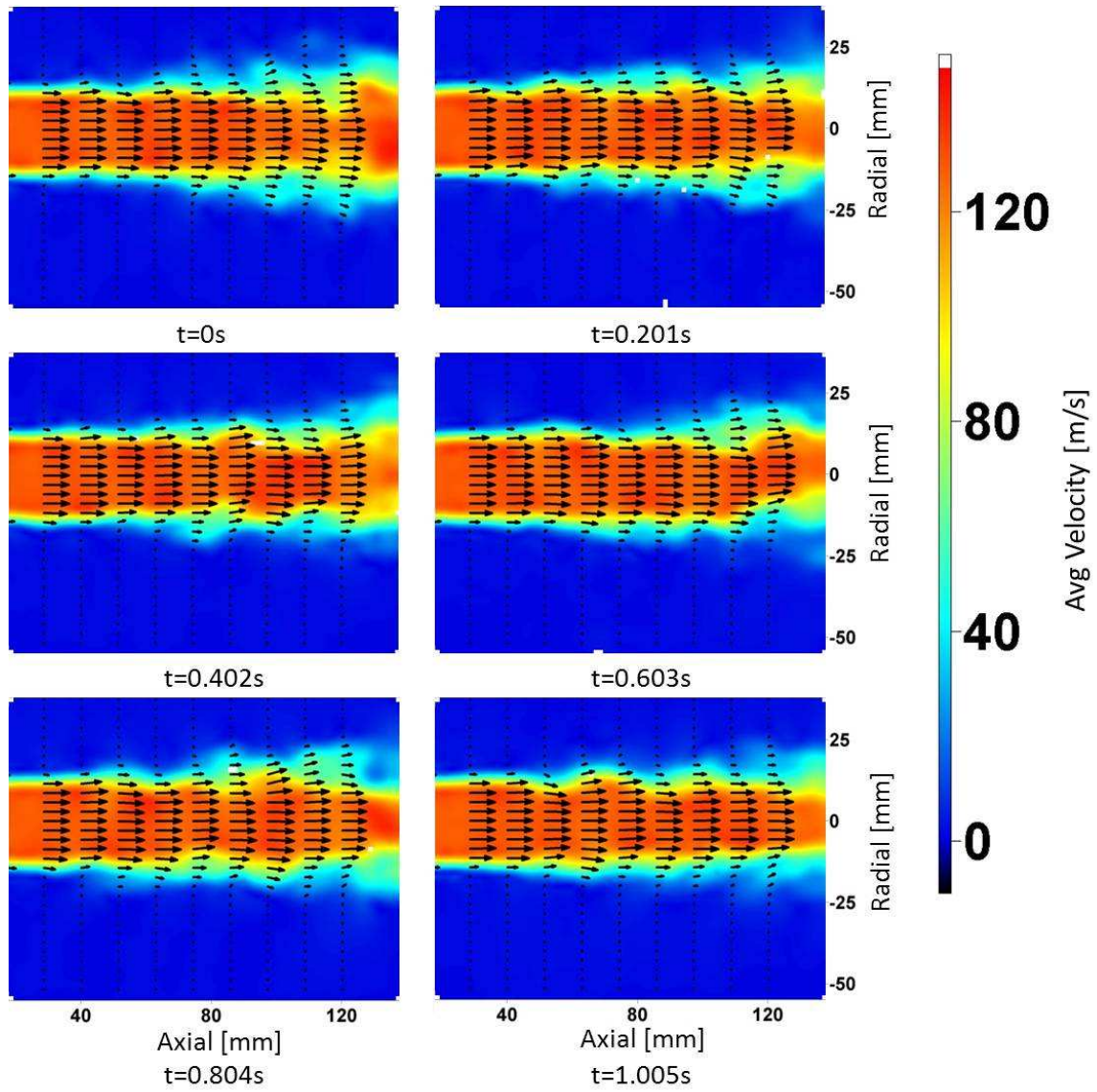


Figure 6.6: $Ma_g=0.35$ instantaneous velocity vector plots taken at 4.973 Hz

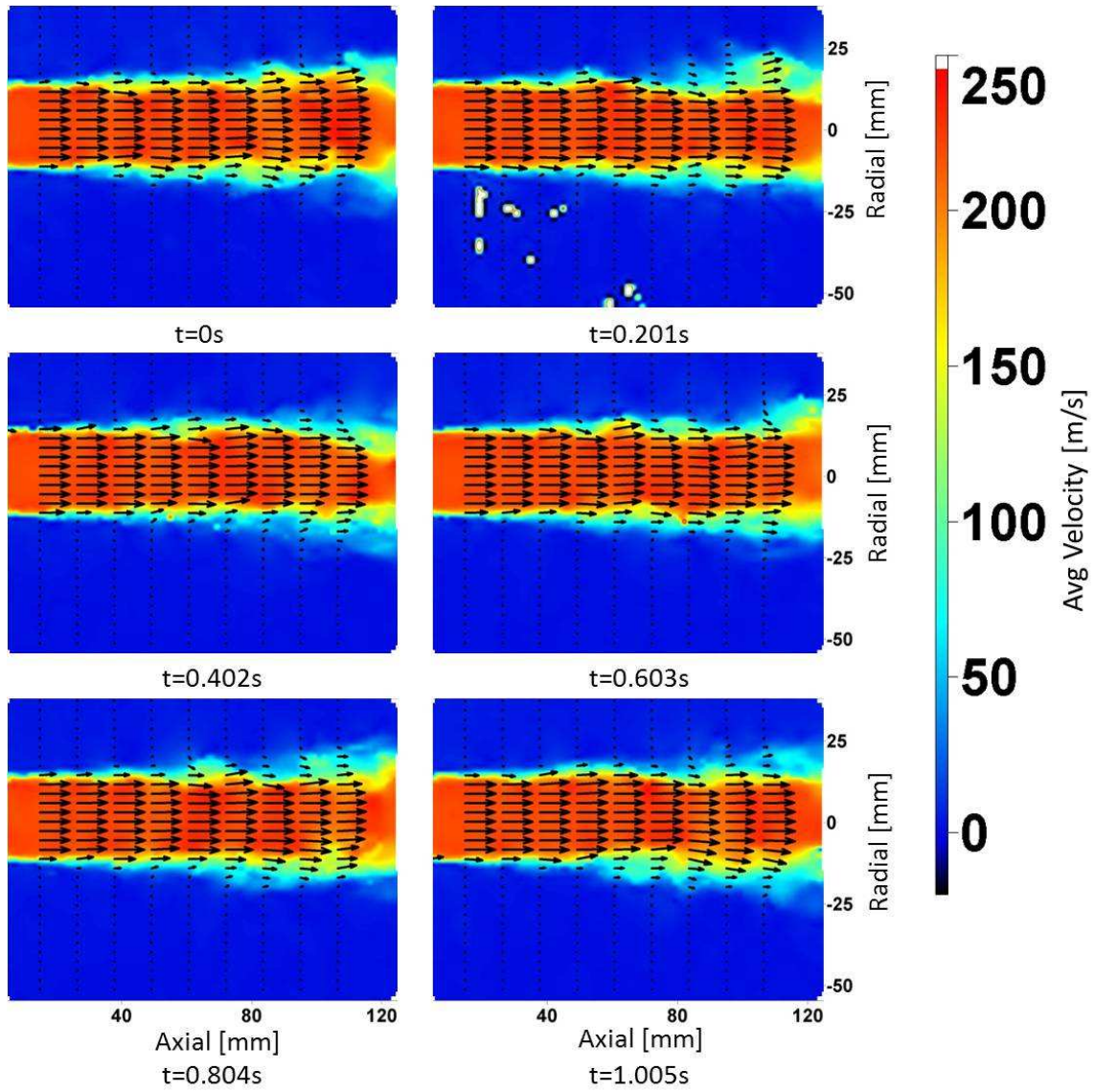


Figure 6.7: $Ma_g=0.58$ instantaneous velocity vector plots taken at 4.973 Hz

The instantaneous images highlight the presence of vortices traversing along the periphery of the jet as the high velocity air entrains the stagnant air in the enclosure. From the progression of instantaneous images for both the $Ma_g = 0.35$ and $Ma_g = 0.58$ air flows, the vortices appear to reduce the cross sectional area of the potential core although this occurs earlier and more frequently for the lower velocity flow whose potential core degrades faster and hence has a higher mixing rate. It is the interaction with these structures which will be noticeable in the spray geometry and spray PIV results presented later in this chapter. While these instantaneous images show that the vortices start to form as early as $x=30$ mm, it is not until $x=60$ for the 50 m/s and $x=80$ for the 130 and 230 m/s flows that this vortex formation seems to penetrate into the core region of the jets.

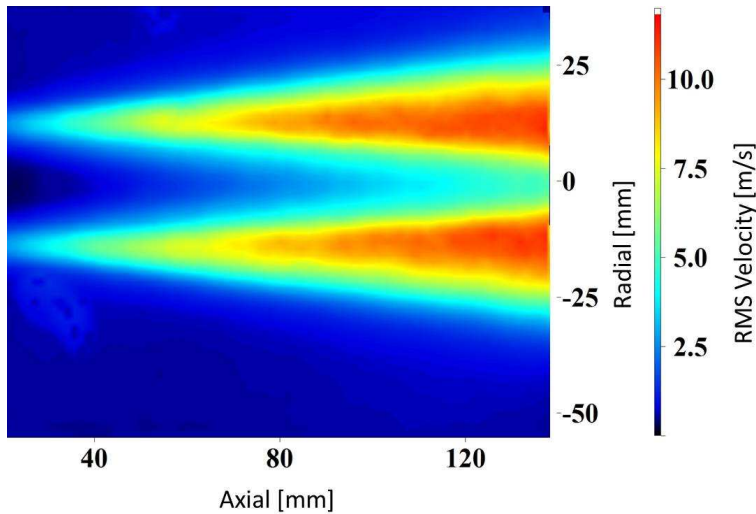


Figure 6.8: RMS of velocity fluctuations for $Ma_g=0.35$ cross-flow conditions

Figures 6.8 and 6.8 further quantify the fluctuating instantaneous velocity at the periphery of the air jet, through the root mean square (RMS) of the fluctuations. It is observed that near the outlet of the jet the velocity remains stable with negligible fluctuations near the jet center while at the periphery of the jet, the velocity magnitudes fluctuate by as much as 4% for the 125 m/s air flow and almost 9% for the 215 m/s air flow. With increasing distance from the outlet of the air jet the velocity RMS increases and continues to penetrate into the center of the potential core, signifying mixing.

To further study the characteristics of the air jet, velocity profiles were taken at locations of $x/D=1, 1.36, 2, 3, 4$ as illustrated in Fig. 6.10.

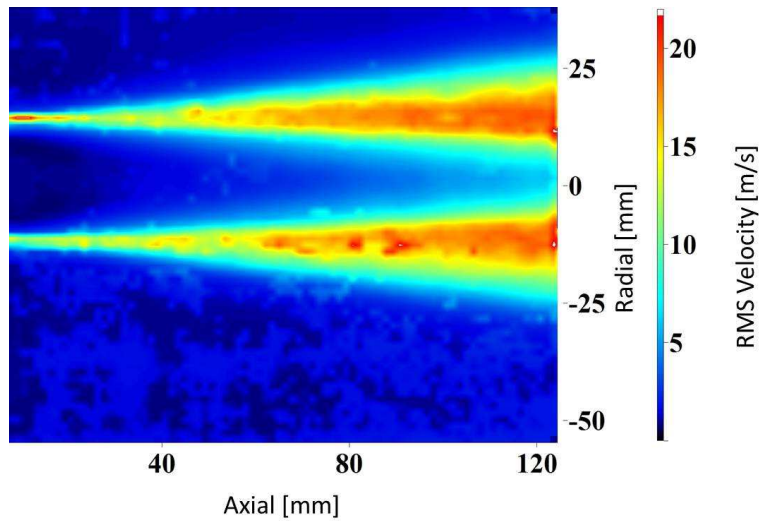


Figure 6.9: RMS of velocity fluctuations for $Ma_g=0.58$ cross-flow conditions

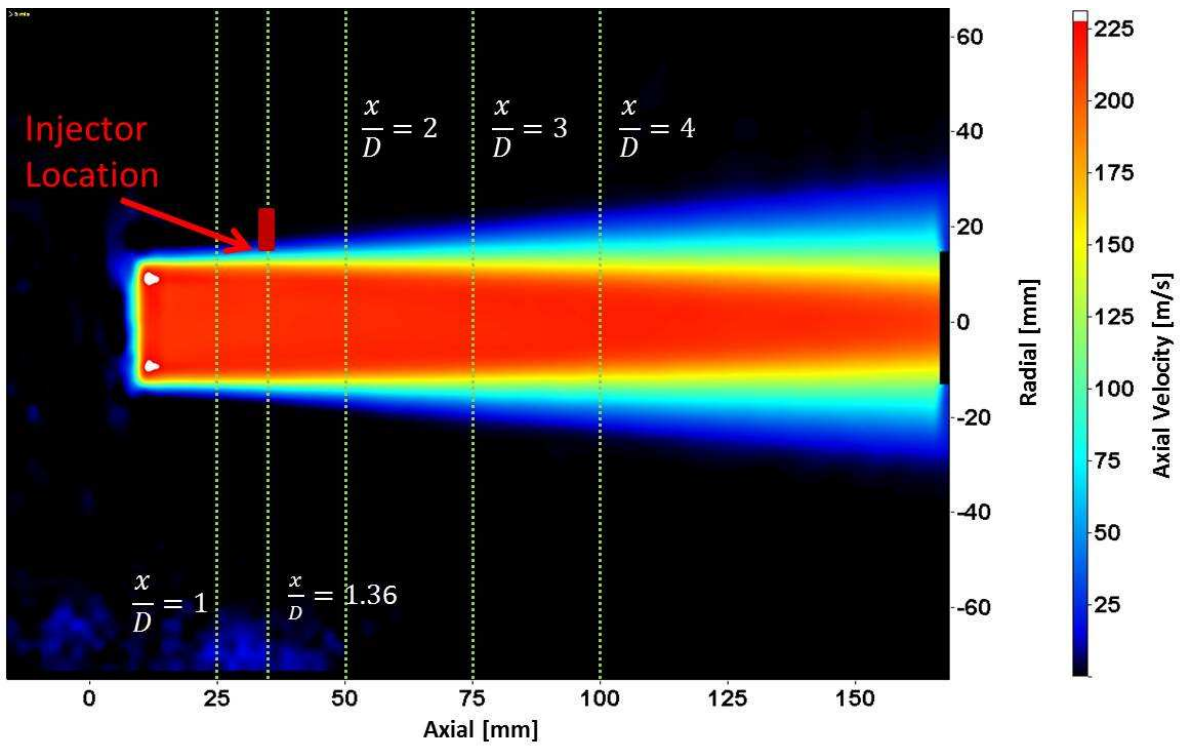


Figure 6.10: Measurement locations for the cross-flow

The location, $x/D = 1.36$, pertains location of the injector during cases where sprays are injected into the cross-flow. During the characterization of the air jet, the injector is not in position. Since the injector is located outside of the air jet, where the shear layer has not grown substantially, it is not expected to impact the measured velocity field. Figure 6.11 defines the axis which are used for the velocity profiles. Here V_x corresponds to the axial velocity which is oriented parallel to the jet center axis, with the positive direction pointing downstream and the negative direction pointing upstream. The radial axis corresponds to the vertical axis with the positive radial direction increasing upwards and decreasing downwards within the field of view. It is important to realize that in three dimensional space the air jet is considered to be symmetric about the center axis, and that in this instance the radial axis definition is only used to define the upper and lower sections of the jet in the planar image. That being said, the radial velocity V_r is still defined based on the symmetry of the air jet. Velocity components that move away from the center axis (upwards or downwards) in the field of view are considered as positive, while components that track towards the center axis are considered negative. This allows for improved assessment of the symmetry of the air jet when considering the radial velocity components.

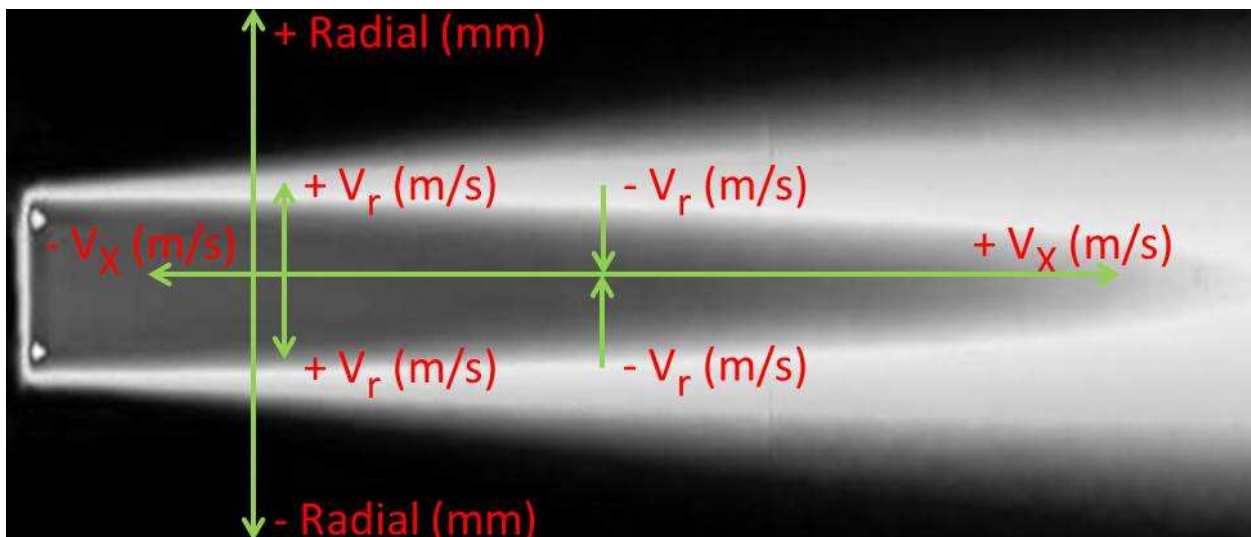


Figure 6.11: Axis definitions for the velocity profiles

Much like the fully developed region of the air jet, the shear layer in the initial region is shown to contain a self-similar nature and to grow linearly as noted by Abramovich [62].

The self-similar nature of the velocity profiles in the shear layer can be represented by

$$\frac{U}{U_o} = \frac{\Delta y_c}{\Delta y_b} \quad (6.5)$$

Where U represents the velocity at some distance y from the center axis of the jet, U_o is the velocity at the centreline ($y = 0$), $\Delta y_c = y - y_c$ where y_c is the distance from the centreline at which the velocity $U_c = 0.5U_o$, and $\Delta y_b = y_{0.9} - y_{0.1}$ where $y_{0.9}$ is the y location at which $U = 0.9U_o$, and $y_{0.1}$ is the y location where $U = 0.1U_o$. The value of Δy_b is considered as the thickness of the shear layer.

Figure 6.12 illustrates that the shear layer for both the $Ma_g = 0.35$ and the $Ma_g = 0.58$ jets satisfy the conditions of self-similarity. In this figure, self-similar velocity profiles are plotted for the shear layer located in the positive and negative radial direction, hence the inverse curves.

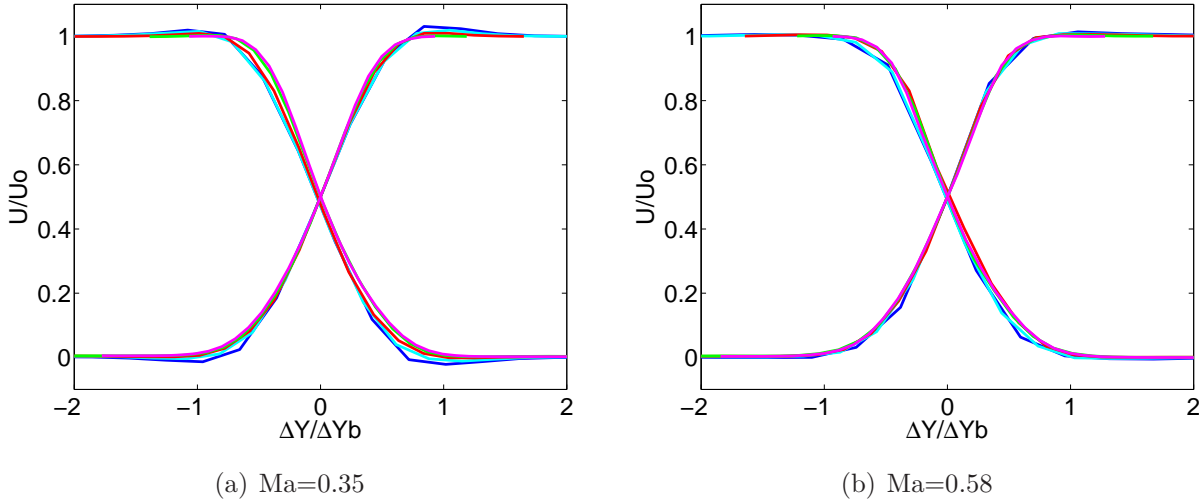


Figure 6.12: Self-similarity of the axial velocity of the air jet measured a) $Ma_g=0.35$ and b) $Ma_g=0.58$. The axial location is $x/D = 1$ (dotted blue line), 1.36 (solid cyan line), 2 (dotted brown line), 3 (solid green line), 4 (dotted purple line).

Plotting the dimensional axial velocity profiles for each x/D location onto the same graph as seen in Fig. 6.13, illustrates how the axial velocity transitions from a top hat profile into the parabolic profile which is characteristic of the fully developed or main region of the jet. Furthermore, for both the $Ma_g = 0.35$ and $Ma_g = 0.58$ air flows, the initial

profiles occurring at $x/D = 1$ show evidence of the vena contracta phenomenon. This phenomenon, which is dependent on the nozzle outlet geometry as illustrated by Quinn [69], is characterized by the narrowing and acceleration of the air jet downstream of the nozzle exit. Here the velocity peaks at the edge of the potential core and then settles to the core velocity near the centerline of the jet.

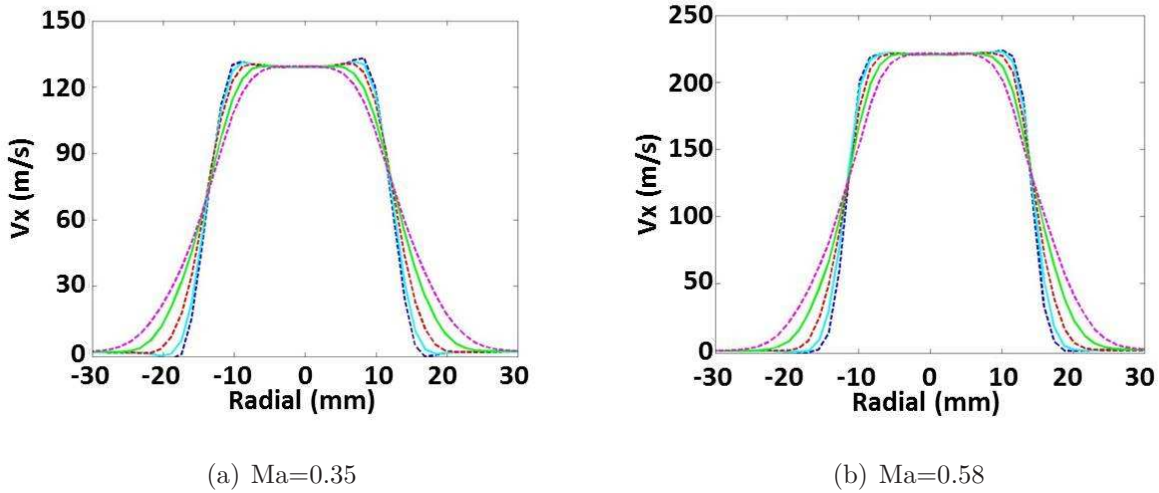


Figure 6.13: Velocity profiles for a) $Ma_g = 0.35$ and b) $Ma_g = 0.58$ plotted for different axial locations $x/D = 1$ (dotted blue line), 1.36 (solid cyan line), 2 (dotted brown line), 3 (solid green line), 4 (dotted purple line).

This vena contracta effect means that air streams maximum contraction occurs slightly downstream of the nozzle exit and is also associated with a maximum velocity. As can be seen, the effect is slight with the maximum velocity at $x/D = 1$ approximately 3% greater than the centreline core velocity.

Figures 6.14-6.16 allow for comparison between the axial and radial velocity, and the TKE profiles at locations upstream ($x/D=1$) and downstream ($x/D=4$) of the fuel injector for both the $Ma_g=0.35$ and 0.58 air flows. Figures depicting the profiles at the remaining locations of $x/D=1.36, 2, 3$ can be found in Appendix A.

Beginning with the axial velocity, it is apparent that the vena contracta effect is more pronounced in the $Ma_g=0.35$ flow. The resultant velocity, peaks at the edge of the potential

core and diminishes with increasing distance from the nozzle outlet, disappearing by $x/D=3$ for both air flows.

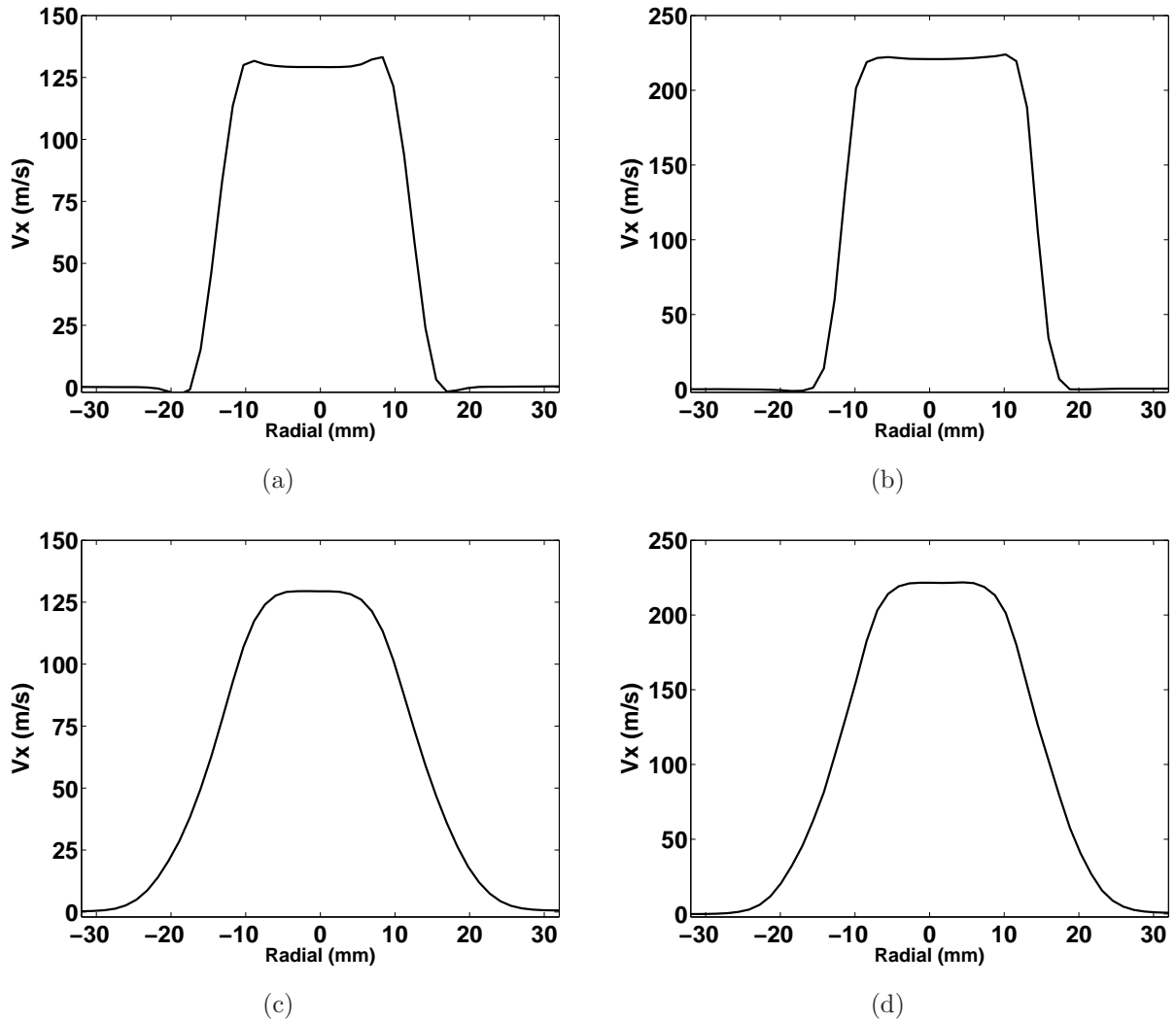


Figure 6.14: Time averaged axial velocity profiles for a) $Ma_g = 0.35$ and b) $Ma_g = 0.58$ air flow at $x/D = 1$; c) $Ma_g = 0.35$ and d) $Ma_g = 0.35$ air flow at $x/D = 4$

Comparing V_r for the $Ma_g=0.35$ air flow, it can be noted that at $x/D=1$ the velocity profile seems to be approximately symmetric with V_r in the shear layer having relatively the same magnitude just above 2 m/s although the peak in the positive radial direction is slightly higher than that in the negative radial direction. This trend is also noticed, and

is more prominent, in the $Ma_g=0.58$ and increases with increasing distance from the air nozzle outlet. Another important aspect about the $Ma_g=0.35$ flow case is that at $x/D=1$ the V_r component in the potential core region remains close to 0, but gives a positive value in the positive radial direction and negative value in the negative radial direction. This means that in this region V_r is not symmetric and the potential core region contains a slight upward V_r component. It is thought that this slight upward draft might be the reason that the V_r peak is greater in the positive radial direction. Looking at $x/D=4$, this upward draft seems to have disappeared, but the V_r which stems from the shear layer of the jet has begun to clearly penetrate towards the axis of the jet. A final aspect of the radial velocity components, which is consistent for both air flows, is the tendency for V_r outside of the air jet to have a negative value indicating that the ambient air is being entrained into the air stream signifying mixing in the shear layer, as noted by Pope [70].

In considering the radial velocity components of the $Ma_g=0.58$ air flow, it is immediately apparent that they are different than those from the $Ma_g=0.35$ air flow. Although the V_r values peak in the shear layer, it is also clearly visible that the component in the positive radial direction is significantly larger than that in the negative radial direction. Furthermore, the presence of the upwards draft within the potential core seems to be significantly higher, with the V_r magnitude approaching that of the peak values in the negative radial direction shear layer. This upwards draft is still present in at $x/D=4$ in the positive radial direction, but has disappeared in the negative radial direction.

In considering the turbulent kinetic energy (TKE) profiles shown in Fig. 6.16 it is seen that the TKE consistently peaks within the shear layer of the air stream. At $x/D=1$ the TKE is negligible within the potential core although it increases in the shear layer. The symmetry of the TKE profiles about the jet center axis is clear, although the peak in the positive radial direction consistently has a slightly higher value, which is mirrored by V_r in the same locations. Another anomaly is the double peak which appears in Fig. 6.16(d).

6.2 Sprays in Quiescent Ambient Air

Characterization of the fuel spray in quiescent ambient conditions allows for an understanding of the spray behaviour independent of the cross-flow. Results collected under quiescent conditions are also useful when interpreting the results of the spray interaction

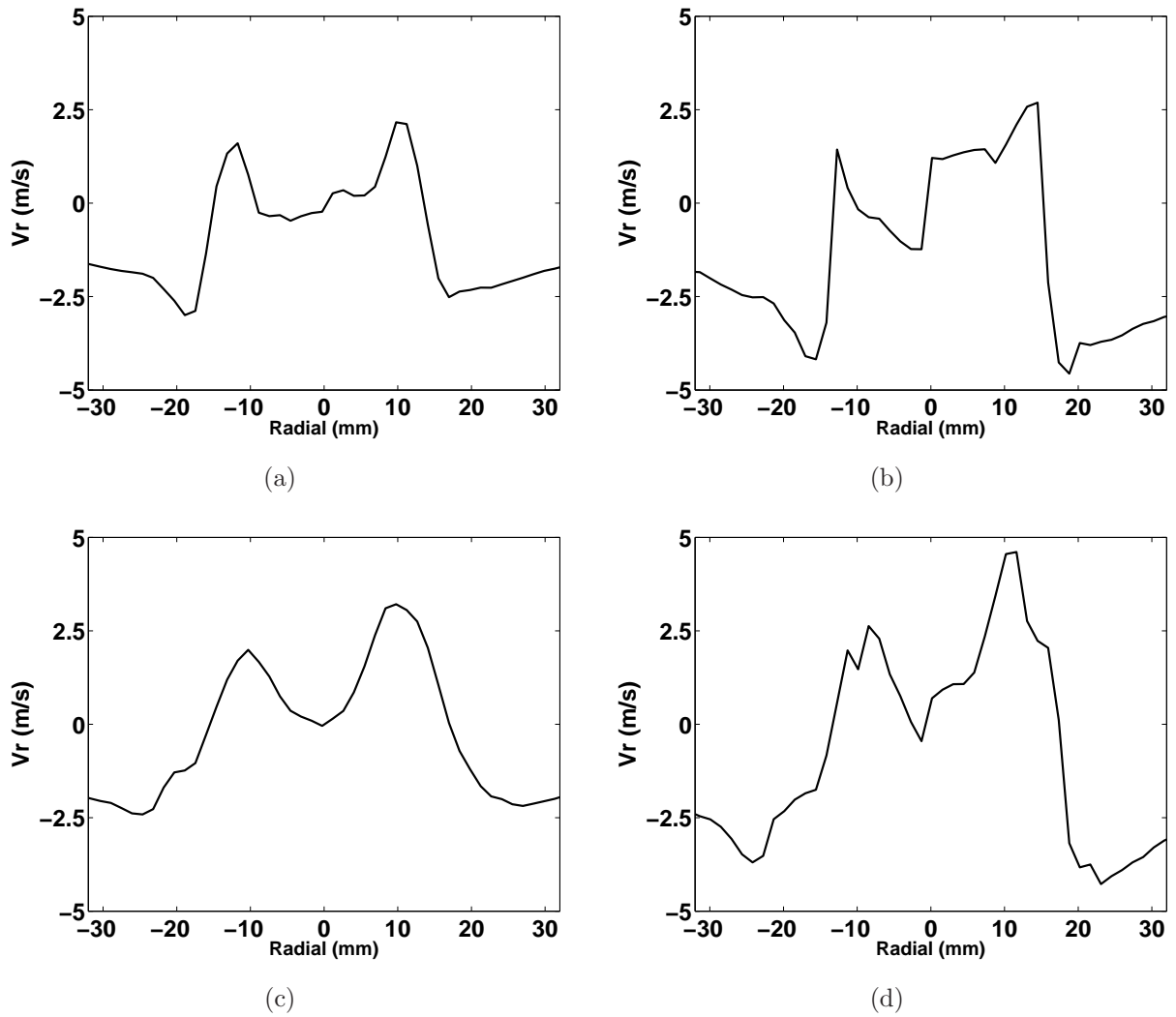


Figure 6.15: Time averaged radial velocity profiles for a) $Ma_g = 0.35$ and b) $Ma_g = 0.58$ air flow at $x/D = 1$; c) $Ma_g = 0.35$ and d) $Ma_g = 0.35$ air flow at $x/D = 4$

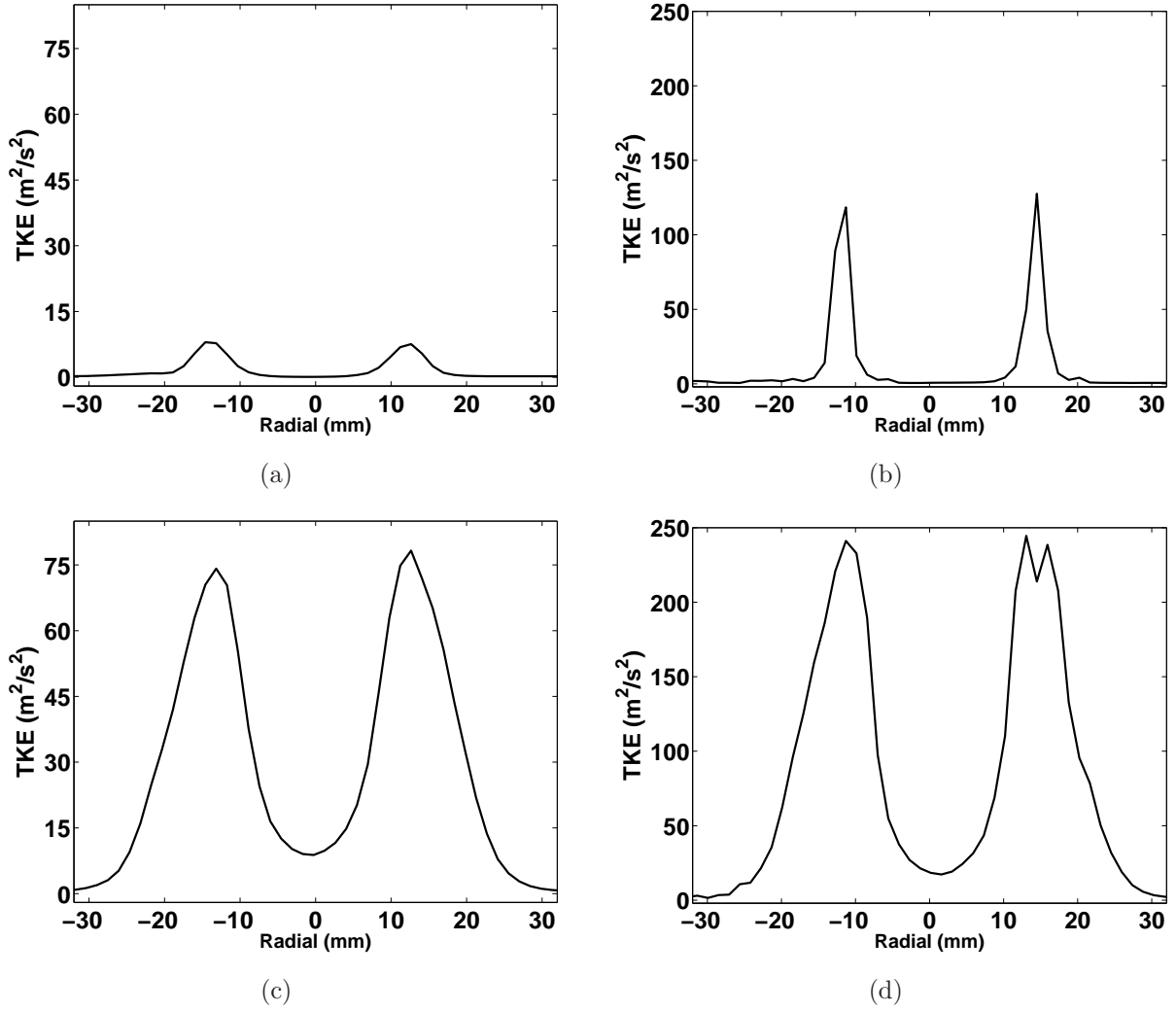


Figure 6.16: Turbulent kinetic energy profiles for a) $\text{Ma}_g = 0.35$ and b) $\text{Ma}_g = 0.58$ air flow at $x/D = 1$; c) $\text{Ma}_g = 0.35$ and d) $\text{Ma}_g = 0.35$ air flow at $x/D = 4$

with the cross-flow. In this section, volumetric images of fuel sprays injected into quiescent conditions, with P_{inj} of 10 MPa and 15 MPa, are used to characterize the performance of the injector. Measurements were collected at 0.1 ms intervals between 0 to 1.5 ms after SOF allowing for the development of spray width, spray angle, and penetration length to be assessed. Figures 6.17 and 6.18 illustrate the development, at increments of 0.5 ms, of the 10 and 15 MPa sprays respectively in order to illustrate the changes from the beginning of the injection event until the end. The complete set of results can be found in Appendix B.

Each image is scaled so that the image width correlates to 100 mm such that the spray development can be easily observed and compared. In analysing the sprays it is apparent that spray plumes remain distinct from about 40% of the penetration length to the end, while the initial 40% seems to show higher plume-to-plume interaction. Remembering that this volumetric technique averages the fuel concentration over the depth of the spray, this suspected interaction could also reflect the averaging of symmetric portions about the image plane, namely plumes 3 and 4.

It is also apparent that as the penetration length increases, the relative intensity of the spray plumes decrease, suggesting that the local fuel concentration continues to distribute into the surrounding air, increasing the width of each plume reducing the intensity of the scattered light from the local droplets.

Considering the orientation of the injector, the first and last plumes (2 and 5 as defined in Fig. 3.2) are oriented in the vertical plane, while the middle plumes are oriented out-of-plane as depicted in Fig. 3.2. The elliptical nature of the injector hole pattern leads to the obvious difference in the spray angle when considering the 3 plume and 4 plume orientation. As such, assuming that each plume has the same injection velocity, it can be expected that plume 2 and 5 will have a smaller vertical velocity and so that in the volumetric images will appear to penetrate less.

The following 3 subsections will provide further details of the spray behaviour and the effects of operating pressure, by considering the temporal evolution of spray penetration, spray angle and spray width.

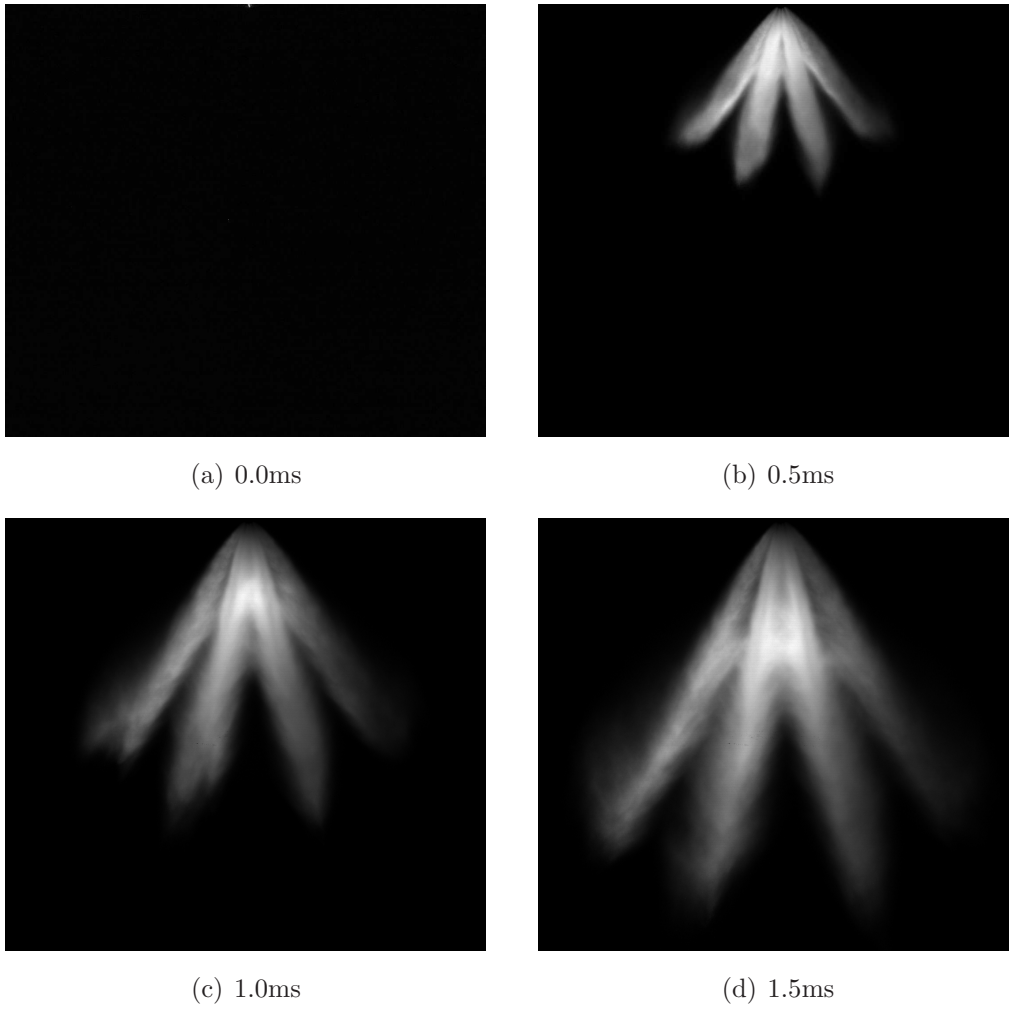


Figure 6.17: Temporal development of 10 MPa spray in quiescent ambient air, corresponding to 0.5 ms increments from 0.0 to 1.5 ms after SOF

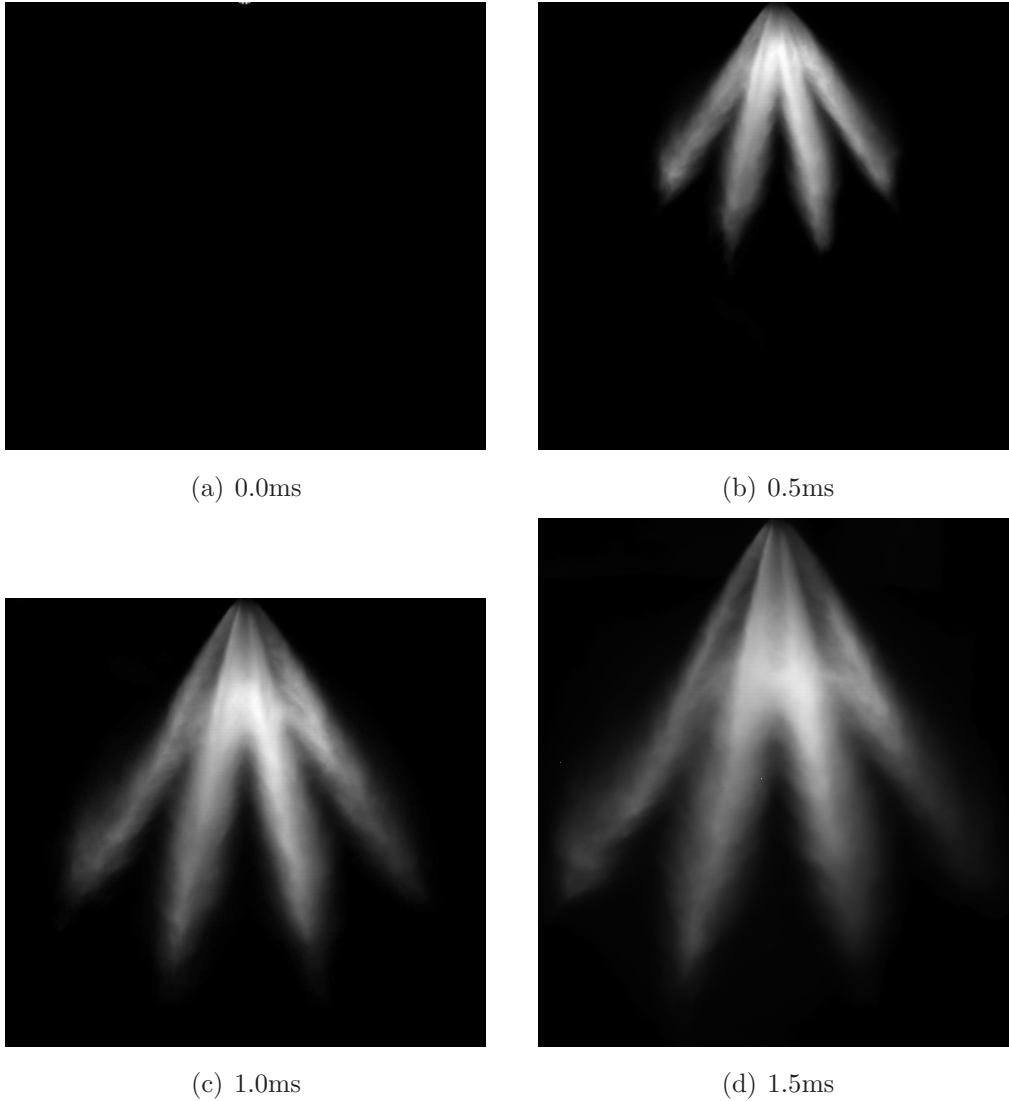


Figure 6.18: Temporal development of 15 MPa spray in quiescent ambient air, corresponding to 0.5 ms increments from 0.0 to 1.5 ms after SOF.

6.2.1 Spray Penetration

Spray penetration measures the maximum distance that the spray has penetrated into the ambient environment projected along the spray axis. Since the multi-plume configuration retains the geometry of the individual plumes, the spray penetration is defined by the penetration of the longest plume. As such, a level of variability can arise depending on which plume has the longest penetration, and between instantaneous images this value can be defined by different plumes. As such, the averaging of 15 instantaneous images reduces this image-to-image variation and gives a more consistent measure of the penetration. Figure 6.19 shows the spray penetration for both the 10 and 15 MPa sprays varying with time after SOF. The black curves represent the 10 MPa injection while the blue data curves

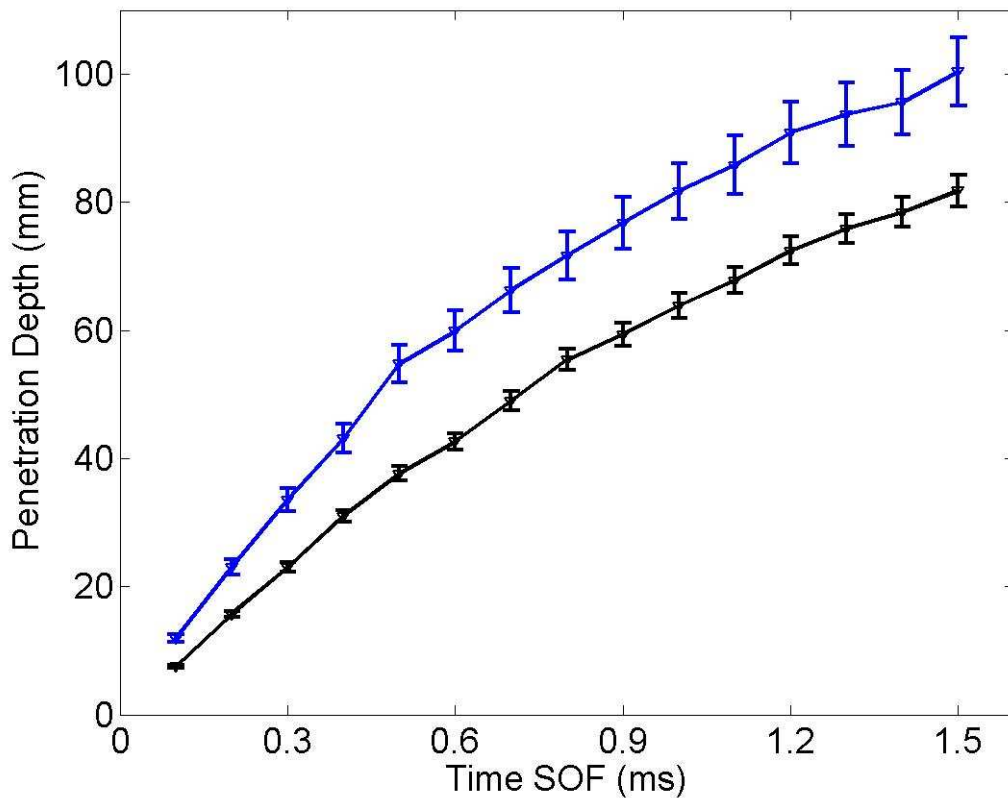


Figure 6.19: Development of penetration depth over time for 10 MPa injection (black) and 15 MPa injection (blue) with error bars expressing the uncertainty from Table 5.6.

represent the 15 MPa. Although the 15 MPa spray consistently has a larger penetration, both sprays experience a decline in the penetration growth rate with increasing time after SOF due to further breakup of the droplets and entrainment of the surrounding air. As noted by Lee et al. [71] who investigated the effect of fuel properties on the spray characteristics of a hollow-cone injector, initially the penetration varies linearly with time after SOF until the breakup point. After this breakup point which is marked by the point where deceleration occurs, the surrounding air is rapidly entrained into the spray. Lee et al. [71] also noted that the penetration curve varied as a function of $t^{0.5}$ after the breakup point which is found in this instance to occur at $t = 0.5ms$ after SOF for both injection pressures. The deceleration of the droplet with increasing distance from the injector tip is due to the drag forces between the droplet and the ambient air as well as the tendency for droplet diameters to decrease due to the secondary breakup and atomization. As the droplets break up, their mass and consequently their inertia reduces.

6.2.2 Spray Angle

Measurement of the spray angle is performed using the procedure outlined in Section 4.2.2. Figure 6.20 indicates that the spray angle decreases as time after SOF increases, and that the rate at which the spray angle decreases also decreases as time after SOF increases. This trend is present regardless of the injection pressure used in this study. Furthermore, it is important to note that the spray angles are relatively close between the 10 and 15 MPa injections, and that in some instances considering the uncertainty, the values might be the same.

The 15 MPa injections typically have a slightly lower spray angle, with the uncertainty range also having a slightly lower value than that of the 10 MPa injection. This is counter to the findings of Varde et al. [16] who noted that spray cone angle increases with increasing pressure for small L/d ratios (they studied 2.2 which is larger than the value used in this study). Since plumes 2 and 5 control the measured spray angle, it would be expected that increased pressure would increase the cone angle of plume 2 and 5 independently which would lead to a small increase in spray angle of the full multi-plume spray. Instead, it appears that the spray angle decreases slightly with increasing injection pressure.

The smaller spray angle for the 15 MPa spray can also be explained using the ideas of the air jet. As was noted in Section 6.1.1 the potential core length increased with increasing

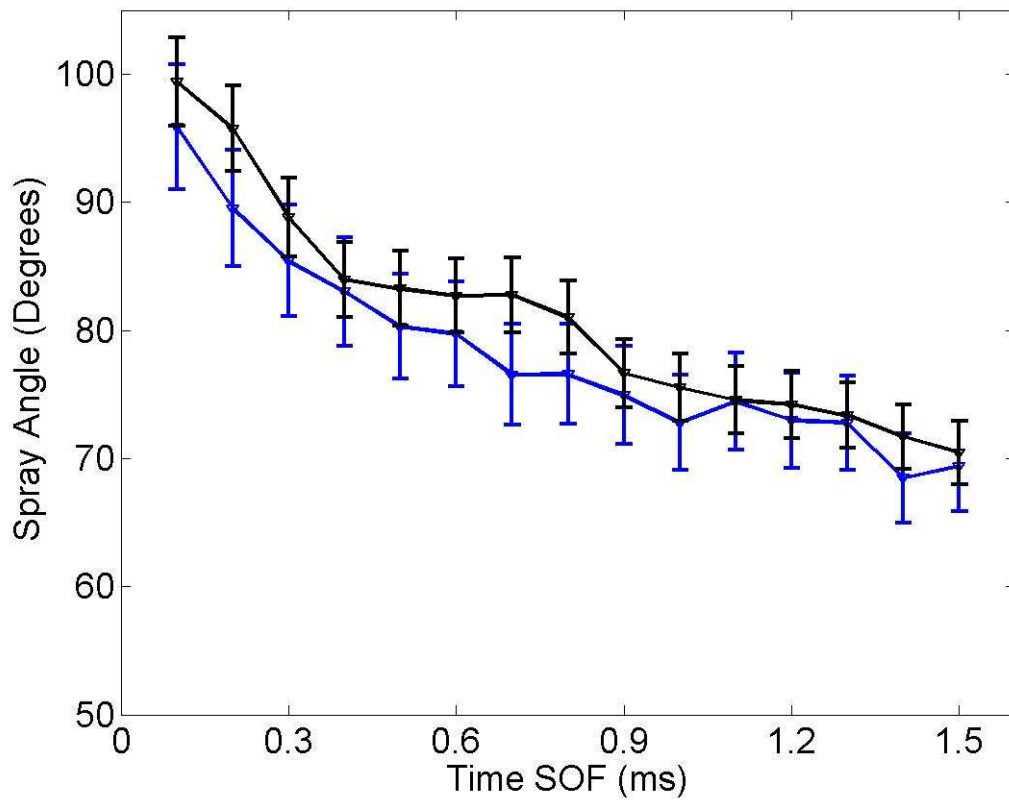


Figure 6.20: Development of spray angle over time for 10 MPa injection (black) and 15 MPa injection (blue) with error bars expressing the uncertainty from Table 5.6

air jet velocity U_o . Since the shear layer develops over the length of the potential core, a longer potential core implies slower shear layer growth. The shear layer is also the location where the stagnant ambient air is entrained by the air jet. Similarly, with the higher liquid injection pressure, the spray penetration increases and at the same time the shear region of the spray plume where ambient air is entrained into the spray, takes longer to develop. Hence, this phenomenon can be used to describe the lower spray angle of the 15 MPa injection, as parallels between air jets and liquid jets have been made previously in literature [62].

Recalling the approach used for measuring the spray angle, it is seen that the location of the points used for the angle calculation is a function of the penetration of the spray at any given time rather than constant as proposed by SAE J2715 [45]. As such, increasing time after SOF means that the points, located at 5% and 25% of the penetration depth, will move further from the injector tip. As illustrated in Fig. 6.19 as the time after SOF increases the rate of growth of the penetration depth decreases, this would mean that the locations of the points used to measure the spray angle will also reach a final position, which seems to occur around 1.5 ms. This also reflects the non-linear nature of the spray edge, which is due to the drag and entrainment of the spray plumes with the surrounding quiescent air.

6.2.3 Spray Width

The spray width measures the total width of the spray, perpendicular to the spray axis. This gives an indication of the widening of the spray over time. From Fig. 6.21 the width of the spray is seen to increase with increasing time after SOF at a decreasing rate.

This indicates the radial velocity of the fuel droplets reduces as it increases its distance from the injector tip. This trend is noticed for both the 10 MPa and the 15 MPa fuel spray, with the 15 MPa (blue line) having a general higher spray width, with the difference increasing with increasing time after SOF. Fig. 6.22 illustrates the measurement locations of the spray angle and the spray width. Since the spray angle is taken at 5-25% of the spray penetration it does not encounter the regions of droplet entrainment which occur due to vortex formation in the ambient air as the spray plume penetrates. Conversely, the measurement of the spray width considers these entrainment regions. Thus the increasing difference in spray width of the higher pressure spray results from the the higher initial

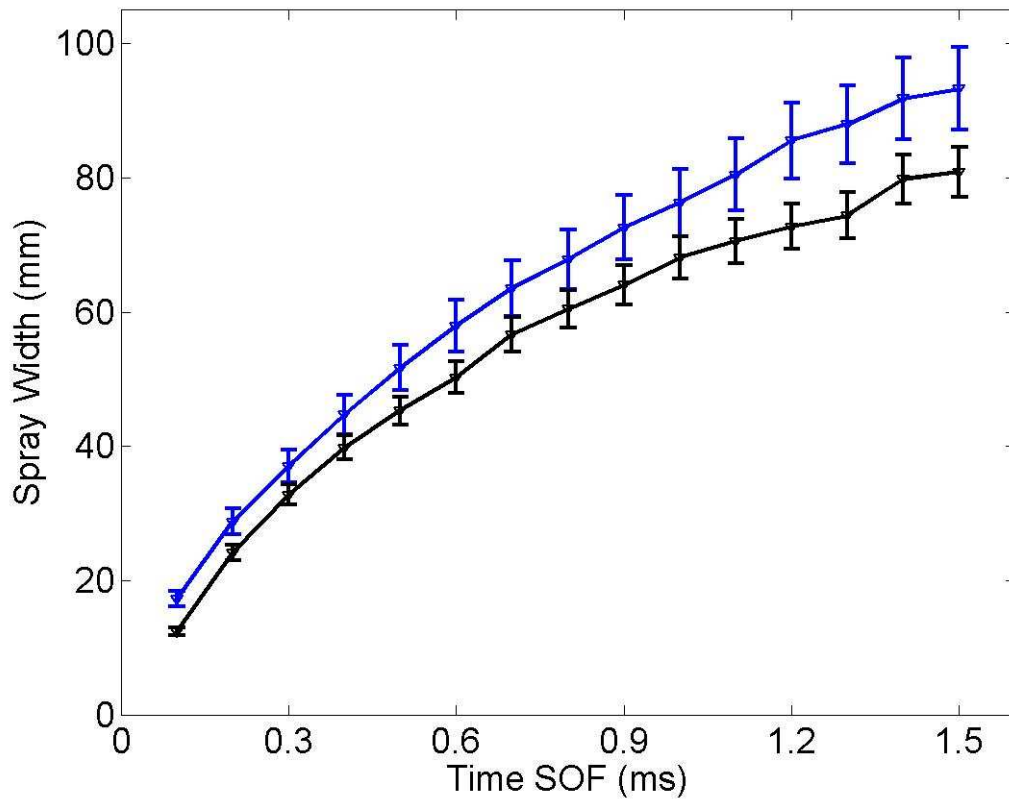


Figure 6.21: Development of spray width over time for 10 MPa injection (black) and 15 MPa injection (blue) with error bars expressing the uncertainty from Table 5.6

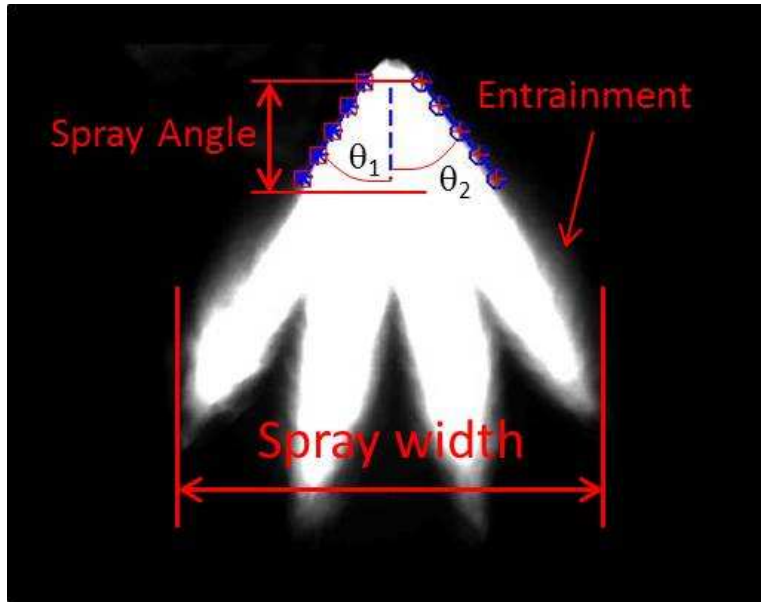


Figure 6.22: Comparison between the measurement locations of the spray width and the spray angle with respect to the quiescent spray into ambient air.

momentum ,which increases the penetration depth, and the increased entrainment of the smaller diameter droplets into the ambient air. Although the relatively large uncertainty range for both curves also leads to the conclusions that the curves be almost exactly the same.

6.3 Sprays in Cross-Flow Conditions

The next section covers the characterization of the fuel spray when it is injected into the cross-flow. The results are separated into those drawn from the planar images which describes the changes to the geometry of the spray and then the PIV results which analyze the velocity distribution within the spray. Through these results an understanding of the mixing of the fuel spray will be gained.

Table 6.2 gives the calculated momentum ratios (Eqn. 2.3) and Weber numbers (Eqn. 2.1 and 2.11) for the given spray conditions, ordered by decreasing momentum ratio. The Ma_g number is used to indicate the free stream cross-flow conditions as characterized in Section 6.1 and We_l is used to indicate the liquid Weber number of the fuel sprays under

P_{inj} (MPa)	Ma_g	\mathbf{q}	We_g	We_1	Re_1
15	0.35	991	213	2.1×10^5	6.2×10^6
10	0.35	665	213	1.4×10^5	5.1×10^6
15	0.58	371	617	2.3×10^5	7.2×10^6
10	0.58	249	617	1.5×10^5	5.9×10^6

Table 6.2: Non-dimensional parameters for sprays in cross-flows

quiescent conditions. We_1 for the present study is large, hence the nozzle is operating in the atomization regime. Ashgriz et al. [11] illustrate the tendency for SMD to decrease with increasing injection pressure although the rate of change also decreases with increasing pressure, leading to the assumption that under ambient conditions, the 15 MPa injections will have a smaller SMD than the 10 MPa injections.

6.3.1 Planar Images

The planar images of the fuel spray interacting with the cross-flow were captured and processed using the techniques outlined in Chapter 4. The information that is gathered can be used to analyse the geometric aspects of the spray.

Figures 6.23 and 6.24, highlight the temporal evolution of the 15 and 10 MPa injection pressures into the $\text{Ma}_g = 0.35$ cross-flow from 0.1 to 1 ms after SOF in 0.3 ms increments, while Figs. 6.25 and 6.26 show the temporal evolution of the 15 and 10 MPa, into the $\text{Ma}_g = 0.58$ cross-flow over the same span. The full data sets can be found in Appendix C with the spray axis as discussed in Section 6.3.1.

For each scenario, it can be observed that the initial sprays (0-0.3 ms in $\text{Ma}_g = 0.35$ cross-flow and 0-0.2 ms in $\text{Ma}_g = 0.58$ cross-flow) retain the multi-hole injection characteristics similar to the injections into quiescent conditions. However the cores of each plume (the darkest portion of the spray) merge into a single core surrounded by a cloud of droplets.

For each spray cross-flow condition, this single plume remains intact except for the 15 MPa injection into the $\text{Ma}_g = 0.35$ scenario in which the momentum of the spray droplets



(a) 0.1ms



(b) 0.4ms



(c) 0.7ms



(d) 1.0ms

Figure 6.23: Development of 15 MPa fuel spray into $Ma_g = 0.35$ cross-flow conditions in 0.3 ms increments from 0.1 ms after SOF to 1.0 ms after SOF, corresponding to $q = 991$, $We_l = 2.1 \times 10^5$, and $We_g = 213$

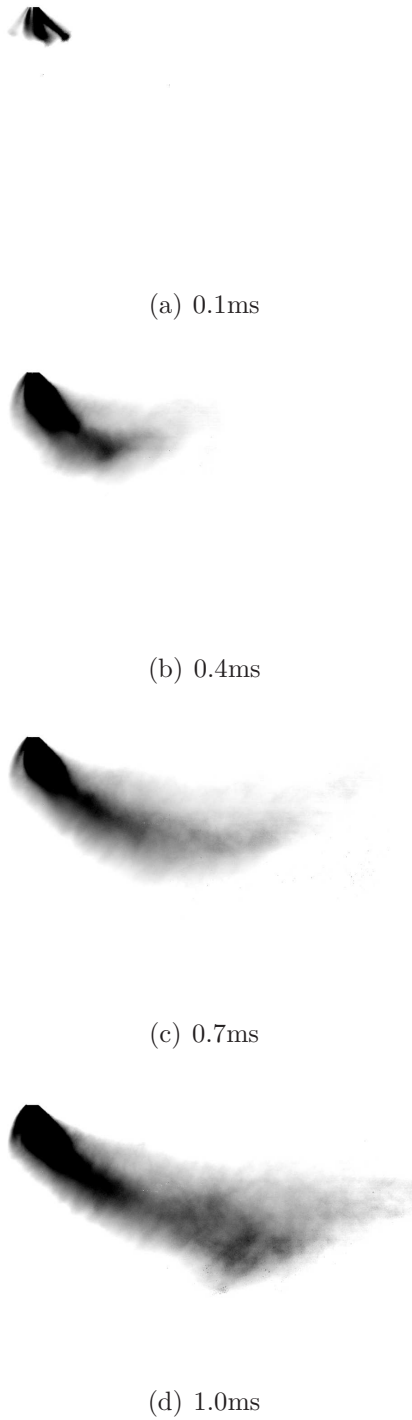


Figure 6.24: Development of 10 MPa fuel spray into $Ma_g = 0.35$ cross-flow conditions in 0.3 ms increments from 0.1 ms after SOF to 1.0 ms after SOF, corresponding to $q = 665$, $We_l = 1.4 \times 10^5$, and $We_g = 213$

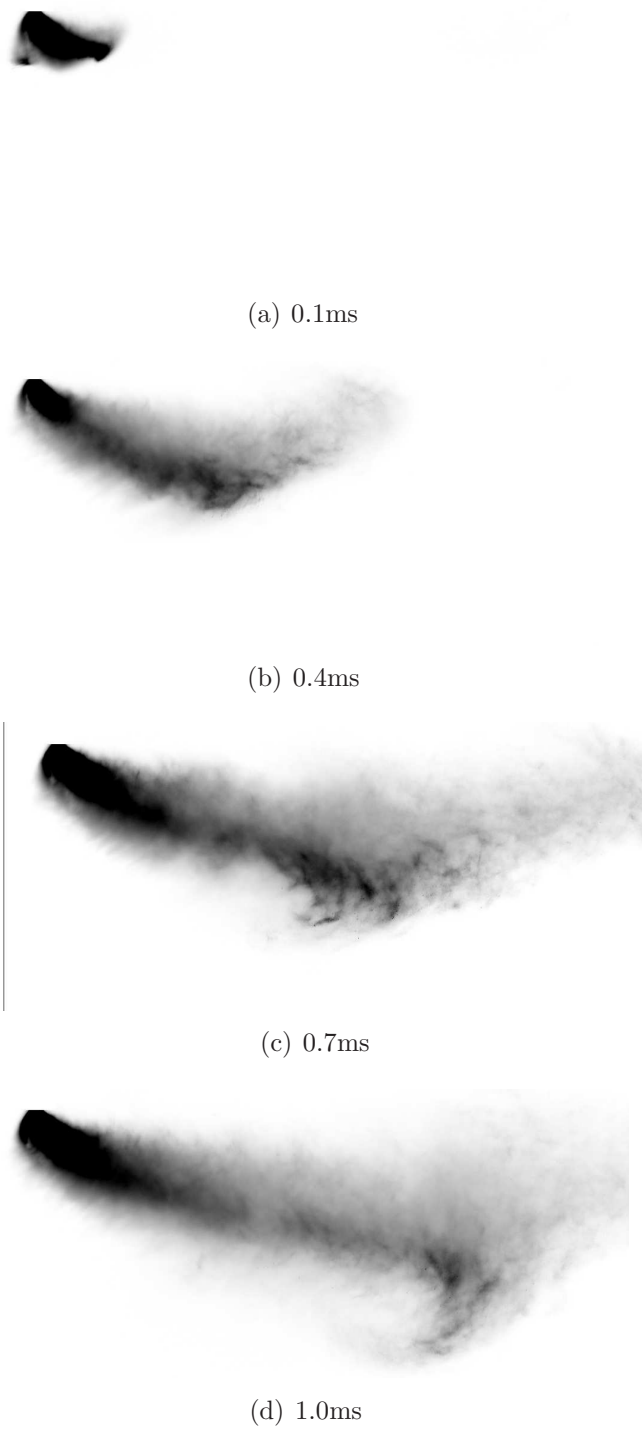


Figure 6.25: Development of 15 MPa fuel spray into $Ma_g = 0.58$ cross-flow conditions in 0.3 ms increments from 0.1 ms after SOF to 1.0 ms after SOF, corresponding to $q = 371$, $We_l = 2.3 \times 10^5$, and $We_g = 617$

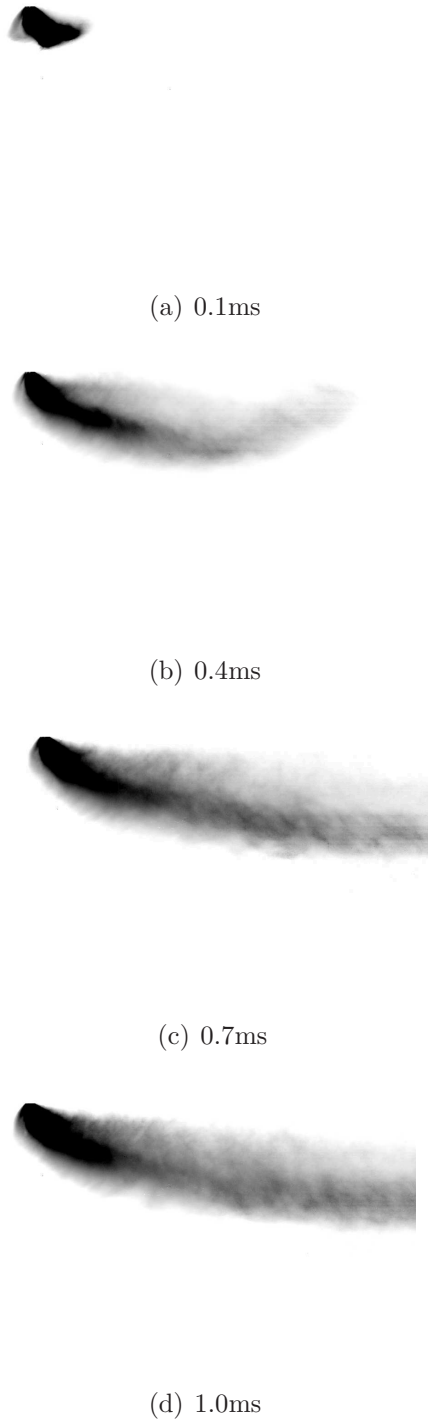


Figure 6.26: Development of 10 MPa fuel spray into $Ma_g = 0.58$ cross-flow conditions in 0.3 ms increments from 0.1 ms after SOF to 1.0 ms after SOF, corresponding to $q = 249$, $We_l = 1.5 \times 10^5$, and $We_g = 617$

allow for a concentrated cloud to penetrate through the cross-flow. In this instance the level of mixing is limited.

The following sections evaluate the mixing of the injection and cross-flow by examining the penetration of the spray into the cross-flow, the propagation of the spray upstream and downstream of the injector parallel to the cross-flow axis, the trajectory spray plume core, and the velocity of the droplets within the plume.

Spray Penetration

The penetration of the spray into the cross-flow indicates the level to which the spray is influenced by the cross-flow. The further the spray is able to penetrate transversely into the cross-flow, the greater the surface area on which the cross-flow acts. Figure 6.27 quantifies the penetration of each spray and cross-flow condition with the 15 MPa injections in blue, and the 10 MPa injections appearing in black, while the $Ma_g = 0.35$ is denoted with an asterisk and the $Ma_g = 0.58$ is denoted with a triangle.

From Fig. 6.27 it is observed that the 15 MPa injection penetration curves appear to be quite similar over time, although the $Ma_g = 0.58$ cross-flow reduces the penetration after 0.1 ms after SOF when compared with the penetration curve for $Ma_g = 0.35$ cross-flow conditions. This suggests that momentum of the fuel spray in the direction of the spray axis (transverse to the cross-flow) is unchanged by the cross-flow, and hence injections which initially have more momentum will penetrate further into the spray. For the 10 MPa injection into the $Ma_g = 0.35$ cross-flow the same behaviour exhibited with the penetration increasing at a decreasing rate as the time after SOF increases. The average magnitude of this penetration is smaller than that of the 15 MPa as would be expected due to the reduced momentum of the fuel spray. These behaviours substantiate the assumption behind the spray axis derivation discussed in Section 2.2 which assumes that initially the liquid is injected normal to the cross-flow axial direction.

Interestingly, the injection of the 10 MPa spray into the $Ma_g = 0.58$ cross-flow shows substantially different behaviour. The penetration curve begins in the same manner with the magnitude slightly less than that of the 10 MPa injection into the $Ma_g = 0.35$ cross-flow from 0.2 to 0.9 ms after SOF. After 0.9 ms after SOF the penetration ceases to increase and remains constant. This is indicative of the cross-flow fully entraining the fuel droplets, dissipating the transverse momentum. Since the ability of droplets to track the flow is

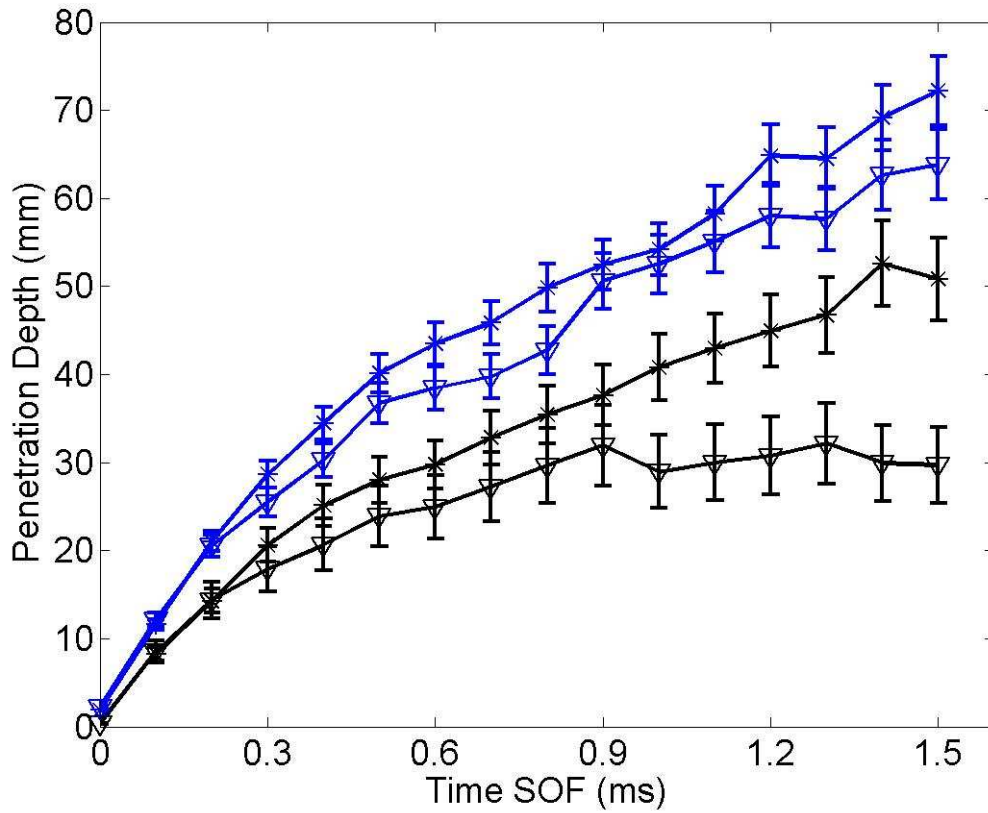


Figure 6.27: Development of spray penetration into the cross-flow over time for 10 MPa (black) and 15 MPa (blue) into $Ma_g = 0.35$ (*) and $Ma_g = 0.58$ (∇) with error bars expressing the uncertainty from Table 5.7

based on the droplet size as discussed in Section 3.3.3, it can be hypothesized that the mean droplet size has decreased enough to produce a Stokes number which is smaller than 1.

As previously mentioned, the growth rate of penetration decreases as time after SOF increases. This can be attributed to the tendency for the penetrating fuel to lose momentum due to drag forces present in the cross-flow and due to the loss of mass due to stripping and further break-up. As droplets are produced, they are quickly removed from the plume and carried with the air flow downstream of the injector. The penetration depth which marks the furthest droplets from the injector tip measured along the injector axis shows that only the $q = 249$ or $Ma_g = 0.58$ and 10 MPa injection remains entirely within the cross-flow. The other sprays, while the majority of their mass might be within the jet, are still able to fully penetrate through the cross-flow which has a width of 40-50 mm depending on the location where penetration occurs.

Spray Tail Length

The second geometric parameter which is measured for the spray cross-flow interaction is the total tail length. The total tail length is subdivided into 2 parts as outlined in Section 4.3.2, which are the upwind and downwind tail lengths. Evaluation of the downwind tail length indicates the ability of droplets to be carried by the cross-flow, while the upwind tail length is a measure of plume 2 and its ability to penetrate upstream of the injector.

The first observable feature of Fig. 6.28 is the linear increase in tail length before the tail extends outside of the field of view. Note that the blue curves represent the 15 MPa injection and the black curves represent the 10 MPa injection, while the asterisks represents the $Ma_g = 0.35$ cross-flow, and the triangle represents the $Ma_g = 0.58$ cross-flow.

It becomes apparent that the total tail length is primarily a function of Ma_g , with increasing Ma_g leading to an increased tail length. This is due to the fact that the cross-flow immediately strips away the smallest and most buoyant particles from the injection and carries them downstream. These particles represent the furthest liquid downstream of the injector at any point and control the total tail length which is mainly a function of the downwind tail length as can be seen when comparing Figs. 6.28 and 6.31.

Figure 6.29 demonstrates the tendency for small droplets to be quickly entrained by the air flow. Measurements taken 17 mm downstream of the injector, and at the bottom

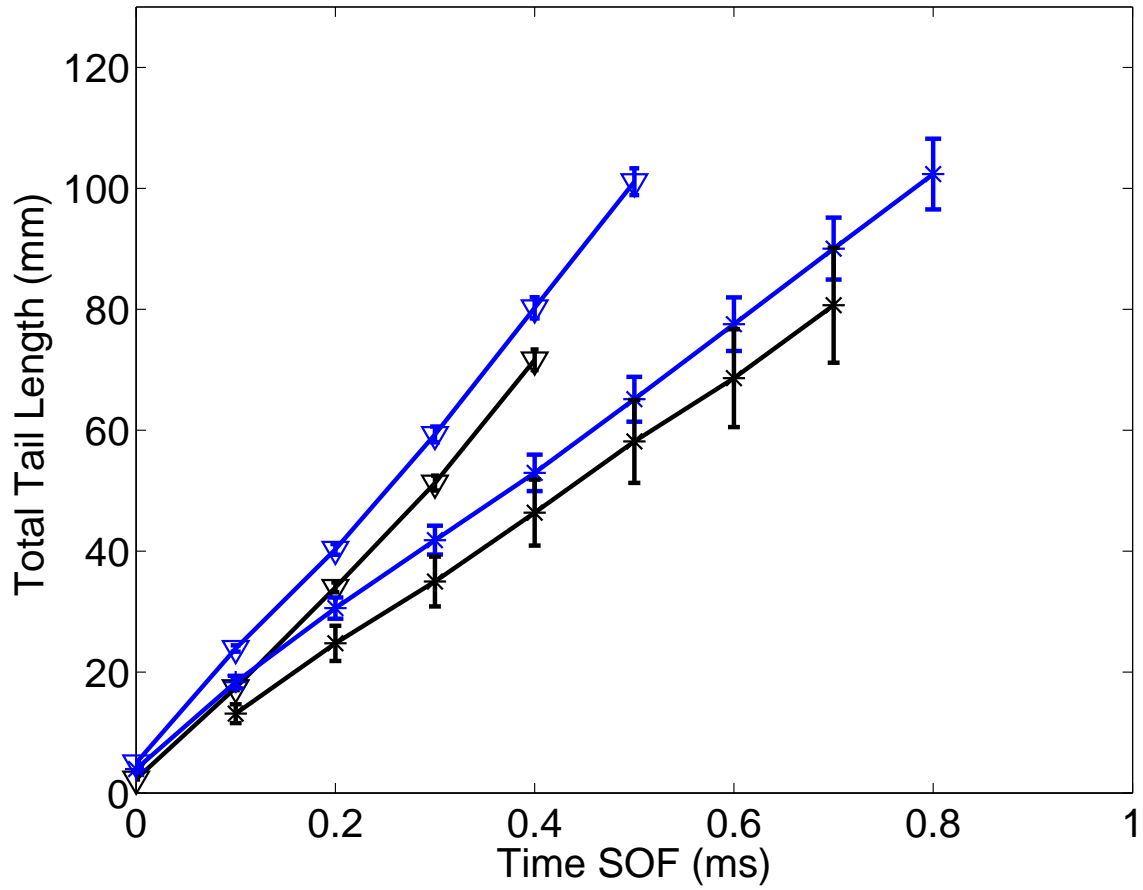


Figure 6.28: Development of the total tail length over time for 10 MPa (black) and 15 MPa (blue) into $Ma_g = 0.35$ (*) and $Ma_g = 0.58$ (∇) with error bars expressing the uncertainty from Table 5.7

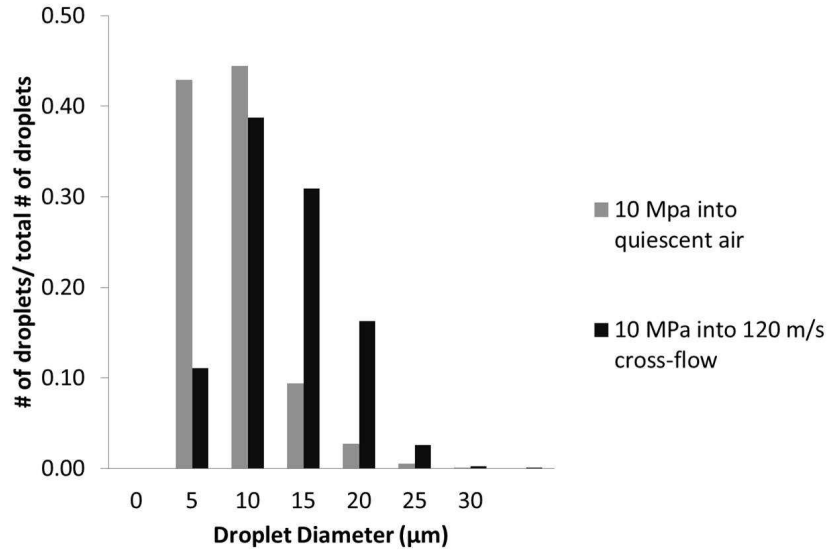


Figure 6.29: Droplet size distribution for 10 MPa injections into quiescent and 120 m/s cross-flow conditions. Measurements recorded at an axial distance of 51 mm and a radial distance of -13 mm, per Fig. 6.10

edge of the theoretical potential core for 10 MPa injections into the quiescent and cross-flow conditions, illustrate that in cross-flowing conditions the local droplet size distribution has larger values than in quiescent conditions. This is because the cross-flow removes the smaller droplets from the measurement domain leaving the larger droplets to be quantified. Calculating the SMD at this location for both conditions, it is found that the 10 MPa injection into quiescent conditions results in a value of $10.76 \mu\text{m}$ and $14.66 \mu\text{m}$ for the 10 MPa injection into the 120 m/s cross-flow, at this location.

The injection pressure, and consequently We_1 , plays a moderate role, with higher We_1 leading to a slightly increased average total and downwind tail length. This is thought to be a function of the improved atomization which accompanies higher injection pressures. The smaller droplets produced by the higher injection pressure would decrease the calculated local Stokes number (Section 3.3.3), increasing the likelihood that they are entrained by the cross-flow.

Figure 6.30 illustrates that at the same location within the spray, the higher injection pressure droplets display smaller diameters than the lower injection pressure spray at the same location, and at the same cross-flow conditions. The calculated SMD gives values of

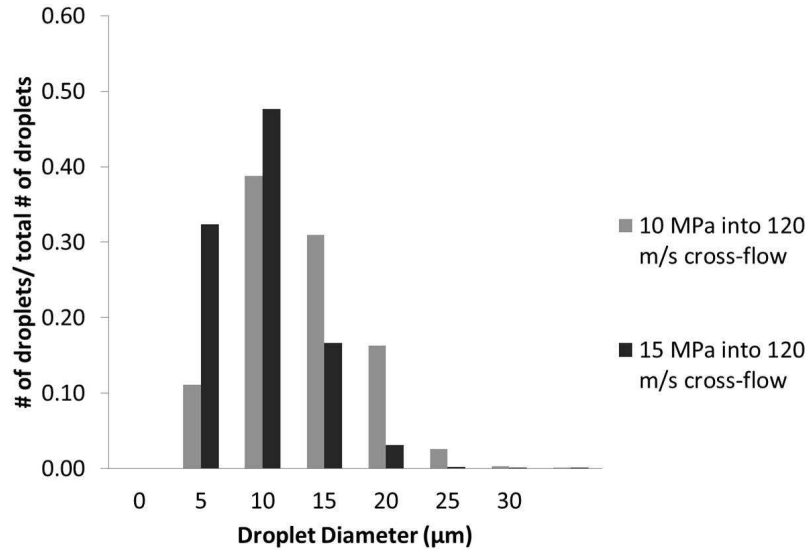


Figure 6.30: Droplet size distribution for 10 and 15 MPa injections into 120 m/s cross-flow conditions. Measurements recorded at an axial distance of 51 mm and a radial distance of -13 mm, per Fig. 6.10

10.66 μm for the 15 MPa injection and 14.66 μm as previously mentioned for the 10 MPa injections.

Calculations of the tail tip velocity can be performed for each set of conditions using the linear slopes from Fig. 6.28. The linear appearance means that the rate at which the tail length increases remains relatively constant. For the $\text{Ma}_g = 0.58$ cross-flow conditions, the 15 MPa injection tail velocity is 194 m/s while for the 10 MPa injection it is 184 m/s . For the $\text{Ma}_g = 0.35$ cross-flow the tail velocities are 121 and 116 m/s for the 15 and 10 MPa injections respectively. The slightly higher velocity of the 15 MPa injections is consistent with the conclusion of the droplets having a smaller Stokes number signifying improved entrainment and reduced drag.

Figure 6.32 depicts the change in the upstream penetration of plume 2, which is highlighted in Fig. 3.2. The geometric orientation of the injector results in plume 2 being injected in the vertical (image) plane along the center plane of the cross-flow. As such, the upstream penetration is only measuring fuel issuing from this port. It is observed that the fuel spray is able to penetrate upstream into the air flow passed the injector axis. Looking at Fig. 6.32, it is evident that for each spray there exists a peak in the upwind tail length.

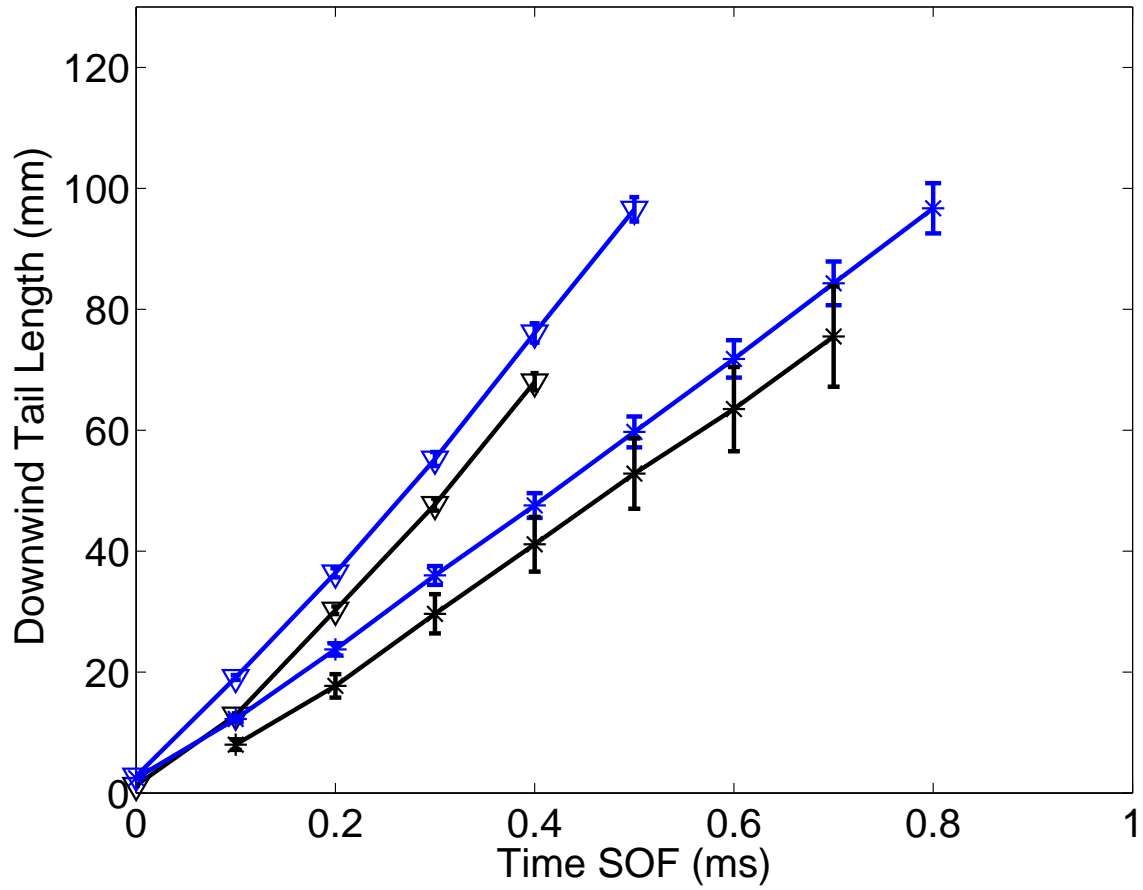


Figure 6.31: Development of the downwind tail length over time for 10 MPa (black) and 15 MPa (blue) into $Ma_g = 0.35$ (*) and $Ma_g = 0.58$ (∇) with error bars expressing the uncertainty from Table 5.7

After this peak, the upwind tail length decreases and remains relatively constant. The magnitude and time after SOF at which this peak occurs, appear to be independent of the P_{inj} and primarily influenced by the Ma_g .

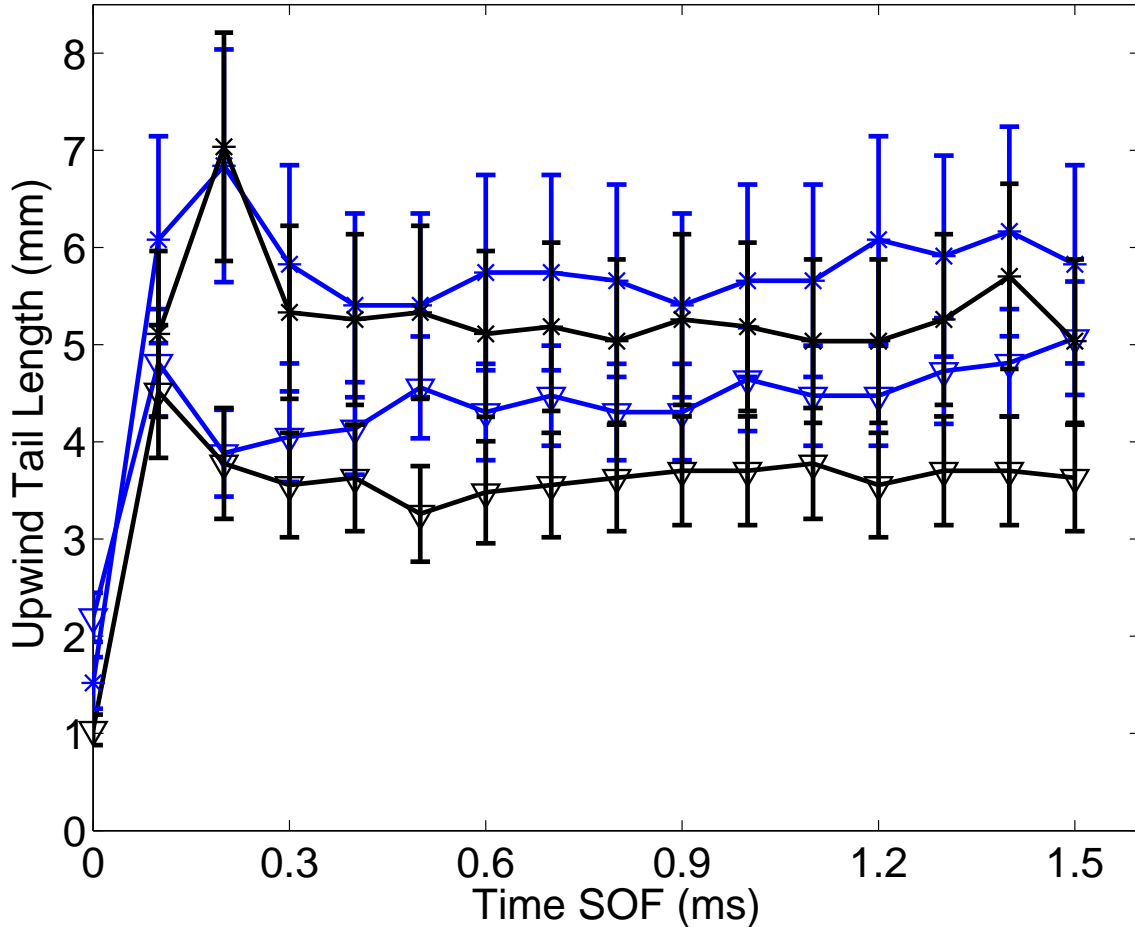


Figure 6.32: Development of the upwind tail length over time for 10 MPa (black) and 15 MPa (blue) into $Ma_g = 0.35$ (*) and $Ma_g = 0.58$ (∇) with error bars expressing the uncertainty from Table 5.7

The upwind tail length magnitude, after the peak, remains a function of Ma_g but also is dependent on P_{inj} , with higher P_{inj} resulting in a higher upwind tail length. Overall, the magnitude of the upwind tail length remains relatively constant after the occurrence of the peak with a slight increase observed for the 15 MPa injection into the $Ma_g = 0.35$ cross-flow, but a stronger increase observed in the 15 MPa injection into the $Ma_g = 0.58$

cross-flow with the magnitude approaching that of the peak for this scenario.

Lee et al. [72] and Sallam et al. [22] studied turbulent and non-turbulent round jets in cross-flows respectively, for conditions of We_g upto 282, q upto 200, and We_l upto 32,200. Both authors noted that the time required for column break-up to occur is a constant given by

$$\frac{t_b}{t^*} = C_{yb} \quad (6.6)$$

where t^* is the characteristic aerodynamic time given by $(\rho_l/\rho_g)^{1/2}d_j/u_o$, and C_{yb} is the empirical constant. The authors found that for a given injector size, the breakup time is mostly impacted by changes in the free stream velocity, with an increase in velocity decreasing the time until break-up. This is consistent with the result of Fig. 6.32 showing the smaller upstream penetration length, and also, the earlier penetration peak for the higher velocity, $Ma_g=0.58$ flow.

The report produced by Hamady et al. [73] looks at the injections from various injectors for SIDI applications. In examining the SMD for each injector style with increasing time after SOI, it became apparent that initially the SMD was increased due to nozzle opening effects which lowered the momentum and reduced the atomization quality. However, the SMD would decrease quickly and settle at a mean value once the solenoid valve was fully open. Thus, it is believed that the initial peak in the upstream tail length is due to the increased SMD during nozzle opening. Since the cross-flow acts perpendicular to the spray axis, it will carry droplets downstream. In the case of plume 2, larger droplets would have an increased resistance to being carried downstream and although their momentum may be less than the smaller well atomized droplets occurring when the needle is fully open, they remain upstream of the spray axis longer, causing the peak in upwind penetration.

Spray Axis Deflection

Prediction of the spray axis as outlined in Section 4.3.2 shows the behaviour of the spray core, which is defined as the area of the spray with a high liquid fraction. Appendix C shows the raw data points for the spray axes for time steps between 0.1 ms and 1.0 ms after SOF, for both the $Ma_g = 0.35$ and 0.58 cross-flows. The axis points represent the locations of maximum intensity which is used as an indicator of maximum fuel concentration as indicated previously.

From the results presented in Appendix C it is apparent that decreasing the momentum ratio of the liquid jet to the cross air flow, q , increases the rate at which the multi-plume spray begins to resemble a single plume spray (with one main core region surrounded by a cloud of droplets). This is primarily a function of the cross-flow velocity, as the most noticeable difference is between the $Ma_g=0.35$ and $Ma_g=0.58$ cross-flows rather than between the 10 and 15 MPa injection conditions.

Furthermore it is also anticipated that the results corresponding to short times after SOF are also increasingly impacted by variations in laser sheet intensity when considering the windward and leeward plumes of the spray.

These two issues impact the ability of the axis detection algorithm to adequately determine the spray axis, and hence results between 0.1 and 0.2 ms after SOF as well as 0.3 ms for $Ma_g=0.35$ cross-flow are not considered when detecting the spray axis.

For single-plume sprays, the spray axis is non-dimensionalized using the injector diameter. Since the present study looks at the multi-plume spray, an equivalent diameter d_{eq} given by

$$d_{eq} = 2\sqrt{ab} \quad (6.7)$$

is calculated using the elliptical area formed by the location of the holes on the injector tip, shown in Fig. 6.33. Here a and b are the major and minor axis of the ellipse. For the present study $a=1.926$ mm and $b=1.707$ mm.

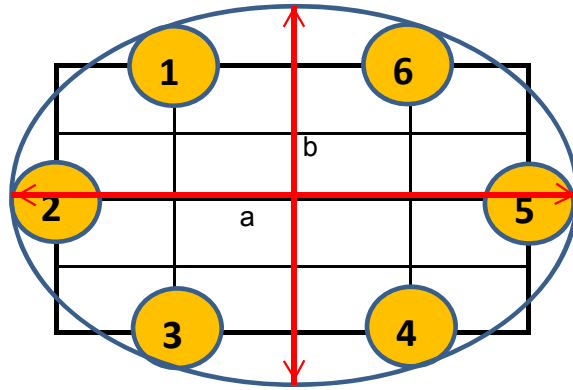


Figure 6.33: Schematic illustrating the ellipse used to calculate the equivalent diameter of the injector.

The non-dimensionalized spray axes are plotted for each time step in Figs. 6.34-6.37.

Table 6.3 lists the colors and symbols used to indicate time after SOF in Figs. 6.34 - 6.37 for the spray axes.

Time after SOF	Color
0.3	red
0.4	green
0.5	cyan
0.6	yellow
0.7	magenta
0.8	black
0.9	blue
1.0	brown

Table 6.3: Legend for spray axis plots used in Figs. 6.34-6.37

Analysing the spray axis at each time step for $q=991$, which are illustrated in Fig. 6.34 and Appendix C, it is observed that the spray core (high concentration region) is able to penetrate through the cross-flow. The high concentration, and relatively high momentum of the fuel within the core, limits the impact of the cross-flowing air. Hence, the spray axis continues to penetrate through the cross-flow with increasing time after SOF, as depicted by Fig. 6.34. Eventually the rate of penetration decreases as reflected by the grouping of the spray axes for 0.8 – 1.0 ms after SOF. This is similar to the decrease in the penetration depth growth rate observed in sprays into quiescent conditions, seen in Fig. 6.27. This result is expected since the drag forces acting on sprays also resist propagation of the spray plumes transversely through the cross-flow.

The spray axes corresponding to $q=665$, which are illustrated in Fig. 6.35, are independent of the time after SOF, except for 0.4 ms and 0.5 ms after SOF, which are represented by the green and cyan curves respectively. These two axes detach at locations of $x/d_{eq} = 7.5$ and 13, ceasing to follow the same relationship as the rest of the spray axes. Here, the decreased injection pressure reduces the droplet size, as illustrated in Fig. 6.30, and the liquid momentum, allowing for the axes to be easily deflected by the cross-flow.

Figure 6.36 depicts the spray axes results for conditions of $q=371$. Here the spray axes appears to be independent of time after SOF, until $x/d_{eq}=25$. At this point, there seems to be a variation in the spray axis, with that of time step 1.0 ms after SOF decreasing its

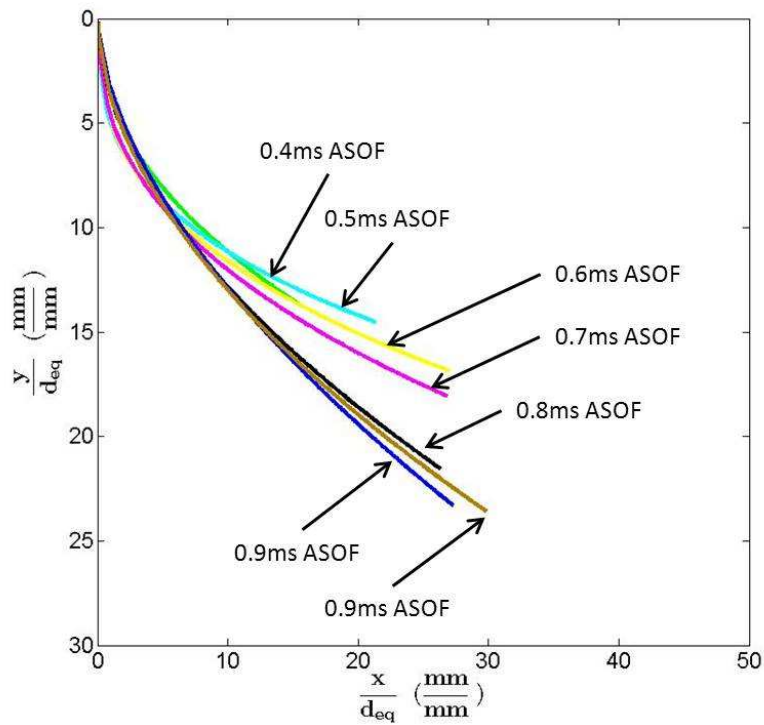


Figure 6.34: Spray axis for 15MPa injection into $Ma_g=0.35$ cross-flow for 0.4-1.0 ms after SOF, corresponding to $q = 991$, $We_l = 2.1 \times 10^5$, and $We_g = 213$. See Table 6.3 for color and symbol definitions

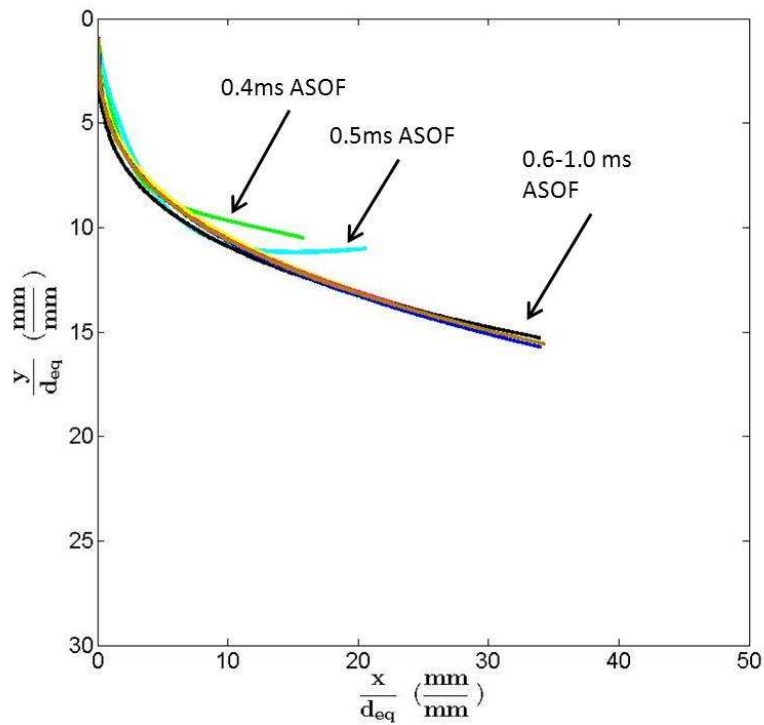


Figure 6.35: Spray axis for 10MPa injection into $Ma_g=0.35$ cross-flow for 0.4-1.0 ms after SOF, corresponding to $q = 665$, $We_l = 1.4 \times 10^5$, and $We_g = 213$. See Table 6.3 for color and symbol definitions

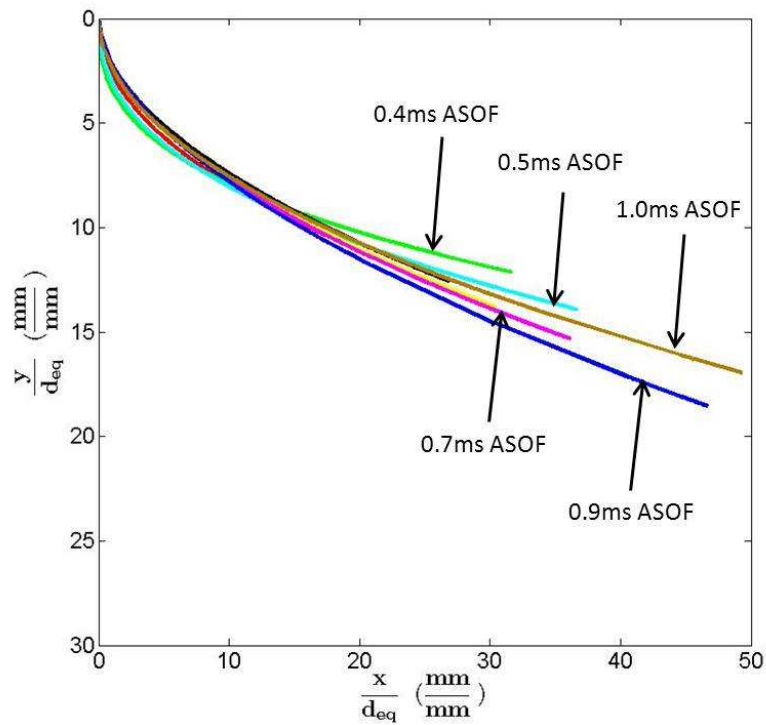


Figure 6.36: Spray axis for 15MPa injection into $Ma_g=0.58$ cross-flow for 0.3-1.0 ms after SOF, corresponding to $q = 371$, $We_l = 2.3 \times 10^5$, and $We_g = 617$. See Table 6.3 for color and symbol definitions

slope when compared to 0.7-0.9 ms after SOF. It is important to note that at this location, the spray axes penetrate through the theoretical boundary of the cross-flow potential core. Thus, the spray ceases to experience cross-flowing conditions. This is similar to the spray conditions corresponding to $q=991$ as discussed above.

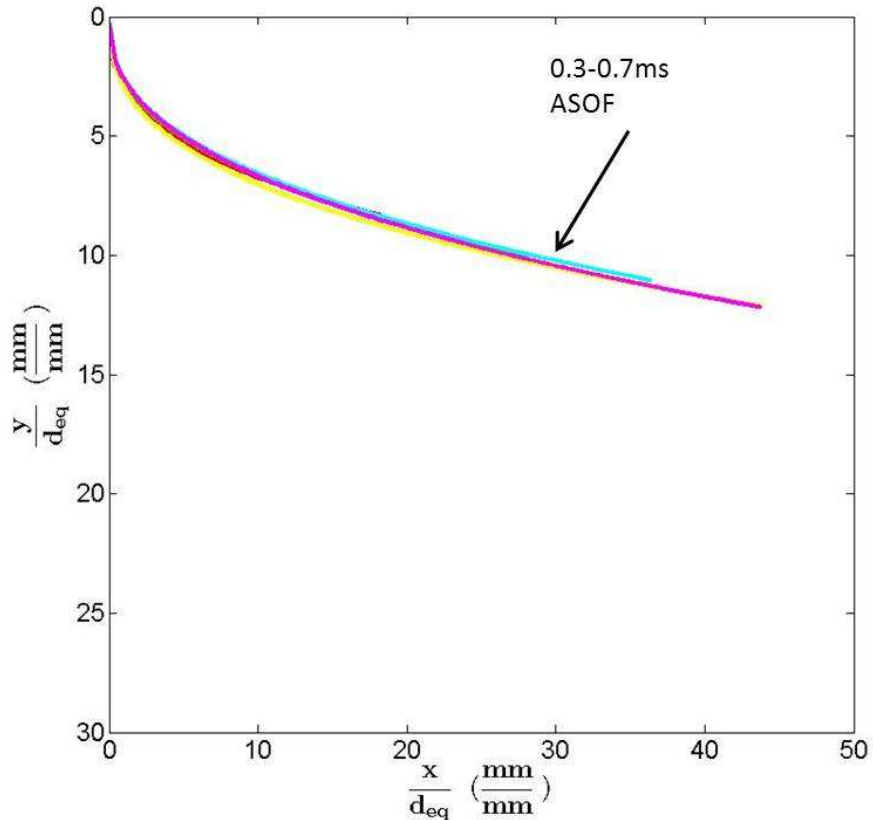


Figure 6.37: Spray axis for 10MPa injection into $Ma_g=0.58$ cross-flow for 0.3-0.7 ms after SOF, corresponding to $q = 249$, $We_l = 1.5 \times 10^5$, and $We_g = 617$. See Table 6.3 for color and symbol definitions

Finally, the results for $q=249$ show that at this momentum ratio, the spray axes are completely independent of time after SOF. In this instance, the spray core remains within the theoretical potential core, and continues to experience cross-flowing conditions.

Dismissing the results of the 15 MPa injection into the $Ma_g=0.35$ cross-flow and portions of the spray axes for the 15 MPa injection into the $Ma_g=0.58$ cross-flow, due to

the early penetration through the flow, the equation predicting the spray axis found in Eq. 2.23 is fitted to the remaining spray axes. The constants for this fit are found in Table 6.4 . This correlation fits the data well with the r^2 value reading 97.6%, and the RMS of the error only 0.535. These results are depicted, in Fig. 6.38, by the magenta curve.

Equation	A	B	C	m	n	r^2	Squared Sum of Error	RMS of Error
Eq. 2.23	0.3597	1.608	0.535	0.4147	0	0.976	4652	0.535
Eq. 6.8	12.53	1.509	2.219×10^{-5}	-0.1748	1.684	0.981	3763	0.481

Table 6.4: Correlation curve fit parameters

The black curve in this figure represents a new correlation expressed by

$$\frac{y}{d_{eq}} = Aq^m \ln\left[B + Cq^n \left(\frac{x}{d_{eq}}\right)\right] \quad (6.8)$$

The major difference between this new correlation and Eq. 2.23 is the influence of q inside of the natural logarithm and stems from the derivation of Eq. 2.10, discussed in section 2.2. The derivation is founded in the force balance on a droplet in cross-flow conditions. It was noted that the constants in this equation contain the drag coefficient, C_{dy} , which Mashayek et al. [11] note is dependent on the liquid and gas phase velocities. Exploiting this dependence they state that the constant in front of the natural logarithm must vary with q which leads to Eq. 2.23. However, the presence of C_{dy} inside the natural logarithm (as part of constant C) is not considered. Thus, it is expected that a similar dependence must be used within the natural logarithm as found in Eq. 6.8, with empirical constants found in Table 6.4 . It is apparent that Eq. 6.8 predicts the axes slightly better, improving the r^2 value to 98.3 %, and decreasing the RMS of the error and the Squared Sum of Error(SSE). From Fig. 6.38, it is noticed that Eq. 6.8 improves the prediction of the spray axes for $q=249$ and 665 , but that for $q=371$ there is not a marked improvement.

The empirical values for the two fits were obtained using MATLAB's non-linear least squares curve fitting toolbox, and are valid for the range of experimental conditions listed

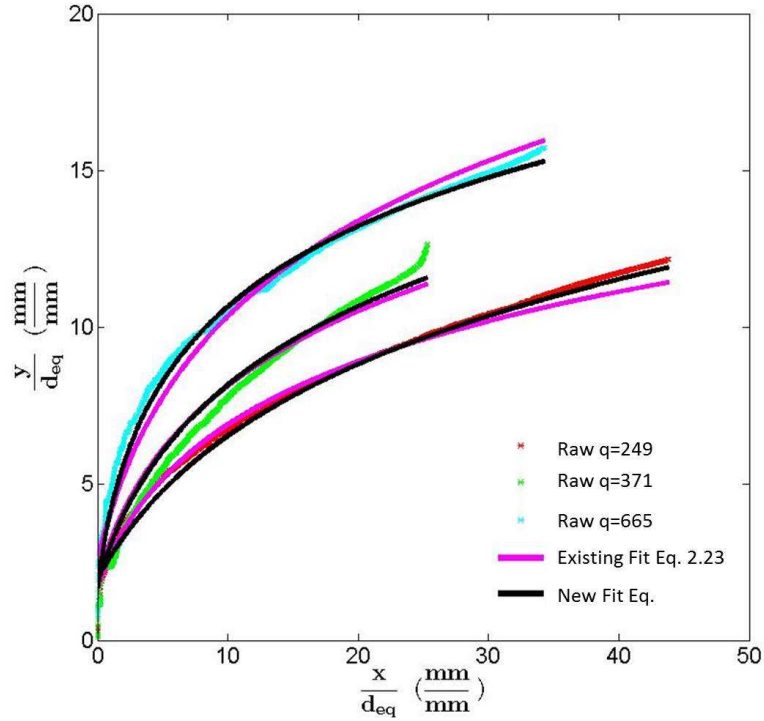


Figure 6.38: Comparison of existing correlation (magenta) with correlation expressed by Eq. 6.8 (black) for 10 MPa injection into $Ma_g=0.58$ and $Ma_g=0.35$ cross-flow and 15 MPa injection into $Ma_g=0.58$ cross-flow.

Variable Range
$249 \leq q \leq 665$
$213 \leq We_g \leq 617$
$1.4 \times 10^4 \leq We_l \leq 2.1 \times 10^4$

Table 6.5: Conditions for the new multi-plume spray axis correlation(Eq. 6.8 and the existing spray axis correlation(Eq. 2.23)

in Table 6.5 As such, it is apparent that the spray axes of the multi-plume sprays studied in this work, can be predicted using a model similar in form to those used for single plume sprays. Furthermore, the accuracy of these models are improved upon through the inclusion of q in the natural logarithm.

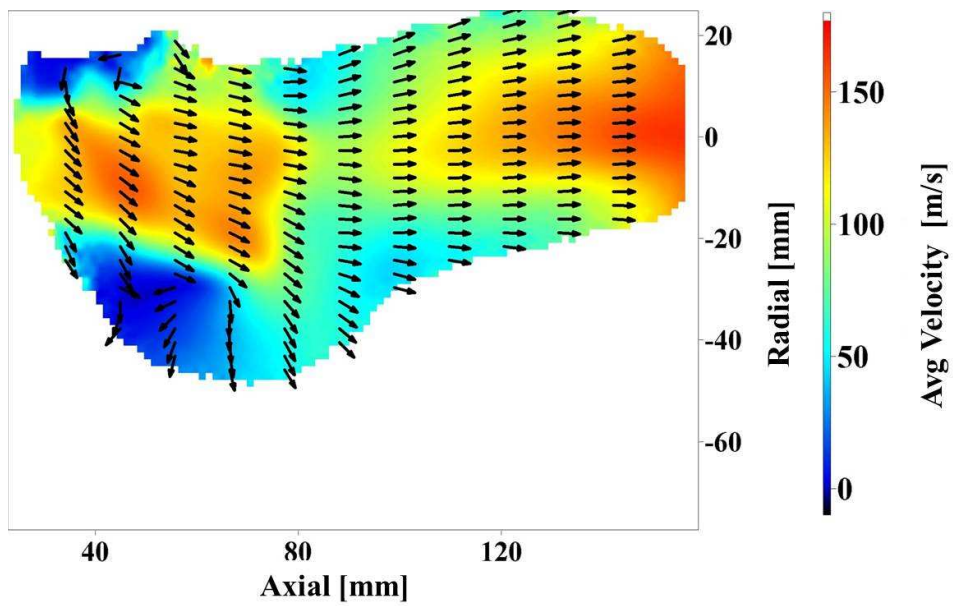
6.3.2 Spray PIV

The use of PIV allows for the quantification of droplet velocity throughout the spray as well as the detection of large scale structures. Information about droplet velocity indicates the level to which the cross-flow is able to redirect droplets and entrain them within the air flow. Figure 6.39 gives the mean velocity vector maps at 1 ms after SOF for each set of conditions. 1 ms after SOF was selected to allow for the spray to be dilute enough to perform PIV.

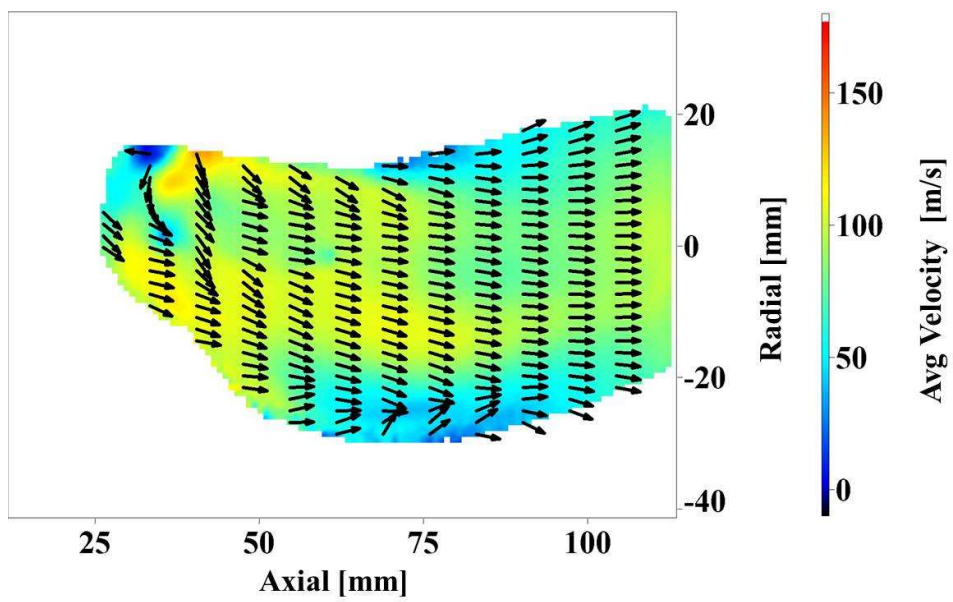
Looking at the velocity maps, for $Ma_g=0.35$ and 15 MPa and $Ma_g=0.58$ and 15 MPa seen in Figs. 6.39(a) and 6.39(c) respectively, it is noticed that the maximum velocity downstream of the injector tip, which is located 34 mm in the axial direction and 15 mm in the radial direction from the air nozzle, is greater than the independent cross-flow velocity measured in Table 6.1. Here the cross-flow momentum is imparted to the droplets without significant change to the initial droplet momentum, giving a resultant value that is greater than both the cross-flow and injector initial values.

For the $Ma_g=0.35$ and 10 MPa and $Ma_g=0.58$ and 10 MPa set of conditions seen in Figs. 6.39(b) and 6.39(d) respectively, the opposite is true. For the $Ma_g=0.35$ and 10 MPa there is a small region near the injector tip which displays elevated velocity, while the bulk of the flow displays velocities which are smaller than the cross-flow initial velocity. This leads to the conclusion that the droplets, which have a larger SMD are still influenced by the cross-flow and translated along the cross-flow axis, but to a lesser extent than the 15 MPa injected sprays which typically have a smaller SMD due to the higher injection pressure.

The same can be noted for the $Ma_g=0.35$ and 15 MPa condition, which does not show any velocities above the cross-flow initial velocity. Instead what can be noted for this spray is that velocity vectors quickly align with the cross-flow axis at an axial distance of 100 mm, retaining a small amount of momentum in the negative radial direction. This can be

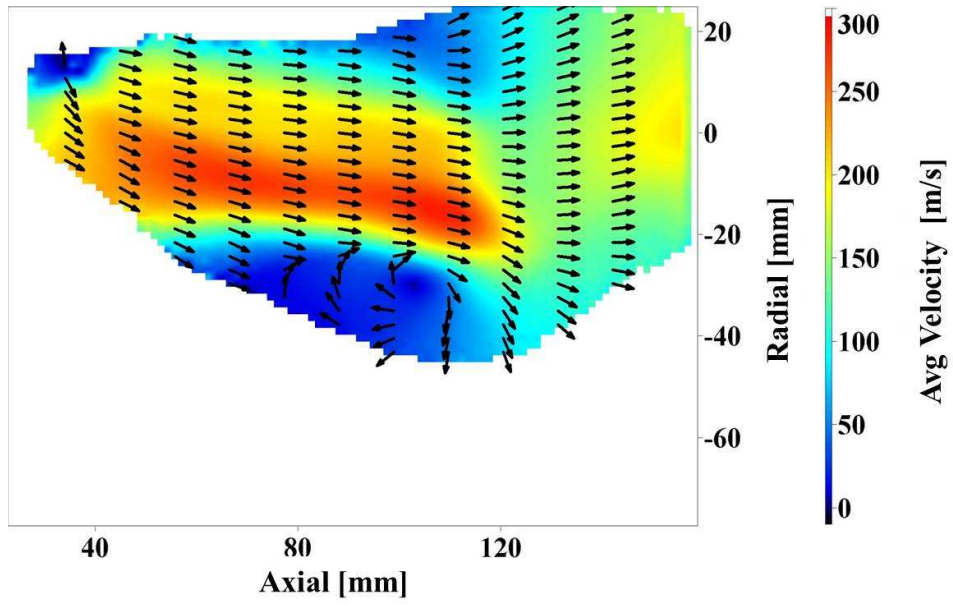


(a) $Ma_g=0.35$ and 15 MPa ($U_o=125$ m/s)

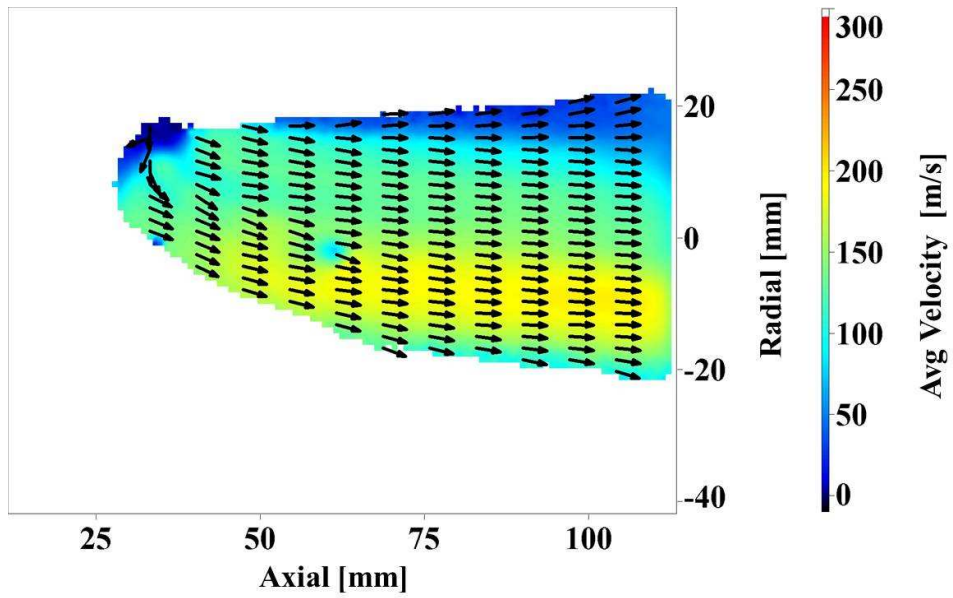


(b) $Ma_g=0.35$ and 10 MPa ($U_o=125$ m/s)

Figure 6.39: Velocity vector map for fuel sprays 1 ms after SOF



(c) $Ma_g=0.58$ and 15 MPa ($U_o=215$ m/s)



(d) $Ma_g=0.58$ and 10 MPa ($U_o=215$ m/s)

Figure 6.39: Time averaged velocity vector map for fuel sprays 1 ms after SOF

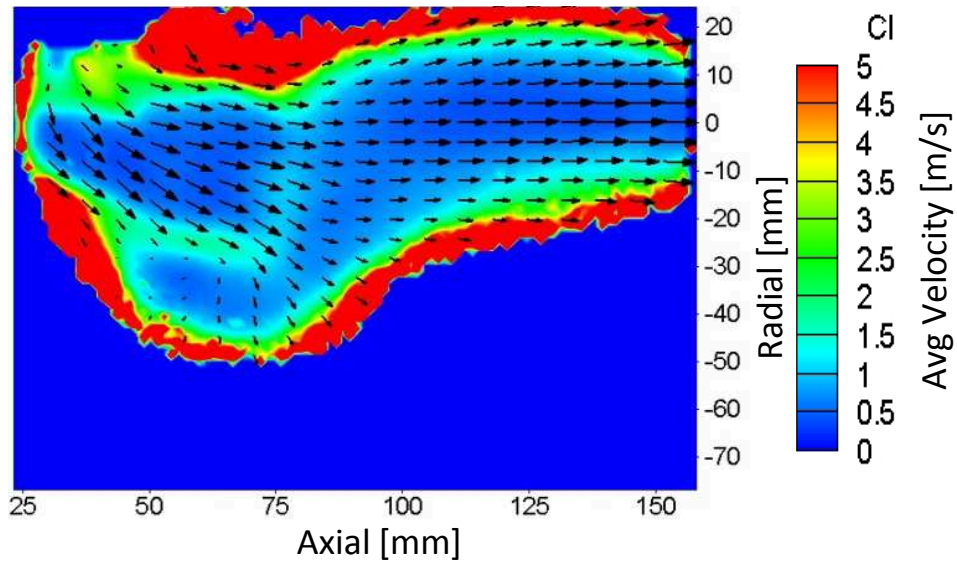
attributed either to the initial injection momentum, or to the tendency for the cross-flow to spread outwards as mixing occurs at the periphery of the air jet. This behaviour is also noticed in Figs. 6.39(d) and 6.39(b) at an axial distance of 80 mm, while Fig. 6.39(c) does not align within the field of view which extends to 157 mm.

Figures 6.40(a)–(d) map the variability in the magnitude of the velocity vectors throughout the spray. These contour plots show the velocity magnitude variability at any location within the spray, to within $1.96 \times \sigma$ which is the margin of error used to calculate the 95% confidence interval. Hence, sprays injected into the cross-flow experience minimal variation in velocity within the main body of the spray. However, variations upwards of 5 m/s can be seen at the periphery of the sprays, as depicted by Figs. 6.40(a)-(d). It is important to note that the contour plots do not account for changes in the direction of the velocity vectors.

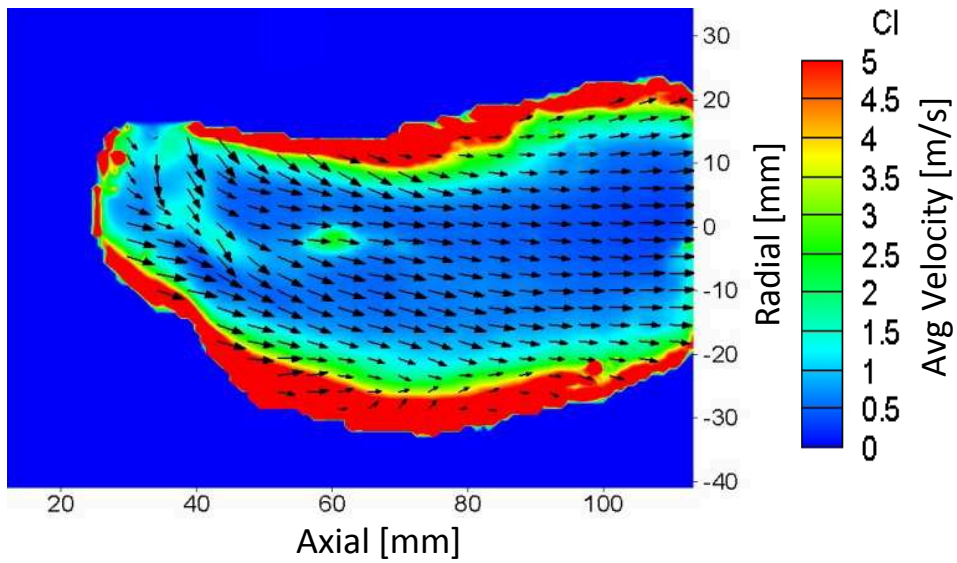
Finally, Figs. 6.41(a)-(d) quantify the number of instantaneous vectors included in the calculation of the mean velocity at each location. Although, 2000 sets of PIV data were recorded for each set of conditions, vector filtering, image processing, and variation of the instantaneous spray shape within the cross-flow reduce the number of vectors included in the calculation. As a result, the mean velocity within the main body of the spray is calculated based on 1800-1600 instantaneous vectors, while at the periphery of the spray the number drops to 0. Together, Figs. 6.40 and 6.41 validate that within the main body of the spray, the mean velocity magnitude is relatively stable, with a high occurrence of vectors and a low variability in the velocity magnitude.

In summary, the PIV of the spray plume has been used to quantify the mean velocity of the fuel droplets, illustrating that the lower injection pressure tends to experience an overall deceleration of droplet velocity, while the higher injection pressure leads to droplets being entrained by the cross-flow without significant loss of their initial momentum. Furthermore, it is illustrated that mean velocity magnitudes within the spray plumes are relatively stable, demonstrating small variability in the set of instantaneous images, appearing in 80-90 % of the instantaneous images.

A complete summary of the results and conclusions will be presented in the following chapter along with recommendations for future work and extensions to the present study.

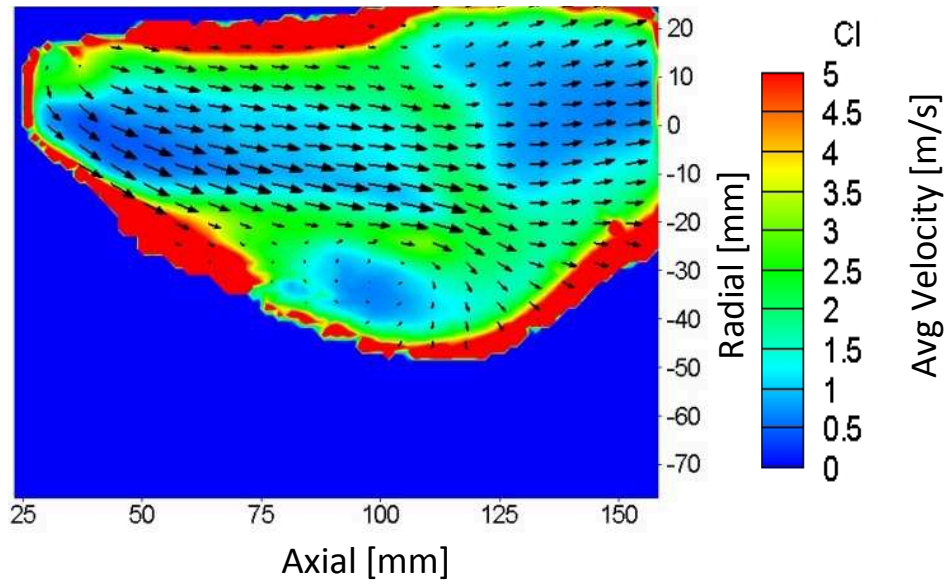


(a) $Ma_g=0.35$ and 15 MPa ($U_o=125$ m/s)

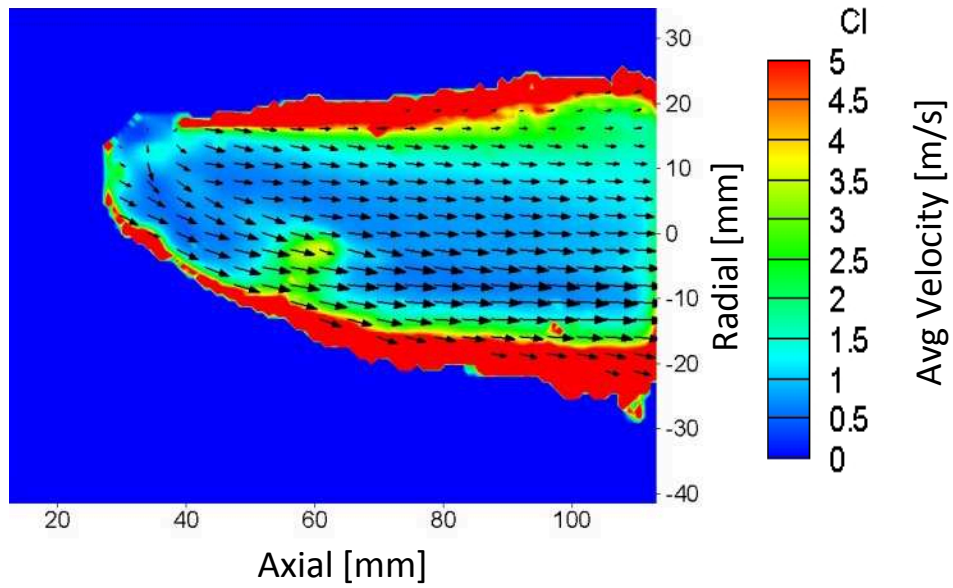


(b) $Ma_g=0.35$ and 10 MPa ($U_o=125$ m/s)

Figure 6.40: Time averaged velocity variability vector map for fuel sprays 1 ms after SOF

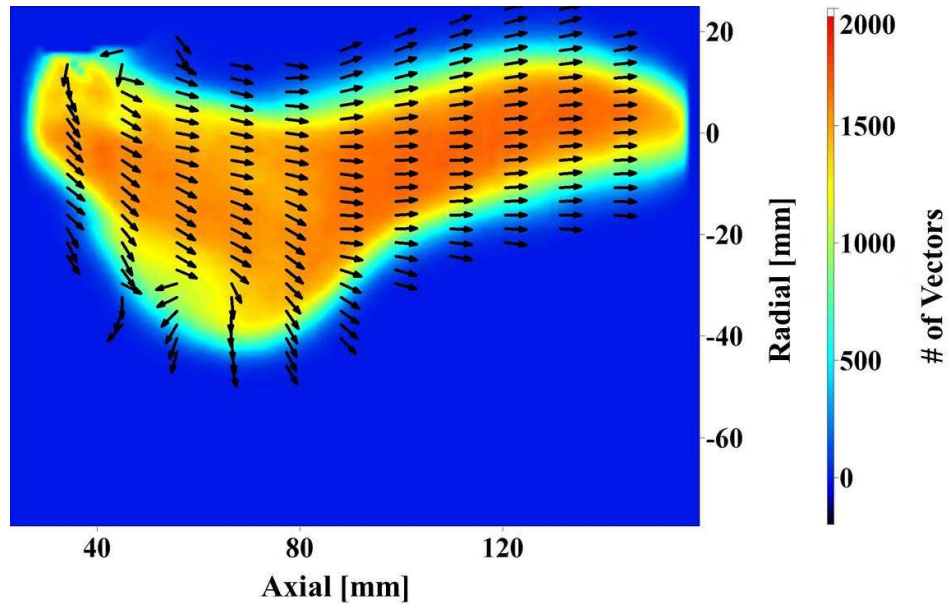


(c) $Ma_g=0.58$ and 15 MPa ($U_o=215$ m/s)

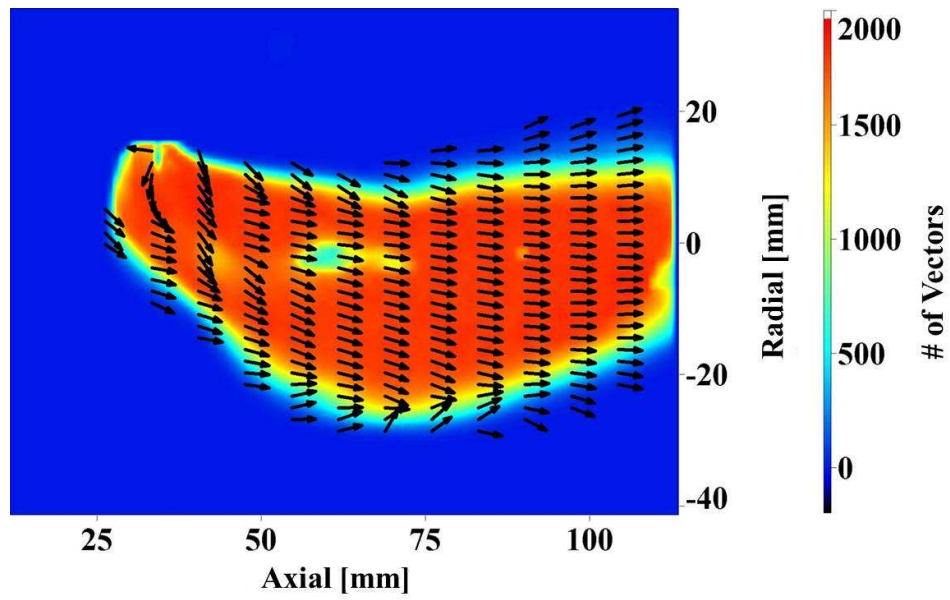


(d) $Ma_g=0.58$ and 10 MPa ($U_o=215$ m/s)

Figure 6.40: Velocity variability map for fuel sprays 1 ms after SOF

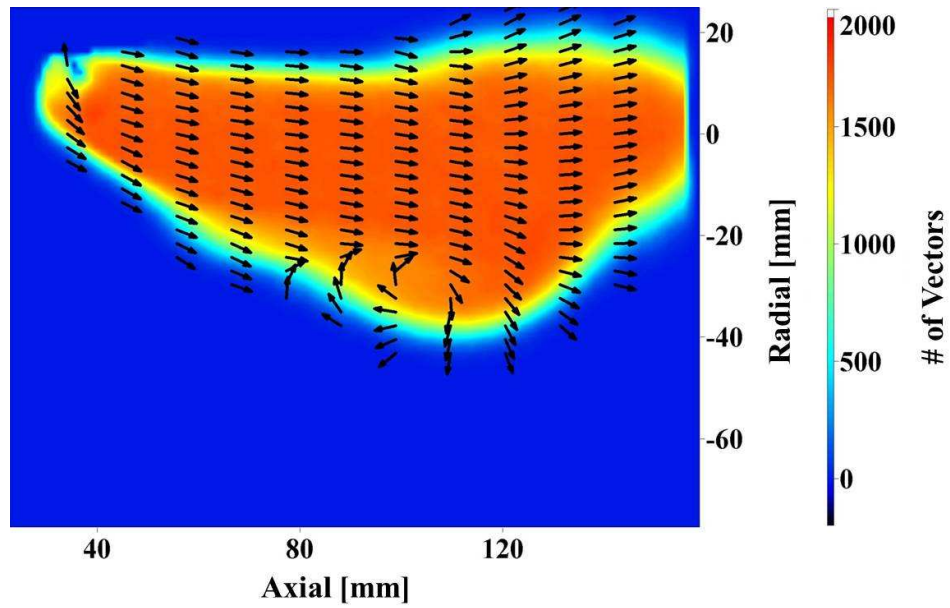


(a) $Ma_g=0.35$ and 15 MPa ($U_o=125$ m/s)

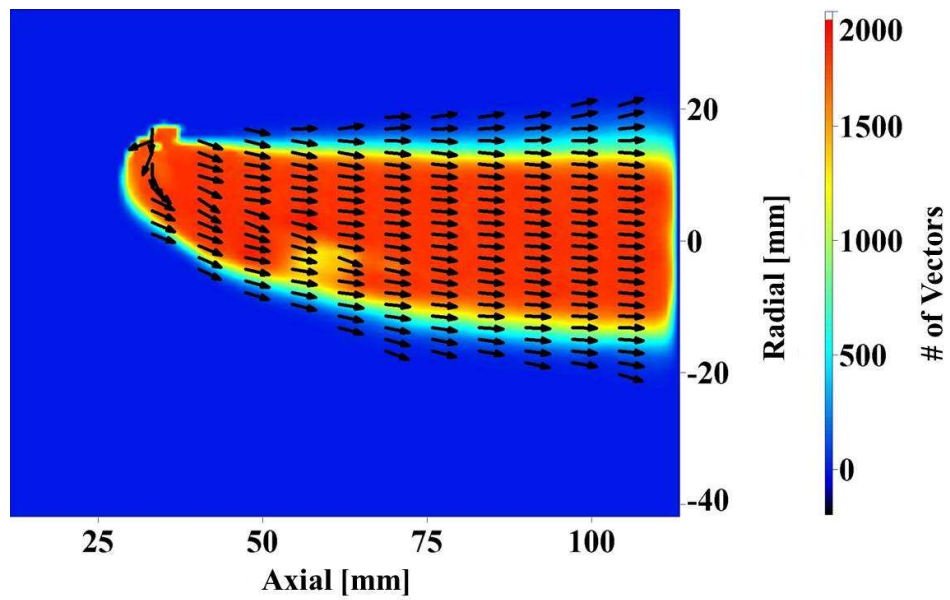


(b) $Ma_g=0.35$ and 10 MPa ($U_o=125$ m/s)

Figure 6.41: Number of vectors map for fuel sprays 1 ms after SOF indicating the number of vectors used in calculating the mean velocity



(c) $Ma_g=0.58$ and 15 MPa ($U_o=215$ m/s)



(d) $Ma_g=0.58$ and 10 MPa ($U_o=215$ m/s)

Figure 6.41: Number of vectors map for fuel sprays 1 ms after SOF indicating the number of vectors used in calculating the mean velocity

Chapter 7

Conclusions and Recommendations

An experimental system for investigating the interaction between the multi-plume sprays issuing into a high-velocity cross-flow has been developed and characterized. Axial and radial velocities along with turbulent kinetic energy have been measured for the cross-flow using Particle Imaging Velocimetry (PIV) techniques, and the length of the potential core identified for 2 different core velocities between Mach number 0.3 and 0.6.

Macroscopic spray characteristics such as penetration depth, spray angle and spray width have been measured for the multi-plume spray in quiescent conditions for a range of time steps from start of fuel (SOF) allowing for the characterization of the injector performance before introducing the spray into the cross-flow.

Also, tail length and penetration of the spray into the cross-flow are calculated from images for the range of time steps after SOF. The same images are also used to adapt methodologies from single plume studies for use in multi-plume analysis and to predict the axis of the spray plume corresponding to the axis of highest fuel concentration.

Furthermore, PIV measurements of the spray plume are performed at 1.0 ms after SOF. Droplet velocities are calculated for the spray, allowing for discussion on the impact of the cross-flow on the spray plumes.

Lastly, the experimental uncertainty has been quantified for the measurements and is included with the analysis presented in the results.

The above measurements and developed analysis tools were used to assess the interaction of the fuel spray and cross-flow and allow for the assessment of the level of mixing

that occurs. The results have been incorporated into the validation process for spray-air interaction used in the design of SIDI engines.

7.1 Conclusions

Results show that the air jet developed for the high-velocity cross-flow displays evidence of the vena contracta effect leading to a slight dog-eared velocity profile close to the air jet outlet. The resulting velocity maximum which occurs at the periphery of the potential core is less than 3 % of the potential core velocity and dissipates with increasing axial location x/D from the nozzle outlet. Furthermore, the length of the potential core is shown to increase with increasing Ma_g number indicating a reduced level of mixing with increasing levels of compressibility. Finally, the axial velocity within the shear layer displays the self-similarity which is noted in literature, but also displays a slight upward draft when considering the radial velocity profiles. This upward draft does appear to dissipate by $x/D=4$ and hence the potential core is deemed a suitable high-velocity cross-flow for the study.

Examining the multi-plume sprays into quiescent conditions, it is immediately apparent that the higher injection pressure consistently leads to a larger penetration depth, and that this penetration initially follows a linear relationship. After the breakup point at time $t=0.5$ ms after SOF, the penetration begins to follow the $t^{0.5}$ relationship per findings in literature.

Alternatively, the spray angle of the multi-plume spray decreases with increasing injection pressure at a given time after SOF which is contrary to literature, but is thought to be similar to the reduction in the mixing rate of the air jet with increasing velocity. It is also observed that the spray angle continually decreases at a decreasing rate with increased time after SOF, suggesting that there is an asymptotic value which can be selected to represent the injector and is independent of injection pressure.

The results for the multi-plume sprays injected into the cross-flowing air illustrate that the tail length is primarily influenced by the velocity of the cross-flow, with increasing air velocity resulting in an increased tail length. The liquid Weber number We_1 plays a secondary role with increased We_1 leading to a minor increase in the tail length. The tail length is dictated by the ability of the cross-flowing air to entrain the finest droplets in the

atomized spray and carry them downstream. As such, higher velocity cross-flow signifies an increased distance that entrained droplets are able to travel downstream for a given time, while the increased We_1 signals finer atomization of the spray leading to droplets being entrained more easily. Furthermore, the penetration of the spray upwind of the injector is primarily a function of air velocity and the momentum with which the cross-flow can break up or entrain the upwind plume. It is also hypothesized that needle opening effects are producing a peak early on in the upwind penetration due to the production of larger droplets which take longer to be entrained by the air flow.

Alternatively, the penetration of the spray into the cross-flowing air stream is found to be governed solely by the injection pressure. This finding is consistent with the assumptions which are the foundation for the existing spray axis models which consider that the momentum of the injected mass and the momentum of the cross-flowing air act perpendicular and independently of each other. Thus, higher injection pressure results in higher initial momentum which translates into a larger penetration into the cross-flow. For the present study, the multi-plume sprays issuing into the cross-flow begin to resemble single-plume sprays issuing into cross-flowing air as early as 0.3 ms after SOF. Before this point, sprays retain the characteristics of individual plumes. Once these characteristics dissipate the spray contains a high concentration core region which is followed by a cloud of atomized droplets. The highest concentration within this core region is assumed to correlate with the highest pixel intensity. Using this methodology and compensating for light sheet bias, the spray axis is determined. The spray axis is found to be independent of the time after SOF at which the images are taken, but rather is more heavily impacted by the injection pressure and the air velocity. The spray axes can be predicted well using the logarithmic models, found in literature for single-plumes. A modified form of the logarithmic model is developed, improving the accuracy of spray axis prediction in the range of studied conditions.

Lastly, the measurement of droplet velocity for sprays injected into the cross-flow at 1 ms after SOF show that 10 MPa injections tend to align with the cross-flow axis faster than the 15 MPa sprays, although, for the 15 MPa spray this happens quicker for the 125 m/s cross-flow. However, the 15 MPa spray demonstrates, an increase in the velocity magnitude of the droplets downstream of the injector tip. This increase is due to the momentum of the cross-flow which increases the droplet velocity along the cross-flow axis without impacting the droplet momentum in the radial direction. The 10 MPa sprays

experience mean velocities which are either in-line or lower than the initial cross-flow velocity leading to the conclusion that the a lower amount of cross-flow momentum is imparted to the droplets than for the 15 MPa injection.

7.2 Recommendations

It is recommended that the similar analysis be applied to a comprehensive data set which looks at a wider range of momentum ratio and gas phase Weber number. This will allow for the calculation of the coefficients of the power-law model which has been extended from single-plume sprays to multi-plume-sprays. Furthermore, the effects that gas phase Weber number and momentum ratio should be incorporated into the model.

Another extension of the present work is the measurement and control of the fuel temperature. Currently, temperature effects are ignored, although localized heating from the cross-flow does occur. Improved measurement and control of this temperature will allow for the comparison of an evaporating and non-evaporating spray and the impacts on the measured characteristics.

Further improvements into the application of spray PIV are also recommended. Currently, noise from multiple scattering between out of plane droplets obscures the image leading to a reduction in accuracy of the droplet velocity measurements. The addition of a fluorescent tracer to fuel spray will allow for the in-plane droplets to be clearly detected. Rhodamine which is used to shift the wavelength of unwanted reflections can be used as such a tracer. The use of a narrow bandpass filter will allow only the fluorescing wavelength to reach the image sensor and remove the scattering from the laser sheet. Furthermore, this technique can be extended to include Laser Sheet Drop Sizing (LSDS) measurements which allow for the global drop size distribution to be measured. This information would allow for investigation into the level of atomization enhancement that occurs by introducing a spray into a high-velocity cross-flow. Particle imaging, which uses high power optics to resolve individual particles, in conjunction with the LSDS technique will also provide information about the mechanisms of droplet breakup which occurs in the presence of the cross-flow.

For measurement of droplet sizing, in order to improve the accuracy of the results a fluorescent tracer can be added to the fuel spray such that the droplets which are exposed

to the laser sheet will emit at a different wavelength. Using a narrow bandpass filter, the fluorescing wavelength can be imaged and the noise present from the multiple scattering of the laser light can be further eliminated.

References

- [1] Carsten Baumgarten. *Mixture Formation in Internal Combustion Engines*. Springer, Verlag Berlin Heidelberg, 2006.
- [2] F. Zhao, M.C. Lai, and D.L. Harrington. Automotive spark-ignited direct-injection gasoline engines. *Progress in Energy and Combustion Sciences*, 25:437–562, 1999.
- [3] M. Bahattin, C. Ozdalyan, and B. Ozdalyan. *Fuel Injection*, chapter Gasoline Direct Injection, pages 1–18. Sciyo, Europe, 2010.
- [4] R. Leonhard. Bosch di-motronic gasoline direct injection-the technology of direct injection, May 2003.
- [5] H. Ren, Y. Tian, Q. Ma, and J. Luo. Analysis of flow field in the cylinder of gasoline engine before and after being turbocharged. *Emerging Intelligent Computing Technology and Applications*, 304:124–131, 2012.
- [6] G. M. Faeth. Structure and atomization properties of dense turbulent sprays. In *23rd Symposium (International) on Combustion*, pages 1345–1352. The Combustion Institutes, 1990.
- [7] G. M. Faeth, L. P. Hsiang, and P. K. Wu. Structure and breakup properties of sprays. *International Journal of Multiphase Flow*, 21:99–127, 1995.
- [8] J. O. Hinze. Fundamentals of the hydrodynamic mechanism of splitting in dispersion processes. *AIChE Journal*, 1:289–295, 1955.
- [9] L. P. Hsiang and G. M. Faeth. Drop deformation and breakup due to shock wave and steady disturbances. *International Journal of Multiphase Flow*, 21:545–560, 1995.

- [10] M. Y. Leong, V. G. McDonell, and S. G. Samuelsen. Mixing of an airblast-atomized fuel spray injected into a crossflow of air. Technical Report CR2000-210467, NASA, October 2000.
- [11] A. Mashayek and N. Ashgriz. *Handbook of Atomization and Sprays*, chapter Atomization of a Liquid Jet in a Crossflow, pages 657–684. Springer, New York, 2011.
- [12] A. Mashayek and N. Ashgriz. Model of deformation of drops and liquid jets in gaseous crossflows. *AIAA*, 47, 2009.
- [13] J. M. Desantes, J. J. L. Arregle, and J. M. Garcia. Turbulent gas jets and diesel-like sprays in a crossflow: A study on axis deflection and air entrainment. *Fuel*, 85:2120–2132, 2006.
- [14] P-K. Wu, K.A. Kirkendall, and P.F. Fuller. Breakup processes of liquid jets in subsonic crossflows. *Journal of Propulsion and Power*, 13, 1997.
- [15] A. Mashayek and N. Ashgriz. Improved model for the penetration of liquid jets in subsonic crossflows. *AIAA*, 46, 2008.
- [16] K.S. Varde. Spray cone angle and its correlation in a high pressure fuel spray. *The Canadian Journal of Chemical Engineering*, 63:183–187, 1985.
- [17] A. Amighi, M. Eslamian, and N. Ashgriz. Trajectory of a liquid jet in high pressure and high temperature subsonic air crossflow. In *Proceedings of 11th International Conference on Liquid Atomization and Spray Systems*, Vail, Colorado, USA, July 2009. Paper No. 225.
- [18] R.D. Ingebo. Penetration of drops into high velocity airstreams. Technical Report TM X-1363, NASA, 1967.
- [19] J. N. Stenzler, J. G. Lee, and A. Santavicca. Penetration of liquid jets in a cross-flow. *Atomization and Sprays*, 16:1–20, 2006.
- [20] R. Ragucci, A. Bellofiore, and A. Cavaliere. Breakup and breakdown of bent kerosene jets in gas turbine conditions. *Proceedings of the Combustion Institute*, 31:2231–2238, 2007.

- [21] T. Inamura. Trajectory of a liquid jet traversing subsonic airstreams. *Journal of Propulsion and Power*, 16, 2000.
- [22] K. Sallam, C. Aalburg, and G.M. Faeth. Breakup of round nonturbulent liquid jets in gaseous crossflow. *AIAA*, 42, 2004.
- [23] T. Inamura, N. Nagai, and T. Watanabe. Disintegration of liquid and slurry jets traversing subsonic airstreams. *Experimental Heat Transfer, Fluid Mechanics and Thermodynamics*, 1993.
- [24] J. Becker and C. Hassa. Breakup and atomization of a kerosene jet in crossflow at elevated pressure. *Atomization and Sprays*, 12:49–67, 1993.
- [25] R.R. Lakhamraju. Liquid jet breakup studies in subsonic airstream at elevated temperatures. Master’s thesis, University of Cincinnati, 2005.
- [26] S. Tambe. Liquid jets in subsonic crossflow. Master’s thesis, University of Cincinnati, 2004.
- [27] J. Mazallon, Z. Dai, and G.M. Faeth. Aerodynamic primary breakup at the surface of nonturbulent round liquid jets in crossflow. In *36th Aerospace Sciences Meeting and Exhibition*, Reno, NV.
- [28] M. K. Kim, J. Song, J. Hwang, and Y. Yoon. Effects of canted injection angles on the spray characteristics of liquid jets in subsonic crossflows. *Atomization and Sprays*, 20:749–762, 2010.
- [29] M. Costa, M.J. Melo, and J.M.M. Sousa. Spray characteristics of angled liquid injection into subsonic crossflows. *American Institute of Aeronautics and Astronautics*, 44:646–653, 2006.
- [30] J. Abraham, A. Khan, and V. Magi. Jet-jet and jet-wall interactions of transient jets from multi-hole injectors. *SAE Technical Paper Series*, 1999.
- [31] D. Yu, M.S. Ali, and J.H.W. Lee. Multiple tandem jets in cross-flow. *Journal of Hydraulic Engineering*, 132:971–982, 2006.
- [32] Stavros Tavoularis. *Measurement in Fluid Mechanics*. Cambridge University Press, New York, 2005.

- [33] I.E. Idelchik. *Handbook of Hydraulic Resistance 3rd Edition*. CRC Press, Boca Raton, 1994.
- [34] T. Morel. Comprehensive design of axisymmetric wind tunnel contractions. *Journal of Fluids Engineering*, 97:225–234, 1975.
- [35] E. G. Tulapurkara and V. V. K. Bhalla. Experimental investigation of morel’s method for wind tunnel contractions. *Journal of Fluids Engineering*, 110:45–48, 1988.
- [36] P. R. Bradshaw and C. Pankhursta. The design of low-speed wind tunnels. *Progress in Aeronautical Sciences*, 5:1–69, 1964.
- [37] LaVision Inc. Light sheet optics, November 2011.
- [38] R. J. Adrian and J. Westerweel. *Particle Image Velocimetry*. Cambridge University Press, New York, 2011.
- [39] C.T. Crowe, R.A. Gore, and T.R. Troutt. Particle dispersion by coherent structures in free shear flows. *Particle Science and Technology: An International Journal*, 3:149–158, 1985.
- [40] K. Luo, M. Klein, J.R. Fan, and K.F. Cen. Effects on particle dispersion by turbulent transition in a jet. *Physics Letters A*, 357:345–350, 2006.
- [41] C.T. Crowe, R.A. Gore, and T.R. Troutt. Particle mixing in free shear flows. *Progress in Energy and Combustion Science*, 14:171–194, 1988.
- [42] E. K. Longmire and J. K. Eaton. Structure of a particle-laden round jet. *Journal of Fluid Mechanics*, 236:217–257, 1992.
- [43] J.N. Chung and T.R. Troutt. Simulation of particle dispersion in an axisymmetric jet. *Journal of Fluid Mechanics*, 186:199–222, 1989.
- [44] E.C. Willert. Assessment of camera models for use in planar velocimetry calibration. *Experiments in Fluids*, 41:135–143, 2006.
- [45] Gasoline Fuel Injection Standards Committee. Gasoline fuel injector spray measurement and characterization. Technical Report J2715, SAE International, March 2007. Surface Vehicle Recommended Practice.

- [46] D. L.S. Hung, D. L. Harrington, A. H. Gandhi, L. E. Markle, S. E. Parish, J. S. Shakal, H. Sayar, S. D. Cummings, and J. L. Kramer. Gasoline fuel injector spray measurement and characterization- a new sae j2715 recommended practice. *SAE International Journal of Fuels and Lubricants*, 1:534–548, 2008.
- [47] N. Mitroglou, J.M. Nouri, M. Gavaises, and C. Acroumanis. Spray characteristics of a multi-hole injector for direct-injection gasoline engines. *International Journal of Engine Research*, 7:255–270, 2006.
- [48] LaVision Inc. *Flowmaster*, June 2011. 1105011-4.
- [49] R.J.M. Bastiaans. *Cross-Correlation PIV: Theory, Implementation and Accuracy*. Eindhoven University of Technology, Faculty of Mechanical Engineering, 2000.
- [50] LaVision Inc. *DaVis 8.1 Software*, September 2012. 1105xx.
- [51] J.V. Pastor, J. Arregel, and A. Palomares. Diesel spray image segmentation with a likelihood ratio test. *Applied Optics*, 40, 2001.
- [52] V. Macian, R. Payri, A. Garcia, and M. Bardi. Experimental evaluation of the best approach for diesel spray images segmentation. *Experimental Techniques*, 36, 2012.
- [53] J. M. Desantes, J. J. L. Arregle, and J. M. Garcia. A contribution to the study of a diesel spray interacting with a crossflow. *Atomization and Sprays*, 16:511–530, 2006.
- [54] M. Raffel, C. Willert, and J. Kompenhans. *Particle Image Velocimetry: A Practical Guide*. Springer, 1998.
- [55] V. Weitbrecht, G. Kuhn, and G.H. Jirka. Large scale piv measurements at the surface of shallow water flows. *Flow Measurements and Instrumentation*, 13:237–245, 2002.
- [56] A.K. Prasad. Stereoscopic particle image velocimetry. *Experiments in Fluids*, 29:103–116, 2000.
- [57] B. M. Wilson and B. L. Smith. Uncertainty on piv mean and fluctuating velocity due to bias and random errors. *Measurement Science and Technology*, 24, 2013.
- [58] B. H. Timmins, B. W. Wilson, B. L. Smith, and P. P. Vlachos. A method for automatic estimation of instantaneous local uncertainty in particle image velocimetry measurements. *Experiments in Fluids*, 53:1133–1147, 2012.

- [59] M. Stanislas, K. Okamoto, C. J. Kahler, and J. Westerweel. Main results of the second international piv challenge. *Experiments in Fluids*, 39:170–191, 2005.
- [60] C.D. Ungate, D.R.F. Harleman, and G.H. Jirka. Large scale piv measurements at the surface of shallow water flows. Technical Report MIT-EL 75-014, M.I.T. Energy Laboratory, February 1975.
- [61] A. Sedaghat, X. Liu, J. Whitty, and X. Tang. Wind power of small wind turbines in turbulent open jets. *Scientia Iranica B*, 19:272–281, 2012.
- [62] G. N. Abramovich. *The Theory of Turbulent Jets*. The MIT Press.
- [63] J. H. W. Lee and V. H. Chu. *Turbulent Jets and Plumes A Lagrangian Approach*. Springer Publishers, 2003.
- [64] Y. Antoine, F. Lemoine, and M. Lebouche. Turbulent transport of a passive scalar in a round jet discharging into a co-flowing stream. *European Journal of Mechanics-B/Fluids*, 20:275–301, 2012.
- [65] K.B.M.Q. Zaman. Asymptotic spreading rate of initially compressible jets-experiment and analysis. *Physics of Fluids*, 10:2652–2660, 1998.
- [66] I. M. Milanovic and K. J. Hammad. Piv study of the near-field region of a turbulent round jet. In *Proceedings of the ASME 2010 3rd Joint US-European Fluids Engineering Summer Meeting*, Montreal, CA, August 2010.
- [67] G.S. Elliott and M. Samimy. Compressibility effects in free shear layers. *Physics of Fluids A*, 2, 1990.
- [68] Z. Wang and Y. Andreopoulos. Density and compressibility effects in turbulent subsonic jets part 1: Mean velocity field. *Experiments in Fluids*, 48:327–343, 2009.
- [69] W.R. Quinn. Upstream nozzle shaping effects on near field flow in round turbulent free jets. *European Journal of Mechanics B/Fluids*, 25:279–301, 2006.
- [70] Stephen. B. Pope. *Turbulent Flows*. Cambridge University Press, New York, 2000.
- [71] K. Lee and R.D. Reitz. Investigation of spray characteristics from a low-pressure common rail injector for use in a homogeneous charge compression ignition engine. *Measurement Science and Technology*, 15:509–519, 2004.

- [72] K. Lee and C. Aalburg. Primary breakup of turbulent round liquid jets in uniform crossflows. *AIAA Journal*, 45, 2007.
- [73] F. J. Hamady, J. P. Hahn, and K. H. Hellman. High-speed/high resolution imaging of fuel sprays from various injector nozzles for direct injection engines. Technical Report EPA/AA/TDG/94-03, U.S. Environmental Protection Agency, September 1994.

APPENDICES

Appendix A

Axial and Radial Velocity, and TKE Plots for Air Jet

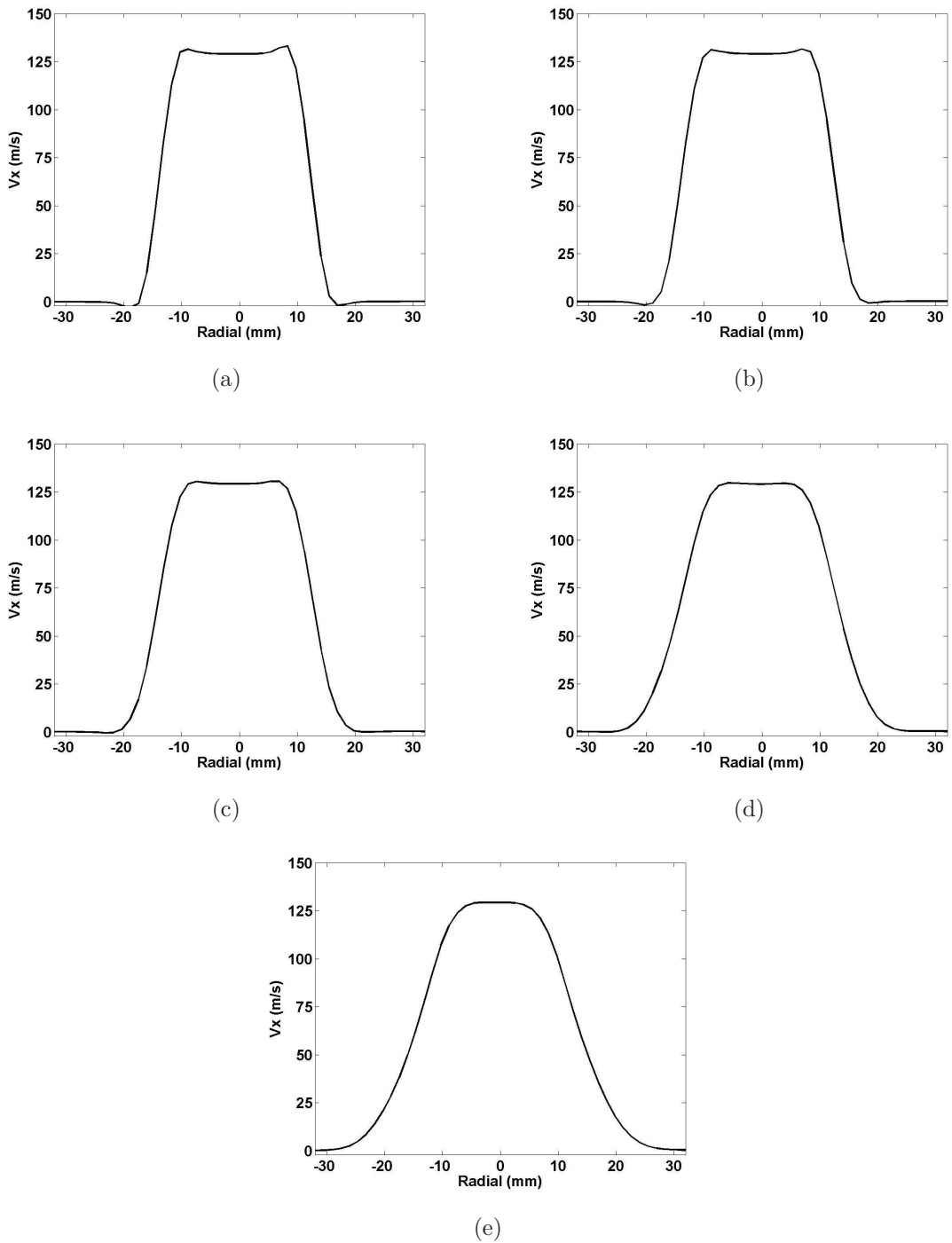


Figure A.1: Axial velocity profiles for $Ma_g = 0.35$ ($U_o=125$ m/s) at locations a) $x/D = 1$, b) $x/D = 1.36$, c) $x/D = 2$, d) $x/D = 3$, e) $x/D = 4$

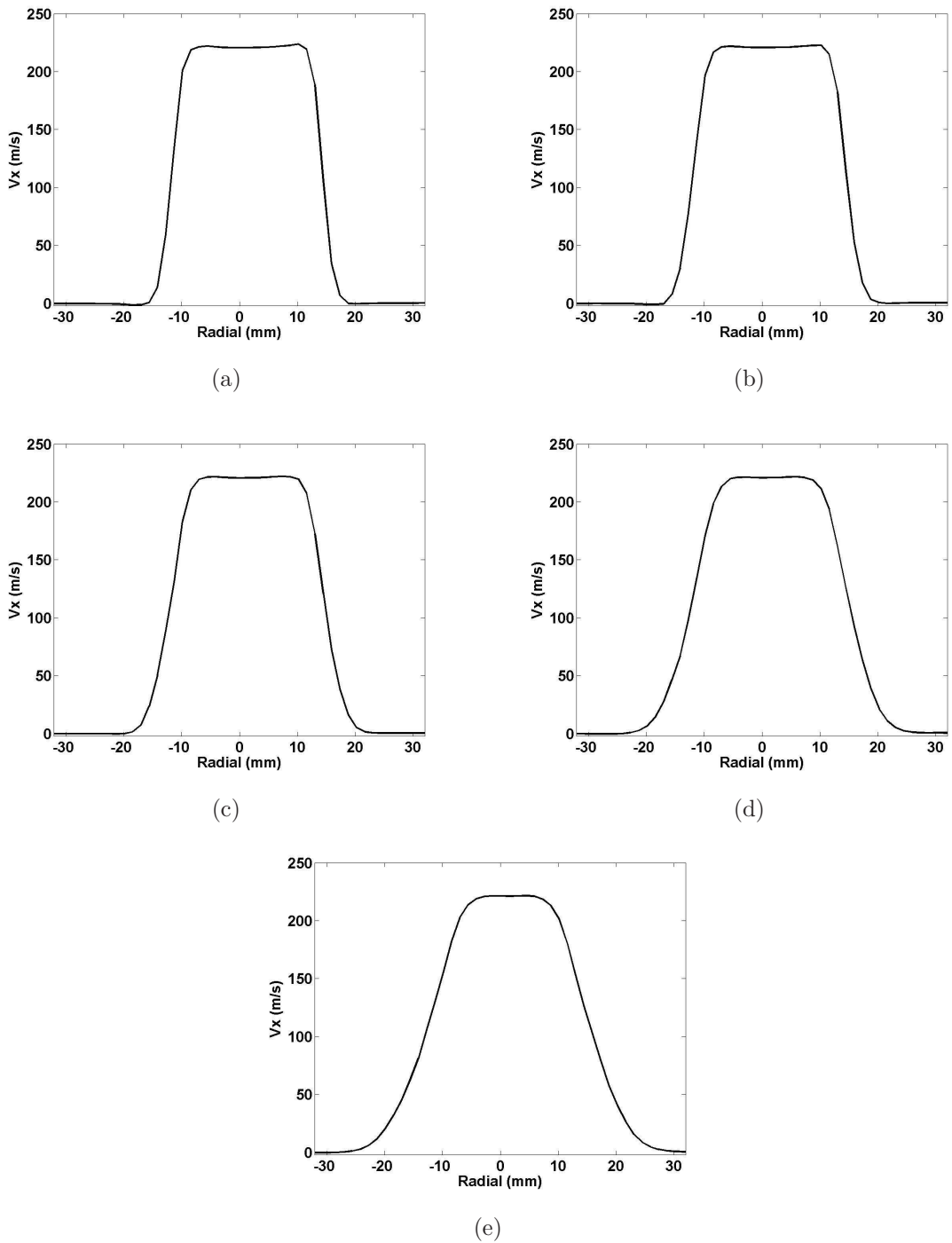


Figure A.2: Axial velocity profiles for $Ma_g = 0.58$ ($U_o=215$ m/s) at locations a) $x/D = 1$, b) $x/D = 1.36$, c) $x/D = 2$, d) $x/D = 3$, e) $x/D = 4$

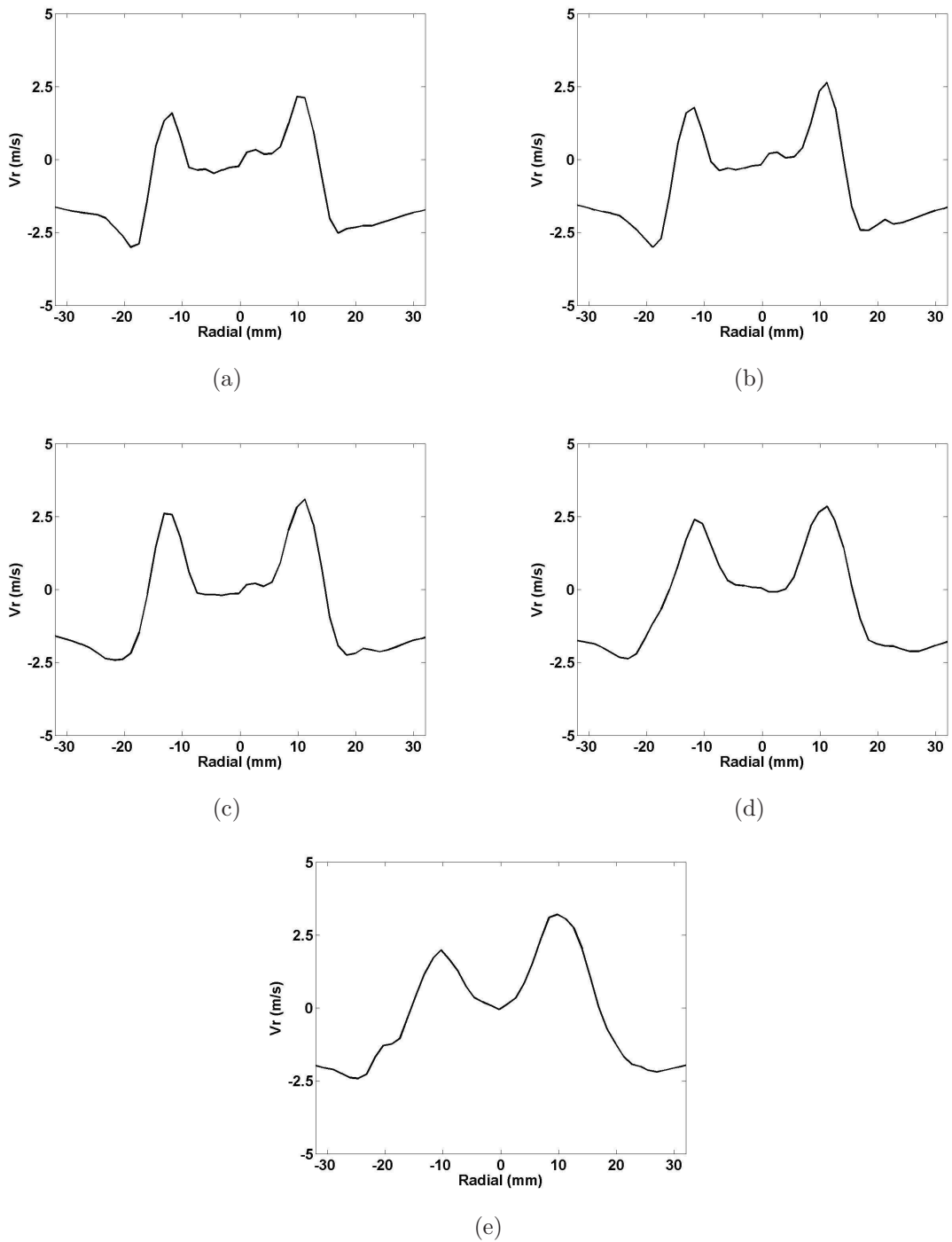


Figure A.3: Radial velocity profiles for $Ma_g = 0.35$ ($U_o=125$ m/s) at locations a) $x/D = 1$, b) $x/D = 1.36$, c) $x/D = 2$, d) $x/D = 3$, e) $x/D = 4$

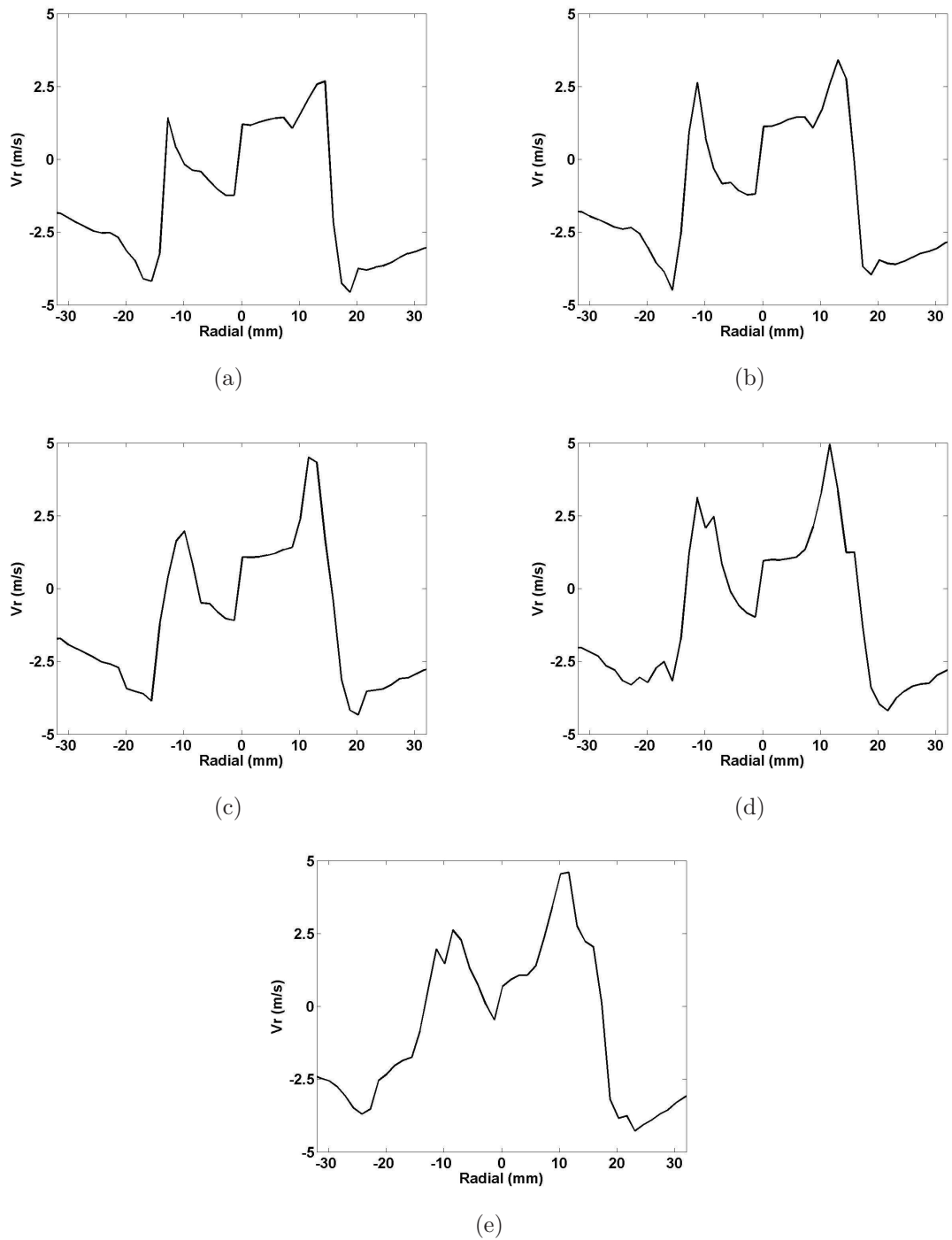


Figure A.4: Radial velocity profiles for $Ma_g = 0.58$ ($U_o=215$ m/s) at locations a) $x/D = 1$, b) $x/D = 1.36$, c) $x/D = 2$, d) $x/D = 3$, e) $x/D = 4$

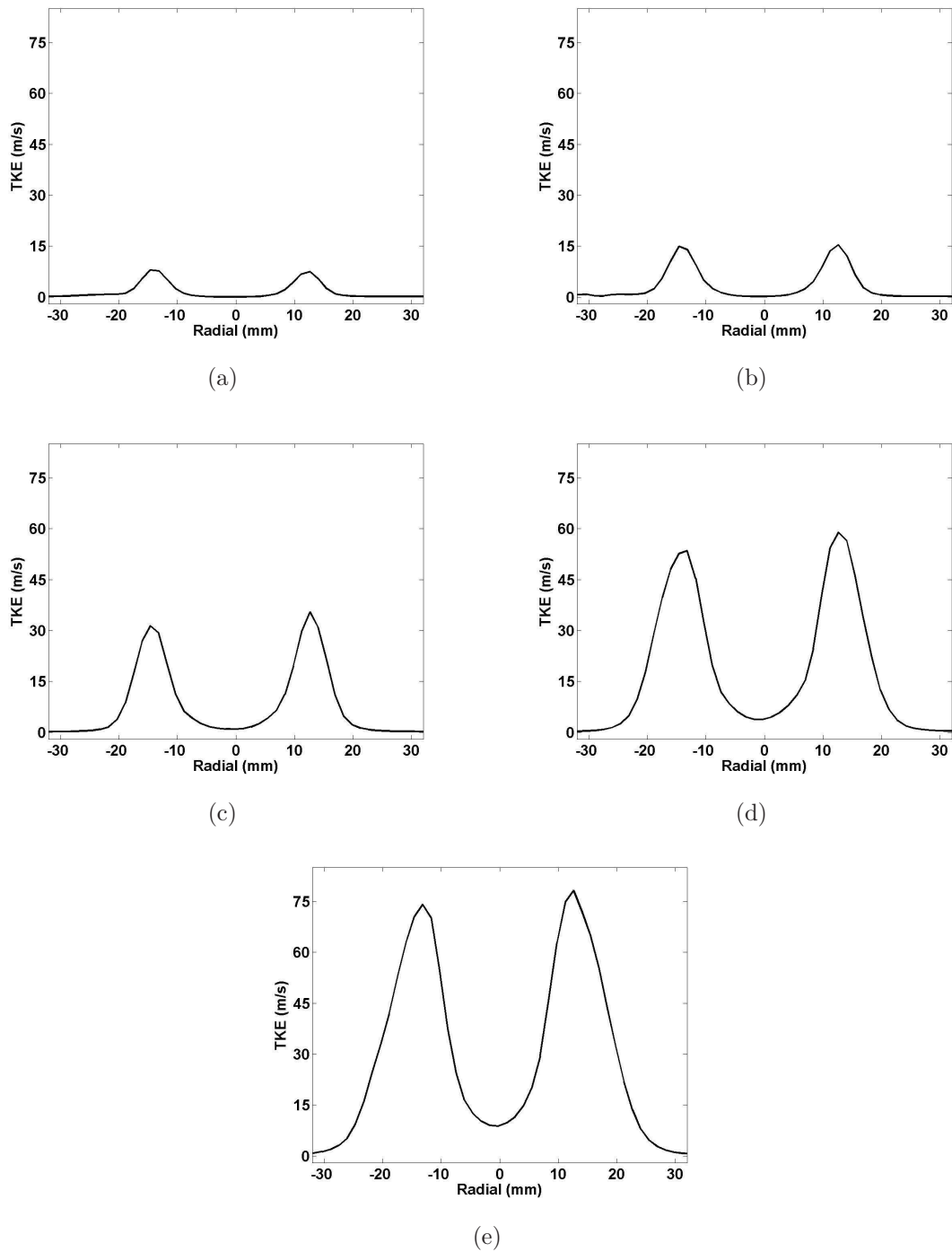


Figure A.5: Turbulent kinetic energy profiles for $Ma_g = 0.35$ ($U_o=125$ m/s) at locations a) $x/D = 1$, b) $x/D = 1.36$, c) $x/D = 2$, d) $x/D = 3$, e) $x/D = 4$

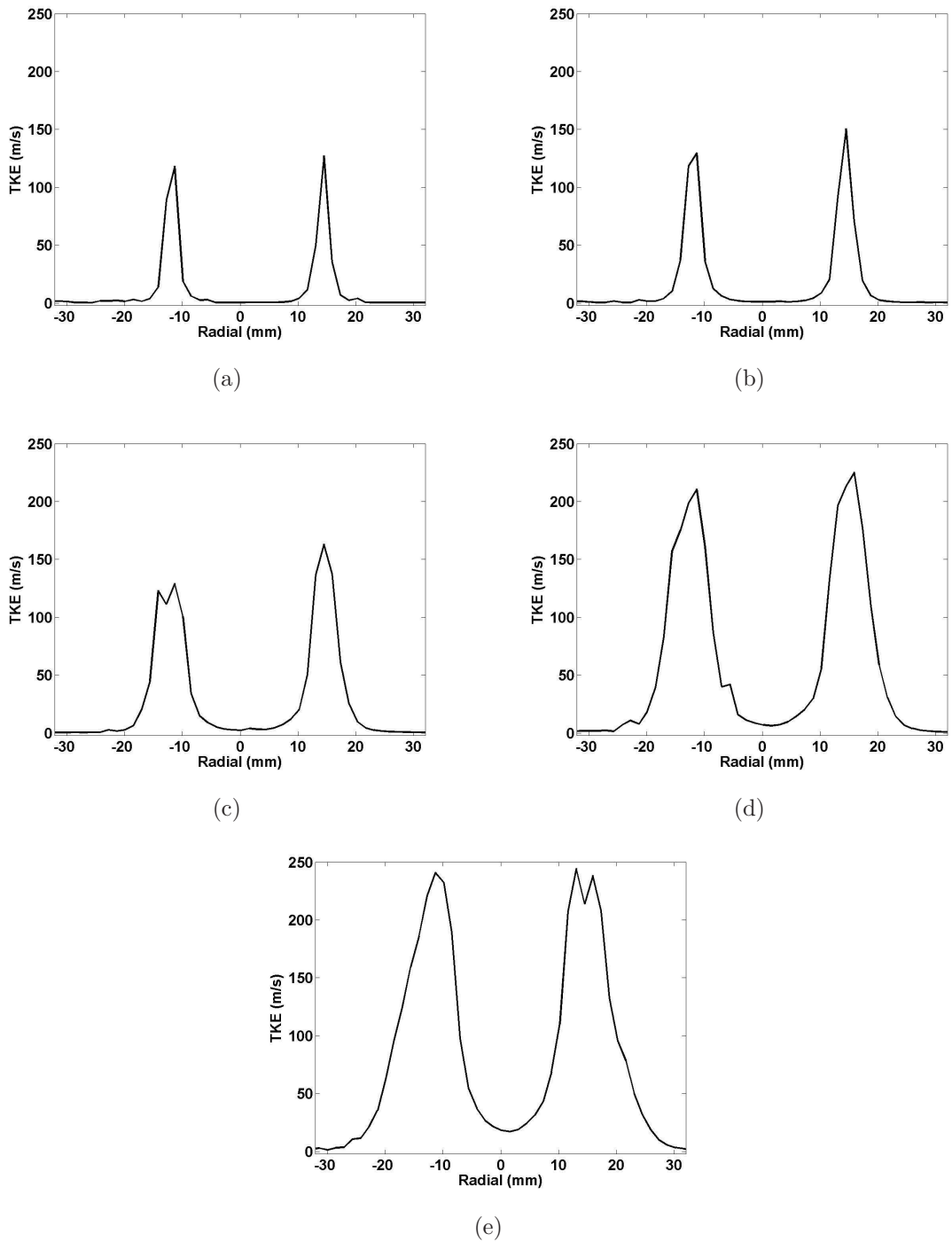
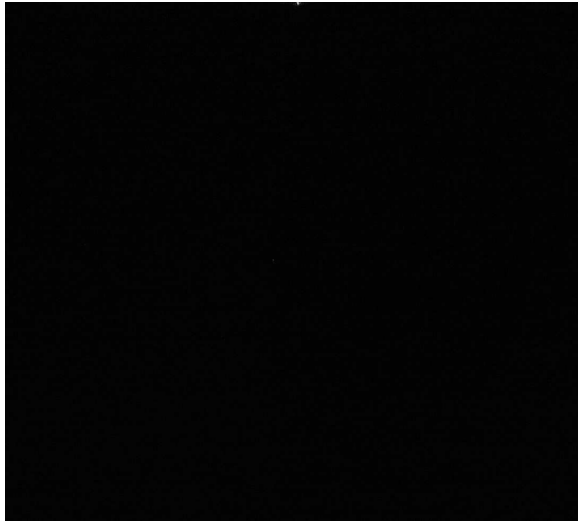


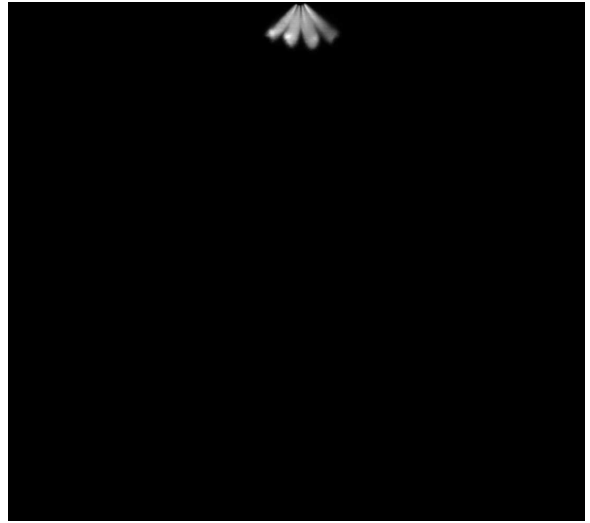
Figure A.6: Turbulent kinetic energy profiles for $Ma_g = 0.58$ ($U_o=215$ m/s) at locations a) $x/D = 1$, b) $x/D = 1.36$, c) $x/D = 2$, d) $x/D = 3$, e) $x/D = 4$

Appendix B

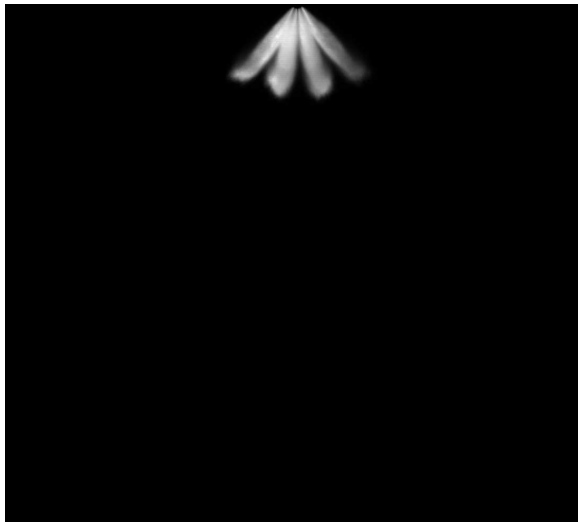
Images of Temporal Evolution of Quiescent Sprays



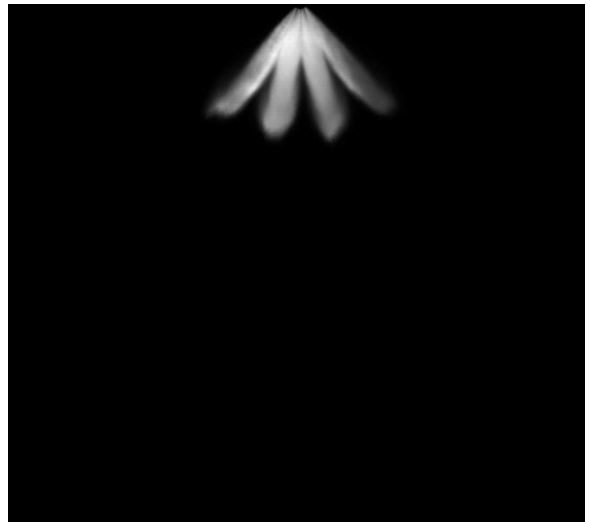
(a) 0.0ms



(b) 0.1ms

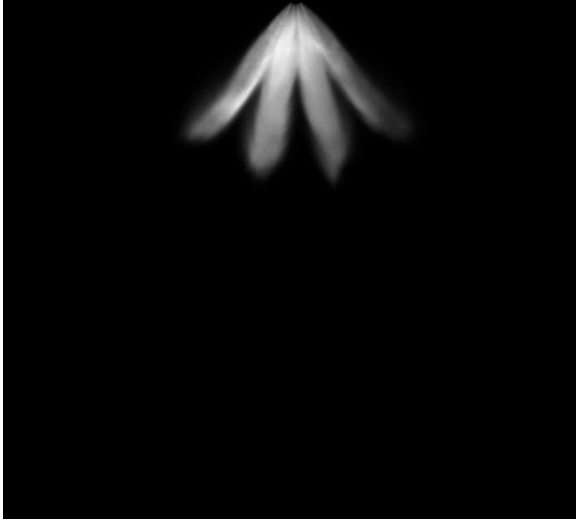


(c) 0.2ms



(d) 0.3ms

Figure B.1: 10MPa spray development in quiescent conditions corresponding to 0.1ms increments from 0.0 ms after SOF to 0.3 ms after SOF



(e) 0.4ms



(f) 0.5ms



(g) 0.6ms

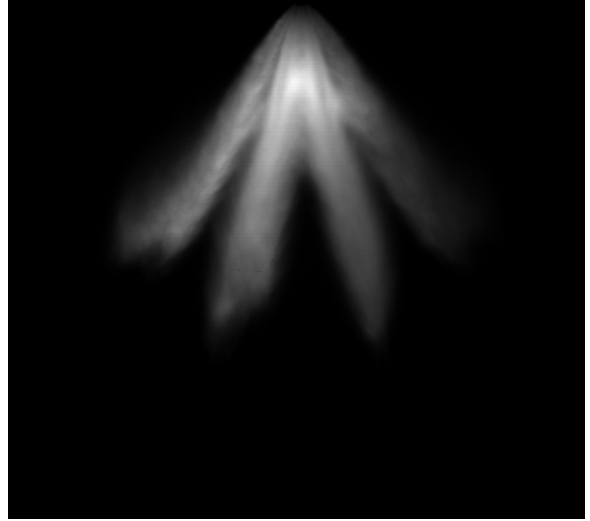


(h) 0.7ms

Figure B.1: 10MPa spray development in quiescent conditions corresponding to 0.1ms increments from 0.4 ms after SOF to 0.7 ms after SOF



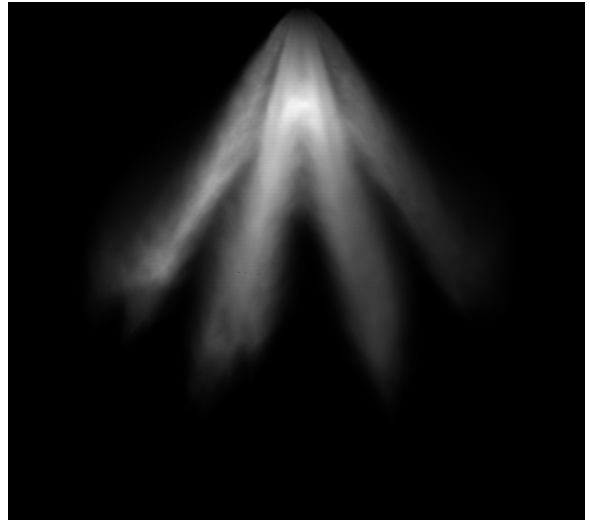
(i) 0.8ms



(j) 0.9ms



(k) 1.0ms

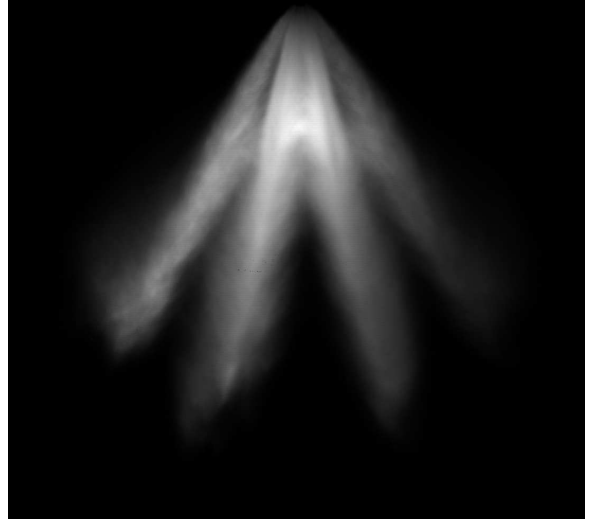


(l) 1.1ms

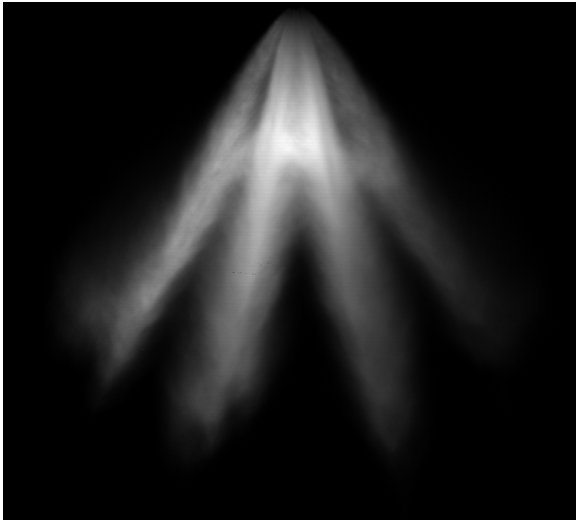
Figure B.1: 10MPa spray development in quiescent conditions corresponding to 0.1ms increments from 0.8 ms after SOF to 1.1 ms after SOF



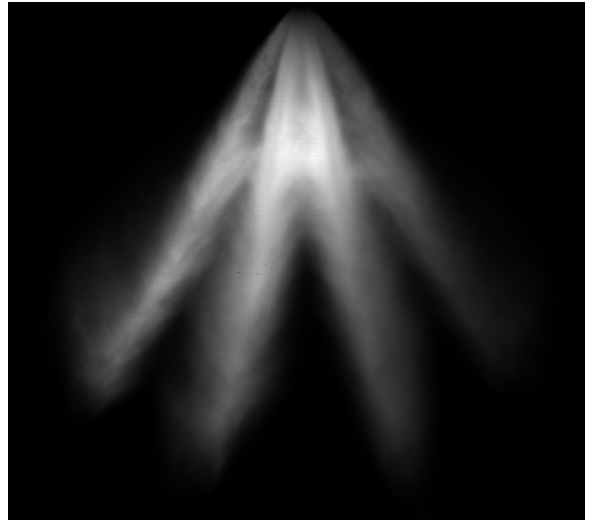
(m) 1.2ms



(n) 1.3ms

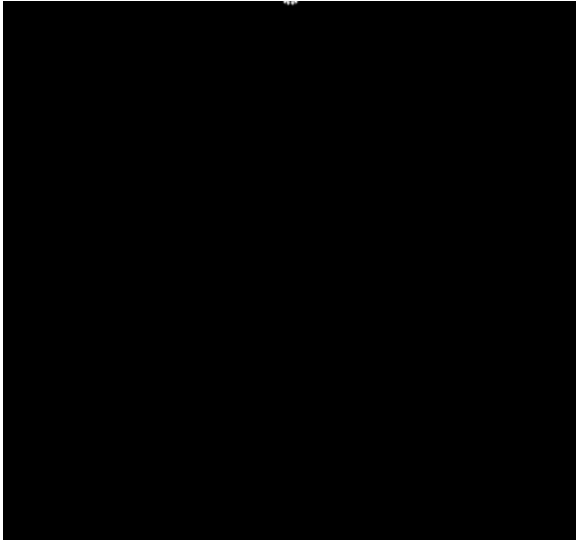


(o) 1.4ms

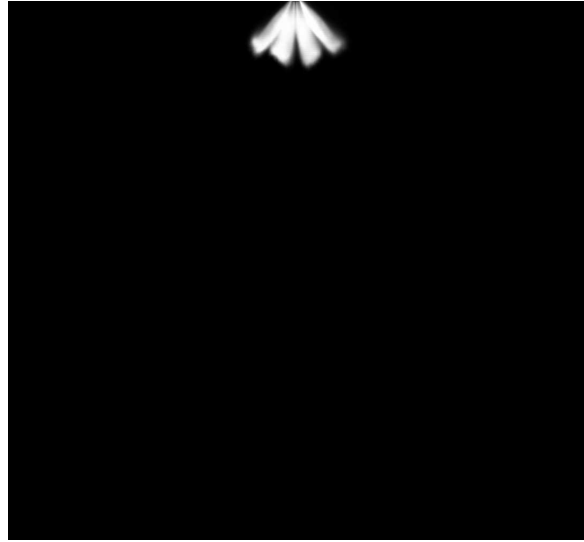


(p) 1.5ms

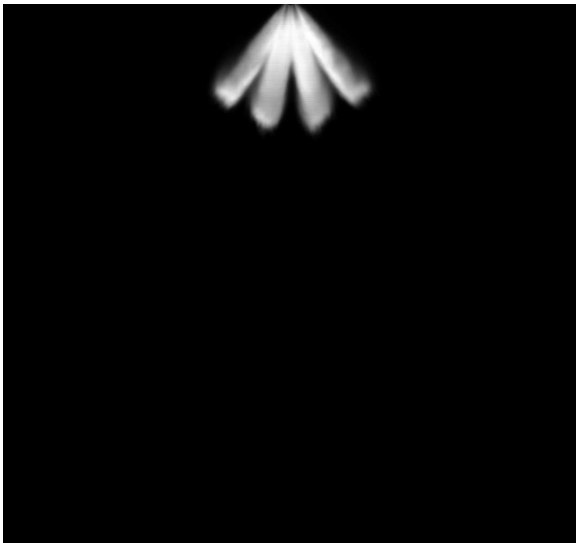
Figure B.1: 10MPa spray development in quiescent conditions corresponding to 0.1ms increments from 1.2 ms after SOF to 1.5 ms after SOF



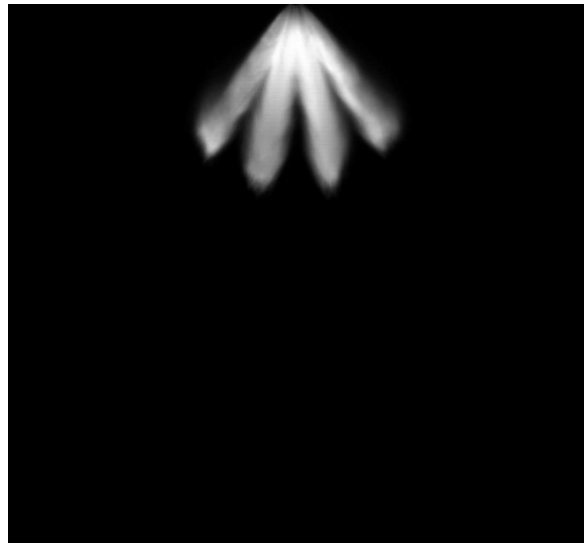
(a) 0.0ms



(b) 0.1ms

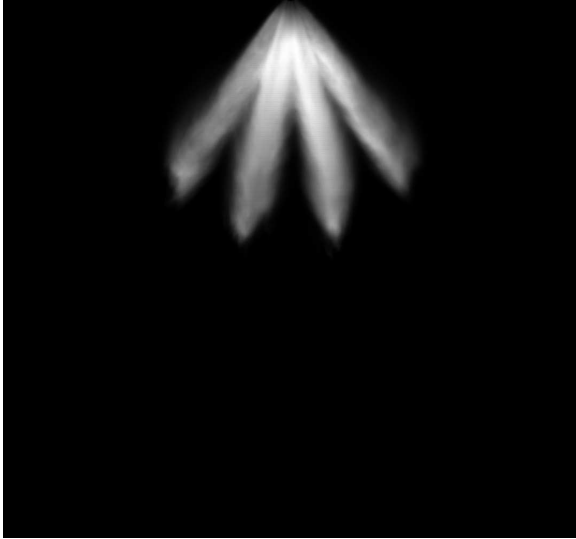


(c) 0.2ms



(d) 0.3ms

Figure B.2: 15MPa spray development in quiescent conditions corresponding to 0.1ms increments from 0.0 ms after SOF to 0.3 ms after SOF



(e) 0.4ms



(f) 0.5ms



(g) 0.6ms



(h) 0.7ms

Figure B.2: 15MPa spray development in quiescent conditions corresponding to 0.1ms increments from 0.4 ms after SOF to 0.7 ms after SOF



(i) 0.8ms



(j) 0.9ms

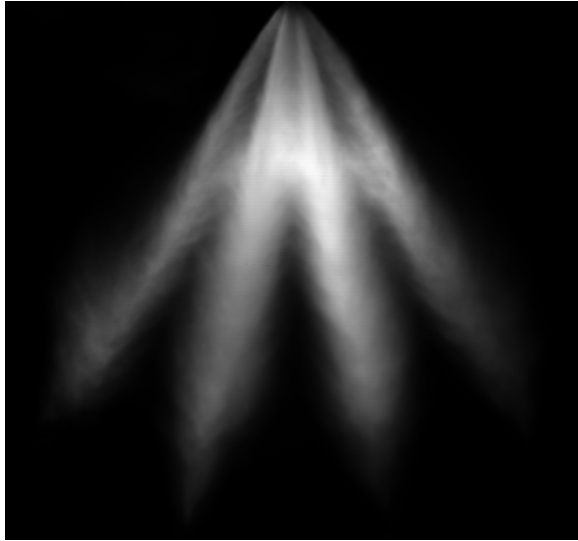


(k) 1.0ms



(l) 1.1ms

Figure B.2: 15MPa spray development in quiescent conditions corresponding to 0.1ms increments from 0.8 ms after SOF to 1.1 ms after SOF



(m) 1.2ms



(n) 1.3ms



(o) 1.4ms

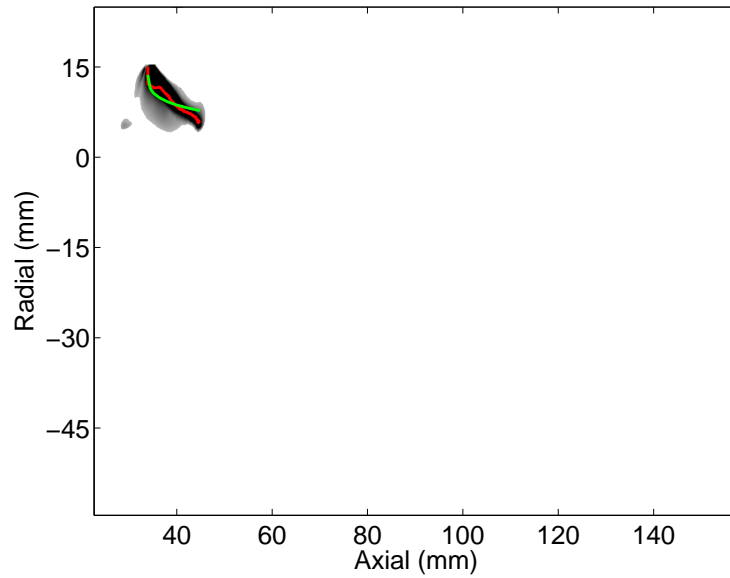


(p) 1.5ms

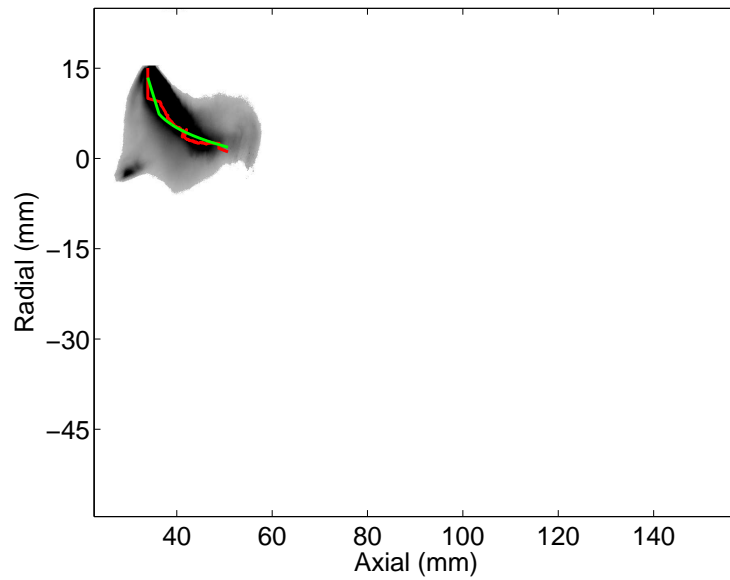
Figure B.2: 15MPa spray development in quiescent conditions corresponding to 0.1ms increments from 1.2 ms after SOF to 1.5 ms after SOF

Appendix C

Images of Spray Axis and Raw Data for Sprays into Cross-flows

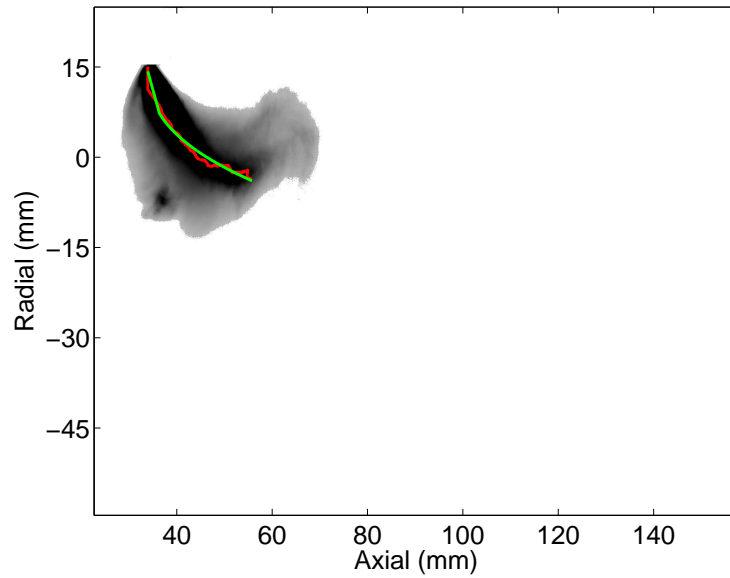


(a) 0.1ms

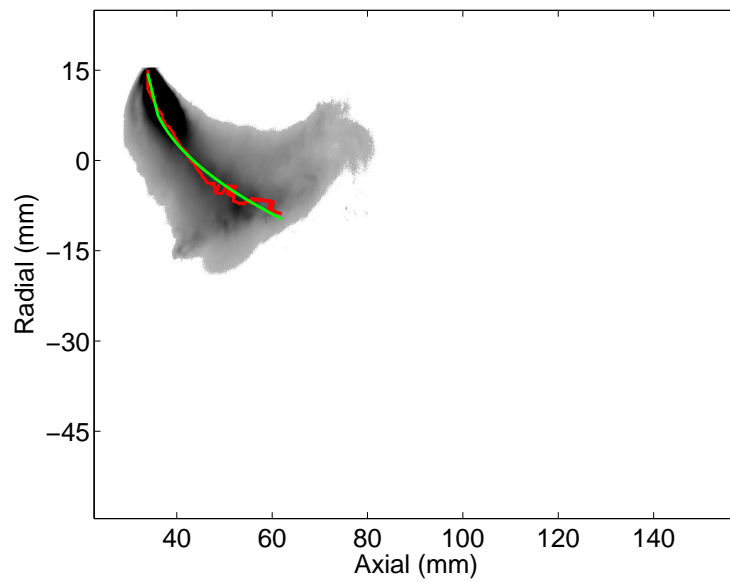


(b) 0.2ms

Figure C.1: Development of 15MPa fuel spray into $Ma_g = 0.35$ cross-flow conditions in 0.1 ms increments from 0.1 ms after SOF to 0.2 ms after SOF, corresponding to $q = 991$, $We_l = 2.1 \times 10^5$, and $We_g = 213$. Red line represents raw bend axis data, and the green line represents the curve fit.

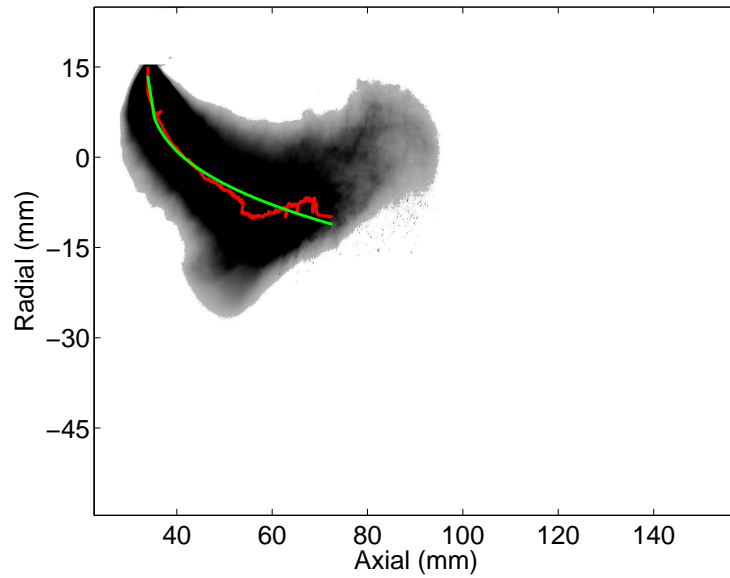


(c) 0.3ms

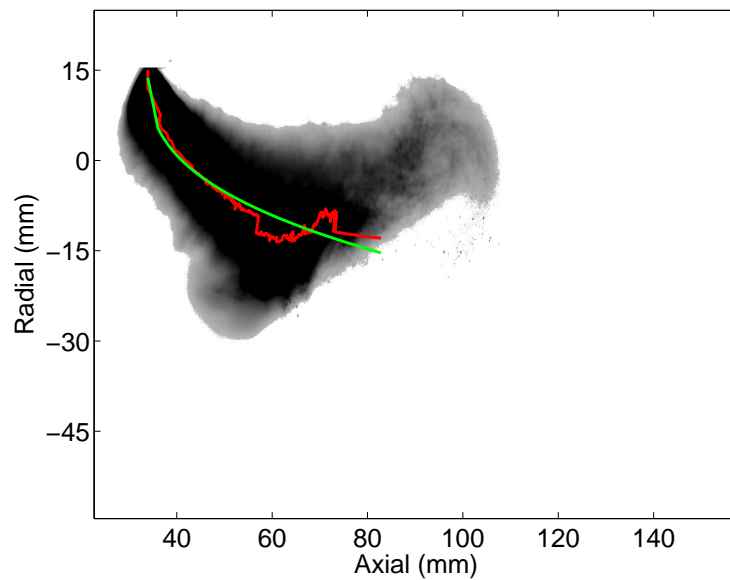


(d) 0.4ms

Figure C.1: Development of 15MPa fuel spray into $Ma_g = 0.35$ cross-flow conditions in 0.1 ms increments from 0.3 ms after SOF to 0.4 ms after SOF, corresponding to $q = 991$, $We_l = 2.1 \times 10^5$, and $We_g = 213$. Red line represents raw bend axis data, and the green line represents the curve fit.

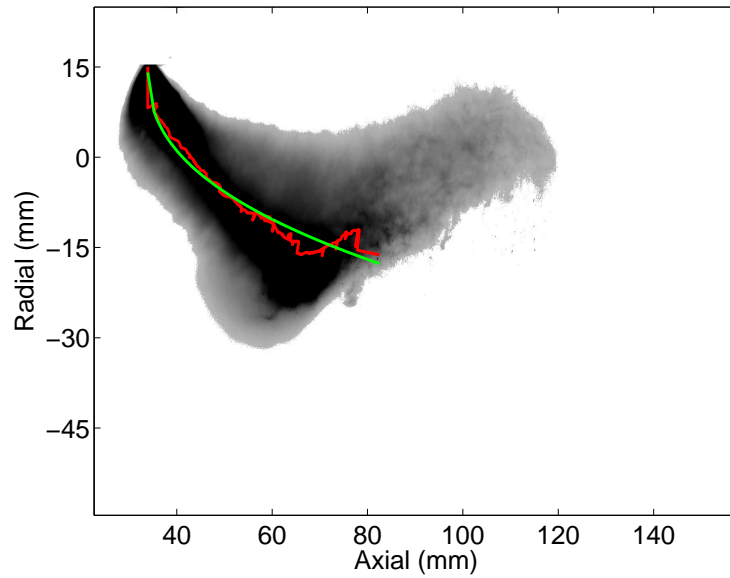


(e) 0.5ms

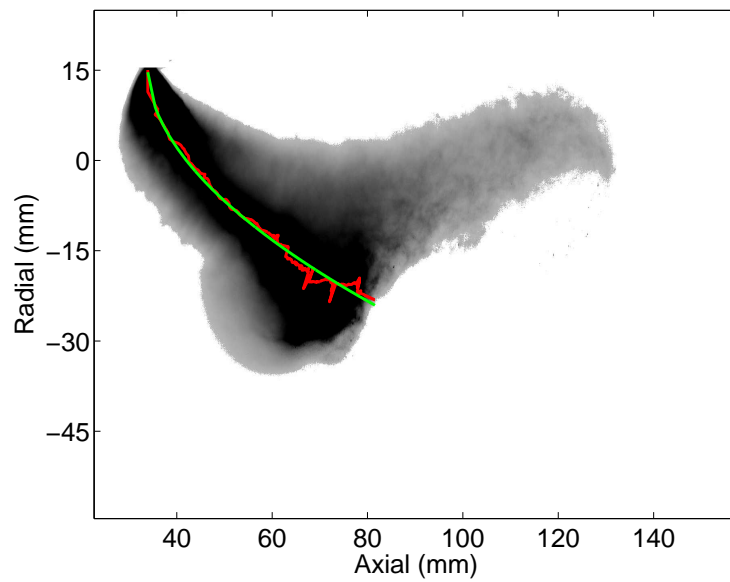


(f) 0.6ms

Figure C.1: Development of 15MPa fuel spray into $Ma_g = 0.35$ cross-flow conditions in 0.1 ms increments from 0.5 ms after SOF to 0.6 ms after SOF, corresponding to $q = 991$, $We_l = 2.1 \times 10^5$, and $We_g = 213$. Red line represents raw bend axis data, and the green line represents the curve fit.

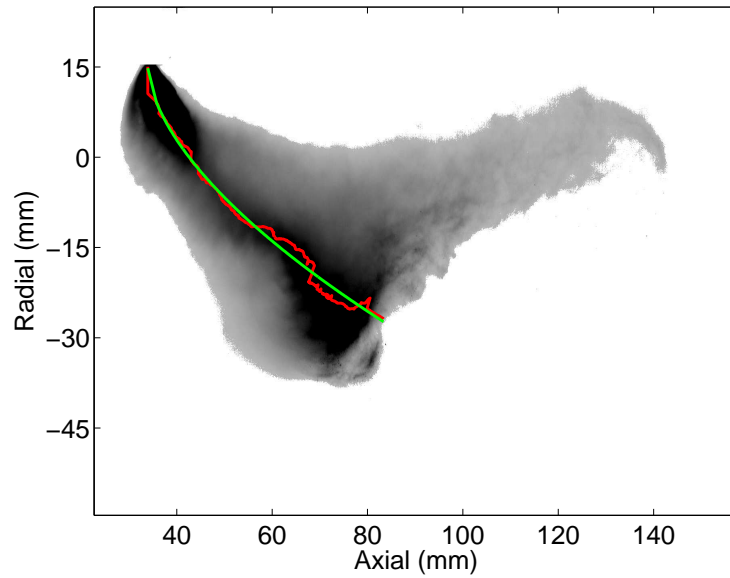


(g) 0.7ms

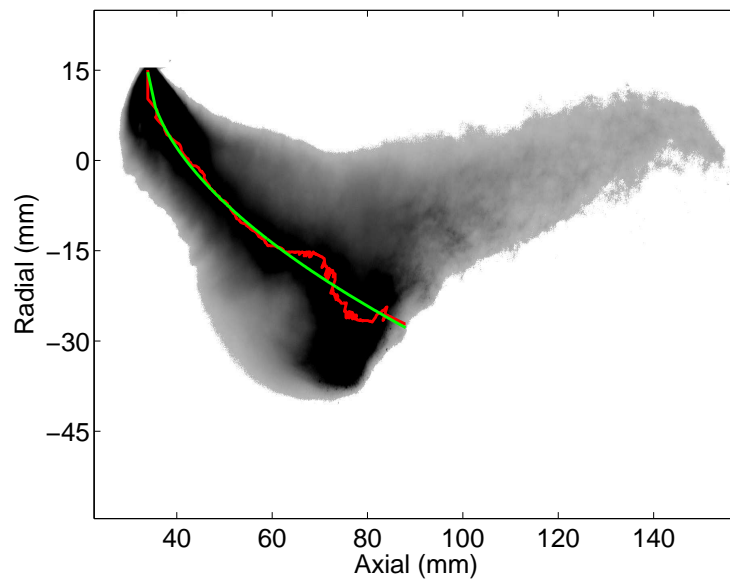


(h) 0.8ms

Figure C.1: Development of 15MPa fuel spray into $Ma_g = 0.35$ cross-flow conditions in 0.1 ms increments from 0.7 ms after SOF to 0.8 ms after SOF, corresponding to $q = 991$, $We_l = 2.1 \times 10^5$, and $We_g = 213$. Red line represents raw bend axis data, and the green line represents the curve fit.

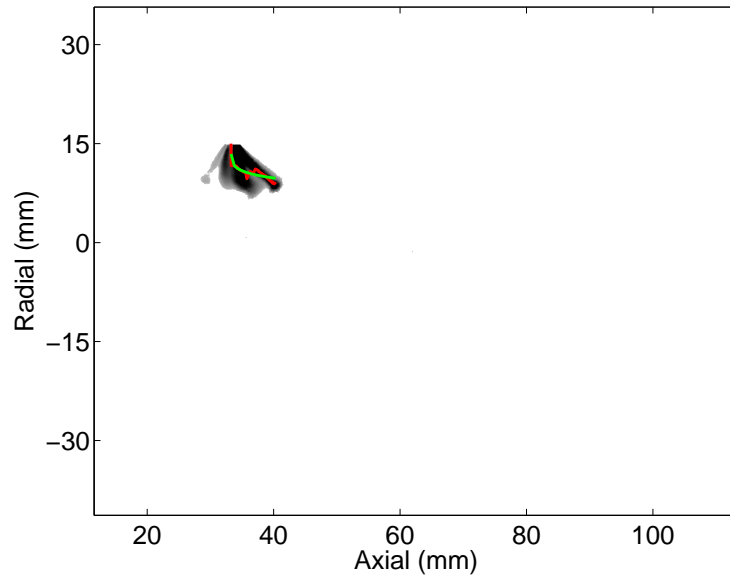


(i) 0.9ms

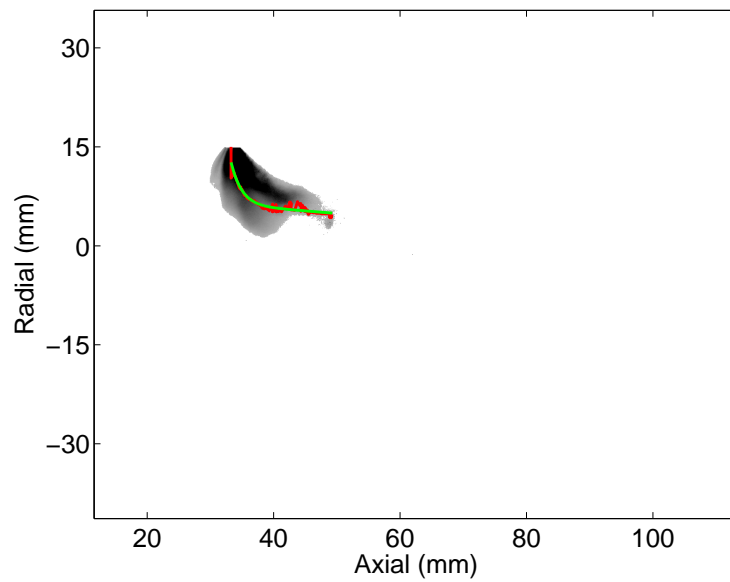


(j) 1.0ms

Figure C.1: Development of 15MPa fuel spray into $Ma_g = 0.35$ cross-flow conditions in 0.1 ms increments from 0.9 ms after SOF to 1.0 ms after SOF, corresponding to $q = 991$, $We_l = 2.1 \times 10^5$, and $We_g = 213$. Red line represents raw bend axis data, and the green line represents the curve fit.

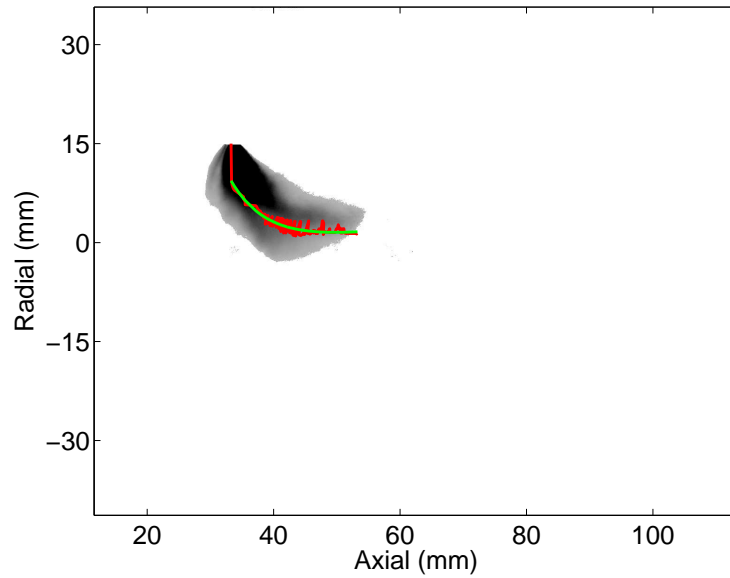


(a) 0.1ms

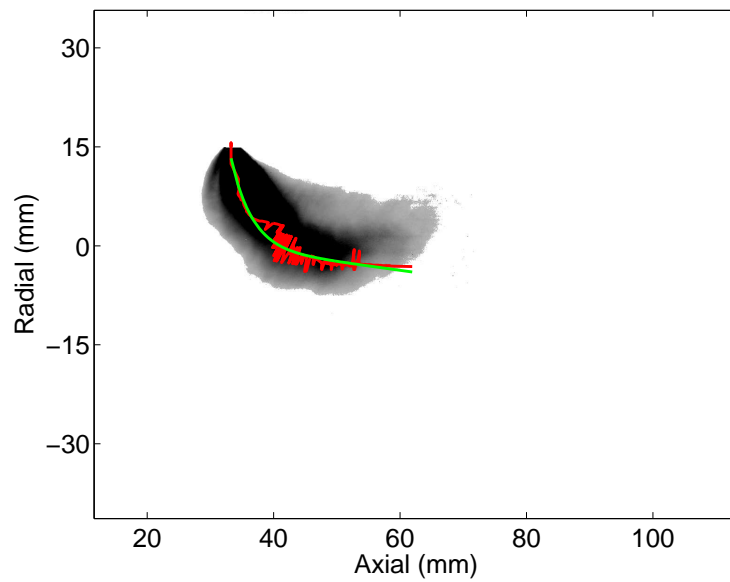


(b) 0.2ms

Figure C.2: Development of 10MPa fuel spray into $Ma_g = 0.35$ cross-flow conditions in 0.1 ms increments from 0.1 ms after SOF to 0.2 ms after SOF, corresponding to $q = 665$, $We_l = 1.4 \times 10^5$, and $We_g = 213$. Red line represents raw bend axis data, and the green line represents the curve fit.

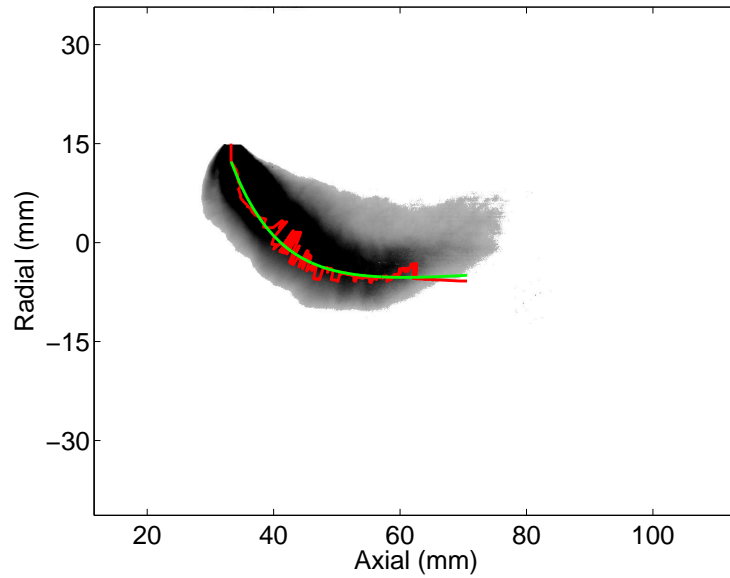


(c) 0.3ms

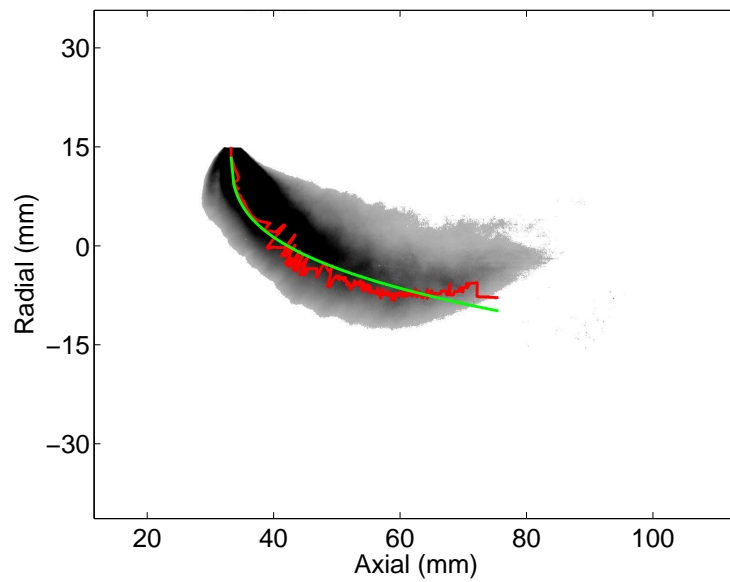


(d) 0.4ms

Figure C.2: Development of 10MPa fuel spray into $Ma_g = 0.35$ cross-flow conditions in 0.1 ms increments from 0.3 ms after SOF to 0.4 ms after SOF, corresponding to $q = 665$, $We_l = 1.4 \times 10^5$, and $We_g = 213$. Red line represents raw bend axis data, and the green line represents the curve fit.

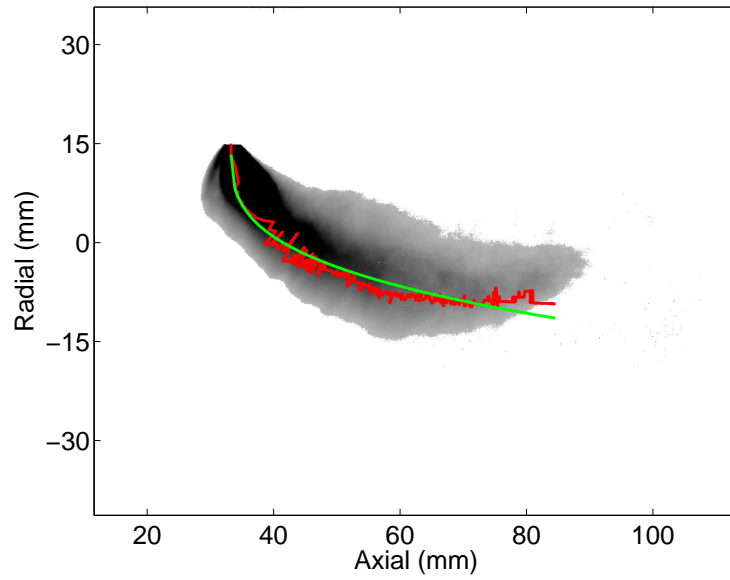


(e) 0.5ms

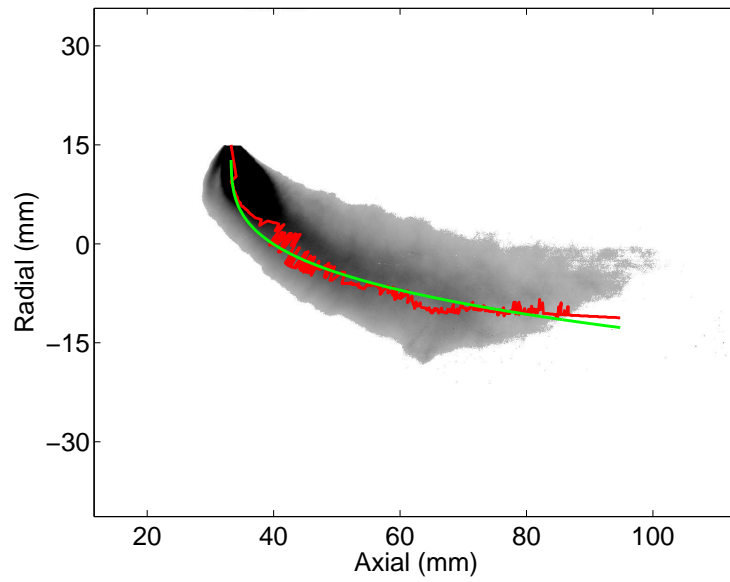


(f) 0.6ms

Figure C.2: Development of 10MPa fuel spray into $Ma_g = 0.35$ cross-flow conditions in 0.1 ms increments from 0.5 ms after SOF to 0.6 ms after SOF, corresponding to $q = 665$, $We_l = 1.4 \times 10^5$, and $We_g = 213$. Red line represents raw bend axis data, and the green line represents the curve fit.

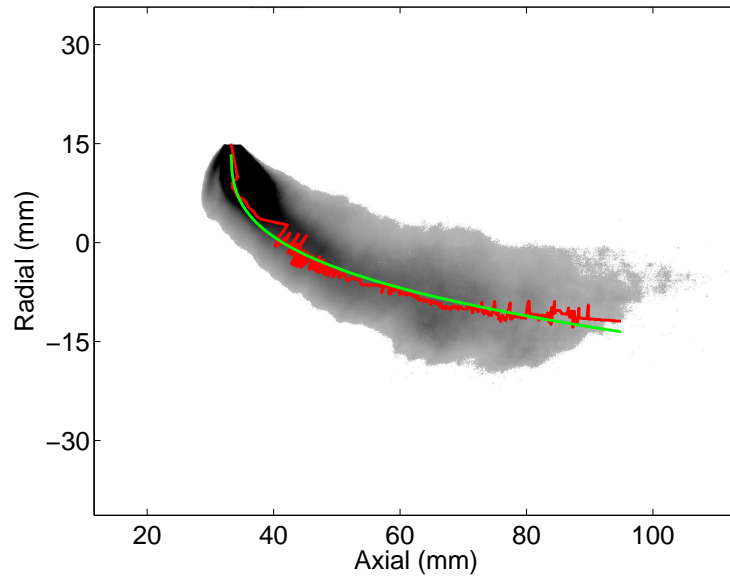


(g) 0.7ms

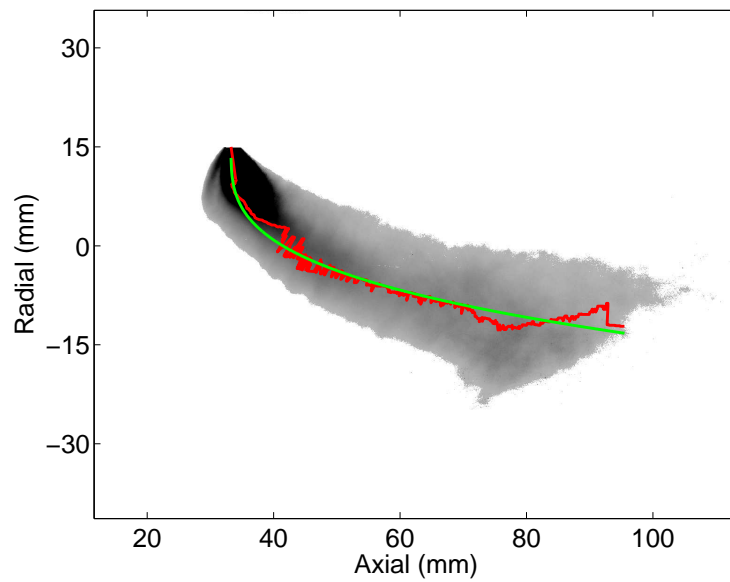


(h) 0.8ms

Figure C.2: Development of 10MPa fuel spray into $Ma_g = 0.35$ cross-flow conditions in 0.1 ms increments from 0.7 ms after SOF to 0.8 ms after SOF, corresponding to $q = 665$, $We_l = 1.4 \times 10^5$, and $We_g = 213$. Red line represents raw bend axis data, and the green line represents the curve fit.

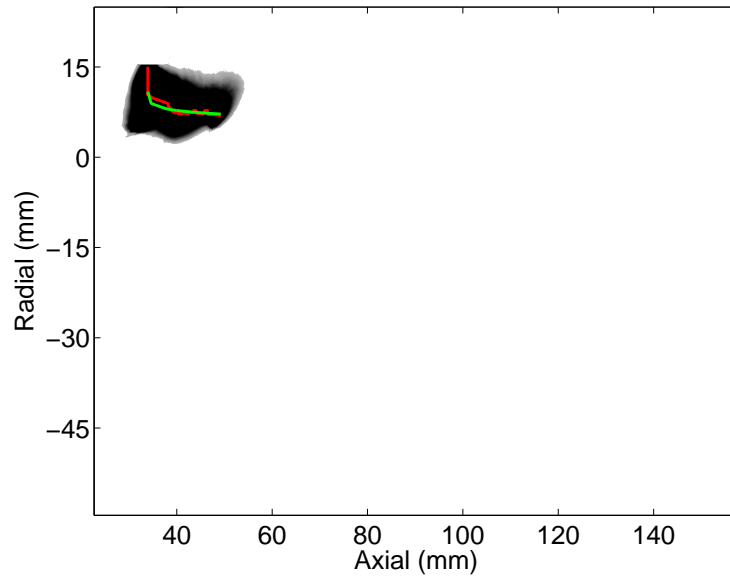


(i) 0.9ms

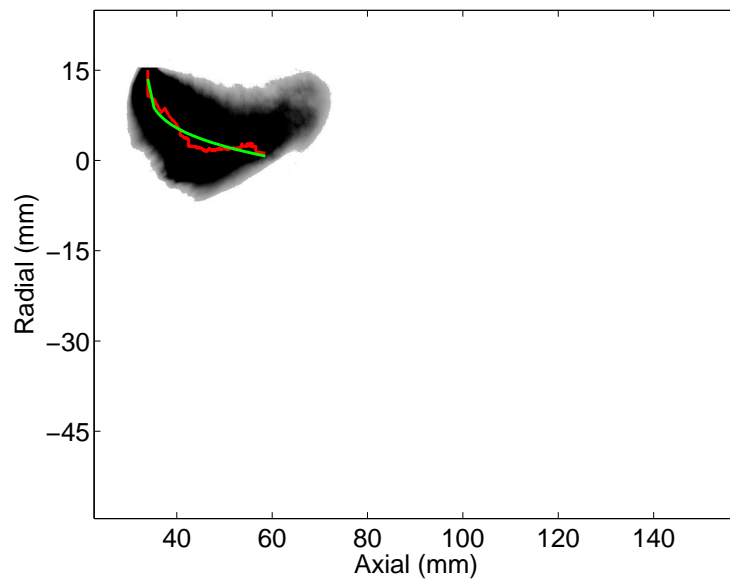


(j) 1.0ms

Figure C.2: Development of 10MPa fuel spray into $Ma_g = 0.35$ cross-flow conditions in 0.1 ms increments from 0.9 ms after SOF to 1.0 ms after SOF, corresponding to $q = 665$, $We_l = 1.4 \times 10^5$, and $We_g = 213$. Red line represents raw bend axis data, and the green line represents the curve fit.

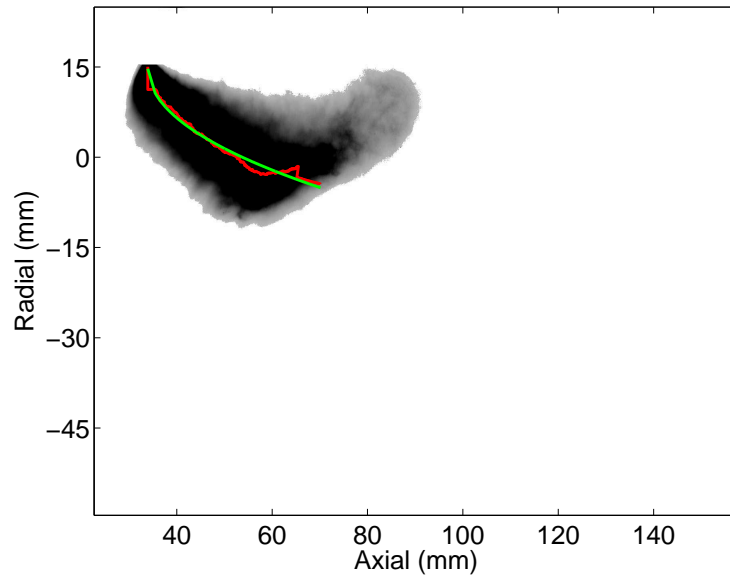


(a) 0.1ms

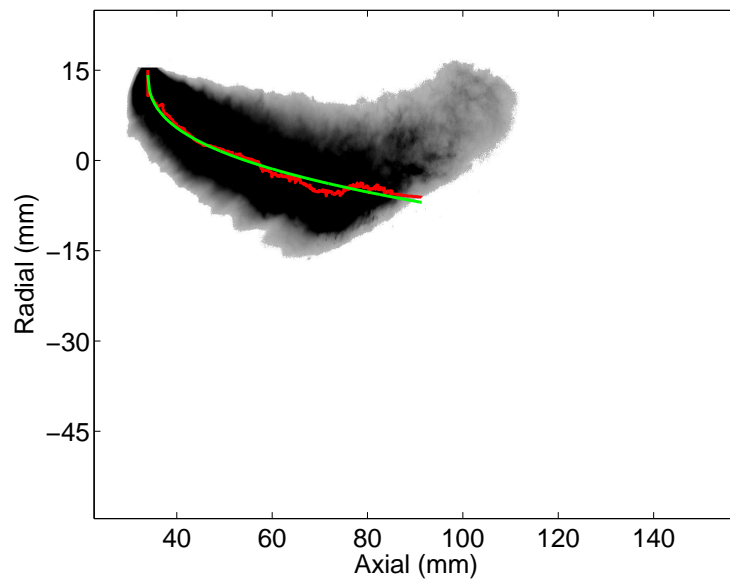


(b) 0.2ms

Figure C.3: Development of 15MPa fuel spray into $Ma_g = 0.58$ cross-flow conditions in 0.1 ms increments from 0.1 ms after SOF to 0.2 ms after SOF, corresponding to $q = 371$, $We_l = 2.3 \times 10^5$, and $We_g = 617$. Red line represents raw bend axis data, and the green line represents the curve fit.

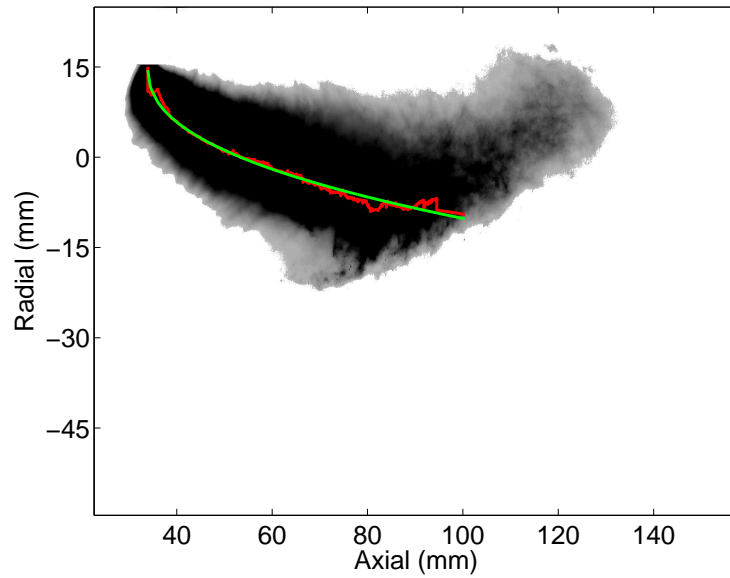


(c) 0.3ms

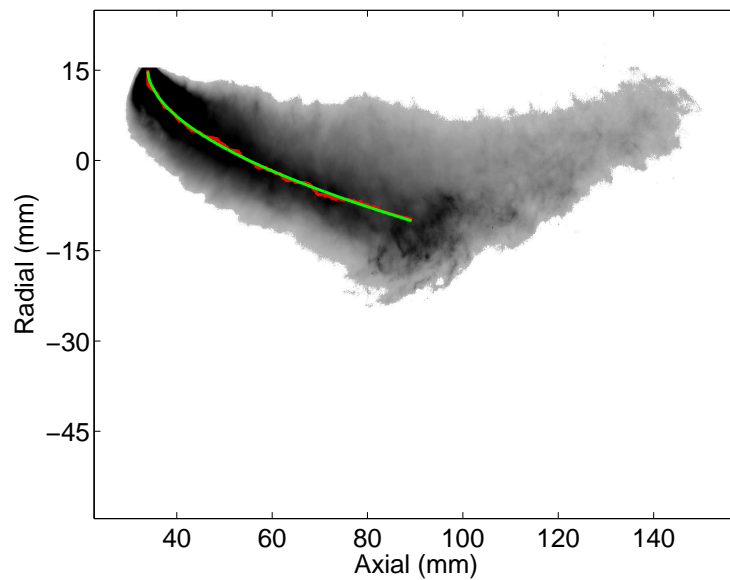


(d) 0.4ms

Figure C.3: Development of 15MPa fuel spray into $Ma_g = 0.58$ cross-flow conditions in 0.1 ms increments from 0.3 ms after SOF to 0.4 ms after SOF, corresponding to $q = 371$, $We_l = 2.3 \times 10^5$, and $We_g = 617$. Red line represents raw bend axis data, and the green line represents the curve fit.

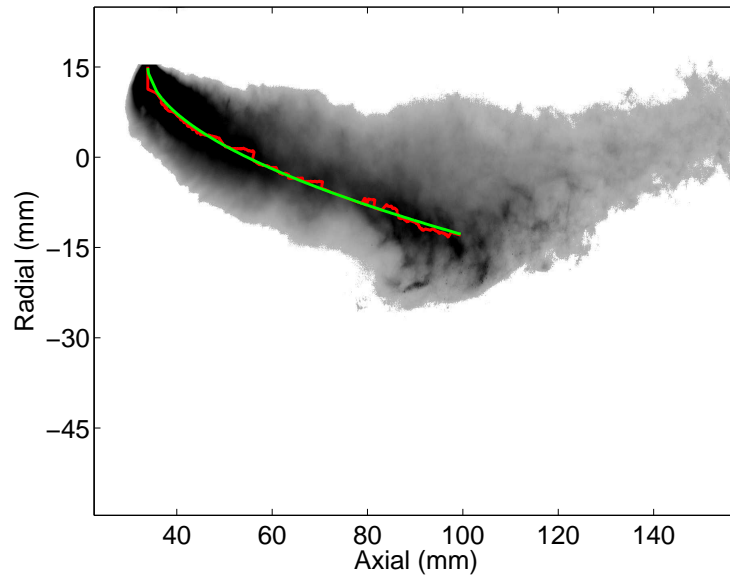


(e) 0.5ms

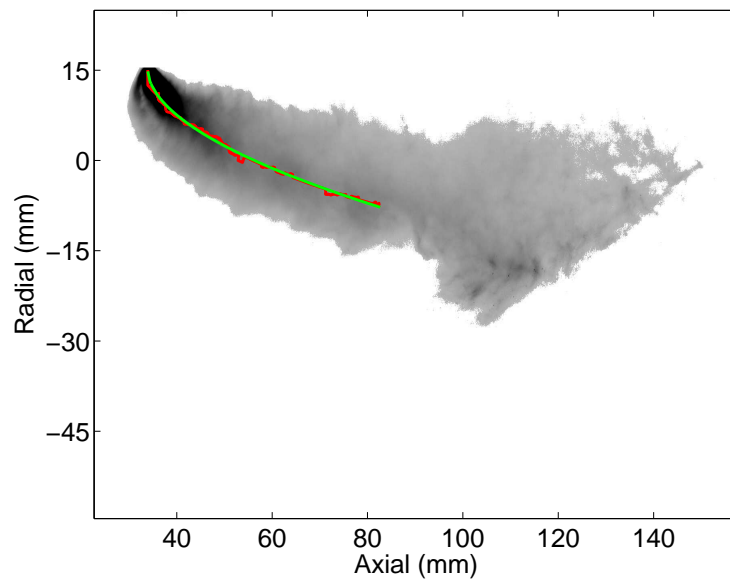


(f) 0.6ms

Figure C.3: Development of 15MPa fuel spray into $Ma_g = 0.58$ cross-flow conditions in 0.1 ms increments from 0.5 ms after SOF to 0.6 ms after SOF, corresponding to $q = 371$, $We_l = 2.3 \times 10^5$, and $We_g = 617$. Red line represents raw bend axis data, and the green line represents the curve fit.

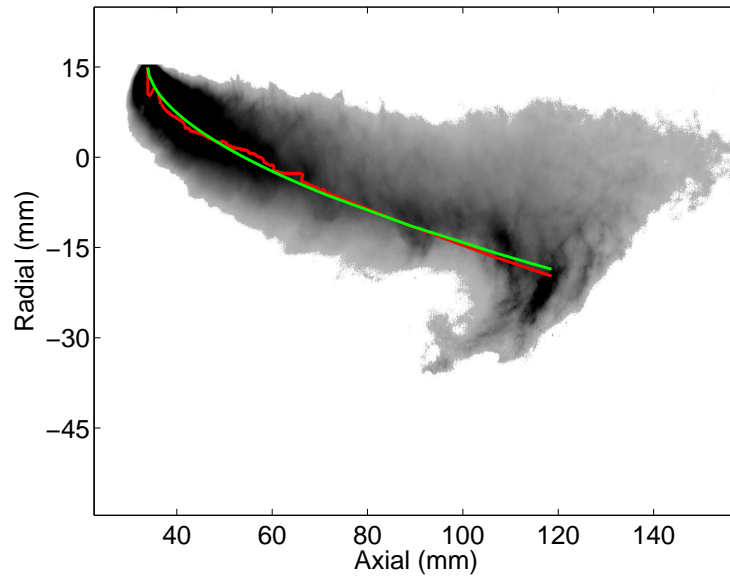


(g) 0.7ms

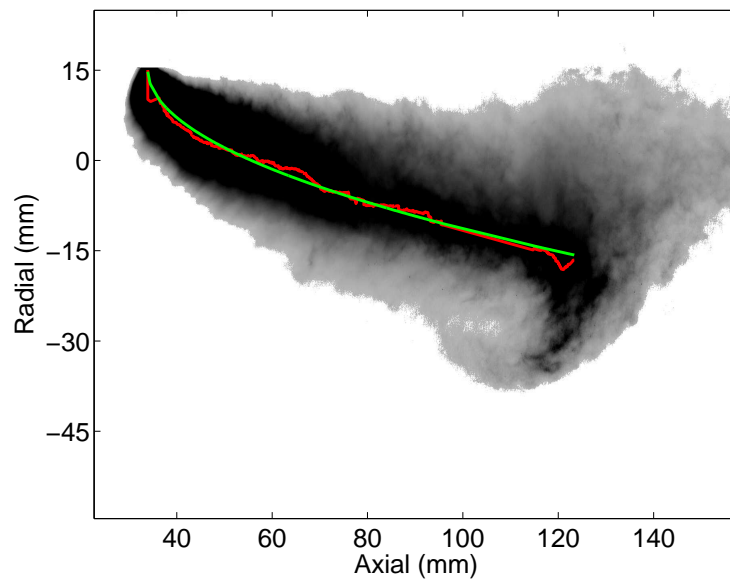


(h) 0.8ms

Figure C.3: Development of 15MPa fuel spray into $Ma_g = 0.58$ cross-flow conditions in 0.1 ms increments from 0.7 ms after SOF to 0.8 ms after SOF, corresponding to $q = 371$, $We_l = 2.3 \times 10^5$, and $We_g = 617$. Red line represents raw bend axis data, and the green line represents the curve fit.

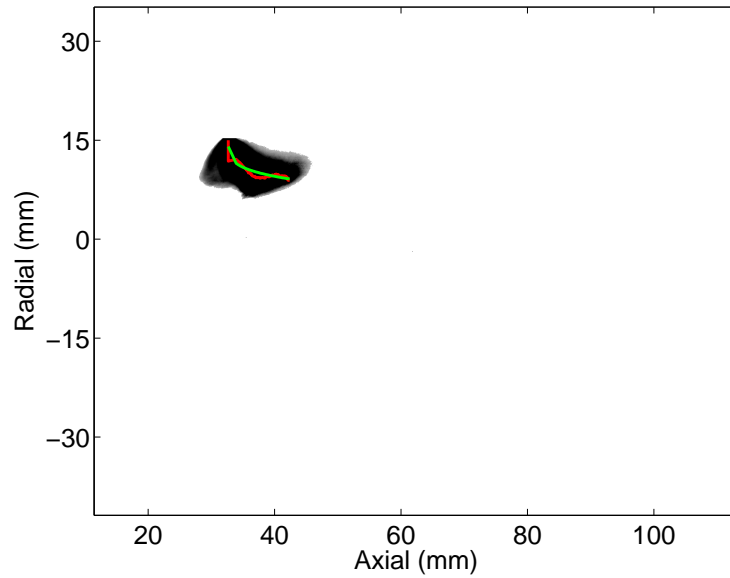


(i) 0.9ms

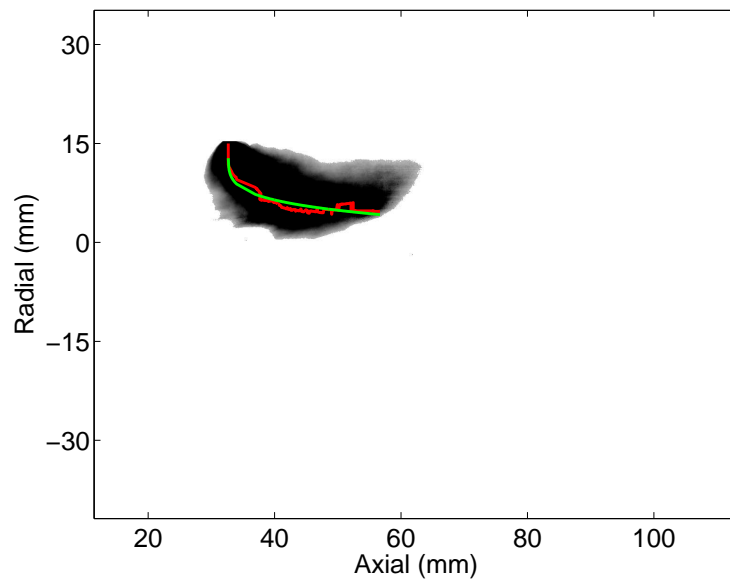


(j) 1.0ms

Figure C.3: Development of 15MPa fuel spray into $Ma_g = 0.58$ cross-flow conditions in 0.1 ms increments from 0.9 ms after SOF to 10 ms after SOF, corresponding to $q = 371$, $We_l = 2.3 \times 10^5$, and $We_g = 617$. Red line represents raw bend axis data, and the green line represents the curve fit.

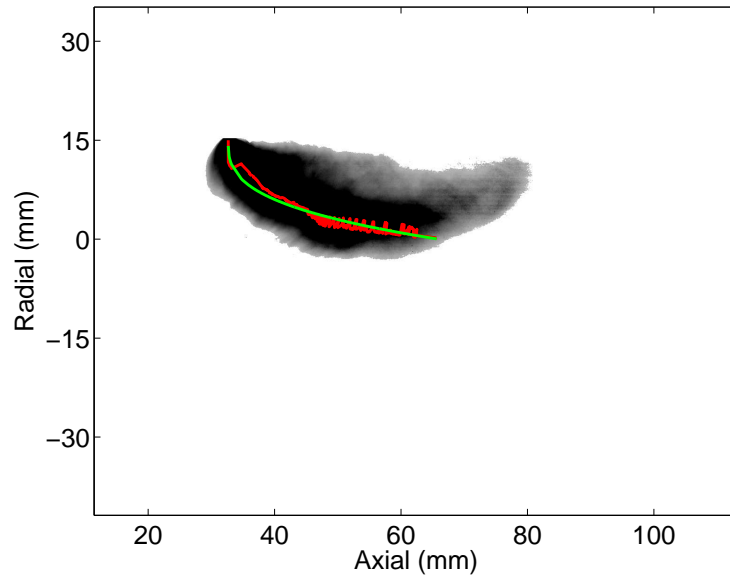


(a) 0.1ms

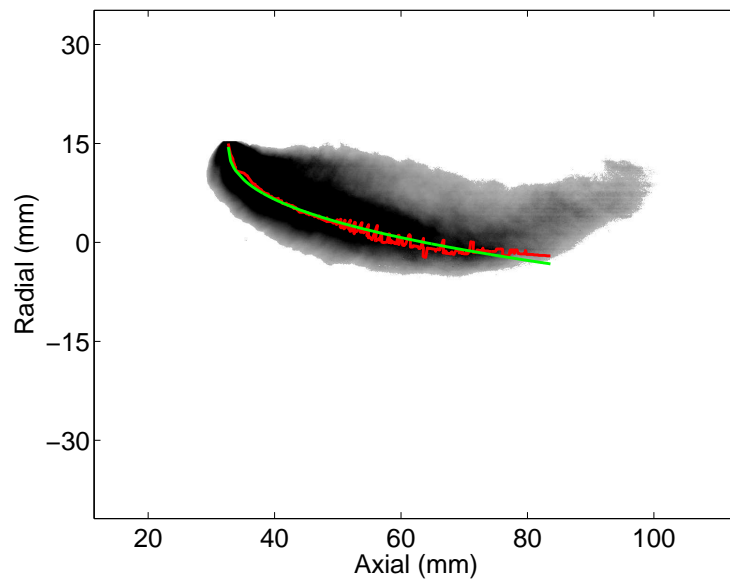


(b) 0.2ms

Figure C.4: Development of 10MPa fuel spray into $Ma_g = 0.58$ cross-flow conditions in 0.1 ms increments from 0.3 ms after SOF to 0.4 ms after SOF, corresponding to $q = 249$, $We_l = 5.79 \times 10^4$, and $We_g = 617$. Red line represents raw bend axis data, and the green line represents the curve fit.

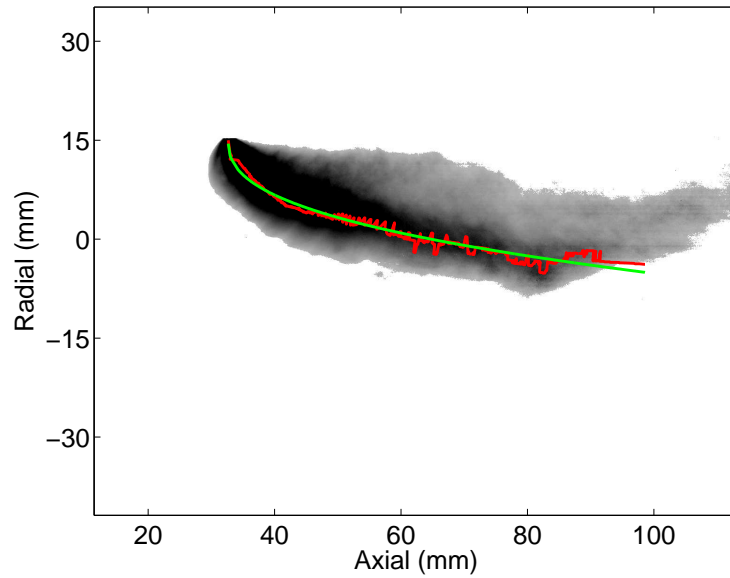


(c) 0.3ms

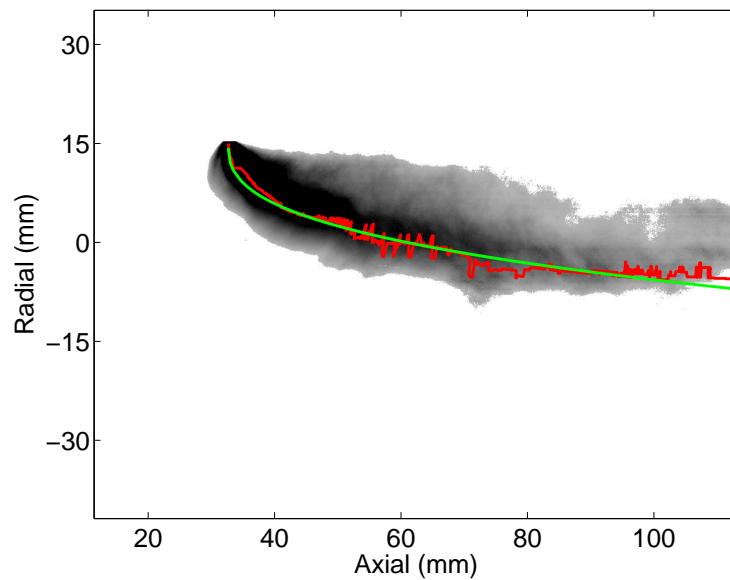


(d) 0.4ms

Figure C.4: Development of 10MPa fuel spray into $Ma_g = 0.58$ cross-flow conditions in 0.1 ms increments from 0.3 ms after SOF to 0.4 ms after SOF, corresponding to $q = 249$, $We_l = 1.5 \times 10^5$, and $We_g = 617$. Red line represents raw bend axis data, and the green line represents the curve fit.

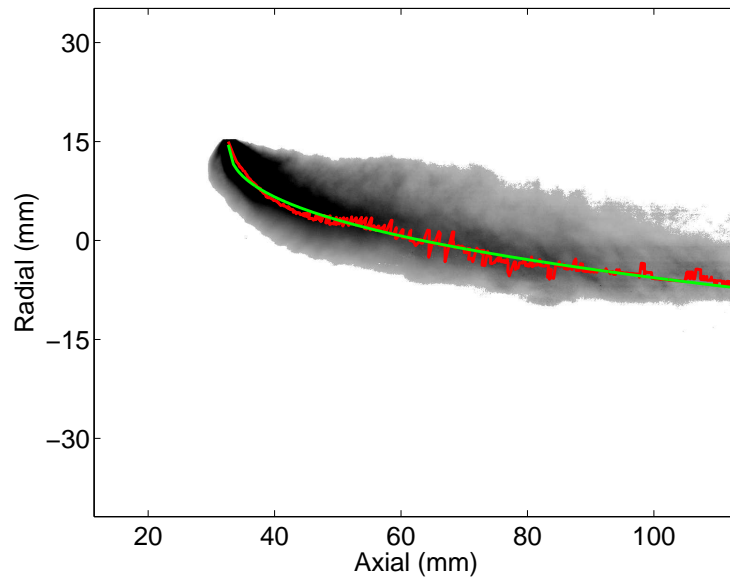


(e) 0.5ms



(f) 0.6ms

Figure C.4: Development of 10MPa fuel spray into $Ma_g = 0.58$ cross-flow conditions in 0.1 ms increments from 0.5 ms after SOF to 0.6 ms after SOF, corresponding to $q = 249$, $We_l = 1.5 \times 10^5$, and $We_g = 617$. Red line represents raw bend axis data, and the green line represents the curve fit.



(g) 0.7ms

Figure C.4: Development of 10MPa fuel spray into $Ma_g = 0.58$ cross-flow conditions 0.7 ms after SOF, corresponding to $q = 249$, $We_l = 1.5 \times 10^5$, and $We_g = 617$. Red line represents raw bend axis data, and the green line represents the curve fit.

Appendix D

Curve Fit Parameters for Spray Axis and Correlation Values

Table D.1: Definition for spray axis predictions

Ma_g	P_{inj} (MPa)	Time after SOF (ms)	Fitting Equation	a	b	c	d
0.35	15	0.1	$a * x^b$	3.6310	0.3186	N/A	N/A
0.35	15	0.2	$a * x^b$	5.3165	0.3378	N/A	N/A
0.35	15	0.3	$a * x^b$	5.2825	0.4164	N/A	N/A
0.35	15	0.4	$a * x^b$	5.2512	0.4659	N/A	N/A
0.35	15	0.5	$a * x^b$	7.4022	0.3474	N/A	N/A
0.35	15	0.6	$a * x^b$	7.1161	0.3748	N/A	N/A
0.35	15	0.7	$a * x^b$	6.6249	0.4116	N/A	N/A
0.35	15	0.8	$a * x^b$	4.9116	0.5366	N/A	N/A
0.35	15	0.9	$a * x^b$	4.2517	0.5888	N/A	N/A
0.35	15	1.0	$a * x^b$	4.8608	0.5449	N/A	N/A
0.35	10	0.1	$a * x^b$	3.6816	0.1907	N/A	N/A
0.35	10	0.2	$a * e^{b*x} +$ $c * e^{d*x}$	8.7836	0.0085	-6.5663	-0.6144
0.35	10	0.3	$a * e^{b*x} +$ $c * e^{d*x}$	15.9705	-0.0076	-10.3467	-0.1695
0.35	10	0.4	$a * e^{b*x} +$ $c * e^{d*x}$	15.3264	0.0076	-13.8055	-0.3122
0.35	10	0.5	$a * e^{b*x} +$ $c * e^{d*x}$	23.0667	-0.0036	-20.3702	-0.1288
0.35	10	0.6	$a * x^b$	7.3454	0.3259	N/A	N/A
0.35	10	0.7	$a * x^b$	7.7987	0.3103	N/A	N/A
0.35	10	0.8	$a * x^b$	8.9135	0.2752	N/A	N/A
0.35	10	0.9	$a * x^b$	7.6962	0.3178	N/A	N/A
0.35	10	1.0	$a * x^b$	7.7858	0.3120	N/A	N/A
0.58	15	0.1	$a * x^b$	5.7135	0.1270	N/A	N/A
0.58	15	0.2	$a * x^b$	5.3707	0.3118	N/A	N/A

0.58	15	0.3	$a * x^b$	3.5752	0.4811	<i>N/A</i>	<i>N/A</i>
0.58	15	0.4	$a * x^b$	4.9200	0.3700	<i>N/A</i>	<i>N/A</i>
0.58	15	0.5	$a * x^b$	4.3015	0.4219	<i>N/A</i>	<i>N/A</i>
0.58	15	0.6	$a * x^b$	2.9425	0.5337	<i>N/A</i>	<i>N/A</i>
0.58	15	0.7	$a * x^b$	2.9549	0.5359	<i>N/A</i>	<i>N/A</i>
0.58	15	0.8	$a * x^b$	2.8561	0.5346	<i>N/A</i>	<i>N/A</i>
0.58	15	0.9	$a * x^b$	2.7827	0.5615	<i>N/A</i>	<i>N/A</i>
0.58	15	1.0	$a * x^b$	3.1746	0.5053	<i>N/A</i>	<i>N/A</i>
0.58	10	0.1	$a * x^b$	3.1410	0.2869	<i>N/A</i>	<i>N/A</i>
0.58	10	0.2	$a * x^b$	5.8159	0.1945	<i>N/A</i>	<i>N/A</i>
0.58	10	0.3	$a * x^b$	4.3593	0.3554	<i>N/A</i>	<i>N/A</i>
0.58	10	0.4	$a * x^b$	3.8516	0.3959	<i>N/A</i>	<i>N/A</i>
0.58	10	0.5	$a * x^b$	3.7355	0.4009	<i>N/A</i>	<i>N/A</i>
0.58	10	0.6	$a * x^b$	4.3638	0.3695	<i>N/A</i>	<i>N/A</i>
0.58	10	0.7	$a * x^b$	3.7406	0.4058	<i>N/A</i>	<i>N/A</i>